IntechOpen

Natural Hazards

Risk, Exposure, Response, and Resilience

Edited by John P. Tiefenbacher

Natural Hazards - Risk, Exposure, Response, and Resilience

Edited by John P. Tiefenbacher

Published in London, United Kingdom







IntechOpen






Supporting open minds since 2005

Natural Hazards – Risk, Exposure, Response, and Resilience
http://dx.doi.org/10.5772/intechopen.77841
Edited by John P. Tiefenbacher

Contributors
Taro Kakinuma, Sevda Özel, Wael Zatar, Tamás János Katona, Walter Salazar, Garth Mannette, Kafele Reddock, Clevon Ash, Xueying Zhao, Zhang Shunfu, Zhao Xiaoqiu, Jian Zhu, Igor Sheremet, Orietta Nicolis, Francisco Plaza, Rodrigo Salas, Theobald Mue Mue Nji, Roland Azibo Balgah, Sergio H. Henrique Franchito, Manoel A. Gan, Julio P. Reyes Fernandez, Carlos Burguillos

First published in London, United Kingdom, 2019 by IntechOpen
IntechOpen is the global imprint of INTECHOPEN LIMITED, registered in England and Wales, registration number: 11086078, The Shard, 25th floor, 32 London Bridge Street
London, SE19SG – United Kingdom
Printed in Croatia

British Library Cataloguing-in-Publication Data
A catalogue record for this book is available from the British Library

Additional hard and PDF copies can be obtained from orders@intechopen.com

Natural Hazards – Risk, Exposure, Response, and Resilience
Edited by John P. Tiefenbacher
p. cm.
Print ISBN 978-1-78984-085-8
Online ISBN 978-1-78984-086-5
eBook (PDF) ISBN 978-1-78985-441-1

Meet the editor

Dr. John P. Tiefenbacher (BS, Carroll College, Wisconsin; MS, University of Idaho; and PhD, Rutgers University) is a professor in the Department of Geography at Texas State University in San Marcos, Texas. Dr. Tiefenbacher's research focuses on environmental (nature-society) geography. He has published on topics regarding the spatial patterns of environmental problems, the modeling of patterns of geomorphological, hydrological, and atmospheric processes, human perceptions, behavioral and spatial responses to hazards, attitudes about places and natural communities, and geographical aspects of wine. His current research focuses on adaptation to climate change, the responses of wine growers to changing climates in several regions of the world, and the modeling and assessment of the factors that determine future groundwater availability in Oaxaca, Mexico.

Contents

Preface XIII

Section 1
Assessing Risk: Elucidating Extreme Events 1

Chapter 1 3
Assessing Seismic Hazard in Chile Using Deep Neural Networks
by Francisco Plaza, Rodrigo Salas and Orietta Nicolis

Chapter 2 17
Strong Rainfall in Mato Grosso do Sul, Brazil: Synoptic Analysis and Numerical Simulation
by Sergio H. Franchito, Manoel A. Gan and Julio P. Reyes Fernandez

Chapter 3 29
Natural Hazards and Nuclear Power Plant Safety
by Tamás János Katona

Section 2
Revealing Hazard: Imagining Exposure and Impact 51

Chapter 4 53
Estimation of Shear Wave Velocity Profiles Employing Genetic Algorithms and the Diffuse Field Approach on Microtremors Array: Implications on Liquefaction Hazard at Port of Spain, Trinidad
by Walter Salazar, Garth Mannette, Kafele Reddock and Clevon Ash

Chapter 5 81
Long-Wave Generation due to Atmospheric-Pressure Variation and Harbor Oscillation in Harbors of Various Shapes and Countermeasures against Meteotsunamis
by Taro Kakinuma

Chapter 6 111
Identification and Assessment of Hazard of Development in Gypsum Karst Regions: Examples from Turkey
by Sevda Özel

Chapter 7 125
Dam Retirement and Decision-Making
by Zhao Xueying, Zhang Shunfu and Zhao Xiaoqiu

Chapter 8 143
Seismic Hazard of Viaduct Transportation Infrastructure
by Wael Zatar

Section 3
Grasping Response: Contending with Consequences 161

Chapter 9 163
Determinants of Coping Strategies to Floods and Droughts in Multiple Geo-Ecological Zones
by Theobald Mue Nji and Roland Azibo Balgah

Chapter 10 185
Emergency Communications Network for Disaster Management
by Carlos Alberto Burguillos Fajardo

Chapter 11 215
Interview of Natural Hazards and Seismic Catastrophe Insurance Research in China
by Jian Zhu

Section 4
Finding Strength by Finding Weakness: Creating Resilience in Response to Vulnerabilities 235

Chapter 12 237
Multiset-Based Assessment of Resilience of Sociotechnological Systems to Natural Hazards
by Igor Sheremet

Preface

When we interact with nature, we generally do so to gain something like space, resources, or some other advantage; and we may get just what we expect. But we may also generate risks or dangers with which we must eventually contend. Undesirable outcomes present challenges for our lives, health, or properties. Hazard management requires our awareness and understanding of the sources of risk. How is it manifested? What triggers dangerous conditions? What can be done to avoid hazards? Can we live with extreme events?

This volume includes 12 studies that address aspects of hazards from several perspectives. This research was undertaken by scholars working in diverse settings on an array of hazardous processes. The chapters are organized into four sections that reflect themes of this collection: risk assessment, hazard assessment, human responses to perceived or realized hazards, and social vulnerability and resilience. This preface introduces these themes and briefly describes the studies to highlight their connections.

In the first section, "Assessing Risk: Elucidating Extreme Events," three studies reflect the use of mathematical modeling and risk assessment to predict the dimensions and distributions of earthquakes, torrential rainstorms, and the intersections of extreme natural events and nuclear power plants. In "Assessing Seismic Hazard in Chile Using Deep Neural Networks," Plaza, Salas, and Nicolis employ machine-learning techniques, principally neural networks, to tackle the vexing problem of anticipating earthquakes. In "Strong Rainfall in Mato Grosso do Sul, Brazil: Synoptic Analysis and Numerical Simulation," Franchito, Gan, and Reyes Fernandez mathematically model meteorological conditions synoptically to determine the development of a torrential rainstorm that struck southwestern Brazil. And in "Natural Hazards and Nuclear Power Plant Safety," Katona asks whether the challenge of preparing nuclear facilities for the contingencies associated with an array of extreme natural events exceeds the industry's ability to plan for them.

The second section of this book, "Revealing Hazard: Imagining Exposure and Impact," contains five studies that examine the nature of the hazards generated by natural events impacting people and their built environments. Each study involves mathematical and graphical modeling of both the physical processes that yield the "natural" risks and the human processes that drive either activities that might be impacted or the use of hazardous environments. In "Estimation of Shear-wave Velocity Profiles Employing Genetic Algorithms and the Diffuse Field Approach on Microtremors Array: Implications on Liquefaction Hazard at Port of Spain, Trinidad," Salazar, Mannette, Reddock, and Ash employ genetic algorithms to estimate shear-wave velocity and examine the implications of microtremors in a coastal setting in Trinidad. In "Long-wave Generation Due to Atmospheric-pressure Variation and Harbor Oscillation in Harbors of Various Shapes and Countermeasures against Meteotsunamis," Kakinuma models the meteorology of pressure patterns over the East China Sea that generate atmospheric disturbances that can be transferred to ocean surfaces. These oscillations are amplified to produce long-period sea waves, so-called "meteotsunamis" that can impact coastlines,

such as the ports of Japan. Özel discusses the challenges of Turkey's karst landscapes and their attendant hazards from human use and occupancy in "Identification and Assessment of Hazards of Development in Gypsum Karst Regions." Zhao, Zhang, and Zhao, in "Dam Retirement and Decision Making," appraise two approaches (economics based and risk based) to evaluate decisions to retire and remove impoundments in China. They provide a case study of Heiwa Reservoir in east-central China to demonstrate these assessments. And in "Seismic Hazard of Viaduct Transportation Infrastructure," Zatar conducts experiments to understand the implications of the design and manufacturing of concrete forms for the stability, persistence, and failure of viaducts during strong earthquakes.

The third section, "Grasping Response: Contending with Consequences," contains three papers that describe analyses of human responses to emergencies and disasters. In "Determinants of Coping Strategies to Floods and Droughts in Multiple Geo-ecological Zones," Nji and Balgah investigate the aspects of people's lives that drive coping choices after natural disasters in Cameroon. In "Emergency Communications Network for Disaster Management," Burguillos describes a method to establish an emergency communications network for disaster conditions that may have disrupted or destroyed public and private terrestrial infrastructures. And in "Interview of Natural Hazard and Seismic Catastrophe Insurance Research in China," Zhu evaluates the prospects for the development and marketing of earthquake insurance in China, particularly considering the vulnerability of industrial structures to seismic activity.

And in the final section, "Finding Strength by Finding Weakness: Creating Resilience in Response to Vulnerabilities," is Sheremet's chapter: "Multiset-based Assessment of Resilience of Socio-technological Systems to Natural Hazards." Sheremet conceptualizes a method to evaluate the vulnerabilities of industrial-economic systems to extreme natural events. This work, like the others that precede it in this volume, demonstrates the profound importance of understanding the ramifications of our decisions to interact with nature and extreme natural processes. We make the hazards with which we must contend.

John P. Tiefenbacher
Texas State University,
San Marcos, Texas, USA

Section 1

Assessing Risk: Elucidating Extreme Events

Chapter 1

Assessing Seismic Hazard in Chile Using Deep Neural Networks

Francisco Plaza, Rodrigo Salas and Orietta Nicolis

Abstract

Earthquakes represent one of the most destructive yet unpredictable natural disasters around the world, with a massive physical, psychological, and economical impact in the population. Earthquake events are, in some cases, explained by some empirical laws such as Omori's law, Bath's law, and Gutenberg-Richter's law. However, there is much to be studied yet; due to the high complexity associated with the process, nonlinear correlations among earthquake occurrences and also their occurrence depend on a multitude of variables that in most cases are yet unidentified. Therefore, having a better understanding on occurrence of each seismic event, and estimating the seismic hazard risk, would represent an invaluable tool for improving earthquake prediction. In that sense, this work consists in the implementation of a machine learning approach for assessing the earthquake risk in Chile, using information from 2012 to 2018. The results show a good performance of the deep neural network models for predicting future earthquake events.

Keywords: deep neural networks, conditional intensity function, DFANN, RNN-LSTM, seismic hazard prediction

1. Introduction

Chile is a one of the most seismic countries in the world, with an average of a major earthquake (> 8 in Richter scale) every 10 years. The last major earthquake in Chile was registered on February 27, 2010, that affected almost 80% of the Chilean population, registering 525 deaths and several wounded. Therefore, having a better approximation or additional information on where, when an event of that magnitude could occur would represent an invaluable tool for managing and designing public policies regarding natural disasters [1, 2]. However, earthquake prediction is a very challenging task, due to its highly complex, chaotic, or nonlinear nature, and also, their occurrence depend on a multitude of variables that in most cases are yet unidentified [3, 4].

Ogata [5] introduced epidemic-type aftershock sequence (ETAS) models for seismic hazard estimation; those models and their multiple extensions [6–11] are statistical models that use a given parametrization of the expected number of events in a given region conditional on the past events, also known as the conditional ground intensity function (GIF). The GIF is associated with the occurrence rate of an earthquake and its triggering function at time t and within an (x,y) location. Aftershocks are then estimated following the seismic aftershock propagation law or Omori's law [12]. Also, it is widely used for earthquake forecast applications [11, 13, 14]. Although the ETAS models are very good for estimating the intensity function and forecasting triggering events, they normally fail to predict the risk of main events

due to their limitations in identifying foreshock events. Then, their performance could also be affected by the use of very large datasets.

Joffe et al. [15] stated that current techniques are insufficiently sensitive to allow for precise modeling of future earthquake occurrences. The above raises the importance for new approaches that consider broader and bigger sources of information. In that sense, deep learning (DL) models have state-of-art accuracy for most of the problems where statistical learning models are applied and where a precise mathematical formulation is hard to obtain. Moreover, DL methods, like deep feedforward artificial neural networks (DFANNs) and recurrent neural networks with long short-term memory (RNN-LSTM), have appeared in the last few years, with incredible success to a variety of problems: speech recognition, language modeling, translation, time series anomaly detection, and stock market prediction, to name a few [16]. This paper presents a temporal deep learning approach for ground intensity function estimation in Chile, using historical information from seismic event catalogs.

2. Methods

The general purpose for this work is to use a deep learning (DL) approach with deep feedforward artificial neural networks (DFANNs) and a recurrent neural networks with long short-term memory (RNN-LSTM) for ground intensity function estimation. First, the data are preprocessed to estimate the daily ground intensity function; then the output is used as input for the DL networks (DFANN and RNN-LSTM). Finally, both DL approaches are compared to find the best model. A description of the proposed procedure is shown in **Figure 1**.

2.1 Data

The database consisted of 86,000 seismic event records occurred in Chile, from 2000 to 2017, obtained from the National Seismological Center (http://www.sismologia.cl); each record consists of a time location (year, month, day, hour, minute, and second), a spatial location (latitude and longitude), depth (in kilometers), and magnitude (on Richter scale). **Figure 2** shows the spatial distribution of seismic events with magnitude superior to 6 (in Richter scale).

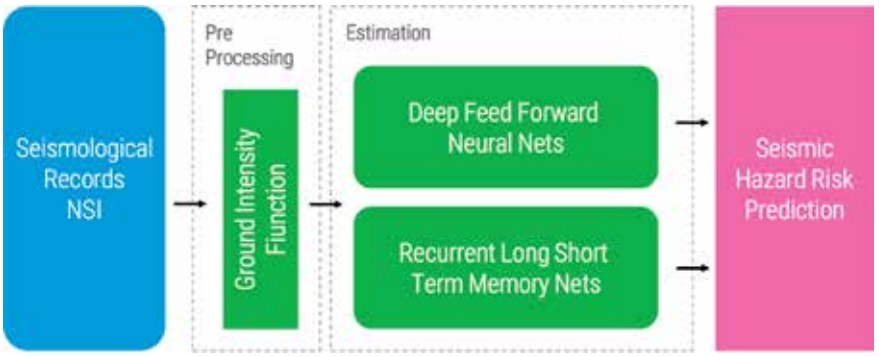

Figure 1.
Scheme for the two modular DL neural network framework: data preprocessing and estimation modules. In the data preprocessing module, all data are analyzed and prepared as inputs for the following modules; this considers estimating the daily ground intensity function. The estimation module will receive inputs from the previous model and use DFANN and RNN-LSTM DL to estimate and predict the ground intensity function.

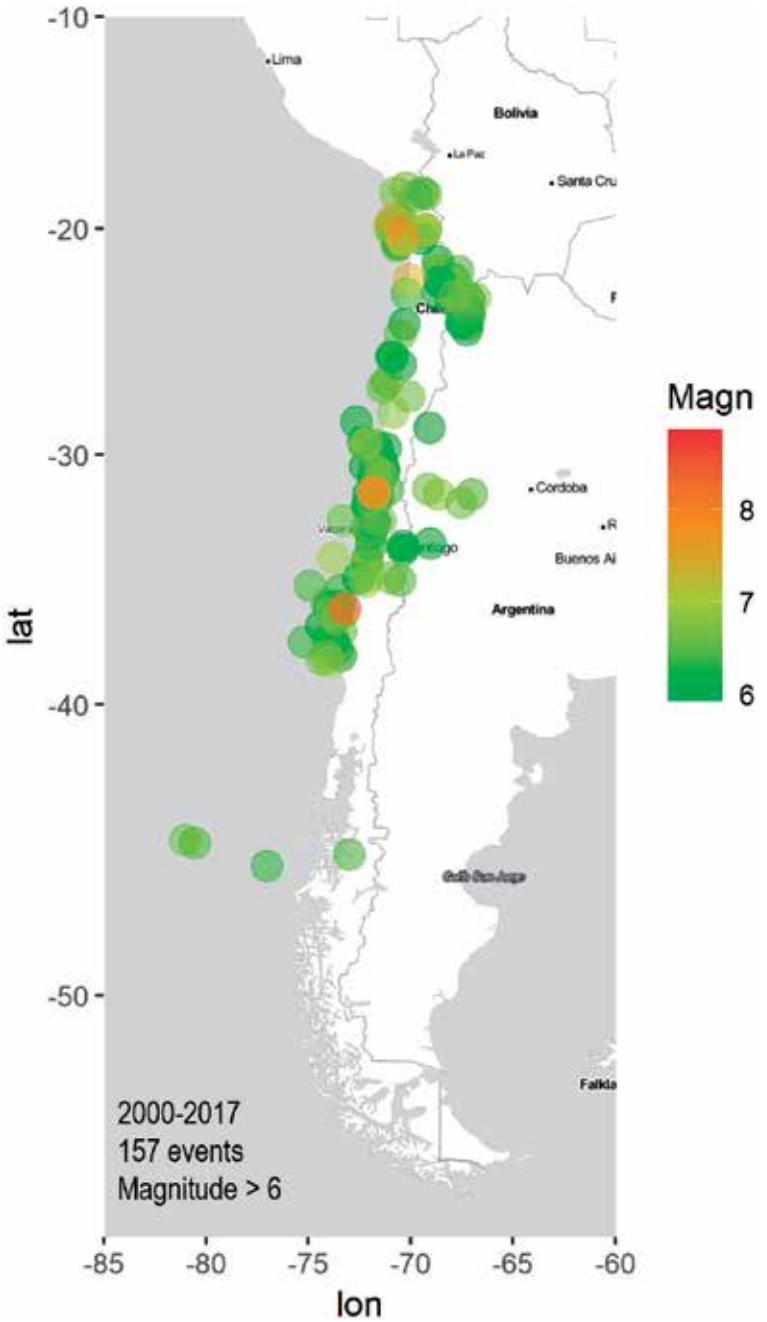

Figure 2.
Spatial distribution of seismic events (magnitude >6 Richter) for the period 2000–2017 in Chile.

2.2 Data preprocessing module

The data preprocessing module consists of estimating the conditional intensity function that represents a way of specifying how the present depends on the past in an evolutionary point process [17]. Point process models have become essential components in the assessment of seismic hazard. A particular class is given by the

self-exciting temporal point process which models events whose rate at time t may depend on the history of events at times preceding t, allowing events to trigger new events (see [18, 19] and the references within). These models appeared for the first time in applications to population genetics, and for this they are also known as epidemic-type models. Ogata [5, 20] introduced the epidemic-type aftershock sequence (ETAS) models for modeling seismic events. These models are characterized by a parametric intensity function which represents the occurrence rate of an earthquake at time t conditional on the past history of the occurrence.

ETAS models and its successive extensions have proven to be extremely useful in the description and modeling of earthquake occurrence times and locations. Self-exciting point process models [5, 19] were initially introduced in time and successively extended to the space [19]. The temporal self-exciting point processes can be defined in terms of the conditional ground intensity function (GIF):

$$\lambda_g(t|\mathcal{H}_t) = \lim_{\Delta t \downarrow 0} \frac{E[N\{(t, t + \Delta t)\}|\mathcal{H}_t]}{\Delta t} \tag{1}$$

where $N(A)$ is the number of events occurring at time $t \in A$ and $\{\mathcal{H}_t : t \geq 0\}$ is the history of all events up to time t. By denoting $t_i \in [0, T)$, a simple point process with $t_i < t_{i+1}$,the GIF can be written as

$$\lambda_g(t|\mathcal{H}_t) = \mu + \sum_{i:t_i<t} c(m_i) g(t - t_i) \tag{2}$$

where the component μ can be considered the base rate that prevents the process to die out, m_i is the magnitude at the time t_i, and g is the triggering function which determines the form of the self-excitation [5]. This process with intensity function $\lambda_g(t|\mathcal{H}_t)$ is also known as marked self-exciting point process, where the mark is given by the magnitude associated to each event. For example, the magnitude of an earthquake also influences how many aftershocks there will be.

Different parameterizations have been proposed for the functions m and f. Ogata [5] proposed the use of $c(m) = e^{\beta(m-M_t)}$ and $f(t) = \frac{K}{(t+c)^p}$, where the parameter β measures the effect of magnitude in the production of aftershocks and f is the modified Omori formula [12], with t representing the time of occurrence of the shock, K a normalizing constant depending on the lower bound of the aftershocks, and c and p are characteristic parameters of the seismic activity of a given region.

The ground intensity function estimation can be estimated using the PtProcess library available in R [21].

3. Estimation module

Once the GIF databases are obtained for each magnitude (>3, >4, >5 and >6), they are structured for estimation with the DL models. The database is separated in two groups, training and test (67 and 33% of the data, respectively). A lookback of 3 is used, meaning that the output in time t will be estimated considering a window of t_{-1}, t_{-2}, t_{-3} inputs. Also both models were trained with 100 epochs.

3.1 Deep feedforward neural networks (DFANNs)

Deep feedforward artificial neural network (DFANN), also called feedforward neural networks or multilayer perceptron, is the most popular and widely known artificial neural network. In this network, the information is propagated in a

forward direction, from the input nodes through the hidden nodes (if any) and to the output nodes. As stated by [22, 23], DFANNs are universal approximators, and the universal approximation theorem states that "every bounded continuous function with bounded support can be approximated arbitrarily closely by a multilayer perceptron by selecting enough but a finite number of hidden neurons with appropriate transfer function" [22, 24].

The goal of a DFANN is to approximate some function f^* by mapping $\hat{y} = f(\boldsymbol{x};\theta)$ and learn the value of the parameters θ that result in the best function approximation for f^* [25].

The DFANN model consists a set of elementary processing elements called neurons. These units are organized in an architecture with three types of layers: the input or sensory layer, the hidden, and the output layers. The neurons corresponding to one layer are linked to the neurons of the subsequent layer without any type of bridge, lateral, or feedback connections. The connections symbolize the flux of information between neurons. **Figure 3** illustrates the architecture of this artificial neural network with $\boldsymbol{r}$ hidden layers.

DFANN operates as follows. The input signal is received by the neurons of the input layer; these neurons are just in charge of propagating the signal to the first hidden layer, and they do not make any processing. The first hidden layer processes the signal (applying a nonlinear transformation or transfer function) and transfers it to the subsequent layer; the second hidden layer propagates the signal to the third and so on. The number of hidden layers gives the depth of the model, hence the term "deep." When the signal is received and processed by the output layer, it generates the response.

The knowledge of the DFANN is registered, by the learning algorithms, in the connections between the neurons of each layer $\boldsymbol{\theta} = \{\boldsymbol{\theta}_1, \boldsymbol{\theta}_2, \ldots, \boldsymbol{\theta}_r\}$, called weights. Several learning algorithms have been created to estimate the weights, where the most

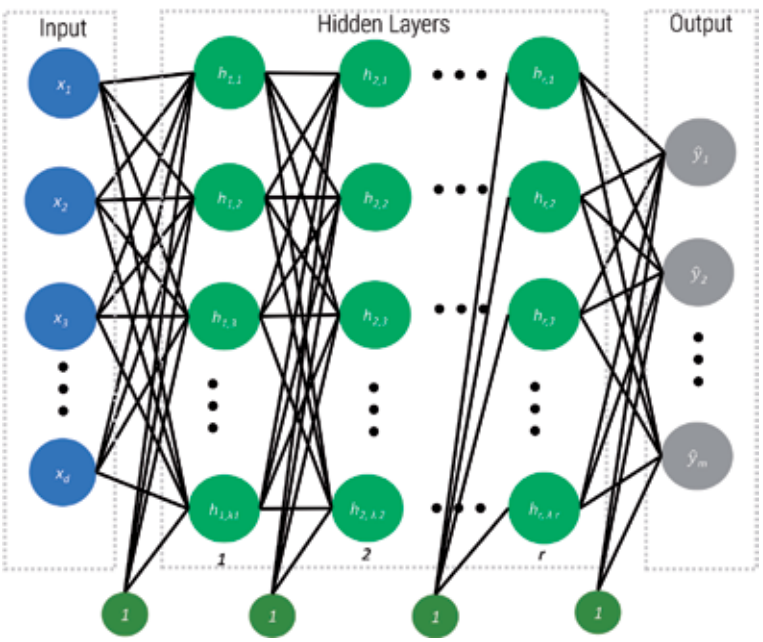

Figure 3.
Deep feedforward artificial neural network (DFANN).

popular and the first being the backpropagation, also known as generalized delta rule, popularized by [26]. The backpropagation learning algorithm is a supervised learning method and is an implementation of the Delta rule. It requires the desired output for any given input to be able to compute the output error. The main idea of the algorithm is to have a backward propagation of the errors from the output nodes to the inner nodes. For the construction of the backpropagation learning algorithm, we need to compute the gradient of the error of the network with respect to the network's modifiable weights. A DFANN network with 4 hidden layers and 12 neurons in each layer was implemented for this work.

3.2 Recurrent neural networks with long short-term memory (RNN-LSTM)

As firstly proposed by Rumelhart [26], recurrent neural networks have a primitive type of memory, in the form of recurrent layers that can operate in time [27]. Each recurrent layer takes both the output of the previous layer and an internal output of the current layer as inputs. Thus, RNNs are ideal for dealing with time series data [27]. RNNs can solve the purpose of sequence handling to a great extent but not entirely; they are great when it comes to short contexts, but to be able to build a story and remember it, the models need to be able to understand and remember the context behind longer sequences, just like a human brain. This is not possible with a simple RNN. Long short-term memory (LSTM) networks [28] are a type of RNN precisely designed to escape the long-term dependency issue of recurrent networks. LSTM recurrent networks (RNN-LSTM) have memory cells that have an internal recurrence (a self-loop), in addition to the outer recurrence of the RNN. The latter adds a nonlinear transformation to the inputs [28]. These memory cells, A, are controlled mainly by the memory door, the forgetting door ($\boldsymbol{h}_t$), and the output door. The memory door activates the entry of information to the memory cell, and the forgetting door selectively erases certain information in the memory cell and activates the storage to the next entry [29]. Finally, the output door decides what information the memory cell will emit [30]. The LSTM network structure is illustrated in **Figure 4**. Each cell has three gate activation functions σ and two output activation functions defined by tanh as a nonlinear transfer function.

In addition, they classify and predict based on time series data, since there may be delays of unknown duration between important events in a series of time. It allows clearly remembering events selected from far away in the past, which contrasts with basic NRs, for which the memory of an event decays over time [27].

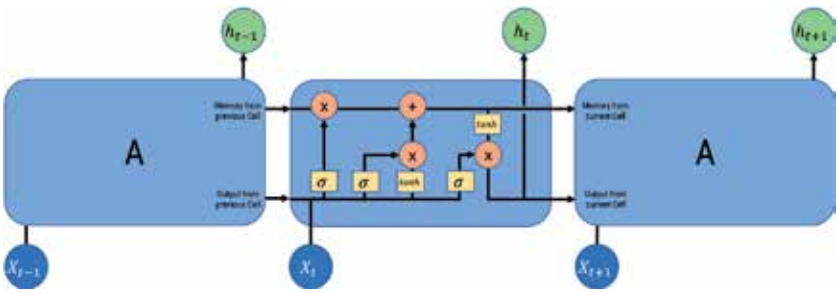

Figure 4.
LSTM cells structure, based on the work by [31].

A 1-layer RNN-LSTM with 12 cells was implemented for this work. Both DL models were implemented using Keras, with TensorFlow as backend, in Python.

4. Results

Figure 5 shows GIF estimation for the data preprocessing module, estimated for magnitudes >3, >4, >5, and >6, respectively. Note that with higher magnitudes, the GIF time series become thinner, due to the decrease of seismic events that fit in the category.

The structure implemented for both DFANN and RNN-LSTM models is shown in **Figure 6**.

The DFANN model performs slightly better than the RNN-LSTM models, in particular for lesser magnitudes (>3). **Table 1** shows the training and test performance measures (root mean square error, RMSE) for each magnitude group and DL model. Both models show better performances with magnitude >3, that is, when more information are available.

Also, a representation of the training and test results for the best model are shown in **Figure 7**. The model captures the trend very well; however, it does not perform accordingly in terms of the magnitude of the intensity function.

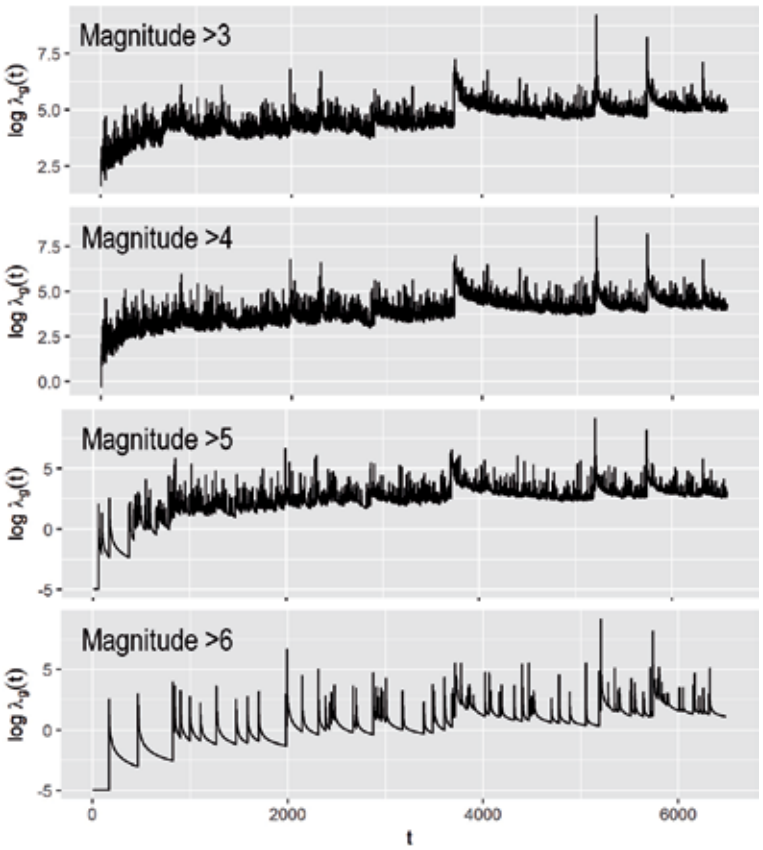

Figure 5.
Ground intensity function (GIF) estimation.

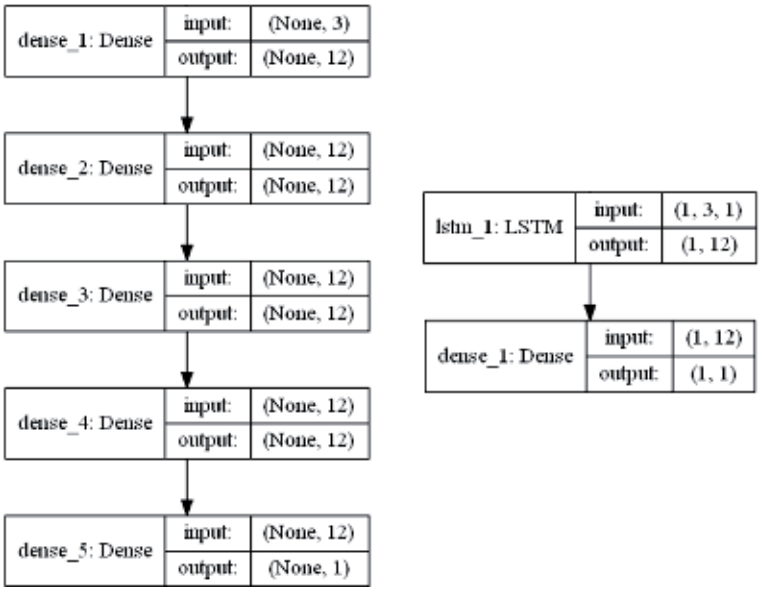

Figure 6.
Structure for the DL models, for both DFANN (on the left) and RNN-LSTM (on the right).

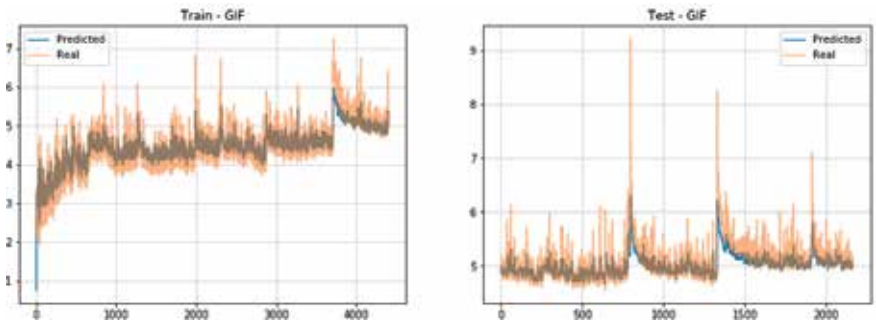

Figure 7.
Training and test groups for the best model (DFANN, Mag > 3).

RMSE training/test		
Mag	**DFANN**	**RNN-LSTM**
>3	**0.3478/0.2603**	0.5651/0.5167
>4	0.4624/0.3440	0.6698/0.4732
>5	0.5894/0.4457	0.7572/0.4449
>6	0.4226/0.4654	0.7941/0.4741

In bold the best model.

Table 1.
Root mean square error (RMSE) of the training and test groups for each DFANN and RNN-LSTM deep learning models.

5. Discussion

This work introduces a novel approach to predict the temporal ETAS-GIF alternative to the statistical approach proposed by [14]. The deep learning method has recently been used for predicting locations of aftershock events [31] especially based on ground motion data. The first use of a feedforward neural network for the prediction of seismic hazard was introduced by [32] in the spatial domain.

Possible extensions of the deep learning approach could be to include the ground motion together to other variables [30, 31] as inputs of the model and to incorporate the spatial dimension for a spatiotemporal prediction [33–35]. Some statistical techniques could be used for identifying possible patterns and inputs [36–37].

Also, since seismic events could be characterized by different features depending of the different locations of the principal events, we think that DL neural network models could be used for characterizing earthquakes in some specific seismic areas such as the local ETAS models [7, 11].

Different neural networks models could be used for comparing earthquake predictions [38]. For example, Bayesian DL neural networks could be used for a new prediction scenario considering the uncertainty of major earthquake occurrences and the probability of recurrence in a similar way to the Bayesian approach proposed by [32]. Additionally, other DL and machine learning approaches as convolutional neural networks (CNN), generative networks (GN), and random forest regression (RFR) could be implemented by incorporating the spatial component and allowing to "generate" new prediction seismic risk maps.

However, the main limitation of neural networks is that they are considered "black boxes" since it is difficult to quantify the correlation between the involved variables and their uncertainty.

6. Conclusion

This chapter deals with the estimation of seismic risk given by the temporal ETAS conditional intensity function. To achieve this goal, two deep learning models were implemented: a deep feedforward artificial neural network and a recurrent long short-term memory network. The results show a good estimation, in particular with the DFANN model. However, it should be pointed out that both implemented models could be improved by adding more hidden layers or stacking more LSTM layers in the DFANN and RNN-LSTM models, respectively. Also, exogenous variables (such as ground motion among others) could be considered for improving the predictions. Since the proposed model only considers a temporal model, extensions to the prediction of earthquake locations will be considered in future works. We think that deep learning algorithms could be useful tools for many earthquake prediction approaches.

Acknowledgements

The authors thank the National Research Center for Integrated National Disaster Management (CIGIDEN), CONICYT/FONDAP/15110017 (Chile) and CONICYT PFCHA/DOCTORADO BECAS CHILE/2018 – 21182037 for financing this work.

Author details

Francisco Plaza[1,2], Rodrigo Salas[1,3] and Orietta Nicolis[4,5*]

1 University of Valparaíso, Valparaíso, Chile

2 Institute for Fisheries Development (IFOP), Valparaíso, Chile

3 Center for Research and Development for Health Engineering, CINGS-UV, Chile

4 University of Andres Bello, Viña del Mar, Chile

5 National Research Center for Integrated National Disaster Management (CIGIDEN), Chile

*Address all correspondence to: orietta.nicolis@unab.cl

References

[1] Lomnitz C. Major earthquakes of Chile: A historical survey, 1535-1960. Seismological Research Letters. 2004;**75**(3):368. Available from: http://dx.doi.org/10.1785/gssrl.75.3.368

[2] Norio O, Ye T, Kajitani Y, Shi P, Tatano H. The 2011 eastern Japan great earthquake disaster: Overview and comments. International Journal of Disaster Risk Science. 2011;**2**(1):34-42

[3] Sobolev GA. Methodology, results, and problems of forecasting earthquakes. Herald of the Russian Academy of Sciences. 2015;**85**(2):107-111

[4] Cimellaro GP, Marasco S. Earthquake prediction. In: Introduction to Dynamics of Structures and Earthquake Engineering. Switzerland: Springer International Publishing AG a part of Springer Nature; 2018. pp. 263-280

[5] Ogata Y. Statistical models for earthquake occurrences and residual analysis for point processes. Journal of the American Statistical Association. 1988;**83**(401):9-27

[6] Lombardi AM, Cocco M, Marzocchi W. On the increase of background seismicity rate during the 1997-1998 Umbria-Marche, Central Italy, sequence: Apparent variation or fluid-driven triggering? Bulletin of the Seismological Society of America. 2010;**100**(3):1138-1152

[7] Ogata Y. Significant improvements of the space-time ETAS model for forecasting of accurate baseline seismicity. Earth, Planets and Space. 2011;**63**:217-229

[8] Bansal A, Ogata Y. A non-stationary epidemic type aftershock sequence model for seismicity prior to the December 26, 2004 m 9.1 Sumatra-Andaman islands mega-earthquake. Journal of Geophysical Research - Solid Earth. 2013;**118**(2013):616-629

[9] Kumazawa T, Ogata Y, et al. Nonstationary ETAS models for nonstandard earthquakes. Annals of Applied Statistics. 2014;**8**(3):1825-1852

[10] Guo Y, Zhuang J, Zhou S. An improved space-time ETAS model for inverting the rupture geometry from seismicity triggering. Journal of Geophysical Research - Solid Earth. 2015;**120**(5):3309-3323

[11] Nicolis O, Chiodi M, Adelfio G. Windowed ETAS models with application to the Chilean seismic catalogs. Spatial Statistics. 2015;**14**:151-165

[12] Utsu T. A statistical study on the occurrence of aftershocks. Geophysical Magazine. 1961;**30**:521-605

[13] Daley DJ, Vere-Jones D. An Introduction to the Theory of Point Processes. New York, USA: Springer; 2003. 469p

[14] Nicolis O, Chiodi M, Adelfio G. Space-time forecasting of seismic events in Chile. In: Earthquakes-Tectonics, Hazard and Risk Mitigation. Rijeka: InTech; 2017

[15] Joffe H, Rossetto T, Bradley C, O'Connor C. Stigma in science: The case of earthquake prediction. Disasters. 2018;**42**(1):81-100

[16] Liu W, Wang Z, Liu X, Zeng N, Liu Y, Alsaadi FE. A survey of deep neural network architectures and their applications. Neurocomputing. 2017;**234**:11-26

[17] Rasmussen JG. Temporal point processes: The conditional intensity function. Lecture Notes; 2011

[18] Reinhart A et al. A review of self-exciting spatio-temporal point processes and their applications. Statistical Science. 2018;**33**(3):299-318

[19] Hawkes AG. Spectra of some self-exciting and mutually exciting point processes. Biometrika. 1971;**58**(1):83-90

[20] Ogata Y. Space-time point-process models for earthquake occurrences. Annals of the Institute of Statistical Mathematics. 1998;**50**(2):379-402

[21] Harte D et al. PtProcess: An R package for modelling marked point processes indexed by time. Journal of Statistical Software. 2010;**35**(8):1-32

[22] Hornik K, Stinchcombe M, White H. Multilayer feedforward networks are universal approximators. Neural Networks. 1989;**2**(5):359-366

[23] White H. Artificial Neural Networks: Approximation and Learning Theory. Cambridge, MA, USA: Blackwell Publishers, Inc; 1992

[24] Cybenko G. Approximation by superpositions of a sigmoidal function. Mathematics of Control, Signals, and Systems. 1989;**2**(4):303-314

[25] Goodfellow I, Bengio Y, Courville A, Bengio Y. Deep Learning. Vol. 1. Cambridge: MIT press; 2016

[26] Rumelhart DE, Hinton GE, Williams RJ. Learning representations by back-propagating errors. Nature. 1986;**323**(6088):533-536

[27] Cady F. The Data Science Handbook. Hoboken, USA: John Wiley & Sons, Inc; 2017

[28] Hochreiter S, Schmidhuber J. Long short-term memory. Neural Computation. 1997;**9**(8):1735-1780

[29] Gers FA, Schmidhuber J, Cummins F. Learning to Forget: Continual Prediction with LSTM. 9th International Conference on Artificial Neural Networks: ICANN '99, Edinburgh, UK; 1999. p. 850-855

[30] Gers FA, Schraudolph NN, Schmidhuber J. Learning precise timing with LSTM recurrent networks. Journal of Machine Learning Research. 2002;**3**(Aug):115-143

[31] Olah C. Understanding LSTM Networks [Internet]. 2015 [cited 2018 Nov 30]. Available from: http://colah.github.io/posts/2015-08-Understanding-LSTMs/

[32] Nomura S, Ogata Y, Komaki F, Toda S. Bayesian forecasting of recurrent earthquakes and predictive performance for a small sample size. Journal of Geophysical Research - Solid Earth. 2011;**116**(B4):1-18

[33] Harichandran RS, Vanmarcke EH. Stochastic variation of earthquake ground motion in space and time. Journal of Engineering Mechanics. 1986;**112**(2):154-174

[34] Atkinson GM, Boore DM. Earthquake ground-motion prediction equations for eastern North America. Bulletin of the Seismological Society of America. 2006;**96**(6):2181-2205

[35] Rezaeian S, Der Kiureghian A. Simulation of orthogonal horizontal ground motion components for specified earthquake and site characteristics. Earthquake Engineering & Structural Dynamics. 2012;**41**(2):335-353

[36] Plaza F, Salas R, Yáñez E. Identifying ecosystem patterns from time series of anchovy (Engraulis ringens) and sardine (Sardinops sagax) landings in northern Chile. Journal of Statistical Computation and Simulation. 2018;**88**(10):1863-1881

[37] Shekhar S, Evans MR, Kang JM, Mohan P. Identifying patterns in spatial

information: A survey of methods. Wiley Interdisciplinary Reviews: Data Mining and Knowledge Discovery. 2011;**1**(3):193-214

[38] Ogata Y. A prospect of earthquake prediction research. Statistical Science. 2013;521-541

Chapter 2

Strong Rainfall in Mato Grosso do Sul, Brazil: Synoptic Analysis and Numerical Simulation

Sergio H. Franchito, Manoel A. Gan and Julio P. Reyes Fernandez

Abstract

Heavy rainfall and strong winds occurred in the South of Mato Grosso do Sul State, Brazil on 5 December 2015. In this study the synoptic conditions responsible for the storms and their social consequences are analyzed. Also, the state-of-art model (WRF) was used to simulate the atmospheric conditions in this severe event. The results showed that the storm had harmful consequences both in the cities of the region and in the interior of the state, with floods, threw down trees and impacts on the energy distribution. The synoptic analysis showed that over the Mato Grosso do Sul State at high levels occurred a region of wind difluence which was associated with convective clouds of large vertical development. This event was responsible for the heavy rainfall and strong winds in the region. The model results showed that the simulations were in good agreement with the observations. Thus, numerical weather forecast using the model may be extremely useful to obtain important information to mitigate the possible adverse effects of future severe weather events. This study forms part of a cooperative Project between National Institute for Space Research and Energy Power Company aimed to mitigate the impacts of severe events.

Keywords: heavy rainfall in Mato Grosso do Sul state, Brazil, impact of severe weather conditions, numerical model simulation

1. Introduction

The distribution and transmission of electric energy sectors are greatly affected by the climatic changes due to the global warming. Climate (and its change) is the main external agent that affects the electric energy distribution and transmission in all the world. The situation is aggravated by the increase of frequency of extreme events like tornadoes and severe storms associated to heavy rainfall, windstorms and high lightning incidence rate. Thus, studies providing useful information of the atmospheric conditions in extreme situations are essential not only for the electric energy sector but also for the national economy and people welfare. In this sense, recently the National Institute for Space Research (INPE), Brazil, and Energy Power Company developed a cooperative project aimed to mitigate the impacts of severe events. This is the first project of the Research and Development Program of the National Agency of Electric Energy (ANEEL) aimed to identify, monitoring and anticipate the occurrence of atypical severe storms that may cause climatic disasters

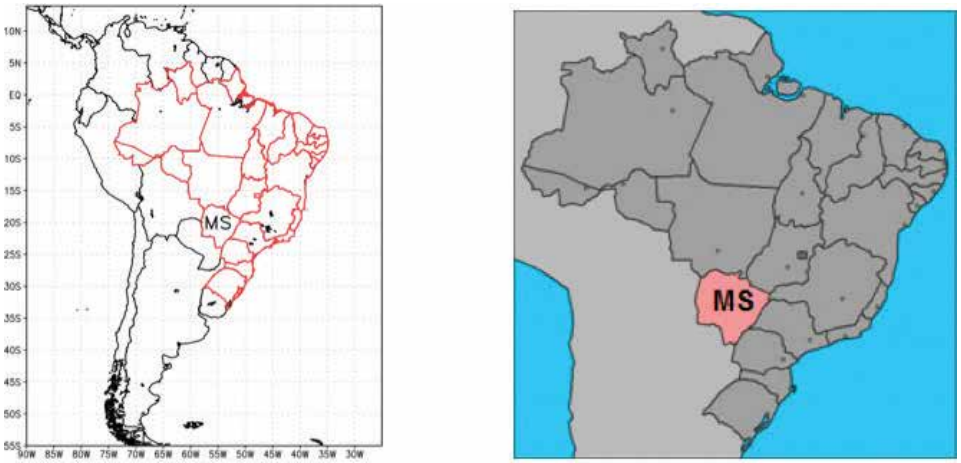

Figure 1.
Model domain of the WRF-NMM 9 km. MS in the figure indicates the location of the Mato Grosso do Sul state.

of high impact on the electric energy distribution and socioeconomic sector. One of the project components is to identify the atmospheric conditions responsible for the severe storm events and the use of a high resolution regional numerical model to obtain the meteorological variables (for example, temperature, winds, pressure, precipitation) that describe in an adequate way the atmospheric conditions favorable for the occurrence of severe storms. The study to be presented here makes part of the above project. In this chapter the event of storms in Mato do Grosso do Sul State, Brazil that occurred on 5 December 2015 is studied.

Episodes of intense rainfall and strong winds affected the south of Mato Grosso do Sul State, (**Figure 1**) during December 2015. Events of severe weather conditions can have harmful impacts on the people life since they cause floods, damage residences, interrupt the vehicles traffic and affect the energy distribution and agricultural actives [1, 2]. This chapter has a two-fold objectives: (1) to analyze the synoptic conditions and social impacts of the rainstorm that occurred on 5 December 2015; (2) to simulate the atmospheric conditions that caused this severe event using a state-of-art regional climate model. The use of a numerical model can give useful information on the evolution of synoptic systems responsible for severe events, which will occur in future and thus can be used to forecast these events. This study is not concentrate on the evaluation of the impacts on people, i.e. it is focused on the predictive model about the meteorological aspects of the storm. The chapter is organized as it follows: Section 2 presents the Data and Methodology; An analyzes of the synoptic conditions and social impacts are shown in Sections 3 and 4, respectively; Section 5 show the numerical simulations and the conclusions are presented in the final of the chapter.

2. Data and methodology

Mato do Grosso do Sul State is located in the Center-West Region of Brazil (**Figure 1**) It occupies an area of 357.125 km^2 with a population of more than 2,5 million of habitants and has a tropical climate. Three vegetation types are present in the region: pasture (east), swampland (west) and tropical forest (south).

In order to analyze the synoptic systems responsible for the severe event on 5 December 2015 data of meteorological variables obtained from the global forecast system (GFS—http://nomadis.ndc.noaa/data/gfsanl) analysis are used. To identify

the synoptic conditions on 5 December 2015 GOES satellite images are used (http://satellite.cptec.inpe.br/home/novoSite/index.jsp). The state-of-art numerical model used is the Weather Research and Forecasting-Nonhydrostatic Mesoscale Model (WRF-NMM) [3]. The damage effect of the rainstorm was illustrated using information of news agencies.

The Non-hydrostatic Mesoscale Model (NMM) core of the Weather Research and Forecasting (WRF) system is a next-generation mesoscale forecast model. The NMM model was developed by the National Oceanic and Atmospheric Administration (NOAA)/National Centers for Environment Prediction (NCEP) based on the Eta model and replaces it in 2005. The model has been designed to be an efficient and flexible mesoscale modeling system for use across a broad range of weather forecast and idealized research applications, with an emphasis on horizontal grid sizes in the range of 1–10 km. although the NMM is a fully compressible, nonhydrostatic mesoscale model it has a hydrostatic option [3]. The model uses a terrain following hybrid sigma-pressure vertical coordinate. A version of WRF-NMM tailored for hurricane forecasting, HWRF (hurricane weather research and forecasting), became operational in 2007.

The WRF/NMM model with 9 km of horizontal resolution was introduced in 2015 in the team of models of the Center of Weather Prediction and Climate Studies (CPTEC) from INPE. The model domain cover the entire South America, with 615X1392 WE/SN grid points.

In the simulation presented in this study, the model was integrated for a period of 84 h, starting from 1200 UTC 04 December 2015 (with spin-up of 12 h). A single domain with 9 km horizontal spatial resolution was configured. Initial and boundary conditions are derived from 6 h global analysis and forecast at 0.25° × 0.25° grids generated by the National Center for Environmental Prediction (NCEP)'s global forecast system (GFS). Analysis fields, including temperature, moisture, geopotential height and wind are interpolated to the mesoscale grid. These derived fields served as initial conditions for the present experiments. The domain is configured with vertical structure of 38 unequally spaced sigma (non-dimensional pressure) levels. The physical parameterizations used in this study are Geophysical Fluid Dynamics Laboratory (GFDL) [4, 5] for

Horizontal spatial resolution	9 km
Simulation duration	84 h
Initial and boundary conditions	0.25 × 0.25 GFS Operational Model
Integration time step	15 s
Map projection	Rotated latitude and longitude
Grid points WE/SN	615 × 1392
Center domain	58.234 W, 21.633S
Horizontal grid system	Arakawa E-grid
Vertical co-ordinate	38 hybrid levels
Radiation parameterization	GFDL/GFDL
Surface layer parameterization	Janjic similarity scheme
Land surface parameterization	Noah Land surface scheme
Cumulus parameterization	Betts-Miller-Janjic scheme
PBL parameterization	Mellor-Yamada-Janjic.
Microphysics	Ferrier scheme

Table 1.
The WRF model configuration used in the simulations.

long and short wave radiation, Noah Land surface scheme [6] for land surface, Mellor-Yamada-Janjic (MYJ) scheme [7] for planetary boundary layer, Ferrier scheme [8] for microphysics, and Janjic similarity scheme [9] for surface layer. **Table 1** shows the model configuration of the present study.

The use of the WRF model for studies of severe storms can be seen for example in [10–12].

Recently, a comparison of the results of the three operational models (WRF, Eta, BRAMS) of CPTEC was made. Tests of accuracy applied to the model results indicated that the WRF model has a better skill and computational performance (not published yet). So, in the present study a subjective (visual) method is used to analyze the WRF simulation of the storm.

The methodology used in the present study makes part of the cooperative project INPE-Energisa Company. Particularly, the use of the high resolution WRF model to predict severe storms is unique. So, the results obtained here may contribute to a better understanding of severe storms conditions and their prediction.

3. Analysis of the synoptic conditions

Figure 2a–f show satellite images for the day 5 December 2015 at 0600 UTC, 0900 UTC, 1200 UTC, 1500 UTC, 1800 UTC and 2100 UTC, respectively. As can

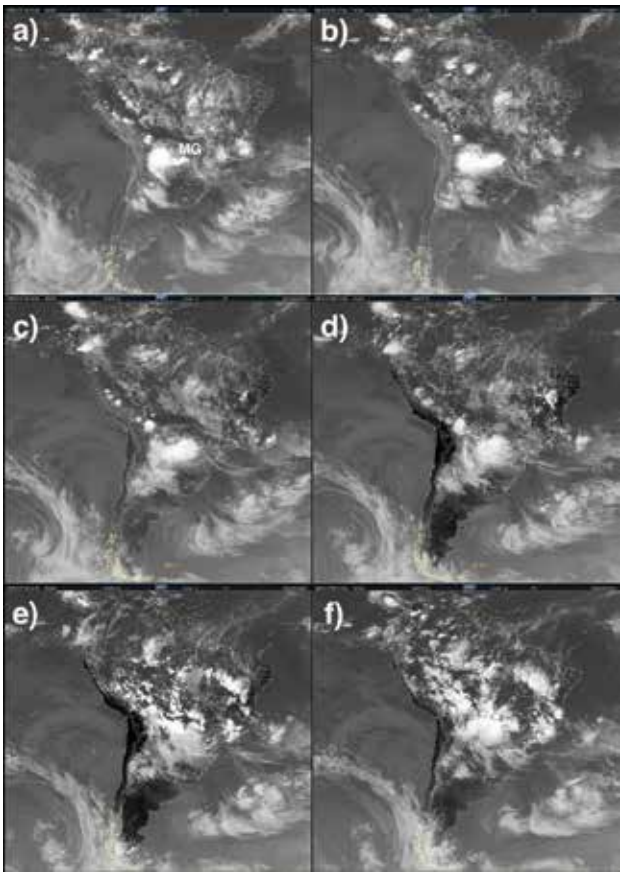

Figure 2.
Satellite images for day 5 December 2015 at (a) 0600 UTC, (b) 0900 UTC, (c) 1200 UTC, (d) 1500 UTC, (e) 1800 UTC, and (f) 2100 UTC (source: . (http://satellite.cptec.inpe.br/home/novoSite/index.jsp). MS indicates the position of Mato Grasso do Sul state.

be seen, strong convective activity started to develop in the south of Mato Grosso do Sul State during the dawn of day 5 December (**Figure 2b** and **c**). In the afternoon many convective clouds developed in most of the state (**Figure 2e** and **f**). These convective clouds were associated with the occurrence of heavy rainfall and strong wind in the region. The values of the Convective Available Potential Energy (CAPE) [13] (**Figure 3**) indicate that the atmosphere became unstable between 0600 UTC and 1200 UTC (**Figure 3a** and **b**, respectively) remaining unstable during the afternoon (**Figure 3c**). This atmospheric instability was caused by the onset of a weak cold front, as shown in **Figure 2a** and **b** and **Figure 4a** and **b**.

The presence of the cold front in the south of Mato do Grosso State provoked the change in the direction of low level winds, as can be seen in **Figure 5**. As can be noted in this figure, northwest strong winds (around 20 m s^{-1}) over Bolivia (come from Amazon region) were directed to the north of Argentina. As the cold front advanced, the direction of the winds over Bolivia changed towards the east and a convergence of mass was created due to the reduction of the magnitude of the strong northwest winds and the confluence with the south winds associated with the high pressure system behind the cold front.

At high levels (at 350 hPa) northwest winds, which come from Amazon region, were also noted (**Figure 6**). These winds rotated in a counter-clockwise direction when they reached Bolivia. It is noted that over the Mato Grosso do Sul State a region of difluence of winds occurred during the day which was associated with convective clouds of large vertical extension. This provoked the heavy rainfall and low level strong winds in many regions of the state.

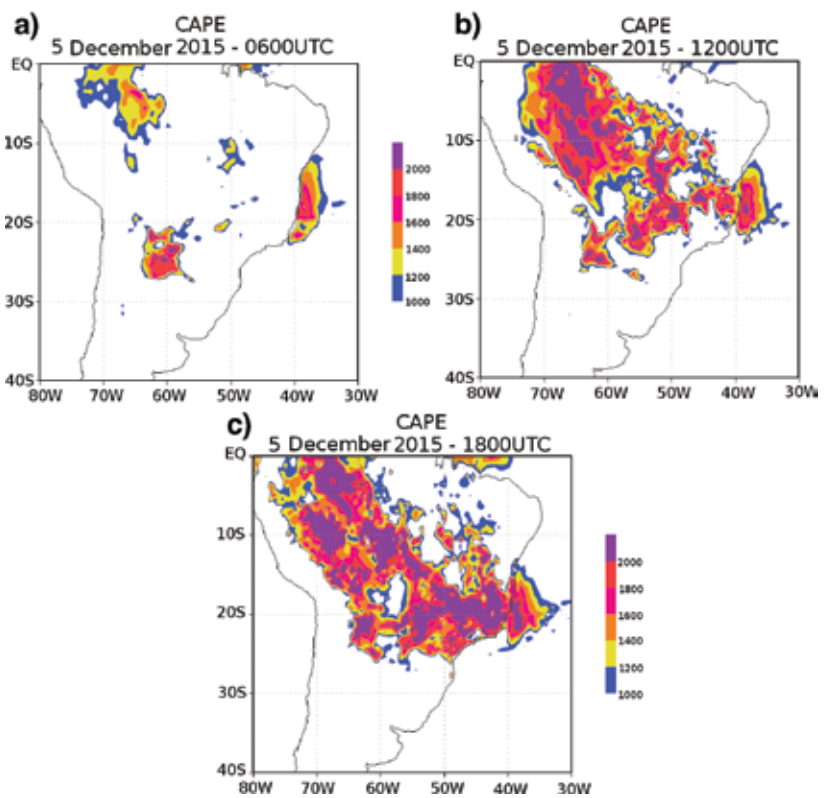

Figure 3.
Values of CAPE for day 5 December 2015 at (a) 0600 UTC, (b) 1200 UTC, and (c) 1800 UTC (source: http://nomads.ncdc.noaa.gov/data/gfsanl).

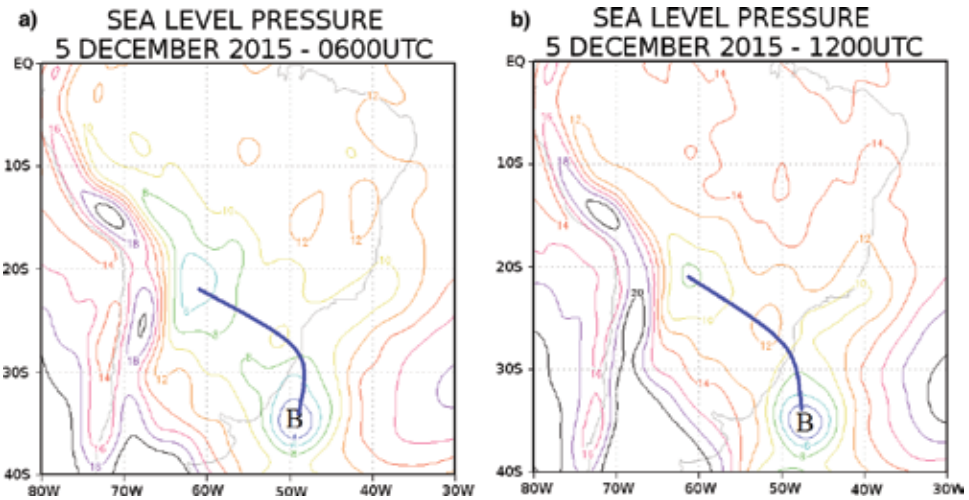

Figure 4.
Sea level surface pressure at (a) 0600 UTC and (b) 1200 UTC for day 5 December 2015. The blue line indicates the position of the cold front. B refers to the position of an extratropical cyclone.

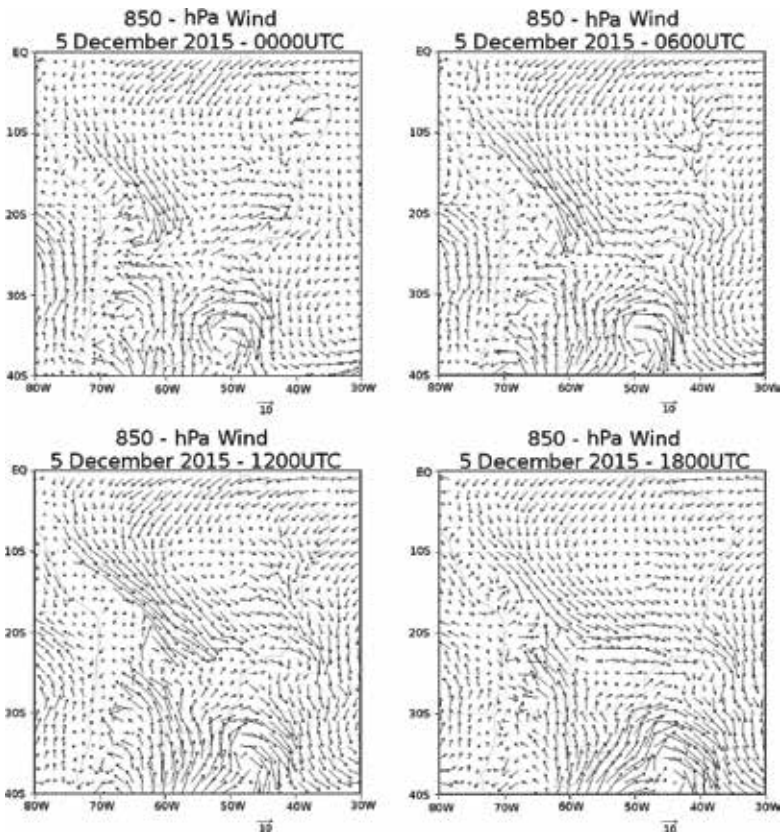

Figure 5.
Low level winds at 850 hPa at 0000 UTC, 0600 UTC, 1200 UTC and 1800 UTC for day 5 December 2015 (source: global forecast system, GFS).

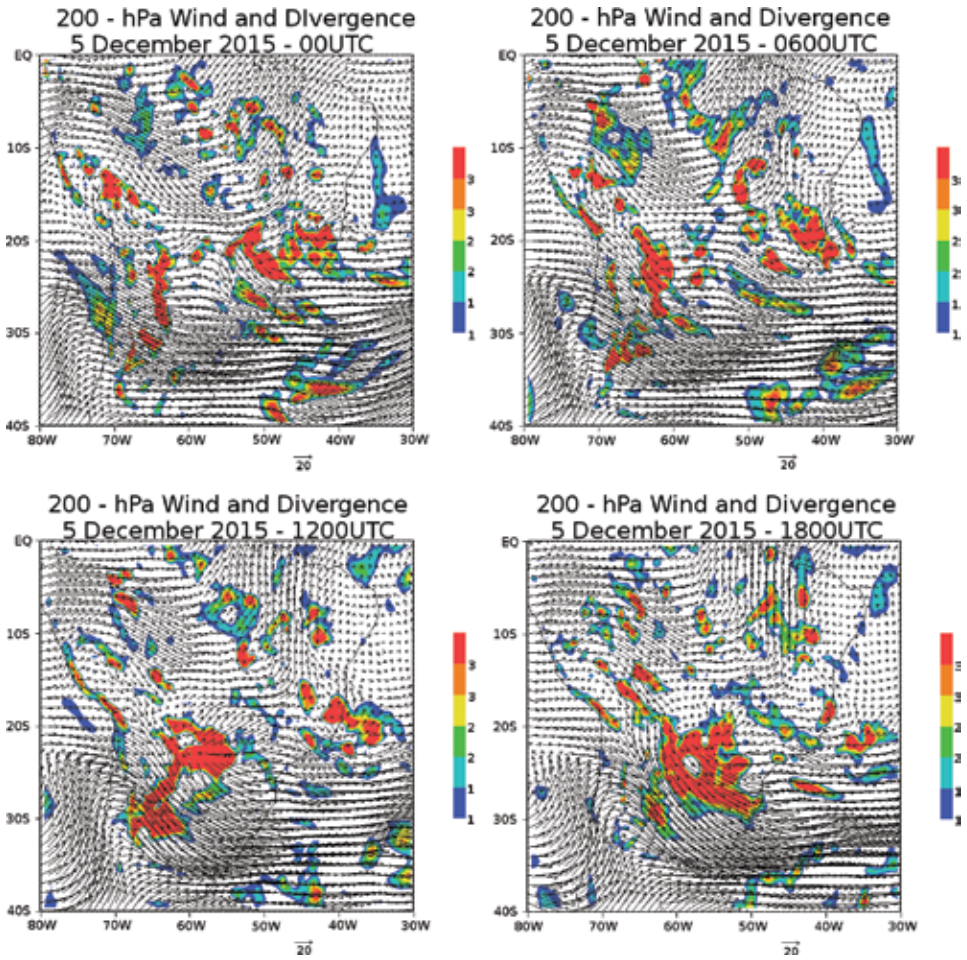

Figure 6.
High level winds and divergence of mass at 200 hPa at 0000 UTC, 0600 UTC, 1200 UTC and 1800 UTC for day 5 December 2015 (source: global forecast system, GFS).

4. Social impacts

The heavy rainfall and strong winds that occurred in the south of Mato do Grosso do Sul State on 5 December 2015 caused damage effects in the region. In the city of Campo Grande (capital of the state) the heavy rainfall persisted by 1 h and 30 min, causing threw down trees and floods in many places. In Jardim, a city at 270 km far from Campo Grande, the strong winds of 42 km h^{-1} also caused harmful effects. Many trees fell down, inclusively over cars, and a circus tumbled due to the intense winds. After the windstorm many residences remained with lack of electric energy by almost 2 h. On 7 December around 100 domiciles retained without electric energy in some places of the city of Jardim. In the highway MS-289, between Amambai e Coronel Sapucaia (two cities of Mato Grosso do Sul State), there was an overflow of a stream let so that the vehicle traffic was interrupted. The storm provoked the interdiction of 14 cities in the south of the state. **Figure** 7 illustrates the damage effects in the region.

Figure 7.
Damage effects caused by the storms on 5 December 2015 in Mato do Grosso do Sul state. Source: http://g1.globo.com/mato-grosso-do-sul/noticia/2015/12/temporal-derrubou-pontes-arvores-e-comprometeu-agua-e-luz-em-jardim.html; http://g1.globo.com/mato-grosso-do-sul/noticia/2015/12/chuva-e-ventania-de-56-kmh-causam-novos-estragos-em-dourados-ms.html).

5. Numerical simulations

In this section the WRF model is used to simulate the atmospheric conditions during the rainstorm on 5 December 2015. We used the WRF-NMM version 3.6.1 [3, 14, 15]. Details of the physical parameterization and model integration were given by [2].

As can be seen in **Figure 8a** and **b**, the sea level surface pressure field is well simulated by the model. There is good agreement between the position of the low pressure center associated with the cold front in the model and observations (point B in **Figure 4**). The change in the direction of low level winds due to the cold front is captured by the model (**Figures 5** and **9**). The model is able to simulate the region of divergence of mass in upper levels over the study region (**Figures 6** and **10**).

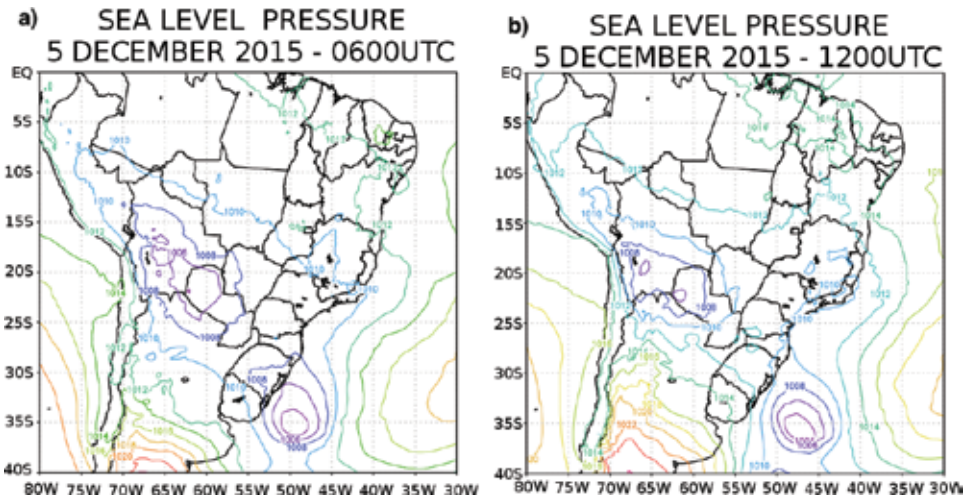

Figure 8.
Simulated sea-level pressure on day 5 December 2015 at (a) 0600 UTC and (b) 1200 UTC.

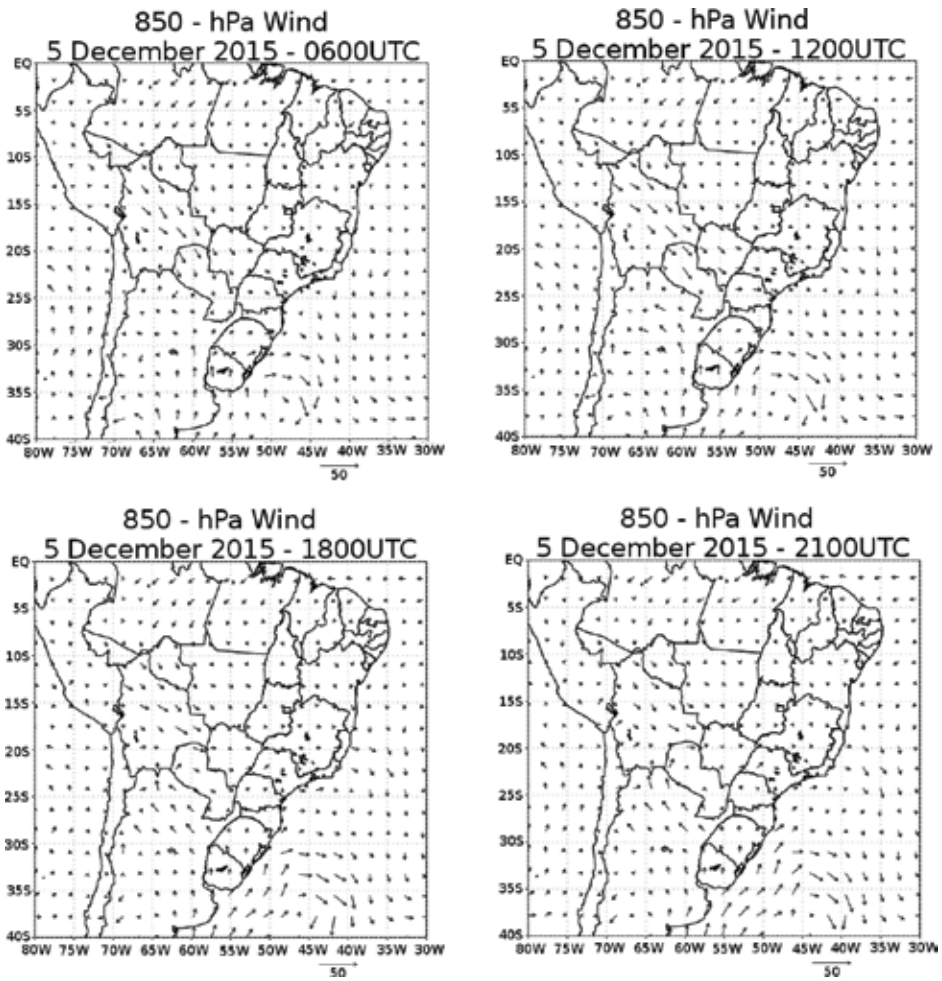

Figure 9.
Simulated low level wind at 850 hPa for day 5 December 2015 at 0600 UTC, 1200 UTC, 1800 UTC, and 2100 UTC. Units: m s^{-1}.

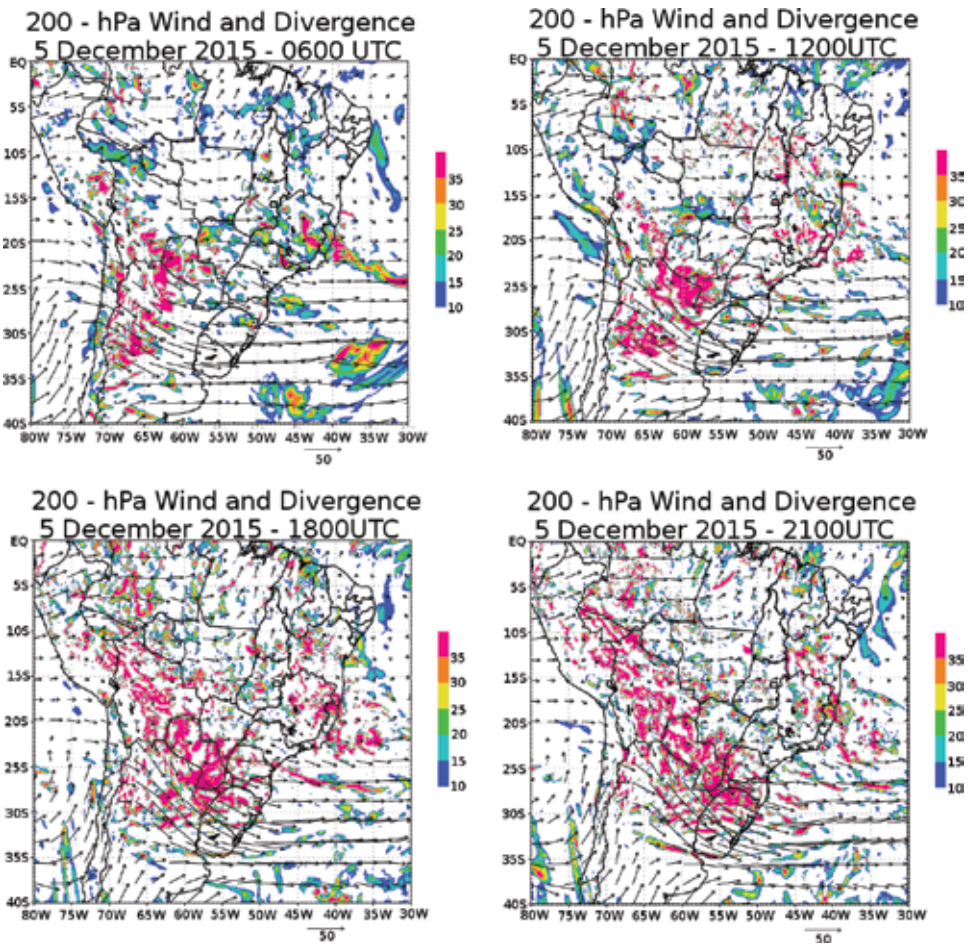

Figure 10.
Simulated divergence ($\times 10^{-5}$ s^{-1}) and high level wind at 200 hPa (m s^{-1}) for day 5 December 2015 at 0600 UTC, 1200 UTC, 1800 UTC and 2100 UTC.

The results presented above suggest that the present model may be an useful tool to forecast future events of severe weather. Nevertheless, many other experiments must be performed to have a better assessment of the model simulations.

6. Conclusions

In this study the synoptic conditions and social impacts of the severe event on 5 December 2015 in the south of Mato Grosso do Sul State, Brazil were analyzed. The results showed that the heavy rainfall and strong winds caused floods, damage in several residences and affected the distribution of electric energy not only in the region but also in the interior of the state. The synoptic analyzes showed that the windstorm was caused by a region of wind difluence at high levels which was associated with convective clouds of large vertical development. The WRF model was used to simulate the atmospheric conditions in this severe event. The modeled values of some meteorological variables were in good agreement with the observations suggesting that the model may be used in future to forecast adverse weather conditions. This study makes part of a cooperative project between the National Institute for Space Research and the Energisa power company aimed to mitigate the

impact of adverse weather conditions. The results obtained here may contribute to a better knowledge of the atmospheric conditions responsible for severe storms and provides subsidies for forecasting these events and thus cooperate with the management of the resources of the energy electric sector and civil defense.

Acknowledgements

This study makes part of the project "Management of the impact of climate severe events on the electric energy network" financed by the Energisa power company.

Conflict of interest

The authors declare that there is no conflict of interest.

Author details

Sergio H. Franchito*, Manoel A. Gan and Julio P. Reyes Fernandez
National Institute for Space Research, INPE, Sao Jose dos Campos, SP, Brazil

*Address all correspondence to: sfranchito@hotmail.com

References

[1] Franchito SH, Gan MA, Rao VB, Santo CME, Conforte JC, Pinto O Jr. Impacts of rainstorms during austral winter in Sao Paulo state, Brazil: A case study. Journal of Geography and Natural Disasters. 2016;**6**:162. DOI: 10.4172/2167-0587.1000162

[2] Franchito SH, Gan MA, Fernandez JPR, Rao VB, Santo CME. Rainstorms during spring in Sao Paulo state, Brazil: A case study of 27-28 September 2015. IIARD International Journal of Geography and Environmental Management. 2017;**3**:12-24

[3] Janjic ZI, Gerrity JP Jr, Nickovic S. An alternative approach to nonhydrostatic modeling. Monthly Weather Review. 2001;**129**:1164-1178

[4] Schwarzkopf MD, Fels SB. The simplified exchange method revisited: An accurate, rapid method for computations of infrared cooling rates and fluxes. Journal of Geophysical Research. 1991;**96**:9075-9096

[5] Lacis AA, Hansen JE. A parameterization for the absorption of solar radiation in the earth's atmosphere. Journal of the Atmospheric Sciences. 1974;**31**:118-133

[6] Ek MB, Mitchell KE, Lin Y, Rogers E, Grunmann P, Koren V, et al. Implementation of NOAH land surface model advances in the NCEP operational mesoscale Eta model. Journal of Geophysical Research. 2003;**108**(22):8851

[7] Janjic ZI. Nonsingular implementation of the Mellor–Yamada level 2.5 scheme in the NCEP Meso model. NCEP Office Note. 2002;**437**:61

[8] Ferrier BS, Lin Y, Black T, Rogers E, DiMego G. Implementation of a new grid-scale cloud and precipitation scheme in the NCEP Eta model. In: Preprints, 15th Conference on Numerical Weather Prediction, American Meteorological Society, San Antonio, TX. 2002. pp. 280-283

[9] Janjic ZI. The surface layer in the NCEP eta model. In: 11th Conf. on NWP. American Meteorological Society, Norfolk, VA. 1996. pp. 354-355

[10] Weiss SJ, Bright DR, Kain JS, et al. Complementary use of short-range ensemble and 455?KM WRF-NMM model guidance for severe weather forecasting at the storm prediction Centre. In: Proceedings of the 23rd Conference on Severe Local Storms, American Meteorological Society. 2006

[11] Litta AJ, Mohanty UC, Bhan SC. Numerical simulation of a tornado over Ludhiana (India) using WRF-NMM model. Meteorological Applications. 2010;**17**(1):64-75

[12] Litta J, Mohanty UC, Kiran Prasad S, Mohapatra M, Tyagi A, Sahu SC. Simulation of tornado over Orissa (India) on March 31, 2009, using WRF-NMM model. Natural Hazards. 2009;**61**(3):1219-1242

[13] Betts AK. Thermodynamic classification of tropical convective soundings. Monthly Weather Review. 1974;**102**:760-764

[14] Janjic ZI. A nonhydrostatic model based on a new approach. Meteorology and Atmospheric Physics. 2003;**82**:271-285

[15] Skamarock WC, Klemp JB, Dudhia J, Gill DO, Barker DM, Duda MG et al. A description of the advanced research WRF version 3; NCAR technical note: NCAR/TN–475+STR. 2008. Available from: http://www.mmm.ucar.edu/wrf/users/docs/arw_v3.pdf [Accessed: 4 Feb 2010]

Chapter 3

Natural Hazards and Nuclear Power Plant Safety

Tamás János Katona

Abstract

The safety of nuclear power plants with respect of natural hazards can be ensured by adequate characterization of hazards and proven design solutions to cope with natural hazard effects. Design and severe accident management require characterization of very rare event. The events identified for the design basis and for the safety analysis are with annual probability 10^{-4}–10^{-5} and 10^{-7}, respectively. In this chapter, a brief insight into the actual issues of natural hazard safety of nuclear power plants and related scientific challenges is provided. The state of the art of ensuring safety of nuclear power plants with respect to natural hazard is briefly presented with focus on the preparedness to the accident sequences caused by rare natural phenomena. The safety relevance of different hazards and vulnerability of NPPs to different hazards are discussed. Specific attention is made to the non-predictable phenomena with sudden devastating effects like earthquakes and fault ruptures. Post-event conditions that affect the on-site and off-site accident management activities are also considered. The "specific-to-nuclear" aspects of the characterization of hazards are discussed. This is a great challenge for the sciences dealing with hazard characterization. The possibility for ensuring nuclear safety is demonstrated presenting cases when the nuclear power plants survived severe natural phenomena.

Keywords: nuclear power plant, safety, design, design basis, severe accident, operational experience

1. Introduction

Nuclear power plants (NPPs) have negligible cradle-to-grave environmental impacts. In spite of this fact, nuclear power plants (NPPs) are potentially high-risk facilities, since the consequences of a severe accident at a nuclear power plant can be enormous. Severe accidents of NPPs affect large area and have environmentally regional and economically global character [1]. The accident at the Chernobyl NPP shows the extent and severity and long-term consequences of the nuclear disasters. Natural hazard safety of nuclear power plants became an eminent importance after the Great Tohoku earthquake on the 11th of March 2011 and subsequent disaster of the Fukushima Daiichi NPP. The case of the Fukushima Daiichi NPP demonstrated the tragic outcome of the interaction between severe natural phenomena and nuclear power plant, that is, the severe natural phenomena are a great threat per itself, but their damaging effects could be multiplied when a natural phenomenon damages a hazardous facility like a

nuclear power plant. The importance of the preparedness to the natural hazards at NPPs has recently been demonstrated when the Hurricane Florence September 2018 endangered the NPPs in North and South Carolinas.

Majority of the existing nuclear power plants will be operated during the twenty-first century, and there are ongoing new construction projects. There are prestigious institutions and authors justifying that the nuclear power is needed for sustainable power supply (e.g., [2]). There are good enough reasons for continuous efforts to ensure and enhance the nuclear safety.

Protection of NPPs against natural hazard effects has been required since earlier times of industrial deployment of nuclear power. Related design requirements were getting more and more stringent with accumulated knowledge on hazards, with their consequences, as well with the development of design methodologies and supporting empirical evidences. All probable at the site natural hazards should be accounted for in the design of NPPs.

The risk due to NPPs is controlled and reduced by design means ensuring very low annual probability of a large release of radioactive substances. The acceptable annual probability limit for large release is $\leq 10^{-6}$. The concept of defense in depth (DiD) is applied for protection of the people and environment [3, 4]. According to this, a hierarchy of protective means and procedures should be designed and implemented for preventing the escalation of a failure to accidents and to maintain the integrity of physical barriers between the radioactive substances and environment, even if a protective feature fails. There are a series of physical barriers nested inside one another for separation of the radioactive substances from the environment: the fuel matrix, the fuel cladding, the primary pressure boundary, and the containment. The effectiveness of barriers should be maintained in every operational state, and the last barrier, the containment, should perform its retaining function as long as possible during accident sequences.

In this chapter, a brief insight into the actual issues of natural hazard safety and related scientific challenges is provided. The state of the art of ensuring safety of NPPs with respect to natural hazard is briefly presented with focus on the preparedness to the accident sequences caused by rare natural phenomena. The safety relevance of different hazards and vulnerability of NPPs to different hazards are discussed. Specific attention is made to the non-predictable phenomena with sudden devastating effects like earthquakes and fault ruptures. Post-event conditions that affect the on-site and off-site accident management activities are also considered. The "specific-to-nuclear" aspects of the characterization of hazards are discussed. Design and severe accident management require characterization of very rare events with annual probability 10^{-4}–10^{-5} for the design basis and up to 10^{-7} for the safety analysis. This is a great challenge for the sciences dealing with hazard characterization. There might be epistemic limitations, and a positivist approach to the possibility of learning the phenomena is questionable. The epistemic issues of natural hazard characterization and management are also briefly considered.

The approach followed in the chapter is a typical positivist, engineering approach. The hazards accounted for in the design of conventional, potentially high-risk industrial facilities, are about hundred times more likely and far less dangerous than the design-basis hazards for the nuclear power plants; apart from this cardinal difference, the development and design of nuclear power plants are carried out according to the same logic as any other technical objects, that is, the design shall be based on evidences, verified knowledge, and experimentally proven methods. The design requirements and safety analysis procedures are briefly presented with the main focus on the rare and unpredictable phenomena.

The statement of the head of the Fukushima Nuclear Accident Independent Investigation Commission should be understood, which recognized the Fukushima

accident as a typical "man-made disaster" that could be foreseen and prevented [5]. In spite of the truth of this statement, the extreme natural phenomena can cause enormous consequences at NPPs. The question is how frequent can an extreme event happen that can trigger a nuclear catastrophe, and whether the risk due to these events can be reduced to an acceptable for the society level?

Nuclear power plants are stigmatized by two severe accidents, Chernobyl accident, and by the Fukushima NPP accident caused by extreme natural phenomena. However, the operation of nuclear power plants is characterized not only by these accidents but also by more than 10,000 reactor years of positive experience. There are studies predicting 50% of chances for occurrence of a Fukushima-type accident within every 60–100 years [6] and auguring decreasing the frequency but increasing the severity of nuclear accidents. The lessons learned from the Fukushima accident changed the paradigm of the design; preparedness to extreme improbable situations became a great importance. In this chapter the availability of proven technical means against natural hazards is demonstrated on the practical examples. The presentation of the manageability of natural hazard effects should not relativize the safety issues, just providing realistic insights compared to those determined by the shock of the Fukushima catastrophe.

Natural hazards can also cause economic impact due to inability of being operated at 100% level, and/or restoration is needed for the restart of the plant. These aspects will gain more importance due to increasing severity, frequency, and duration of some hazards, for example, extremes due to climate change that affect the efficiency of nuclear power plants especially those with freshwater cooling. These aspects of vulnerability are briefly considered.

An overall presentation of the state of the art of hazard evaluation and natural hazard risk management is not intended in the chapter. The focus is limited to the recent practice of the nuclear industry.

2. Hazards and their severity

Nuclear power plant can be constructed and operated at a particular site without undue risk to the health and safety of the public by ensuring the confinement of radioactive substances. From the technical point of view, this means that some fundamental safety functions should be ensured during and after the natural phenomena: the reactor should be shut-down, subcriticality of the reactor core and the spent fuel pool should be ensured, and the fuel in the reactor core and the spent fuel pool should be cooled. The most important function is the retaining capability of the reactor containment that should be kept leak-tight as long as possible.

Plants are designed per principle of defense in depth (DiD) [3, 4], applying overlapping provisions (design, operational, etc.), so that, if a failure were to occur, it would be detected and compensated for or corrected by appropriate measures returning the plant to the normal operational conditions. In case this is not succeeding, a hierarchy of protective means and procedures are designed in preventing the escalation of a failure to accidental event, even if a protective measure fails. These protective means are redundant safety systems that are conservatively designed to withstand even effects of natural hazards beyond those accounted for in the design.

The effects of natural hazards selected for the basis of design are loads defined conservatively and used in the design calculations according to codes and standards. Therefore, in deterministic sense, the effects of natural hazards within the basis of design should not cause accidents, or any failures, called initiating events, leading to accident sequences. Off course, the probability of failure of some systems or structures is not equal to zero, but the adequate design ensures low probability of

failure with high confidence. The conservative design ensures sufficient margin to resist the effects exceeding in some extent the design-basis level.

DiD also means a box-in-box design of physical barriers for confining the radioactive substances. The first barrier is the fuel matrix, the ceramic uranium dioxide pellets, and the second one is the cladding of fuel pins. The third barrier is the pressure-retaining boundary of the primary circuit, and the fourth and very last barrier is the containment building. The heat generation by the decay of fission product in the fuel lasts long after the chain reaction is stopped. If the residual heat will not be removed, the first two barriers the fuel matrix and the cladding tubes containing the pellets will be overheated, melted, and damaged. The third barrier is the pressure-retaining boundary of the primary circuit. The fourth barrier is the containment building.

Severity of natural hazards can be categorized according to the level of DiD affected, complexity, and duration of post-event situation. The highest level of severity is caused by rare, sudden, non-predictable, beyond-design-basis events with high damaging potential that can cause sudden loss of safety functions (that is called as cliff-edge effect). Retaining capability of the containment can be lost, and significant amount of radioactive material can be released. Compared to the above case, less severe are the hazard consequences, when the fundamental safety functions can be restored or ensured by severe accident management measures, that is, the accident sequence can be controlled, and the off-site releases can be limited. Moderate severity are those hazards, effects of which are within the design margins. In this case, the control of accident sequences for limiting the radiological releases and preventing escalation to severe accidents can be ensured by design means and procedures. Less severe are the hazards with effects within the design basis, especially, if a forecast or warning of the occurrence of dangerous event is possible. The effects of these hazards are manageable by operational features and measures.

The economic losses are strictly correlated by the extent of damage, possibility, and effort needed for restoring and restarting the plant operation, doses from releases, needs, and extent of off-site measures (evacuation and decontamination of large area).

Ranking the hazards with respect to safety and economic significance:

A. Sudden, non-predictable, beyond-design-basis event with high damaging potential, beyond-design-basis, significant damages over large region hindering accident management—Large releases due to containment failure, loss of plant, and evacuation of large area (Fukushima Dai-ichi NPP, Great Tohoku Earthquake 2011).

B. Sudden, non-predictable, beyond-design-basis event with high damaging potential but within the designed margins—Justification of safety and restoration works (Kashiwazaki-Kariwa NPP, Niigata-Chuetsu Oki Earthquake, 2007, North Anna NPP, 2011).

C. Sudden, non-predictable event with high damaging potential within the design basis—Outage for limited time (Onagawa NPP, tsunami due to Great Tohoku Earthquake 2011).

D. Events with damage potential, warning, and preventive measures are possible—Outage for limited time or restart after the event (NPPs impacted by Katrina hurricane, 2005; floods at Blayais NPP, France, 1999, and at Fort Calhoun Nuclear Generating Station, USA, in 2011).

E. Warning is possible, and effects are manageable by operational features and measures—Operation at a reduced power level and no safety consequences (Cernavoda NPP, Romania, ow-river level 2009).

An exhaustive list of external hazards that can affect the safety of nuclear power plants, including the list of possible correlated and independent concurrent hazards, are given, for example, in [7]. The nuclear safety regulations use a generic formula requiring identification and characterization of natural phenomena that are specific to the region and which have the potential to affect the safety of the nuclear installation [8–11]. Examples of hazards and their possible primary consequences are presented in **Table 1**.

In **Table 1** examples of hazards are indicated, which can be or should be excluded by proper site selection (collapse of karst, avalanches, landslides). There are examples in **Table 1** for hazards, which can be excluded by engineering means (flood protection, soil improvements). Although the possibility of mitigation of some volcanic effects (tephra fallout, missiles, gas emissions, debris flows) is considered as realistic [12], it is preferable to exclude the volcanic hazard from the design basis of nuclear power plants.

The hazards accounted for in the design of the plant should be differentiated with regard their basic features: possibility of forecast, characteristic time for evolvement of phenomenon, possibility to avoid administrative or operational measures, possibility of protection of the site, and modification of adverse site features.

The earthquakes affect the site and large surrounding region. It is impossible to foresee and it happens suddenly. The effects of earthquake should be "as far as reasonably practicable" managed by design solutions even for the cases exceeding the design basis. The operators should be prepared to manage the post-earthquake extreme situations. Here, the long-lasting effect is caused by the damages at the site and in the area surrounding the plant. The dwellings of the operational personnel and the local infrastructure (transportation, communication) can be affected [13]; therefore, arrangements should be in place for the replacement of personnel and logistical support of the plant.

Contrary to the above example, reliable forecasts can be made for the majority of hydrometeorological extremes, like hurricanes, tornados, typhoons, extreme precipitation and temperatures, and floods. This allows implementation of protective measures and preparation of the NPP for the extreme situation. The operators should have procedures and means for preparedness to the possible abnormal situations. For most meteorological extremes, the implementation of protective design solutions can be combined with operation procedures for both, ensuring the safety and possible fast recovery of normal operation. Reduction of cooling capacity due to clogging of cooling water system can be managed in a similar way.

There are meteorological extremes with extended duration, for example, heat wave and drought. These long-lasting conditions can also affect the operational personnel and the logistical support of the site.

There are hazards having similar effects, for example, the straight wind and tornado missiles and hail cause an impact effect. Obviously, the hazard with the largest impact effect will dominate the design of structures important for safety.

Simultaneously occurring hazards should also be considered in the design. It is interesting to mention that almost 600 possible combinations can be identified according to [7].

There are causally connected hazards where one hazard may cause another hazard, but the other hazard can occur by themselves (like earthquake and tsunami).

HAZARDS	POSSIBLE PRIMARY CONSEQUENCES
Surface faulting at the site	If the hazard is not eliminated by site selection, loss of foundation, structural and lifeline integrity; Ultimate heat sink can also be endangered.
Ground motion vibratory effects	Loss of off-site-power; Loss of integrity and function of non-qualified SSCs; Small break loss of coolant.
Liquefaction	If the hazard is not eliminated by site selection and engineering measures, structural failures and loss of function of foundations, structures, lifeline connections. Damage of earth structures, intake channels – loss of primary heat sink; Ultimate heat sink can also be endangered.
Slope instability	If the hazard is not eliminated by site selection and engineering measures, damage of earth structures, intake channels; Loss of primary heat sink; Ultimate heat sink can also be endangered.
Tsunami	Loss of off-site-power; Loss of function of flooded SSCs.
Volcanic hazards	Eliminate by appropriate site selection
Extreme temperature	Loss of off-site-power; Reduction of cooling capacity; loss of primary heat sink;
Extreme precipitation (rain, snow)	Structural failures and loss of function of non-protected SSCs; Loss of off-site-power.
Straight wind: pressure effects on SSCs, missiles	Loss of off-site-power; Loss of integrity of non-protected structures. (Effects due to wind generated missiles are covered by the effects of tornado missiles.)
Hail	Effects due to hail are covered by other impact effects.
Drought	Reduction of cooling capacity and loss of primary heat sink – operational issues.
Tornados and cyclones: pressure effects, missiles	Loss of off-site-power and loss of structural integrity of structures not designed for tornado.
Floods, run-off due to precipitation and other cause (e.g., storm surge, wind waves, tsunami, seiche, tidal bore, landslide, failure of water control structures).	Loss of function of flooded SSCs
Frazil ice formation	Blockage of intake channel, reduction of cooling capacity and loss of primary heat sink.
Collapse, subsidence or uplift of the site surface Collapse, subsidence due to karst, caverns Unsuitable soils	Hazard should be eliminated by site selection or engineering measures, e.g., soil improvement
Other relevant for the site hazards, e.g., wild-fires, debris avalanche, landslides	Hazard should be eliminated by site selection
Biological hazards	Clogging of water intake by fish or jellyfish, clogging of air filters by leaves/insects

Table 1.
Hazards, hazard effects, and possible consequences at NPPs.

There are simultaneous hazards when one hazard is a prerequisite for a correlated hazard (earthquake-liquefaction).

There are associated hazards, which are probable to occur at the same time due to a common root cause or having same physical origin, for example, the storms and lightning and storms and extreme precipitation.

The analysis of the probability of event combinations should consider the duration of the events. The exact coincidence of the demand is decisive for the design and safety. It is possible for more than one independent natural event to occur

simultaneously at the site. Combinations of frequent hazards with similar effects should be considered carefully, since the simultaneous effects can be superimposed. It should be noted that simultaneous occurrence of two independent low-frequency hazards is considered as unreasonable.

3. Designing for safety

As it is shown above, the risks of nuclear power plants due to natural hazards can be controlled in two ways:

a. The hazards can be avoided via site selection deeming the sites unsuitable for the location of NPP.

b. Appropriate design and/or administrative measures shall be implemented for site and plant protection.

In the first case, if the effects of external events affecting the sites and the region cannot be compensated by proven engineering solutions for protection of the NPP, the site should be discarded.

The hazards can be qualified as avoided, if it is physically impossible to occur under the conditions at the site or if the hazard can be considered with a high degree of confidence to be extremely unlikely. For example, landslides should not be expected, if the site is located in a flat area; collapse of karst should not be expected if there are no karst formations below the site. Specific considerations on how to define the acceptable low probability will be given below. Rules and requirements for site survey and selection are given, for example, in [8, 10]. The International Atomic Energy Agency published a series of design guidances focusing on different hazards [12, 14–16].

In the second case, the hazards shall be properly identified, characterized, and accounted for in the design basis as required in [10]. The performance of the plant safety features should be ensured by the design and/or administrative measures for the design-basis hazard effects, that is, for the case of design-basis hazards, very low probability of failure of the safety-related SSCs should be justified with high confidence. The generic design rules and requirements are set, for example, in the [9]. The International Atomic Energy Agency published series of design guidance focusing on different hazards [17, 18]. The applicable design requirements are as follows:

- Apply reasonable design conservatism for design-basis hazards that provides sufficient margins for the case, if the effects of hazards exceeding the level accounted for in the design.
- Apply passive safety features (no need of external or emergency power supply).
- Develop pre-event preparedness and post-event procedures.
- Apply adequate means and procedures to coop with hazards that are predictable.
- Ensure that the safety systems intended to be used in design-basis accidents will be not adversely affected by the natural hazards.
- Ensure sufficient resources at multiunit sites.
- Consider temporary limitation of the off-site logistical support.

The generic design principles applicable are related either to system engineering or structural and layout aspects. These are:

- Diversity via employing different principles of operation.
- Redundancy of components and systems.
- Independence of system and components.
- Using failsafe components.
- Avoiding structural interactions.
- Ensuring physically separation of redundant safety systems.

The design solutions can also be classified as:

- Systems-solutions: inherently safe design, use of preferable passive safety systems capable to function even in the case of beyond-design-basis hazards.
- Structural solutions: optimized for hazard effect structures with sufficient capacity to avoid sudden loss of function.
- Layout solutions: separating the redundant safety systems.

For the optimal use of design means, the SSCs are usually categorized in accordance of their safety relevance and intended function during and after the natural phenomena. This allows to implement the graded approach regarding design conservatism, quality, and reliability requirements. The safety systems are usually in the highest category that should be designed to withstand high-magnitude low-annual-probability hazardous effects, while the systems needed for the continuous operation only are designed in accordance of nonnuclear building/construction codes and standards for a moderate magnitude and for 10^{-2}–10^{-3} annual probability effects, as usual.

It should be emphasized that the natural hazards affect the entire plant, all facilities at the site, or even the whole region. Therefore, the events could simultaneously challenge several redundant or diverse trains of a safety system, causing multiple failures of SSCs.

In the state-of-the-art practice, plant conditions more severe and complex as those accounted for in the design basis are considered as design extension conditions. In design extension conditions, prevention of severe accident, mitigation of the consequences of complex plant conditions, and the integrity of the containment should be maintained by additional safety features or extension of the capability of safety systems as far as is reasonably practicable.

The chances for multiple failures and complex plant conditions due to natural hazards can be rather large, if the magnitude of event exceeds those accounted for in the design.

4. Safety goal, design basis, and beyond-design-basis hazards

Let us start with a simple consideration. The simplest formulation of the risk due to some damaging effect is the $R = P_{fail} \cdot C$, where P_{fail} is the probability of the failure caused by that effect and leading to the consequences with measure C.

The probability P_{fail} depends on the probability of occurring of an event with damaging effect E, $P(E)$ and on the conditional probability of failure if the effect is equal to E, that is, $P(fail \text{ if } E)$. Thus, the total probability of failure can be written as $P_{fail} = P(E) \cdot P(fail \text{ if } E)$. The state-of-the-art design procedures and standards ensure a very low probability of failure with respect to the effects accounted for in the design, E_{DB}; this can be expressed as $P(fail \text{ if } E \le E_{DB}) \ll 1$. There are hazards damaging the potential of which can be characterized by several parameters; thus, $\boldsymbol{E} = \{E_1, E_2, \cdots, E_n\}$.

In the practice of the nuclear industry, the term "fail" could have several meanings. The term "failure" can be associated to a single component, to a system performing certain safety function, and to the entire plant, respectively. As it has been mentioned above, for ensuring the confinement of radioactive substances, the nuclear power plants are designed per principle of defense in depth. Failure of some structures, systems, and components (SSCs) can trigger a sequence of events at the plant deviating from normal operational conditions. If a sequence was considered in the design basis of the plant, the safe stable condition of the plant should be ensured by safety systems. The safety systems shall ensure the control of reactivity, that is, the chain reaction in the reactor shall be stopped, the heat generated by decay of radioactive fission elements shall be removed from the reactor core to the ultimate heat sink (to the environment), and the radioactive substances shall be confined in the fuel elements.

Thus, the term "fail" can be first linked to the core damage (CD) and to the loss of the first two barriers (fuel matrix and cladding). The annual probability of the core damage, P_{CD}, is limited by the nuclear regulations. The acceptable value for a new design should be less than 10^{-5} summarized over all accident sequences. This can be expressed as $P_{CD} = P(fail \text{ if } E) \cdot P(E) \le 10^{-5}$. Thus, the safety systems should withstand the effects of natural hazards and fulfill their intended functions for avoiding the core damage. The acceptable probability of loss of any safety function due to failure caused by natural hazards should not exceed 10^{-6}/a.

In very improbable cases when the safety features fail, and the conditions are more severe than those accounted for in the design, the radioactive releases shall be kept as low as practicable. The most important objective of this level is the protection of the confinement function. In this case, the term "fail" is linked to the large release (LR) of radioactive substances to the environment. It is as dangerous as earlier it happens in the course of the severe accident. The annual probability of the early large releases, P_{LR}, is also limited by the nuclear regulations. Its allowable value for a new design should be $P_{LR} = P(fail \text{ if } E) \cdot P(E) \le 10^{-6}$ summarized over all accident sequences. It means the acceptable value for a singular sequence should be less approximate by an order of a magnitude.

It is obvious from the above consideration that a hazard could be screened out and neglected on the basis of probabilistic consideration, if the probability of occurrence is less than the acceptable for severe accident probabilistic limit with a high degree of confidence, that is, 10^{-7}/a or less.

Since the consequences of nuclear accidents caused by natural hazards can be enormous, the risk should be reduced by selecting effects for the basis of design with very low annual probability. Therefore, the magnitude of natural hazard accounted for in the design basis should be associated to the probability 10^{-4}–10^{-5} per year depending on the strength or capacity assured by the design. Some exception is the regulation regarding the tornado hazard in the USA, where the tornado hazard is a reality due to meteorological and topographical conditions. The Nuclear Regulatory Commission has determined the best-estimate design-basis tornado wind speeds for new reactors, which correspond to the exceedance frequency of 10^{-7} per year [19]. Probably, the reason for this conservative approach is the complexity of post-event conditions.

The SSCs should be categorized regarding their safety relevance/function. A target performance, P_T, should be set to each category. The hazard exceedance frequency for the design of the particular SSC, H_D, should be selected taking into account the achievable resistance, R_H, that is the conditional probability of failure for the effects with H_D, that is, $P_T = H_D \cdot R_H$.

Care should be taken to the convolved frequency, where there are multiple parameters used to define an event. For example, it is not reasonable to consider a 10^{-4} intensity of a storm with a 10^{-4} duration of a storm unless there is a clear correlation. Obviously, there is a strong correlation between the phenomena having the same physical origin.

Regarding combinations of independent events, the same probabilistic criterion can be applied as for the single event, that is, a 10^{-4}/a earthquake should not be combined with a 10^{-4}/a strong wind. Contrary to this, for example, the combination of a big storm with a high tide could lead to the external flooding of a power plant.

Specific considerations are made in case of causal-related events, like earthquake and liquefaction, earthquake and tsunami, or earthquake and failure of structures protecting the sites.

In case of liquefaction, based on the soil date and the design-basis earthquake magnitude, the conditional probability of liquefaction can be calculated. The total probability—earthquake and liquefaction—should be less than the probabilistic screening criterion for neglecting the liquefaction hazard (see, e.g., [20]). This condition can also be formulated in terms of safety factor with respect to liquefaction. If the site soil conditions are improved by engineering methods, this probability and/or value of safety factor can be applied for acceptance criterion for the soil improvement.

There are multiple causally correlated hazards. For example, possibility of multiple causally linked hazards has been recognized at Tricastin site in France that initiated a focused safety justification in 2017 [21]. The level of the Tricastin site is 6 meters below the nearby channel level. The nuclear site is protected by embarkment. Although the embarkment would resist the maximum historically credible earthquake, it could not be excluded that it would fail if the design-basis earthquake of the plant hits the site. If the site would be flooded, loss of off-site and on-site electrical power supply and failure of the cooling systems of the reactors could be expected. Limited access to the site would hinder the emergency response. In this case the seismic resistance of the embarkment is the key question, since the plant remains safe in case of design-basis earthquake. The probability of loss of safety function in this case is defined by the probability of design-basis earthquake, since the embarkment failure and the consequent flooding are highly probable if a design-basis earthquake happens.

In case of causally linked hazards, the damaging effects of root cause event and the consequential event would not be necessarily simultaneous. The timing of effects should be considered in the design.

The above considerations with the small probabilities may seem like the usual reasoning and magic of the nuclear industry. As a matter of fact, that is the state of the art. However, this is recognized to be not sufficient. The generic design paradigm afore Fukushima Dai-ichi accident was "design for sufficient low probability of effects for ensuring the acceptable risk." The new design paradigm is "to be prepared for the impossible." Since a devastating natural event can never be completely ruled out, the necessary provisions for managing a radiological emergency situation, onsite and offsite, must be planned, tested, and regularly reviewed [22, 23].

5. Difficulties of the safe design

Two fundamental questions have to be answered here:

1. Whether the characterization of rare natural hazards can be performed with high enough assurance? The question is related to the possibility of definition of the hazard curve, which is the annual probability of an event that will occur at the NPP site with a damaging effect exceeding a given threshold.

2. Whether there are proven engineering solutions available for ensuring enough capability of NPPs to withstand safely the effects of hazards? In other words: Whether the design will ensure $P(fail\ if\ E \leq E\ DB) \ll 1$ for the conditional probability of failure? The question is related to the vulnerability/fragility of the NPP.

Presentation of the state-of-the-art methodologies for hazard evaluation is out of scope of the recent chapter. The nuclear industry is adapting the most novel scientific achievements for the site characterization and investigation (see, e.g., [24]). The hazards accounted for in the design are subject to regular review and update in countries where the regime of periodic safety review is established. Most extensive programs for natural hazard evaluation and upgrading and justification of operating plant safety have been implemented in the USA and several Eastern-European countries, where the operators should deal with the issues of underestimation of the seismic hazard for the design basis. Summary description of these programs is given in [25–28]. Events, like the Great Tohoku Earthquake, triggered an overall review, correction, and justification of hazard evaluation at the plants (see the stress test initiated by the European Union and the reviews and upgrading programs in several countries, e.g., [29, 30]).

The Fukushima accident is the worst-case example for improper characterization of tsunami hazard. The NPPs can be protected from the flooding due to tsunamis, assuming that the design-basis wave height is adequately defined and the uncertainties of the tsunami characterization are properly compensated by the conservative design. Contrary to the Fukushima Dai-ichi plant, the 14-m high seawall protected the Onagawa NPP from flooding due to tsunami [31].

The basic difficulties of the hazard characterization are the epistemic and aleatoric uncertainties that should be evaluated and accounted for.

Considering the design-basis hazards, the uncertainty is compensated by conservative approach: in the definition of the demand and calculation of the resistance of the SSCs. The generic design rules are fixed in the nuclear regulations and acceptable standards (see, e.g., [9] and [32, 33]).

It should be emphasized, that in the engineering practice, prediction of the effects of hazardous phenomena is recognized to be "a posteriori" uncertain. Therefore, the design should cope with this uncertainty not only within the design basis but also beyond.

It is required that the NPPs should be prepared for the unexpected exceedance of E_{DB} and the sudden loss of safety functions (a cliff-edge phenomena) shall be eliminated. This can be expressed as $P(fail\ if\ E \gtrsim E_{DB}) \lesssim M$, where M is some acceptable probability of failure for unfortunate cases, if the design-basis effect is exceeded by a certain value $E = E_{DB} + \delta E$.

Very important are how large should be the acceptable value of M and δE.

In the case of earthquakes exceeding the design basis, the design should provide an adequate margin to protect items ultimately necessary to prevent escalation of the event sequence to severe accident. According to the regulations, the

best-estimate approach can be adopted for the evaluation of this margin [34]. The high-confidence of low-probability of failure (HCLPF) could be the measure of the seismic margin [35, 36]. For new plants, depending on the regulatory framework and design practice, a HCLPF capacity of at least 1.67 [37] or 1.4 [38] times the design-basis peak ground acceleration is required to be demonstrated. These values are based on the conservatism of the nuclear design standards and justified by extensive studies. In the standard ASCE/SEI 43–05 [33], it is proposed to accept the probability of unacceptable performance less than about 10% for a ground motion equal to 150% of the design-basis ground motion, while for the design basis, the probability of unacceptable performance less than about a 1%.

The above concept can be adopted for other hazards as it is proposed, for example, in [37].

6. Justification of design tools and solutions

The design tools/solutions can be proven:

a. Directly by NPP experiences (events and damages).

b. Indirectly by:

- Reconnaissance and analysis of event consequences and damages (nonnuclear).
- Experiments (shaking table tests, wind tunnels, etc.).
- Numerical analysis and experiments.

From our point of view, the most important are the real NPP experiences regarding natural hazard events and consequences. There are several sources archiving the experiences of extreme natural events. The International Atomic Energy Agency International Seismic Safety Centre collected the information on the earthquake experiences reported by the operators. There are several hundreds of significant earthquakes registered within 300 km epicentral distance from NPPs.

The World Nuclear Association has also collected the data of nuclear accidents that could be compared by other industrial activities [39].

The European Commission Joint Research Centre also published a study on the external hazard-related events at NPPs [40]. According to this study, apart from earthquakes and tsunamis (Fukushima case), the fouling events (biological fouling of water intakes affecting also the ultimate heat sink and chemical fouling causing corrosion) and extreme weather conditions, including lightning strikes and floods, are dominating. A few events reported have safety significantly according to the International Nuclear Event Scale.

In the USA the Nuclear Energy Institute published a fact sheet on the response of US NPPs to natural events starting with June 2011 Missouri River (Nebraska) flooding up to September 2018 as the Hurricane Florence threatened the NPPs in the Southeast region of the USA and including also the 23rd of August 2011 beyond-design-basis seismic event at North Anna NPP in Virginia [41].

The examples show that the nuclear plants can withstand and properly respond to extreme natural events, if the design basis defined is adequate that was not the case at the Fukushima site with respect to the tsunami. The industry has the tools, the analytical and testing capabilities, and the consolidated standards to design and build safe plants.

6.1 Justification for possibility protection by the experiences of NPPs

6.1.1 Earthquakes: vibratory ground motion

There are plenty of examples demonstrating that the codes and standards accepted in the nuclear praxis ensure sufficient capacity of SSCs to withstand the ground vibratory effects of earthquakes.

Although the recorded ground motions exceeded those values for what the plants were designed, the safety consequences of the earthquakes were negligible. That was the case of Miyagi earthquake (August 2005) at the Onagawa NPP and the Chūetsu offshore earthquake (July 2007) at the site of the Kashiwazaki-Kariwa NPP [42]. In case of the Great Tohoku earthquake, the behavior of 13 nuclear units in the impacted area on the East shore of the Honshu Island demonstrated high resistance against ground vibrations due to earthquake. Even the Fukushima Dai-ichi plant survived the strong motion period of the earthquake. In August 2011 the North Anna plant in Virginia, USA, also survived a beyond-design-basis earthquake thanks to the designed and built margins. The North Anna case demonstrated also the adequacy of definition of damage criteria formulated in terms of cumulative absolute velocity and justified the correctness of predefined measure of margin. Although the ground motion experienced at the site exceeded the design-basis level, the damaging effect of the earthquake was found below the margin evaluated, and the damages were really negligible [43].

Sufficient capability of plants to withstand beyond-design-basis vibratory motion of earthquakes has been demonstrated by the stress tests performed in the European Union and by focused reviews implemented in other countries. The stress tests have been aimed to the review of seismic hazard assessments for sites of nuclear power plants and to the verification of the design bases, as well as to the evaluation of margins against external hazard (mainly earthquakes and floods) effects, whether the beyond-design-basis hazard effects can cause cliff-edge effect, that is, sudden loss of safety functions due to effects exceeding the design-basis one. Information on these programs in the European Union is provided at http://www.ensreg.eu/EU-Stress-Tests. Information regarding post-Fukushima measures in the USA are available at http://www.nrc.gov/reactors/operating/ops-experience/japan-dashboard.html and for Japan at https://www.nsr.go.jp/english/library/index.html, respectively.

6.1.2 Flooding

Food safety can be ensured by combination of technical and procedural measures, reducing the power generation or shutting down the reactors. The protection of plants against floods is feasible even at rather unfortunate sites like the Tricastin one [21]. In spite of this, floods at some sites caused safety issues. For example, at Fort Calhoun site in 2011 [41], the plant should be protected by extraordinary temporary measures. The flood and fire resulted in a 3-year shutdown of the plant. At Blayais Nuclear Power Plant in 1999 [44], the high tide and storm flooded the plant and caused an event Level 2 according to the International Nuclear Event Scale. Safety upgrading measures and improved procedures have been developed and implemented to achieve the required safety level. The case turned the attention to event combinations that are capable to cause extreme flood event. Both cases reveal the importance of design-basis definition, regular review of the hazard characterization, and checking the protection capabilities and upgrading if necessary.

The NPPs can be protected from the flooding due to tsunamis, assuming that the design-basis wave height is adequately defined and the uncertainties of the tsunami characterization is properly compensated by the conservative design. The case of Onagawa NPP demonstrates that the proper definition of the design-basis tsunami height is an essential precondition of the safety. On the 11th of March 2011 at Onagawa plant, all safety systems functioned as designed, the reactors automatically were shut down, and no damage of safety related systems, structures, and components (SSCs) occurred [31]. The Madras NPP also survived the December 2004 tsunami. Although the fatal underestimation of the design-basis tsunami wave height at the Fukushima Dai-ichi site cannot be compensated simply by designed margins, even in this case, a conscious layout of emergency diesel generator would save the plant.

6.1.3 Meteorological extremes

The extreme cold and heat should not cause design difficulties that is justified by Kola and Bilibino NPPs in subpolar region of Russia and Bushehr NPP in Iran and Madras and Kudankulam NPP in Tamil Nadu, India.

The real experiences demonstrate that the NPPs can be protected from extreme storms and hurricanes [41]. There are proven solutions to protect the NPPs against extreme winds. In August 1992 the Turkey Point NPP survived the Andrew hurricane with 230 km/h wind speed (280 km/h gusts). The Sandy hurricane in October 2012 hit 34 US plants that survived the storm. Turkey Point and St. Lucie NPPs survived the Irma hurricane in 2017.

Considering the consequences of meteorological extremes, the transmission system also can interrupt the operation, especially the combination of extremes, for example, wet snow plus wind and freezing rain plus wind. Since the hydroclimatic hazards are relatively slow and predictable phenomena, safety is also ensured by reducing the power generation or shutting down the reactors.

A design principle can be mentioned here. Considering the same safety-related structures, the impact of aircraft crash is covering the impact effects of other phenomena, for example, the tornado missiles. The latter is covering the impact of hail whatever the size of the hail is. Obviously, the design is made for the largest effect.

6.2 Indirect justification for possibility protection of NPPs

As it has been summarized above, experiences demonstrated that the plants designed in compliance with nuclear standards can survive the effects of the vibratory ground motion even due to disastrous earthquake. However, severe accidents can be caused by phenomena accompanying or generated by the earthquakes. The severe accident of the Fukushima Dai-ichi plant was caused by tsunami. Other earthquake-related damaging phenomena can be the surface faulting and the soil liquefaction.

6.2.1 Liquefaction

In case of new plant, if the potential for soil liquefaction is recognized, the site shall be qualified as unacceptable, unless proven engineering solutions are available for the soil improvement [8]. For screening out the hazard, the factor of safety to liquefaction should be calculated by conservative deterministic method, or a probabilistic liquefaction hazard analysis should be performed. In case of operating NPPs, the liquefaction hazard and its safety relevance have been recognized either by periodic

or focused safety reviews. Typical failure modes due to liquefaction are the tilting due to differential settlement, structural failures caused by tilting, and damages of lifeline connection to different buildings. The basic finding of 41 operating NPPs at soil sites in the USA [45] revealed that the liquefaction is generally not a safety issue. However, if it is the case, liquefaction could be an essential contributor to the core damage. Similar conclusion was made on the basis of seismic PSA for Paks NPP, Hungary. In this case, a justification of sufficient margin against liquefaction consequences should be made applying state-of-the-art techniques and best-estimate methodologies as for beyond-design-basis effects. Example for the sophisticated numerical analysis of liquefaction hazard and its consequences has been made for Paks NPP [46].

6.2.2 Surface displacement

According to earlier regulatory approach, the existence of surface rupture and fault displacement hazard at a site was an exclusion criterion for the site [8, 15]. As a consequence of this, the detailed evaluation of hazard and the engineering treatment of consequences for nuclear power plants remained for long time an early stage of development. The post-Fukushima hazard reviews revealed the issue (a summary description of the issue and relevant publications is given, for example, in [28]). It's trivial, an earthquake happens when two blocks of the earth suddenly slip past one another, and the energy stored up in the block is released in the form of seismic waves. Surface faulting is a displacement that reaches the earth's surface during slip along a fault. However, the manifestation and the measure of the displacement depend on the magnitude and local geology. The surface rupture/fault displacement causes mechanical effects completely differing from the effects of vibratory ground motion. That is the reason why a specific term "capable fault" has been introduced for this type of faults that is based not on seismological but on the engineering considerations. If the fault movement happens just below the plant, the consequences could be tilting, foundation and structural failures, and damages of lifelines due to differential displacements. However, the safety significance of displacement depends on the measure and type of displacement. There are sufficient engineering knowledge and analytical tools to evaluate the consequences of surface displacements as it is stated in [15, 28, 47, 48].

7. Operability of nuclear power plants during and after the events

The operability of the plant is defined by the weakest link, that is, by those non-safety-related SSCs designed/qualified to withstand low-magnitude effects of natural phenomena according to building code or conventional industrial standards (e.g., EUROCODE 8 for earthquakes). These magnitudes usually correspond to the 100 years of return period events. In case of earthquakes, the limit of continuous operation is the operation-based earthquake with approximately 100 years of return period or 475 years as per EUROCODE 8.

If the return period, T, of the lower magnitude hazard effects is 100 years, the probability of exceeding the corresponding magnitude of hazard for the entire operational lifetime (60 years) is $PE_{60} \geq 0.4528$. This is the probability of the shutdown and related economic losses caused by exceedance of magnitude of the operational level.

The relevant hazards limiting the operation for the inland freshwater-cooled plants like the Paks NPP in Hungary are the low flow rate in river and high water temperature. Controlling parameter for freshwater cooled plants is defined in terms of river water temperature measured at some distance from the hot cooling water outflow. In these cases, for safety and environmental protection, the power

generation is reduced, or the reactors are shutting down. The hydrometeorological extremes became more frequent and more severe due to climate changes. Assume that the return period of event with the given limiting magnitude will be 50 years as an average over the 60 years of operation instead of 100 years. In this case, the probability of economic losses will be $PE_{60} \geq 0.7024$. Over the timespan of 60 years, the worsening of hydrometeorological conditions and increase of the magnitude and frequency of extremes will affect the economy of the nuclear power production, especially those plants with freshwater cooling. Even if the values given above for the exceedance probability of magnitude of hazards for continuous operation might be not precise, the tendency is clearly showing the growing probability for economic losses due to climate change for any thermal power plants.

8. Conclusions

The nuclear power plants survived several extreme natural events during 17,825 reactor years of operation (as per the 1st of December 2018). In spite of the Fukushima disaster that was also avoidable, the experience is demonstrating that there are sufficient knowledge and engineering means to ensure the safety of the nuclear power plants and protect the people and environment even in case of severe natural phenomena. In the chapter the conscious approach to hazard and availability of proven technical solutions against natural hazards has been demonstrated on the practical examples.

It has to be recognized, mother Gaia can cause sad surprises, outliers, black swans, and dragon kings that should not be "ab ovo" excluded from considerations. However, these are "products" of probabilistic considerations. Probabilistic considerations that are also accounting the epistemic uncertainty should be the basis of and generic approach to hazard and safety. Although the nuclear industry is widely using the argumentation with the small probabilities, the era of neglecting low probabilities is passed. It may seem to be a fatalist attitude; the new design paradigm is to provide necessary provisions and procedures for managing severe emergency situations, since a devastating natural event can never be completely ruled out.

Living in the word of risk, we should be aware what we do not know, and our lack of knowledge should be compensated consciously. Over the centuries of industrial era, risk has been always compensated by obvious benefits for the society. Obviously and with good reasons, this has changed nowadays. There are obvious and at the same time not fully understandable reasons for sensitivity and low tolerance of the society against the nuclear industry. To overcome this, the nuclear industry is making the necessary moves also with respect to the nuclear safety against natural hazards.

Conflict of interest

The author declares that there are no conflicts of interest that might have any bearing on publishing of information/research reported in the submitted manuscript.

Author details

Tamás János Katona
University of Pécs, Pécs, Hungary

*Address all correspondence to: bata01@t-online.hu

References

[1] Pascucci-Cahen L, Patrick M. Massive radiological releases profoundly differ from controlled releases. In: EUROSAFE Forum, Brussels on 5th and 6th November 2012. Available from: https://www.eurosafe-forum.org/eurosafe2012

[2] International Atomic Energy Agency, Energy, Electricity and Nuclear Power Estimates for the Period up to 2050, Reference Data Series No. 1/37. 2017 edition. Vienna: IAEA; 2017. ISBN: 978-92-0-106117-1

[3] International Nuclear Safety Advisory Group. Basic safety principles for nuclear power plants. In: 75-INSAG-3 Rev. 1. Vienna: International Atomic Energy Agency; 1999. ISBN: 92-0-102699-4

[4] International Nuclear Safety Advisory Group. Defence in depth in nuclear safety. In: INSAG-10. Vienna: International Atomic Energy Agency; 1996. ISBN: 92-0-103295-1

[5] The official report of "The Fukushima Nuclear Accident Independent Investigation Commission" Executive summary, Published by The National Diet of Japan, The Fukushima Nuclear Accident Independent Investigation Commission, © 2012, The National Diet of Japan

[6] Wheatley S, Sovacool BK, Sornette D. Reassessing the safety of nuclear power: Short communication. Energy Research & Social Science. 2016;**15**:96-100. DOI: 10.1016/j.erss.2015.12.026

[7] Decker K, Brinkman H. List of external hazards to be considered in ASAMPSA_E, Reference ASAMPSA_E. Technical report ASAMPSA_E/WP21/D21.2/2015-10. Reference IRSN PSN-RES/SAG/2015-00085. Available from: http://asampsa.eu/wp-content/uploads/2016/06/ASAMPSA_E-WP21-D21.2_External_Hazard_List.pdf

[8] International Atomic Energy Agency. Site Survey and Site Selection for Nuclear Installations, IAEA Safety Standards Series No. SSG-35. Vienna: IAEA; 2015

[9] International Atomic Energy Agency. Safety of Nuclear Power Plants: Design, IAEA Safety Standards Series No. SSR-2/1 (Rev. 1). Vienna: IAEA; 2016. ISBN: 978-92-0-109315-8

[10] International Atomic Energy Agency. Site Evaluation for Nuclear Installations, IAEA Safety Standards Series No. NS-R-3 (Rev. 1), Vienna: IAEA; 2016 (will be superseded by a new IAEA document SSR-1)

[11] Western European Nuclear Regulators Association, Reactor Harmonisation Working Group. Guidance Document Issue T: Natural Hazards, Head Document. WENRA RHWG; 2015. Available from: http://www.wenra.org/media/filer_public/2015/04/23/wenra-rhwg_t1_guidance_on_issue_t_head_document_2015-04-21.pdf. [Accessed: 2016-08-06]

[12] International Atomic Energy Agency. Volcanic Hazards in Site Evaluation for Nuclear Installations: Specific Safety Guide, IAEA Safety Standards Series No. SSG-21. Vienna: IAEA; 2012. ISBN: 978-92-0-128110-4

[13] Katona TJ, Vilimi A. Seismic vulnerability assessment of site-vicinity infrastructure for supporting the accident management of a nuclear power plant. Science and Technology of Nuclear Installations. 2017;**2017**:7. Article ID 2929353. DOI: 10.1155/2017/2929353

[14] International Atomic Energy Agency. Geotechnical Aspects of Site Evaluation and Foundations for Nuclear Power Plants, IAEA Safety Standards Series No. NS-G-3.6. Vienna: IAEA; 2005

[15] International Atomic Energy Agency. Seismic Hazard in Site Evaluation for Nuclear Installations, IAEA Safety Standards Series No. SSG-9. Vienna: IAEA; 2010

[16] International Atomic Energy Agency. Meteorological and Hydrological Hazards in Site Evaluation for Nuclear Installations, IAEA Safety Standards Series No. SSG-18. Vienna: IAEA; 2011

[17] International Atomic Energy Agency. External Events Excluding Earthquakes in the Design of Nuclear Power Plants Series No. NS-G-1.5. Vienna: IAEA; 2003

[18] International Atomic Energy Agency. Seismic Design and Qualification for Nuclear Power Plants, Series No. NS-G-1.6. Vienna: IAEA; 2003

[19] U.S. Nuclear Regulatory Commission. Design-Basis Tornado and Tornado Missiles for Nuclear Power Plants, Regulatory Guide 1.76, Revision 1. March 2007

[20] Katona TJ. Assessment of adequate margin to liquefaction for nuclear power plants. Science and Technology of Nuclear Installations. 2018;**2018**:7 p. Article ID 3740762. DOI: 10.1155/2018/3740762

[21] Autorité de Sureté Nucléaire. Technical notice. Earthquake resistance of the Donzère-Mondragon canal embankment. Available from: http://www.french-nuclear-safety.fr/content/download/153556/1505212/version/1/file/ASN%20Technical%20Note%20Def.pdf

[22] WENRA RHWG Report—Safety of new NPP designs, Study by Reactor Harmonization Working Group RHWG, March 2013. Available from: http://www.wenra.org/media/filer_public/2013/08/23/rhwg_safety_of_new_npp_designs.pdf [Accessed: August 6, 2016]

[23] WENRA Statement—Safety of New NPP Designs. March 2013. Available from: http://www.wenra.org/media/filer_public/2013/04/05/wenra_statement_newdesigns2.pdf [Accessed: August 6, 2016]

[24] Renault PH, Abrahamson NA, Coppersmith KJ, Koller M, Roth PH, Hölker A. PEGASOS Refinement Project, Probabilistic Seismic Hazard Analysis for Swiss Nuclear Power Plant Sites. Vol. 1—Summary Report—©2013-2015 Swissnuclear, Olten 20. December 2013. Rev. 1: 20. December 2014

[25] Campbell RD et al. Seismic re-evaluation of nuclear facilities worldwide: Overview and status. Nuclear Engineering and Design. 1998;**182**:17-34

[26] Gürpinar A, Godoy A. Seismic safety of nuclear power plants in Eastern Europe. Nuclear Engineering and Design. 1998;**182**(1):47-58

[27] Katona TJ. Seismic safety analysis and upgrading of operating nuclear power plants. In: Ahmed W, editor. Nuclear Power. IntechOpen; 2012. DOI: 10.5772/51368. Available from: https://www.intechopen.com/books/nuclear-power-practical-aspects/seismic-safety-analysis-and-upgrading-of-operating-nuclear-power-plants

[28] Katona TJ. Issues of the seismic safety of nuclear power plants. In: Zouaghi T, editor. Earthquakes. IntechOpen; 2017. DOI: 10.5772/65853. Available from: https://www.

intechopen.com/books/earthquakes-tectonics-hazard-and-risk-mitigation/issues-of-the-seismic-safety-of-nuclear-power-plants

[29] OECD NEA. The Fukushima Daiichi Nuclear Power Plant Accident: OECD/NEA Nuclear Safety Response and Lessons Learnt, NEA No. 7161. Paris Cedex 16: OECD/NEA Publishing; 2016. Available from: https://www.oecd-nea.org/pub/2013/7161-fukushima2013.pdf [Accessed: 2018-07-04]

[30] U.S. Nuclear Regulatory Commission. Recommendations for enhancing reactor safety in the 21st century. The Near-Term Task Force Review of Insights from the Fukushima Dai-Ichi Accident [Internet]. 2012. Available from: http://www.nrc.gov/docs/ML1118/ML111861807.pdf [Accessed: August 4, 2016]

[31] IAEA Mission to Onagawa Nuclear Power Station to Examine the Performance of Systems. Structures and Components Following the Great East Japanese Earthquake and Tsunami, Onagawa and Tokyo, Japan. 2012. Available from: http://www.iaea.org/inis/collection/NCLCollectionStore/_Public/44/050/44050829.pdf?r=1 [Accessed: July 4, 2016]

[32] ASME Boiler and Pressure Vessel Code (BPVC). Section III: Rules for construction of nuclear power plant components, division 1. American Society of Mechanical Engineers. 2015. ISBN: 9780791869802

[33] ASCE/SEI 43-05. Seismic Design Criteria for Structures, Systems, and Components in Nuclear Facilities. Virginia: American Society of Civil Engineers; 2005. ISBN: 0-7844-0762-2

[34] International Atomic Energy Agency. Considerations on the Application of the IAEA Safety Requirements for the Design of Nuclear Power Plants, IAEA-TECDOC-1791. Vienna: IAEA; 2016 ISBN: 978-92-0-104116-6

[35] ASME/ANS RA-S-2008. Standard for Level 1/Large Early Release Frequency Probabilistic Risk Assessment for Nuclear Power Plant Applications. New York, NY: The American Society of Mechanical Engineers; 2008. 10016-5990

[36] A Methodology for Assessment of Nuclear Power Plant Seismic Margin (Revision 1), EPRI NP-6041-SLR1. August 1991, amendments April 2013 and October 2015; EPRI Research Reports Center, Palo Alto. Available from: https://www.epri.com/#/pages/product/NP-6041-SLR1/?lang=en-US [Accessed: 2016-08-04]

[37] Gürpinar A, Godoy AR, Johnson JJ. Considerations for Beyond Design Basis External Hazards in NPP Safety Analysis, Transactions, SMiRT-23, Manchester, United Kingdom. August 10-14, 2015. Division IV, Paper ID 424

[38] European Utility Requirements for LWR NPPs. 2012. Revision E. Available from: http://www.europeanutilityrequirements.org/Welcome.aspx

[39] World Nuclear Association. Safety of Nuclear Power Reactors: Appendices, Appendix 1. The Hazards of Using Energy. March 2017. Available from: http://www.world-nuclear.org/information-library/safety-and-security...of-plants/appendices/safety-of-nuclear-power-reactors-appendix.aspx [Accessed: 2018-08-04]

[40] Zerger B, Ramos MM, Veira MP. European Clearinghouse: Report on External Hazard Related Events at NPPs. European Commission Joint Research Centre, Institute for Energy and Transport, JRC83587, EUR 26104 EN. Luxembourg: Publications Office of the European Union; 2013. DOI: 10.2790/91907

[41] Nuclear Energy Institute. History of U.S. Nuclear Plants' Responses to Unusual Natural Events. Fact Sheet, October 10, 2018. Available from: https://www.nei.org/resources/fact-sheets/history-us-nuclear-plants-response-events

[42] IAEA. Preliminary Findings and Lessons Learned from the 16 July 2007 Earthquake at Kashiwazaki-Kariwa NPP, Japan. August 6-10, 2007. Available from: http://www.iaea.org/inis/collection/NCLCollectionStore/_Public/40/010/40010606.pdf [Accessed: July 4, 2016]

[43] Chokshi N C, Li Y, Graizer V. Lessons learned from post-earthquake investigations at north anna nuclear power plant, Presented at International Workshop on "Safety of Multi-Unit NPP Sites against External Natural Hazards", Mumbai, India, October 17-19, 2012. Available from: https://issc.iaea.org/show_Document.php?id=1196, [Accessed: October 24, 2012]

[44] Gorbatchev A, Mattei JM, Rebour V, Vial E. Report on Flooding of Le Blayais Power Plant on 27 December 1999. Eurosafe 2000—Challenges Arising to Nuclear Safety in the Context of Liberalization of the Electricity Markets Papers (p. v). Germany. 2001

[45] NUREG-1742. Perspectives Gained from the Individual Plant Examination of External Events (IPEEE) Program, Final Report. Vol. 1 and 2. U.S. Nuclear Regulatory Commission; 2002

[46] Katona TJ, Győri E, Bán Z, Tóth L. Assessment of liquefaction consequences for nuclear power plant paks. In: 23th Conference on Structural Mechanics in Reactor Technology. Manchester, UK, 2015.08.10-2015.08.14. Paper ID 125

[47] ANSI/ANS-2.30-2015. Criteria for Assessing Tectonic Surface Fault Rupture and Deformation at Nuclear Facilities. Illinois, USA: American Nuclear Society; 2015

[48] Japan Nuclear Safety Institute. Assessment Methods for Nuclear Power Plant against Fault Displacement, JANSI-FDE-03 Rev. 1 (Provisional Translation of Main Text). September 2013. On-site Fault Assessment Method Review Committee. Available from: http://www.genanshin.jp/archive/sitefault/data/JANSI-FDE-03r1.pdf [Accessed: 2016-07-04]

Section 2

Revealing Hazard: Imagining Exposure and Impact

Chapter 4

Estimation of Shear Wave Velocity Profiles Employing Genetic Algorithms and the Diffuse Field Approach on Microtremors Array: Implications on Liquefaction Hazard at Port of Spain, Trinidad

Walter Salazar, Garth Mannette, Kafele Reddock and Clevon Ash

Abstract

This book chapter explains the methodology to determine the shear wave velocity V_S profile employing microtremors array data at Port of Spain, Trinidad, and its implication in the seismic amplification and liquefaction hazard in the city. We divide this study into five sections; firstly, we introduce a description of the spectral autocorrelation method and the genetic algorithm schemes to retrieve the Vs and thickness of soil layers. Secondly, we validate the soil profiles via inspection of the ellipticity pattern at such sites; we also compared the observed horizontal-to-vertical spectral ratios (H/V) with the synthetic ones derived by the Diffuse Field Approach and 1D theoretical SH wave amplification functions. Thirdly, we compute the shear wave velocity in the first 30 m obtained from our genetic inversion and compared with the ones estimated by the empirical formulas based on geomorphological conditions. Fourthly, we present a preliminary liquefaction hazard map based on the level of H/V microtremor ratios and the fundamental period of vibration. Finally, we conclude with further recommendations for planning purposes in the city of Port of Spain.

Keywords: shear wave velocity, genetic algorithms, fundamental period, liquefaction

1. Methods and data

1.1 Array measurement of microtremors

Port of Spain (POS) lies on an alluvial fan deposit and forms a costal aquifer with a high water table comprising poorly sorted gravels, sand, clay, and boulders. The part of today's downtown Port of Spain closest to the sea was once an area of tidal mudflats covered by mangroves which have been reclaimed by anthropological

means. Recent studies suggested a peak ground acceleration of about 0.6 g on rock sites for a 2475 year return period in POS. Salazar et al. [1] presented a high-resolution grid of H/V spectral ratios employing 1181 mobile microtremors at Port of Spain in order to retrieve the S-wave fundamental periods of vibration of the soil and proposed a microzonation map for the city and the correspondent seismic coefficients for building design. So the main objective of this article is to validate such periods through an alternative geophysical method, namely, the microtremors array, and use them to develop a liquefaction hazard map for the city based on the same H/V spectral ratios of microtremors.

Nine microtremors array were done at nine sites in POS located on recent alluvium and reclaimed land (**Figure 1**). The objective of the microtremors array is to obtain the shear wave velocity (V_S) profile at the site by locating seven sensors that measure vertical ambient vibrations in a circular configuration (see **Figure 2** and **Table 1**). Then the main idea of deploying an array is to compare the motion of sensor (1) located in the center of the circle with the motion on sensors (2–4) separated by a distance equal to the radii "r" of the circle located in the vertexes of the triangle. Through the comparison of the vertical motion that comprises Rayleigh waves, it is possible to work backward retrieving the V_S and thickness of the soil and bedrock layers through genetic inversions. So, with the V_S profiles, it is possible to obtain the soil amplification factors to be incorporated in seismic codes for building design.

To perform the microtremors array, we use a Tokyo Sokushin 9-channel SAMTAC 802-H and the sensors VSE-15D6 with a flat response between 0.1 and 100 Hz and a 24-bit recording system of $\Delta t = 0.01$ s equivalent to 100 samples per second; the sensors measured micromotion in terms of velocity (**Figure 3**). We recorded a total of 25 min for each array in a silent environment.

Since we had a recorder with nine channels, we locate in location number 1 three channels corresponding to two horizontal and one vertical component to compute

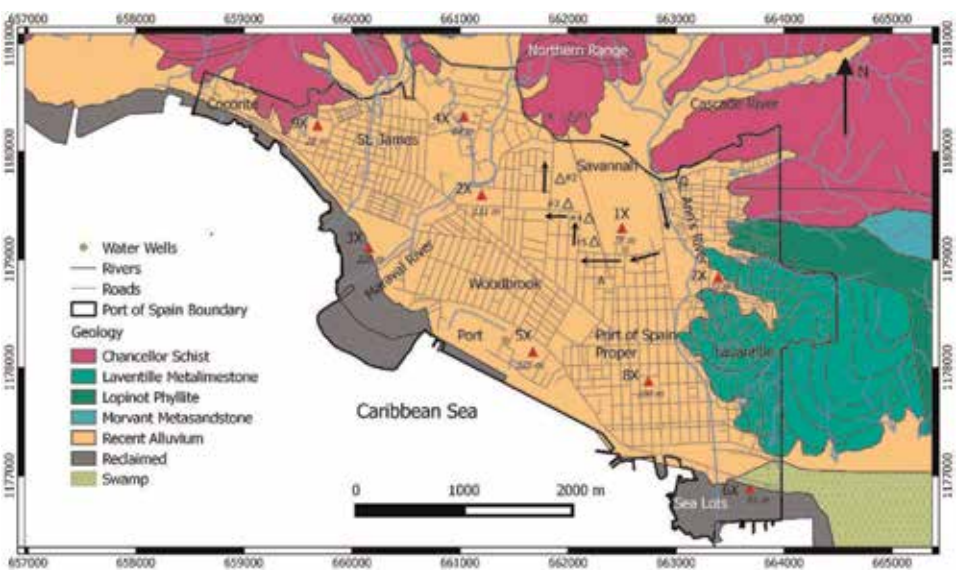

Figure 1.
*Geological map of Port of Spain. The locations of the nine microtremors array are depicted by a red solid triangle and a number with an X (e.g., 1X–9X, see **Table 1**); the corresponding thickness of sediments above the bedrock retrieved from the genetic inversions is depicted in cursive numbers. Water well data near the arrays are depicted with a solid brown circles (see thickness and soil layers classification in Figure 6 and Table 5); open triangles denote boreholes reaching the bedrock; see elevation model of section A-A in **Figure 6**. Arrows in the clockwise direction around the Queen's Park Savannah indicate the flow of constant traffic in the roundabout of 500 m radii.*

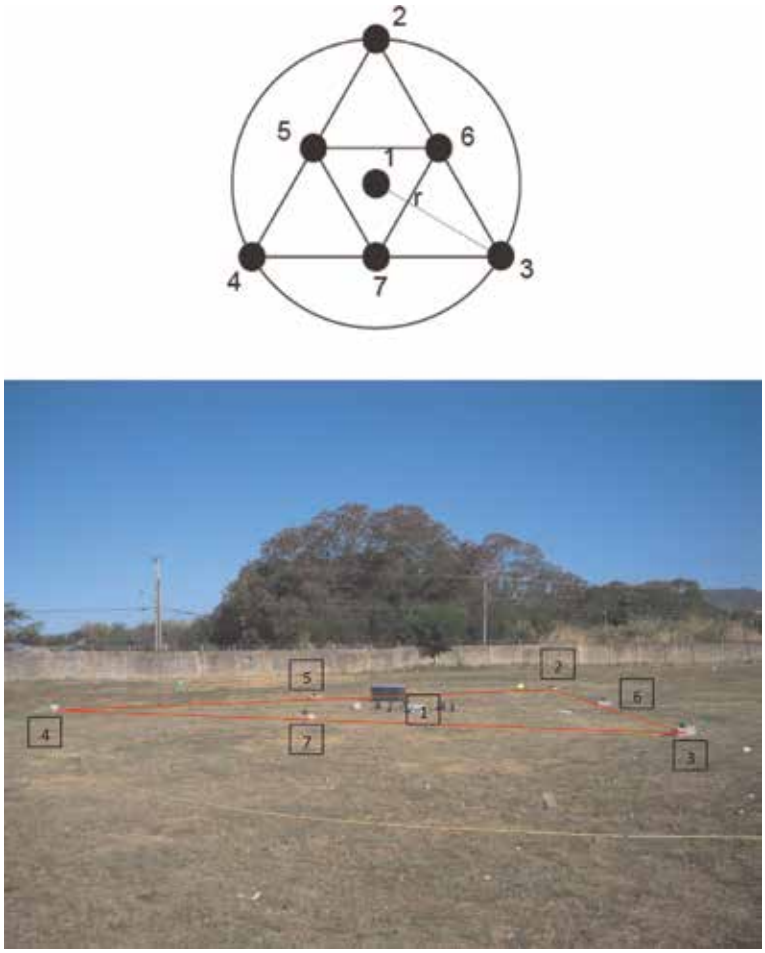

Figure 2.
Top: general microtremors array configuration in a plan view. The sensors 1, 2, 3, and 4 represent the array with the largest radii r, while the sensors 1, 5, 6, and 7 represent the array with the smallest radii r/2. Since we had a recorder of nine channels, we set in location number 1 three channels corresponding to two horizontal and one vertical component, while the remaining numbers (2–7) we locate just one vertical sensor. Bottom: photo of an array at Mucurapo Secondary School (site 3X in ***Figure 1****).*

the H/V spectral ratios [4], while in the remaining location numbers (2–7), we locate just one vertical sensor.

1.2 Spectral autocorrelation (SPAC) and dispersion curve

The comparison of the recorded vertical motion is made in the frequency domain via application of the spatial autocorrelation method (SPAC) [5, 6]. The first step in the SPAC method is to compute the cross spectra S_{ij} through Fourier transformation of the signal, and then the autocorrelation function R_{1j} of the sensor j = (2, 3, 4) in the vertex of the triangle with central site *1* yields as follows:

$$R_{1j}(f) = \frac{S_{1j}(f)}{\left[S_{11}(f)S_{jj}(f)\right]^{0.5}} \tag{1}$$

where f denotes frequency domain.

Array number	Location	Size of the array (radii r)		Maximum wavelength λ (m)	λ/max array size
		Large circle	Small circle		
1X	Queen's Park Savannah	40 m (first) 10 m (second)	20 m (first) 5 m (second)	393	9.8
2X	Nelson Mandela Park	40 m (first) 10 m (second)	20 m (first) 5 m (second)	379	9.5
3X	Mucurapo Secondary School	40 m (first) 10 m (second)	20 m (first) 5 m (second)	447	11.2
4X	Federation Park	20 m (first) 5 m (second)	10 m (first) 2.5 m (second)	280	14
5X	Port Area (Licensing Authority)	40 m (first) 10 m (second)	20 m (first) 5 m (second)	570	14.3
6X	Sea Lots	40 m (first) 10 m (second)	20 m (first) 5 m (second)	213	5.3
7X	St. Dominic's Children's Home	20 m (first) 5 m (second)	10 m (first) 2.5 m (second)	77	3.9
8X	Woodford Square	40 m (first) 10 m (second)	20 m (first) 5 m (second)	248	6.2
9X	St. James Hospital	20 m (first) 5 m (second)	10 m (first) 2.5 m (second)	117	5.9

*See general plan view and photo of an array in **Figure 2**. Maximum wavelength is calculated from dispersion curves on **Figures 5** and **7** as $\lambda = c_o/f$, where c_o is the phase velocity and f denotes frequency in Hz.*

Table 1.
*Selected sites for the microtremors array in Port of Spain (see location in **Figure 1**).*

Then the direction average of the autocorrelation function ρ (SPAC) for the three sensors separated by a radii r gives:

$$\rho(f,r) = \frac{1}{3} \sum_{j=2}^{4} R_{1j}(f,r) \tag{2}$$

The vertical motion is also compared with sensor (1) and sensors (5–7) which corresponds to a radius equal to "r/2" (**Figure 2**). We used several aperture

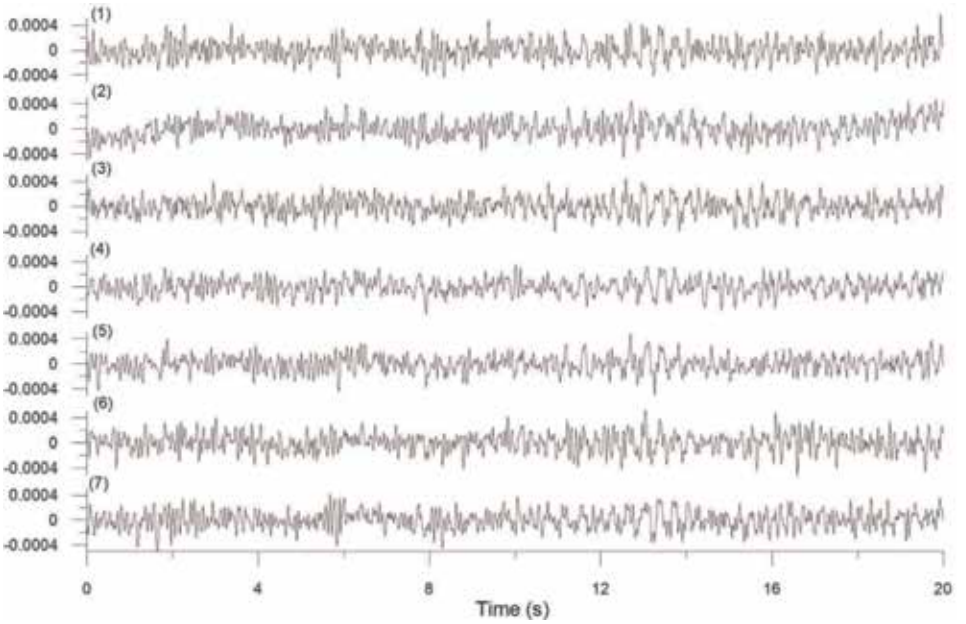

Figure 3.
Example of velocity history (cm/s) for the vertical component of the microtremors array in Mucurapo Secondary School. See the number of channel in the left upper part of each record in accordance to the array configuration in ***Figure 2****. Channel 1 corresponds to the sensor located in the center; sensors 2, 3, and 4 correspond to the radii of 40 m and sensors 5, 6, and 7 to the radii of 20 m in the vertices of the triangles.*

maximum radii between 20 and 40 m depending on the available space at the site of interest, and we repeat the procedure for a small array that corresponds to r/4 and r/8.

We present the results of the SPAC at the Queen's Park Savannah array (site 1X in **Figure 1**), for the radii of 5, 10, 20, and 40 m (**Figure 4**); we calculated the average of the SPAC for 81.92 s of stationary parts of the signal. The SPAC with values of about +1.0 means that the wave motion at short frequencies is very similar regardless of the aperture of the array, and the SPAC decreases as the frequency increases; the negative value in the SPAC represents change of polarity in the wave motion for longer frequencies (shorter periods).

To obtain the observed Rayleigh wave velocity $c_o(f)$, a 0-order Bessel function of first kind $J_o(x)$ is used as follows:

$$\rho(f,r) = Jo(x) = J_o\left(\frac{2\pi fr}{c_o(f)}\right) \tag{3}$$

Employing the argument x of the Bessel function, the phase velocity yields:

$$c_o(f) = \frac{2\pi fr}{x} \tag{4}$$

Figure 5 shows the resulting dispersion curve (phase velocity) for the Queen's Park Savannah array through the SPAC employing a 0-order Bessel function of first kind. To get a single dispersion curve, we averaged the four common parts of each phase velocity from the different array sizes and added the single reliable parts of the dispersion curves corresponding to the maximum and minimum array sizes. Arrays with a bigger aperture are able to retrieve the velocities for low frequencies (long period) of motion and subsequently retrieve a deeper soil structure; arrays with smaller aperture are able to retrieve the velocities for high frequencies (shorter

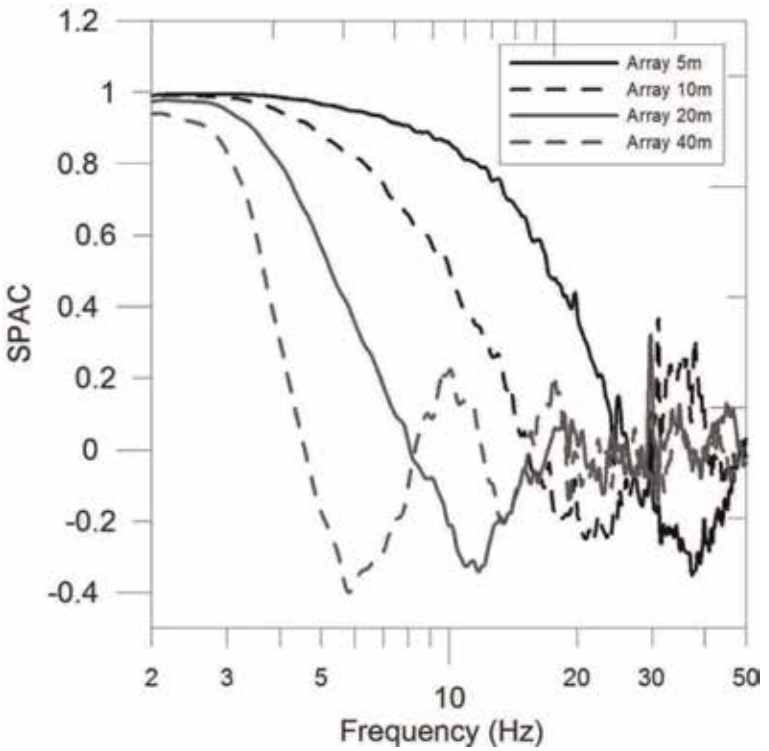

Figure 4.
Spatial autocorrelation coefficient (SPAC) for the Queen's Park Savannah array of microtremors (point 1X in ***Figure 1****).*

period) with a better resolution for soil structures near the surface. Note that each phase velocity in the arrays has unreliable parts for very low- and high-frequency components of motion due to the aperture radii used in each case; in other words, an array has a limited frequency band of usefulness between f_{min} and f_{max} that is dependent on its aperture. Rayleigh waves are dispersive and their velocities decrease with frequency; the reliable parts of each phase velocity must follow such trend eliminating in the average calculation the increase of velocity at low and high frequencies of motion. We noticed that the maximum wavelength at which the phase velocity can be estimated is about 10 times the radii r of the arrays at Queen's Park Savannah (**Figure 5**); the minimum wavelength is about 2 times the radii r of the arrays [7]. To obtain the average velocity at each frequency of motion f, we used N frequencies equally separated by the value of Δ_f in terms of a logarithm scale as follows:

$$log\Delta_f = \frac{log\, f_{max} - log\, f_{min}}{N-1} \tag{5}$$

where f_{max} and f_{min} are the maximum and minimum reliable frequencies for the aperture arrays, respectively (**Figure 5**). In our case, we generally set the value of $N = 20$ and select the corresponding velocity which belongs to the nearest frequency in such interval.

1.3 Inversion of phase velocities through genetic algorithms (GAs)

Genetic algorithms (GAs) are mathematical simulations based on biological evolution of natural selection rules. The soil parameters are digitized to gene type

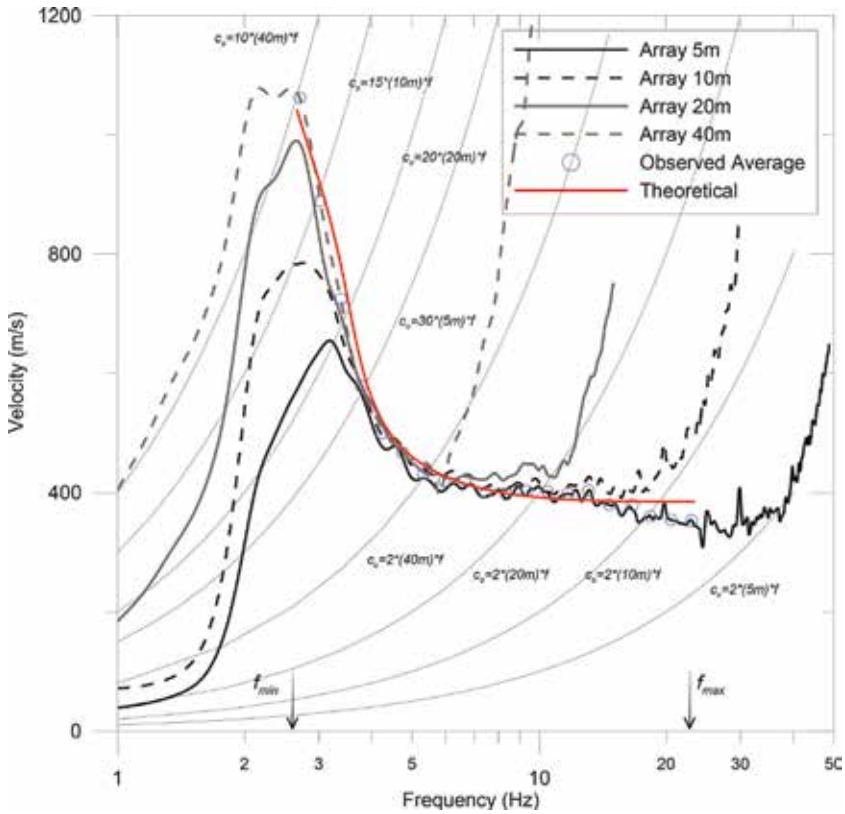

Figure 5.
Dispersion curve of Rayleigh wave (phase velocity) for Queen's Park Savannah array (point 1X in ***Figure 1****). We select the average velocity (open circles) of the four radii r to be used in the genetic inversion. The thin solid lines depict the wavelength that corresponds to 10–30 times and 2 times the radii of the arrays. The red thick solid line depicts the theoretical phase velocity curve that corresponds to best individual (soil profile in* ***Figure 6****) after searching the optimum solution via genetic algorithms;* f_{max} *and* f_{min} *are the maximum and minimum reliable frequencies for the aperture arrays.*

with n bits in series of 0 and 1 defining a priori lower and upper bound limits for the shear wave velocity and thickness of the layer (e.g., 200–600 m/s and 10–100 m, respectively). Each bit represents a gene, and a series of bits concatenated represents a chromosome. So, an optimal solution is searched using the chromosome that best matches the soil model represented by the experimental phase velocity curve developed using the microtremors array after applying the SPAC method. In this work we employed the method of Yamanaka and Ishida [8]. The reproduction of the initial population to a new population relies on the fitness function of each individual applying the three genetic operations modulated by the selection, crossover, and mutation; crossover acts to generate a good, new model with the combination of good parts of chromosomes of two parents; in the mutation operation, a gene is reversed (e.g., from 1 to 0 or vice versa). The mutation procedure is necessary to escape trapping at local minimum solutions.

The selection process begins declaring a misfit function ϕ_k for a k individual is defined as follows:

$$\phi_k = \frac{1}{N}\sum_{i=1}^{N}\left[\frac{c_o(f) - c_c(f)}{\sigma_c(f)}\right]^2 \tag{6}$$

where N is the number of observed data that correspond to the number of the discrete frequencies used in the analysis (see Eq. (5)), $c_o(f)$ is the observed Rayleigh wave velocity retrieved from the SPAC, $c_c(f)$ is the calculated Rayleigh wave velocity, and σ_c is the standard deviation of the calculated velocity based on the average of all n individuals that constitute a population. Note that $c_c(f)$ is obtained theoretically employing the Haskell [9] model for plane waves using the V_S and the thickness of layers produced by the genetic reproduction.

Then a fitness function *fit* is based on the misfit function as follows:

$$fit_k = \frac{1}{\phi_k} \tag{7}$$

In the inversion, the soil model that fits the observed data must have a high value of fitness and survives to a greater extent to the next generation, while the models with a low value of fitness (bad ones) are replaced by newly generated models.

It is noted that some authors (e.g., [10]) suggest that the dispersion curve is not carrying information (or very limited) of the velocity and the position of the bedrock; in such cases both parameters are badly constrained if we set a broad lower and upper bound of V_S for the half space in the bedrock during one round of a GAs' process. According to the seismic refraction data for the region [11], the bedrock yields a V_S of 2000 m/s. However, such V_S value was obtained for the Cariaco sedimentary basin at north eastern Venezuela which is located 225 km away from POS. In order to validate the V_S of 2000 m/s proposed by Schmitz et al. [11], we extended the original GAs employing successive rounds of inversions.

1.4 Successive rounds of genetic inversion

We applied successive rounds of GAs for the array at Queen's Park Savannah and St. Dominic's Children's Home (see site 1X and 7X, **Figure 1**) due to the following reasons:

a. In the Queen's Park Savanna, there is water well information (see **Figure 6**) to compare with the genetic inversion results. The array site is also located inside of a busy roundabout of 500 m radii, so presumably the constant source of the energy of microtremors is guaranteed in this case due to constant traffic activity in clockwise direction (see arrows in **Figure 1**).

b. St. Dominic's Children's Home has the shortest period among the array sites, and it is located 500 m from the roundabout (**Figure 1**). So it would be easy to get a reliable shear wave velocity on bedrock according to the aperture array size and a very shallow structure (**Table 1**).

c. We want to compare the results of (a) and (b).

Then, the procedure for the successive genetic inversions for the Queen's Park Savannah site is as follows:

a. We perform the first round of GAs with broad lower and upper bound limits for both, the soil deposits and the bedrock, namely, Vs = 100–600, 200–700, and 300–800 m/s for the first, second, and third layer, respectively, and thickness H = 5–50 m for all soil layers, and a Vs = 1000–2200 m/s for the bedrock (**Table 2**). The P-wave velocity was calculated from the S-wave velocity using empirical relation determined by Kitsunezaki et al. [12]. Generally, we assume

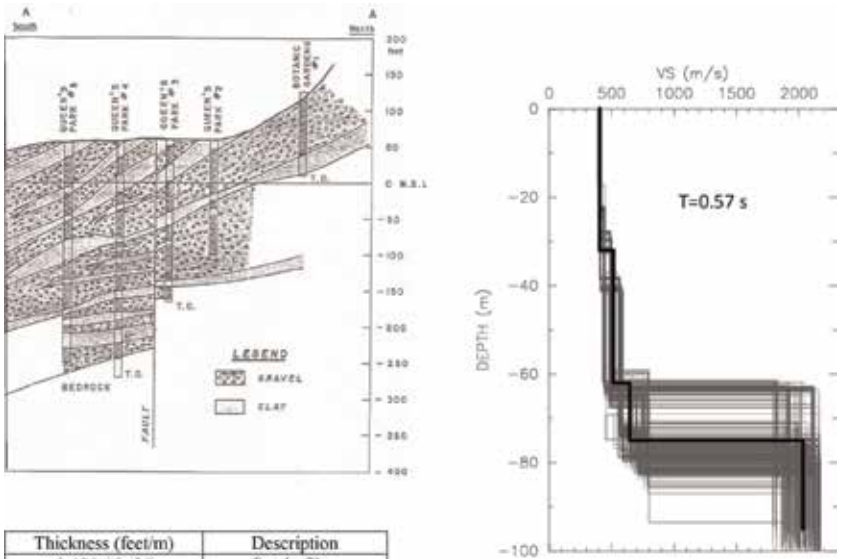

Thickness (feet/m)	Description
0-120 / 0- 36	Sandy Clay
120-190 / 36 – 58	Sand
190-265 / 58 - 81	Sandy Clay
265-320 / 81 - 98	Boulders and gravel
320-345 / 98 - 105	Boulders
345-371 / 105 -113	Shale

Figure 6.
Left: boreholes at Queen's Park Savannah. TD, terminal depth; MSL, mean sea level. Note that the total depth of the boreholes must be accounted above and below the MSL (e.g., depth ≈ 210 + 50 = 260 feet or 80 m). Cross section A-A is located in ***Figure 1*** *depicting boreholes reaching the bedrock in the Queen's Park Savannah (after [2]). Right: Shear wave velocity profile obtained via genetic inversion of phase velocity at Queen's Park Savanna (point 1X in* ***Figure 1****). The best model (thick black line) is considered the average for good models that fits into the 10% of average misfit (thin gray lines) in the final round of successive genetic inversions (****Table 2****). T denotes the fundamental period of the soil.*

that the stiffness of soil increases with the depth, with an overlap in the V_S ranges between two consecutive soil layers to take into account the possibility of velocity reversal when increasing depth. The best model is considered the average for all models that fits into the 10% of average misfit, so we were able to calculate the standard deviation σ for the V_S and thickness H of each layer.

b. We perform a second round of GAs selecting a narrow lower and upper bound limits for V_S for the bedrock from step (a) as the mean ± standard deviation σ (e.g., 1705 ± 116); instead we select a broad lower and upper bound during the genetic reproduction of shear wave velocity and thickness of soil layers as shown in **Table 2** (Vs = 100–600, 200–700, and 300–800 m/s for the first, second, and third layer, respectively, and thickness H = 5–50 m for all layers).

c. We perform a third round of genetic inversion fixing the V_S and thickness of the soil layers within the mean ± standard deviation σ calculated in (b) and select broad lower and upper bound limits for the V_S of bedrock half space (**Table 2**), namely, 1000–2200 m/s. Then a new value of V_S and its standard deviation for the bedrock are estimated in this step.

d. We perform again step (b) with a new narrow lower and upper bound limits for V_S for the bedrock ± σ of the mean of step (c) and selecting again, a broad lower and upper bounds of V_S and thickness of soil layers.

Round	Search Limits			Final Optimal Model		
	Vs(m/s)	Thickness H (m)	Density ρ(g/cm³)	Vs(m/s) ± σ	H (m) ± σ	
1	100-600	5-50	1.6	346 ± 3	9 ± 0.3	Soil
	200-700	5-50	1.7	440 ± 2	44 ± 0.4	
	300-800	5-50	1.8	682 ± 11	27 ± 0.7	
	1000-2200	α	2.4	1705 ± 116	α	Bedrock
2	100-600	5-50	1.6	390 ± 5	18 ± 2	
	200-700	5-50	1.7	446 ± 6	17 ± 4	
	300-800	5-50	1.8	464 ± 46	31 ± 2	
	1589-1821	α	2.4	1752 ± 50	α	
3	385-395	16-20	1.6	389 ± 3	17 ± 0.6	
	440-452	13-21	1.7	447 ± 3	19 ± 1	
	418-510	29-33	1.8	464 ± 9	31 ± 1	
	1000-2200	α	2.4	1899 ± 208	α	
4	100-600	5-50	1.6	405 ± 6	31 ± 9	
	200-700	5-50	1.7	501 ± 71	19 ± 5	
	300-800	5-50	1.8	532 ± 114	22 ± 7	
	1691-2107	α	2.4	1928 ± 107	α	
5	399-411	22-40	1.6	402 ± 3	29 ± 3	
	430-572	14-24	1.7	477 ± 17	22 ± 2	
	418-646	15-29	1.8	513 ± 29	20 ± 3	
	1000-2200	α	2.4	1979 ± 193	α	
6	100-600	5-50	1.6	403 ± 5	32 ± 7	Final model
	200-700	5-50	1.7	513 ± 52	30 ± 8	
	300-800	5-50	1.8	645 ± 126	13 ± 7	
	1786-2172	α	2.4	**2032 ± 104**	α	

σ denotes the standard deviation and α denotes infinite thickness on half space. The arrows indicate the bedrock or sediments information that is used in the subsequent round of GAs.

Table 2.
Example of successive rounds of genetic inversion, search limits, and optimal final model for Queen's Park Savannah site 1X.

e. The schemes (b–d) is repeated till when we find the mean V_S for the soil deposits and bedrock inside of the range Vs mean ± σ of a previous round when selecting a narrow lower and upper bound in the bedrock (e.g., rounds 4 and 6 in **Table 2**).

Then the successive rounds of inversion are based on the effect of fixing the bedrock properties while searching the optimum solutions in one round of GAs

employing broad lower and upper bound limits for the sediments and vice versa through several rounds of inversions in a subsequent manner.

When applying the methodology above to the Queen's Savannah Park array, for each iteration, the total number of unknown parameters yields four velocities and three thicknesses, searching an optimal combination for them in the inversion that matches the experimental phase velocity presented in **Figure 5**. These parameters were digitized as 8-bit binary strings, setting the population size at n = 30 individuals, with a crossover probability of 0.7 and an initial mutation probability of 0.01, terminating the iterations at the 100th generation. Since the algorithm used initial random numbers finding the global minimum solution, we performed for each round of GAs 5 iterations (or inversions) that indeed had different initial random numbers with a total of 15,000 soil models in each round. The final model was selected as an acceptable solution if its average misfit was less than 10% [13, 14].

The GAs' inversion yields a value of $V_S = 2032 \pm 104$ m/s for the bedrock for the sixth round according to (e) above, which is basically the same value of 2000 m/s proposed by Schmitz et al. [11]. The results also yielded a first layer of V_S = 403 m/s with a thickness of 32 m, a second layer of V_S = 513 m/s with a thickness of 30 m, and a third layer of V_S = 645 m/s with a thickness of 12 m that are classified as sand and clay. The soil profile is presented in **Figure 6**. Then the total thickness yields 75 m above a half space constituted by a shear wave velocity of nearly 2000 m/s. We validated our results with the depth of bedrock of about 80 m (260 feet in **Figure 6**) in this area reported by the Water and Sewerage Authority (WASA) [2]. Note that the thickness of 32 ± 7 m of the first layer is similar to the sandy-clay first layer of 36 m with the water well profile presented in **Figure 6**; however, some differences are found to the second and third layer. We attribute such differences due to the fact that such water well information is 200 m apart from the array site. The bedrock in this case is found at the boulders' level.

It is noted a good match between the experimental and calculated (theoretical) phase velocity via application of the Haskell [9] model for plane waves employing the final model presented in **Table 2**. This confirms the effectiveness of the genetic scheme (**Figure 5**).

The authors tested secondly the successive rounds of GAs performing an array at St. Dominic's Children's Home (see site 7X, **Figure 1**) with the shortest period of 0.22 s among the arrays (see **Figure 10h**). Then it would be suitable to find the V_S for the bedrock for a shallower and a simple soil structure. The results are presented in **Table 3**.

It is noted that we found also a value near 2000 m/s for the bedrock when applying the GAs at this site. As it was expected, for the St. Dominic's Children's Home case, the GAs converge faster than for the Queen's Park Savannah case due to a simple and shallower soil structure.

If we fix the V_S for the bedrock as V_S 2032 ± 104 m/s taken from round number six in **Table 2** from GAs in Queen's Park Savanah and perform one round of GAs for St. Dominic's Children's Home, we found practically the same optimal model for the soil profile from the previous process above (**Table 4**).

Further seven microtremors array were made in Port of Spain and distributed in the City (**Figure 1** and **Table 1**); for such cases we fix in the GAs' scheme the V_S 2008 ± 124 m/s in the half space according to round 4 in **Table 3**. The proportion of the maximum wave length and the array size lay between 4 and 14 for all measurements (see **Table 1**). So we assured that the search limits for the thickness of the soil deposits in the GAs' process yield less than the penetration of the Rayleigh waves for each array. A commonly adopted criterion is that the maximum investigation depth is half of the maximum wavelength [15]. Appropriate search limits were decided after several trial runs. The results of the GAs' inversion are

Round	Search Limits			Final Optimal Model		
	Vs(m/s)	Thickness H (m)	Density ρ(g/cm³)	Vs(m/s) ± σ	H (m) ± σ	
1	100-600	5-50	1.6	285 ± 1	9 ± 0. 03	Soil
	300-800	5-50	1.8	552 ± 2	24 ± 0.9	
	1000-2200	α	2.4	1948 ± 200	α	Bedrock
2	100-600	5-50	1.6	284 ± 2	9 ± 0.04	
	300-800	5-50	1.8	552 ± 2	24 ± 0.8	
	1748-2148	α	2.4	2045 ± 93	α	
3	282-286	8-10	1.6	284 ± 0.5	9 ± 0.1	
	550-554	23-25	1.8	551 ± 1	24 ± 0.5	
	1000-2200	α	2.4	1931 ± 239	α	
4	100-600	5-50	1.6	284 ± 2	9 ± 0	Final model
	300-800	5-50	1.8	552 ± 2	24 ± 0.7	
	1692-2170	α	2.4	**2008 ± 124**	α	

σ denotes the standard deviation and α denotes infinite thickness on half space. The arrows indicate the bedrock or sediments information that is used in the subsequent round of GAs.

Table 3.
Example of successive genetic inversion, search limits, and optimal final model for St. Dominic's Children's Home site 7X.

Round	Search Limits			Final Optimal Model		
	Vs(m/s)	Thickness H (m)	Density ρ(g/cm³)	Vs(m/s) ± σ	H (m) ± σ	
1	100-600	5-50	1.6	285 ± 2	9 ± 0.04	Soil
	300-800	5-50	1.8	553 ± 2	24 ± 0.4	
	1928-2136	α	2.4	2047 ± 34	α	Bedrock

*σ denotes the standard deviation and α denotes infinite thickness on half space. We fix the bedrock velocity according to the results of the Succesive Inversion for Queen's Park Savannah (**Table 2**).*

Table 4.
Example of genetic inversion, search limits, and optimal final model for St. Dominic's Children's Home site 7X.

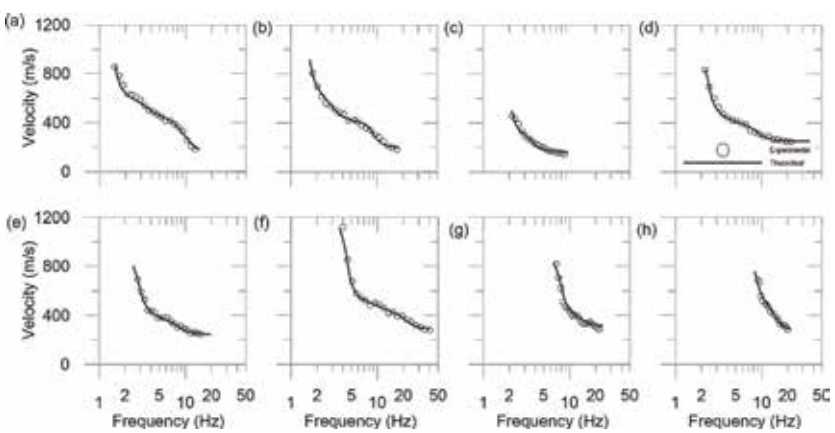

Figure 7.
*Theoretical (line) and experimental (open circles) phase profiles after application of the genetic inversion at eight sites of microtremors array in Port of Spain. (a) Port Area (5X), (b) Mucurapo Secondary School (3X), (c) Sea Lots (8X), (d) Nelson Mandela Park (2X), (e) Woodford Park (8X), (f) Federation Park (4X), (g) St. James hospital (9X), and (h) St. Dominic's Children's home (7X). See locations of microtremors array in **Figure 1**.*

presented in **Figures 7** and **8**. It is observed a good match between the experimental and calculated (theoretical) phase velocity for all array sites. The soil profiles containing the V_S and thickness resulting from the microtremors array analysis are plotted in **Figure 8**. The shear wave velocity in the POS sediments yields from 51 to 750 m/s and the bedrock is located at 28 to 225 m depth with shallow structures in the peripheries near the hills and deeper structures toward the south of the city at the Port Area (**Figure 1**). It is worth mentioning that at the Port Area, very

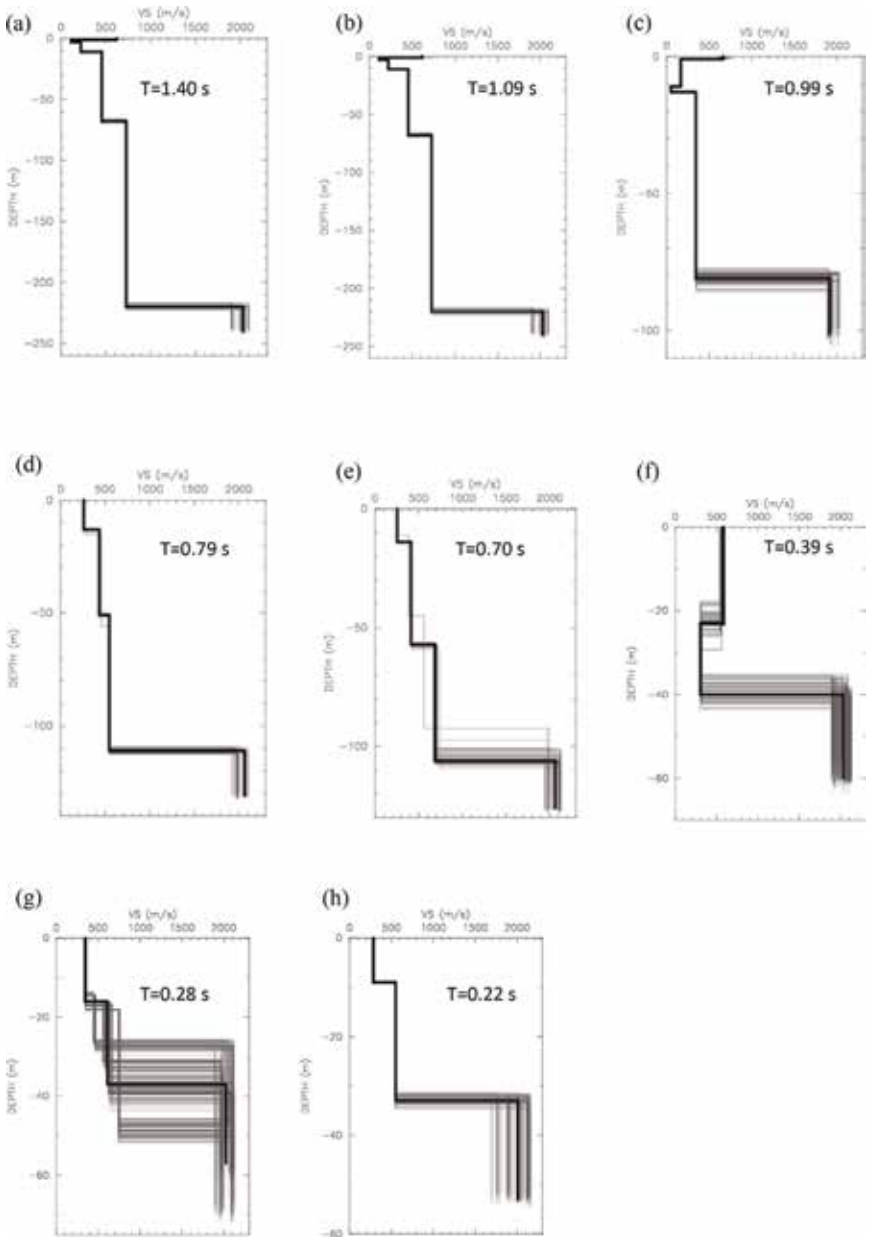

Figure 8.
Mean shear wave velocity (V_S) profiles after application of the genetic inversion at eight sites of microtremors array in Port of Spain. The best model (thick black line) is considered the average for good models that fits into the 10% of average misfit (thin gray lines). (a) Port Area (5X), (b) Mucurapo Secondary School (3X), (c) Sea Lots (8X), (d) Nelson Mandela Park (2X), (e) Woodford Square (8X), (f) Federation Park (4X), (g) St. James hospital (9X), and (h) St. Benedict's Children's home (7X). The sites are ordered from top to bottom from the largest to the shortest fundamental period of soil T (s). See locations of microtremors array in ***Figure 1****.*

consolidated sediments with V_S of about 700 m/s constitute the thicker layers with more than 100 m above the bedrock.

2. Results and discussion

2.1 H/V interpretations: the Diffuse Field Approach and the ellipticity of Rayleigh waves

Despite some authors have performed a joint inversion of the phase velocity and the H/V observed spectral ratios [16], we preferred to validate our Vs profile retrieved from the GAs generating synthetics' H/V ratios via application of the Diffuse Field Approach (DFA) and compare them with the observed ones. If we incorporate the observed H/V curve in a joint inversion, we would force a priori the soil profiles to fit with such curve, issue that the new interpretation of DFA would validate completely in a separate manner.

The soil profiles' results by the GAs' inversion of the previous section are validated via two alternative analyses: (i) the theoretical H/V ratios inferred from the Diffuse Field Approach (DFA) and the observed H/V ratios; (ii) the theoretical H/V ellipticity of Rayleigh waves.

Recently a new interpretation has been proposed and formulated by Sánchez-Sesma et al. [17, 18] and Perton et al. [19] based on a Diffuse Field Approach that the H/V ratios on microtremors can be interpreted as the square root of the ratio of the sum of horizontal displacements for horizontal unit harmonic loads $\mathrm{Im}[G_{11}]$ and $\mathrm{Im}[G_{22}]$ and the imaginary part of vertical displacement for a vertically applied unit harmonic load, $\mathrm{Im}[G_{33}]$, when both the source and the receiver are the same, as follows:

$$\frac{H(\omega)}{V(\omega)} = \sqrt{\frac{Im[G_{11}(\boldsymbol{x},\boldsymbol{x};\omega)] + Im[G_{22}(\boldsymbol{x},\boldsymbol{x};\omega)]}{Im[G_{33}(\boldsymbol{x},\boldsymbol{x};\omega)]}} \tag{8}$$

where ω denotes the circular frequency, x denotes the position vectors for source and receiver which are the same, and the indices (11, 22, and 33) denote the displacement and the direction of the unit applied load, respectively (e.g., 1, north-south; 2, east-west; 3, up-down). Such calculations of the imaginary part of Green's function G in Eq. (8) are performed by the conventional discrete wavenumber summation method developed by Bouchon [20]. Then, the input data to compute H/V synthetics based on this method are the compressional and shear wave velocity, the density, the thickness, and the quality factor of each soil layer that can be retrieved in our case from GAs from the previous section. The details of the method can be found in Sánchez-Sesma et al. [18]. Equation (8) implies energy equipartition of the 3D wave field in space for a distribution of random sources. This interpretation has been revised by Kawase et al. [21] showing that the DFA approach explains well the observed H/V ratios of microtremors in Japan. Such new interpretation depends on the contribution of all waves considered in the Green's function, namely Rayleigh, Love, and body waves.

Konno and Ohmachi [3] and Bonnefoy-Claudet et al. [22] have demonstrated that the H/V curves exhibit in most cases a single peak due to the ellipticity of the fundamental mode of Rayleigh waves through 1D noise simulation; the vanishing of the vertical component occurs nearly to the fundamental resonance period of S waves where a sharp S-wave impedance contrast exists larger than 3.0 between the surface layers and the underlying stiffer formations and when the sources are near and surficial.

We calculated the observed horizontal-to-vertical spectral ratio (H/V) employing the resultant vector of the orthogonal north-south and east-west components of motion and averaging the results for all the stationary parts selected for each record (details of the digital processing of single mobile microtremors are explained [1]). To compute the synthetics' H/V ratios employing the DFA in Eq. (8), we adopted for the surface sediments above the bedrock a low-quality factor of 5.0 for all frequencies to incorporate the effects of total water saturation (since water table in POS can be found just at the surface) yielding high attenuation on wave propagation [23, 24] and a quality factor of 50 for the bedrock [25].

We present the imaginary parts of Green's functions $\mathrm{Im}[G_{11}]$ and $\mathrm{Im}[G_{33}]$ in **Figure 9a** and the H/V synthetics (see Eq. (8)) based on the DFA in **Figure 9b** at Queen's Park Savannah. A good agreement is found among the amplification calculations cited before for both, the fundamental period of vibration and the shape of the overall observed H/V ratios. Despite the fundamental period of 0.57 s can be explained by the ellipticity pattern depicted in **Figure 9c**, it is noted that the DFA

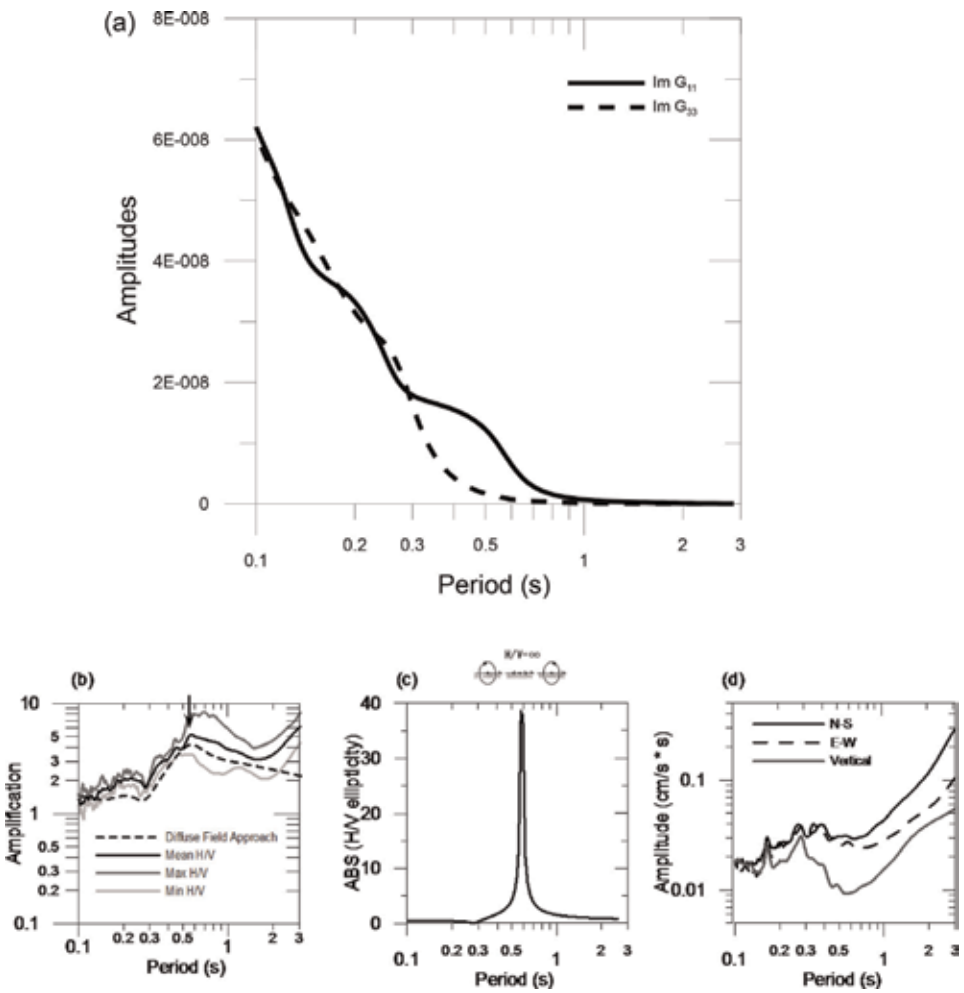

Figure 9.
*(a) Imaginary part of Green's function (Im G11 and Im G33 in Eq. (8)) via application of the Diffuse Field Approach (DFA) for Queen's Park Savanna (Point 1X in **Figure 1**); (b) H/V observed spectral ratio (mean) and H/V synthetics spectral ratios via application of DFA; (c) ellipticity of Rayleigh waves for the first mode of vibration—note that absolute values of ellipticity are drawn; and (d) absolute Fourier velocity spectrum for horizontal (N-S and E-W) and vertical components of motion. Diagram of ellipticity pattern taken from Konno and Ohmachi [3]. The fundamental period of soil T is indicated by the arrow in the H/V spectral ratios.*

yields a more robust interpretation since the amplification factor cannot be measured employing the ellipticity approach.

Also, it is interesting that the change in the ellipticity pattern depicted in **Figure 9c** clearly reflects the change of particle motion from prograde to retrograde at the fundamental period of vibration observed for the theoretical and experimental calculations. The trough in the vertical component confirms the analysis causing the peak observed in the H/V ratios (**Figure 9d**).

Take the theoretical fundamental period T in seconds of a homogenous soil profile over a rigid base equal to:

$$T(s) = \frac{4H}{\overline{Vs}} \tag{9}$$

where H is the thickness of the sediments above the bedrock and $\overline{Vs}$ is the average shear wave velocity. Introducing the values of H and Vs in Eq. (9) as 75 m and 489 m/s resulting from the GAs' inversion (Section 1.4), the period T yields 0.60s coinciding fairly well with the one obtained by the observed H/V spectral ratio technique and the one predicted by the diffuse wave field theory and the ellipticity pattern of Rayleigh waves.

The analysis for the remaining eight microtremors array sites is presented in **Figure 10**. The fundamental periods are well explained for all sites due to ellipticity pattern in the wave motion of microtremors; the DFA confirmed the effectiveness of the application of the H/V spectral technique and the GAs for the city of POS. The deeper profiles are found in the coastal areas (5X) at the Port with a total of about 225 m of sediments and a fundamental period of 1.4 s, this in accordance with water well information at the Port presented in **Table 5** that no bedrock is identified at 100 m depth. Sites in the foot of hills yield the shallower profiles of 25–30 m with fundamental periods less than 0.3 s. Intermediate periods between 0.4 and 1.0 s are found in downtown areas yielding depths between 60 and 110 m. For all array sites, Vs varies from 50 to 2000 m/s, including the bedrock.

An interesting feature of the H/V ratios can be seen for the three sites located in the coastal areas, namely, the Licensing Authority (Port Area), Mucurapo Secondary School, and Sea Lots (**Figure 10a–c**, sites 3X, 5X, and 6X, respectively, **Figure 1**). Short period components between 0.1 and 0.3 s yield a very low amplification or a de-amplification at the three sites. We attribute such phenomena due to the presence of a thin rigid layer in the surface with Vs of about 600 m/s; such feature was introduced in the search limits for the top layers in the GAs at these

Thickness (feet/m)	Description
0–7/0–2	Clay fill
7–20/2–6	Sand + gravel
20–25/6–8	Hard sand
25–110/8–34	Sand + boulders
110–115/34–35	Brown clay
115–200/35–61	Clay and boulders
200–251/61–77	Gravel with streaks of clay
251–338/77–103	Sand + boulders
	No bedrock is identified

Table 5.
*Water well for the Port Area (License Office) site 5X (**Figure 1**).*

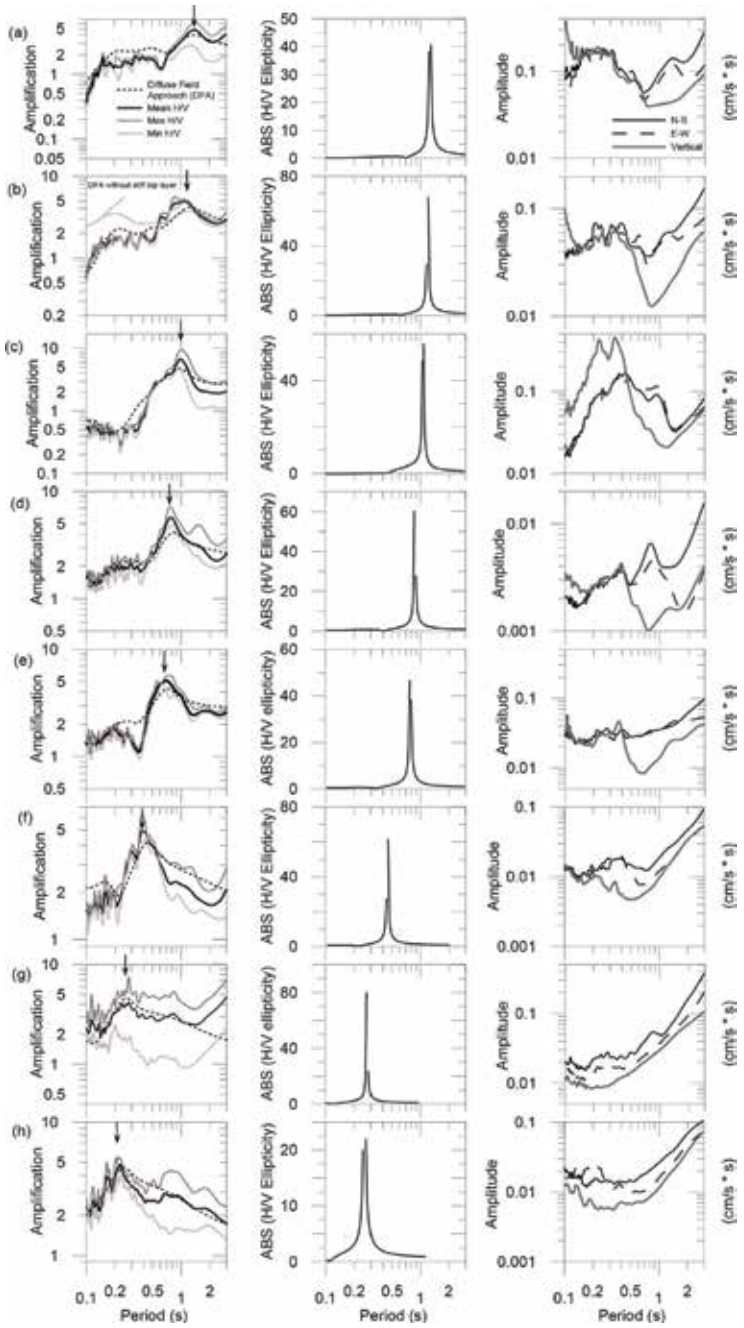

Figure 10.
Left: H/V spectral ratio (observed-mean and synthetic via application of Diffuse Field Approach (DFA)). Center: ellipticity of Rayleigh waves for the first mode of vibration; note that absolute (ABS) values of ellipticity are drawn. Right: absolute Fourier velocity spectrum for horizontal (N-S and E-W) and vertical components of motion. The sites are ordered from top to bottom from the largest to the shortest fundamental period of soil T indicated by the arrows in the H/V spectral ratios. (a) Port Area (5X), (b) Mucurapo Secondary School (3X), (c) Sea Lots (8X), (d) Nelson Mandela Park (2X), (e) Woodford Square (8X), (f) Federation Park (4X), (g) St. James hospital (9X), and (h) St. Benedict's Children's home (7X). See locations of microtremors array in ***Figure 1****.*

sites. We have evidence of existing stiff layers near the surface as it is corroborated by the well logs reported by WASA near the array sites (see Hard Sand deposit in **Table 5**). We attribute the high Vs on the top due to compaction works, deck

constructions at the Port/Coastal Area, and/or a high degree of consolidation due to the constant presence of heavy weight (containers) that are located at these sites for shipping purposes. Note that the DFA predicted very well the H/V ratios in such circumstances as well, for both, the fundamental period and the overall shape of the transfer function. It is noted that this consolidated layer at the top of the Port Area behaves as a low pass filter and does not have an influence in the fundamental period of motion of the whole soil system; such feature was corroborated performing the DFA without the stiff top layer at Mucurapo Secondary School (see **Figure 10b**). Sea Lots site at the South East of POS (see **Figure 1** at site 6X) is characterized by the lowest V_S of 50 m/s for all array sites that correspond to a swamp area overlaid by stiff deposits. Such low values of V_S have been observed in sedimentary stratigraphy of natural intertidal flats [26].

2.2 H/V ratios and 1-D theoretical transfer function for SH-waves

Figure 11 depicts the comparison between the 1-D SH wave amplification employing the Vs profiles obtained by the GAs and the H/V observed spectral ratios. We also adopted for the surface sediments above the bedrock a low-quality

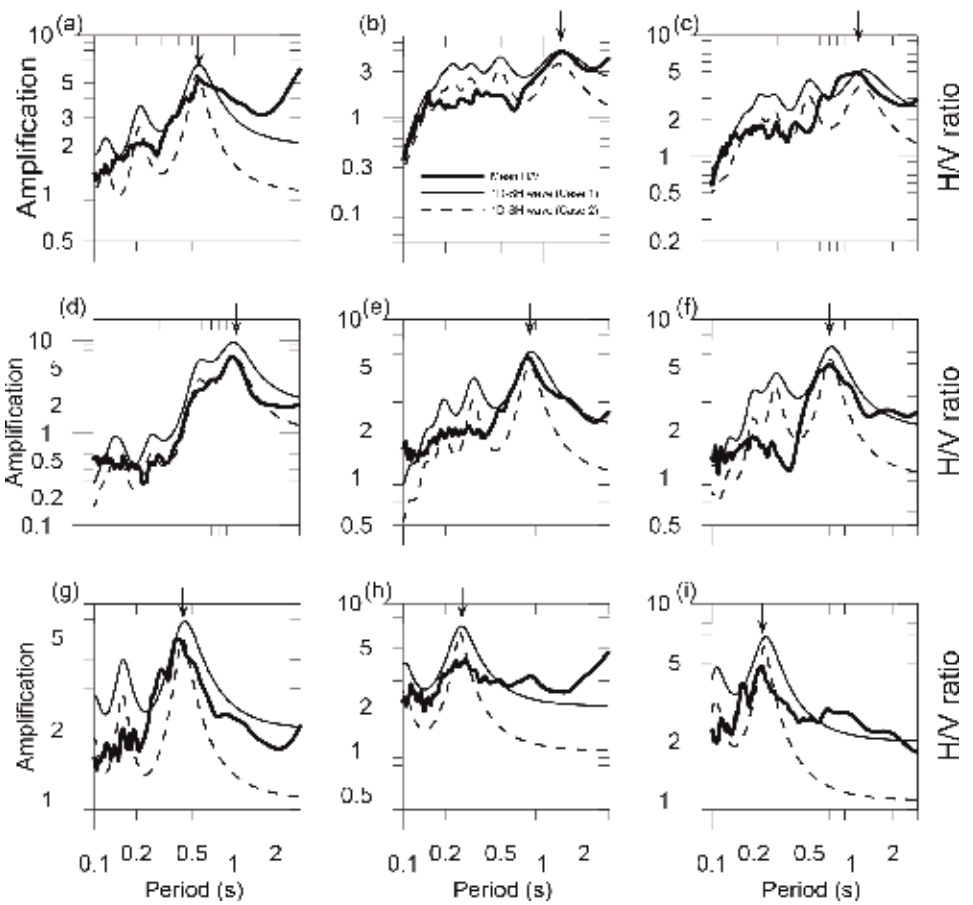

Figure 11.
Comparison of H/V spectral ratios and 1-D SH wave transfer function; case (1) only up wave amplification and case (2) up + down amplification with refraction and reflection in bedrock. (a) Queen's Park Savannah array (1X), (b) Port Area (5X), (c) Mucurapo Secondary School (3X), (d) Sea Lots (8X), (e) Nelson Mandela Park (2X), (f) Woodford Square (8X), (g) Federation Park (4X), (h) St. James hospital (9X), and (i) St. Benedict's Children's home (7X). The fundamental period of soil T is indicated by the arrows.

factor of 5.0 for all frequencies to incorporate the effects of total water saturation. We plotted two kinds of theoretical SH transfer functions, namely, case (1) up + down amplification with refraction and reflection in bedrock and case (2) only up wave amplification. In both cases the 1-D SH wave amplification replicates the fundamental period of the observed H/V ratios; however, in most of the cases, the overall shape of the H/V ratios differs mainly at long period components for case (1) and for short period components for case (2). It is noticed that a level of amplification yield between three and five yields at the predominant peak. This level of amplification is referred to the bedrock motion.

3. V_S30 and fundamental period

An important parameter in the modification of seismic waves propagating toward the surface is the composition of the near-surface soil layers. In different building codes around the world, the average shear wave velocity of the upper 30 m (V_S30) has been adopted to characterize the response of seismic waves to the influence of near-surface strata.

In first instance, we compared the V_S30 obtained from our microtremors array observation and the ones estimated by the empirical formulas of Matsuoka et al. [27] employing 2000 sites in Japan based on geomorphological units.

We calculated the V_S30 from our microtremor results using the following formula:

$$V_S30 = \frac{30}{\sum_{i=1}^{N} \frac{h_i}{V_i}} \tag{10}$$

where h_i and V_i denote the thickness (in meters) and the shear wave velocity of the ith layer; N is the total number of soil layers respectively.

We classified the sites (1X–5X, 8X) as a Gravelly Terrace, Sea Lots (site 6X) as a Reclaimed Land, and St. Dominic's Children's Home to the East (7X) and St. James Hospital to the West (9X) as Mountain Foot Slope sites (see **Figure 1**). The empirical formulas to estimate V_S30 (m/s) for the Gravelly Terrace (Eq. (11)), the Reclaimed Land (Eq. (12)), and the Mountain Foot Slope (Eq. (13)) yield:

$$\log VS30 = 2.493 + 0.072logEv + 0.027logSp - 0.164logDm \pm 0.122(\sigma) \tag{11}$$

$$\log VS30 = 2.373 - 0.124logDm \pm 0.123(\sigma) \tag{12}$$

$$\log VS30 = 2.602 \pm 0.092(\sigma) \tag{13}$$

where Ev is the elevation (m), Sp refers to the Tangent of Slope*1000, Dm yields the distance (km) from mountain or hill, and σ denotes the standard deviation. We took Dm as the shortest distance to the Northern Range or the Laventille Metalimestone foothills (**Figure 1**). The results are presented in **Figure 12**. In general the estimated V_S30 from the empirical formulas of Matsuoka et al. [27] estimates well the velocities obtained by the GA's from our array measurements in the range of ±σ (standard deviation). We also compared the V_S30 of our microtremors array profiles with the ones estimated by Allen and Wald [28] using the topographic slope as a proxy of site conditions employing the USGS Web Server (earthquake.usgs.gov/hazards/apps/vs30/). We retrieved the correspondent predicted V_S30 at the location of each microtremors array. The most noticeable difference is observed for the mountain foot slope in St. James (site 9X). However, we did not find a good correlation when comparing with soil types proposed by

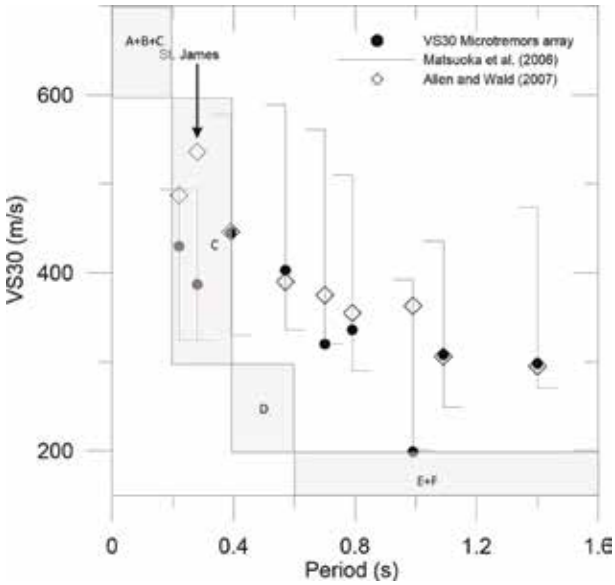

Figure 12.
Comparison of VS30 (m/s) retrieved from our microtremors array and the empirical formulas of Matsuoka [27] and the method of Allen and Wald [28]. The shadowed area represents the classification of Zhao and Xu [29] based on fundamental period of soil and VS30.

Zhao and Xu [29] based on NEHRP classes on V_S30 (shadowed areas in **Figure 12**). This leads to suggest to characterize the soil at POS by the fundamental period rather than the V_S30 [30]; Zhao and Xu [29] suggest also that site period is a better parameter for characterizing soil conditions, in very deep or very soft sediments.

4. Preliminary assessment of liquefaction susceptibility

Nakamura [31] proposed a technique to investigate the liquefaction susceptibility based on microtremor measurements, namely, the vulnerability index K_g for the surface ground, as follows:

$$K_g = \frac{{A_g}^2}{F_g} \tag{14}$$

where A_g is the amplification factor referenced to the engineering bedrock and F_g is the predominant frequency of vibration of the soil profile (the inverse of the period); both values can be taken from the horizontal-to-vertical spectral ratio (H/V) of microtremors; A_g is considered to be the H/V ratio at the predominant frequency. Values of K_g greater than 20 are considered likely to liquefy. The authors computed the liquefaction potential using Eq. (14) at each point and develop an iso-liquefaction potential map interpolating the K_g value of the 1181 single mobile microtremors data employed in Salazar et al. [1] (**Figure 13**). The results are very concerning regarding this hazard because the water table in POS can be found just at the surface, the soil conditions then are saturated sands and gravels, and sometimes poorly consolidated reclaimed land has been placed specially in the coastal areas. The areas with a high liquefaction susceptibility are The Port, Sea Lots, some parts of Woodbrook, a small spot in Cocorite (where in fact reclaimed land exists), and some small areas in the Queen's Park Savannah and Federation Park. Also South

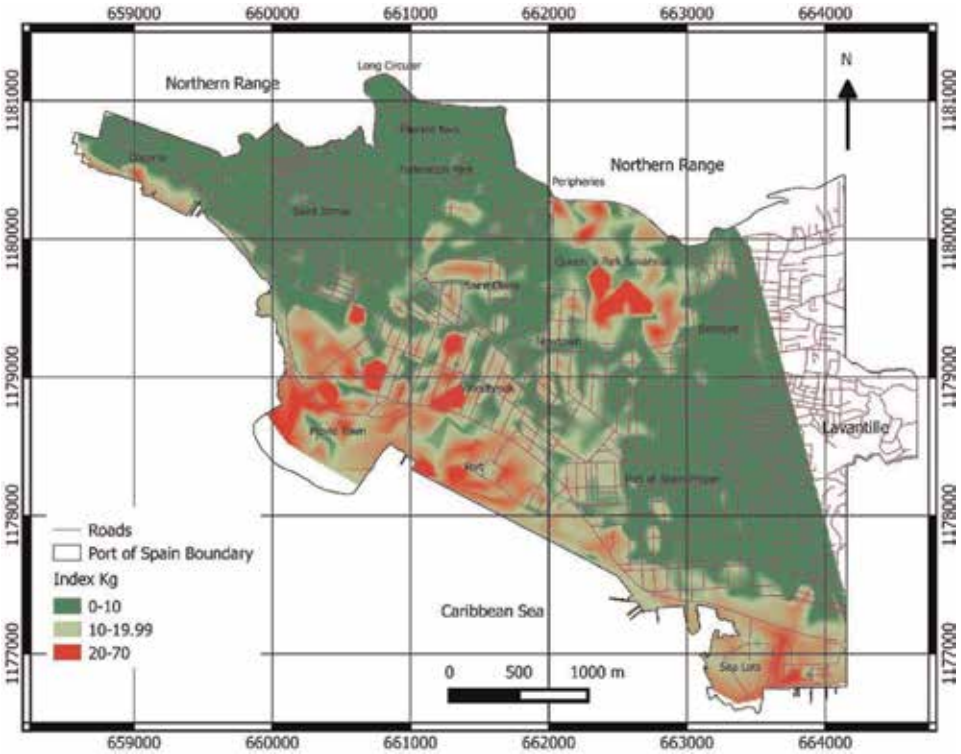

Figure 13.
Preliminary liquefaction hazard map for Port of Spain City, employing Nakamura index K_g, (see Eq. (14)). Zones yielding a K_g above 20 are suggested to a high liquefaction susceptibility.

of Saint James in the Coastal area yields a possibility of high liquefaction potential. Evidence of soil subsidence is already present in some structures near the Port Area as the Lighting House Tower (**Figure 14**). Next to it, the Eric Williams Complex known as the Twin Towers which are one of the tallest buildings in POS (92 m height) has been constructed in the 1980s incorporating piles on their foundations; the eyewitness during the construction process affirmed that some piles sank totally during their driving process due to extremely soft soil conditions found at that time in the coastal area. Several new high-rise buildings including hotels, a water front, high-income class dwellings, amenity centers, and the Port itself are located in this high liquefaction susceptibility area. Ironically, Sea Lots located to the West is characterized by a very low-income social class; it is also a prone area of high potential of liquefaction. It is noted that the study of Kraft [32] employing the methodology of Holzer et al. [33] yielded similar conclusions for POS and another cities of Trinidad employing regional geological map conditions.

5. Conclusions

Shear wave velocity V_S profiles were determined by performing nine microtremors array surveys in Port of Spain (POS), Trinidad, employing the spatial autocorrelation SPAC method and genetic algorithms (GAs); the results yielded V_S between 50 and 2000 m/s at POS. The ellipticity pattern for the first mode of Rayleigh waves explains the resulting predominant peak in the H/V Nakamura ratios for all array sites. We validated the soil profiles retrieved by the SPAC and GAs' schemes comparing the synthetics' horizontal-to-vertical spectral (H/V) ratios

Figure 14.
Leaning lighthouse tower at the Port Area. See the displacement Δ at the top of the structure due to the soil subsidence at its foundation.

generated by the Diffuse Field Approach (DFA) with the observed ones at the array sites and with empirical formulas to estimate the average shear wave velocity of the upper 30 m (V_S30). We conclude that the H/V ratios yield a genuine shear wave fundamental period of vibration of the soil profiles at POS, and that can be used to validate the high-resolution seismic microzonation map proposed by Salazar et al. [1]. The amplification and fundamental period of motion retrieved from the microtremors together with the water table level suggest a high liquefaction potential mainly on the coastal areas. It looks that in terms of seismic amplification and liquefaction hazard, a safe place is the Laventille area at the East characterized geologically by a metalimestone; unfortunately it is classified with the highest crime rate and drug dealers in Trinidad.

The genetic inversion results revealed that the deeper parts of POS are located in the Port Area and South of Woodbrook with a depth of 225 m and the softer materials are located at the South East of POS in Sea Lots with low V_S of 50 m/s which correspond to a buried swamp or mangrove; toward the north of the City, the depth of the sediments decreases substantially from 75 m in the Savannah to 30 m in Saint James and Cocorite to the West. Toward the South East part of POS in Sea

Lots, the depth of sediments yields 80 m. Generally, the V_S in the sediments increases with depth in the range mainly of 50 m/s to 600 m/s, and the variants of the stiffness in the soil are mainly found near the surface due to the reclaimed land —compacted or not—during construction works or the presence of swampy soil to the East of POS. We have also corroborated via successive rounds of genetic inversions that the V_S at the bedrock yields 2000 m/s.

It is worth mentioning that the DFA even reproduced the whole shape of the H/V ratios, including peaks and troughs and the level of amplification; such characteristics cannot be retrieved employing the Rayleigh wave pattern interpretation. It seems that the H/V spectral ratio technique from Nakamura represents a true piece of information regarding the dynamic properties of the sediments above bedrock in terms of identification of the fundamental period of the soil profile when comparing with the one retrieved with the 1-D SH wave theoretical amplification as well; it is noticed that an amplification level yields between three and five at the fundamental period. However, the H/V spectral ratios do not coincide with the whole shape of the 1-D SH transfer function. If we proved just incorporating the fundamental mode in the phase velocity inversion that our resonant peak in the H/V ratios is genuine, then we did not incorporate higher modes in the inversion; however, future research lines on this topic would allow us to introduce the first overtones in new analysis [34]. The V_S30 retrieved from our microtremors array coincides well with the predicted V_S30 of Matsuoka et al. [27] when incorporating geomorphological conditions; however, we did not find a good correlation with NEHRP classification on V_S30 [29] suggesting that the fundamental period is a superior parameter for classification than the V_S30 in this case.

Borehole data in POS reaching the bedrock is very limited, and a parallel research would be focused on conducting boreholes reaching the depth of the bedrock at new strong motion stations or critical facilities, and if possible, to get the V_S employing alternative methods (e.g., cross hole or laboratory soil test); borehole data would help to validate the proposed preliminary liquefaction hazard map and can be used to implement remedial measures against such hazard, especially at the coastal port area. The last hazard peer-reviewed maps for Trinidad and the Eastern Caribbean have been proposed by Bozzoni et al. [35] yielding 0.60 g of peak ground acceleration for POS setting 2475 years return period at a rock site class B in NEHRP classification; such shaking level is strong enough to trigger the liquefaction in the saturated alluvium at POS.

Since our microtremor survey only permits to study the soil behavior in the linear range, the effect of the non-linearity in the soil is still a big question to solve for the area. Future research lines might be focused on a frequency-dependent quality factor as well.

Acknowledgements

The authors thank IntechOpen for inviting us to write a chapter of this book and editor John Tiefenbacher for his sincere and fruitful comments during the revision process.

The microtremor recordings were provided by the Ministry of Planning and Sustainable Development of Trinidad and Tobago and are proprietary.

We used QGIS Open Software version 2.4 and the GCC Fortran Compiler to generate the maps presented in this work. The V_S30 values used in this work were retrieved via WEB server at USGS (earthquake.usgs.gov/hazards/apps/vs30/) last accessed January 9, 2016.

The authors thank the Ministry of Planning and Sustainable Development of Trinidad and Tobago for funding this research being conceived by the first author as a principal investigator while working at the Seismic Research Centre in Trinidad

during 2008–2014. We thank also all the governmental institutions in Trinidad that permit to do the survey in their facilities. We greatly acknowledge Hiroaki Yamanaka (Tokyo Institute of Technology) for providing the first author the original Fortran Codes of Genetic Inversion through the sponsor of the Japanese International Cooperation Agency (JICA) in El Salvador. The Tokyo Sokushin personnel in Japan were always assisting us with our queries regarding the microtremor instrumentation. The authors want to thank Francisco Sánchez-Sesma from Universidad Autónoma de México UNAM for sharing with the first author the Diffuse Field Approach program to compute the synthetics of H/V ratio. His unconditional help has made possible to update this chapter to better understand the amplification phenomena employing microtremor measurements at Port of Spain.

Author details

Walter Salazar[1*], Garth Mannette[2], Kafele Reddock[2] and Clevon Ash[2]

1 Faculty of Engineering and Architecture, Catholic University of El Salvador (UNICAES), El Salvador

2 Seismic Research Centre, The University of the West Indies (UWI), St. Augustine, Trinidad and Tobago

*Address all correspondence to: walter.salazar@catolica.edu.sv

References

[1] Salazar W, Mannette G, Reddock K, Ash C. High-resolution grid of H/V spectral ratios and spatial variability on microtremors at Port of Spain, Trinidad. Journal of Seismology. 2017;**21**:1541-1557. DOI: 10.1007/s 10950-017-9681-1

[2] Crichlow M. Groundwater Recharge in the Queen's Park Savannah. Trinidad: The Water Resource Agency of Trinidad and Tobago WASA; 1989

[3] Konno K, Ohmachi T. Ground-motion characteristics estimated from spectral ratio between horizontal and vertical components of microtremors. Bulletin of the Seismological Society of America. 1998;**88**:228-241

[4] Nakamura Y. A method for dynamic characteristics estimation of subsurface using microtremor on the ground surface. Quick Report of the Railway Research Institute. 1989;**30**(1):25-33

[5] Aki K. Space and time spectra of stationary stochastic waves, with special reference to microtremors. Bulletin of the Earthquake Research Institute. 1957; **35**:415-457

[6] Okada H. The Microtremor Survey Method. The Society of Exploration Geophysicist. Oklahoma: Tulsa; 2003. 135 pp

[7] Miyakoshi K, Okada H, Suqun S. A range of wavelengths to estimate the phase velocities of surface waves in microtremors. In: Proc. 94th SEGT Conf. 1996. pp. 178-182 (in Japanese)

[8] Yamanaka H, Ishida H. Application of genetic algorithms to an inversion of surface-wave dispersion data. Bulletin of the Seismological Society of America. 1996;**86**:436-444

[9] Haskell NA. The dispersion of surface waves on multi-layered media. Bulletin of the Seismological Society of America. 1953;**43**:17-34

[10] Scherbaum F, Hinzen K, Ohrnberger M. Determination of shallow shear wave velocity profiles in the Cologne, Germany area using ambient vibration. Geophysical Journal International. 2003;**152**:597-612

[11] Schmitz M, Alvarado L, Lüth S. The velocity structure of the Cariaco sedimentary basin, northeastern Venezuela, form the refraction seismic data and possible relation to earthquake hazard. Journal of South American Sciences. 2005;**18**(2):89-105

[12] Kitzunezaki CNG, Kobayashi Y, Ikawa T, Horike M, Saito T, Kurota T, et al. Estimation of P- and S-wave velocity in deep soil sediments for evaluating ground vibrations in earthquake. Journal of Japan Society for Natural Disaster Science. 1990;**9**(3):1-17 (in Japanese)

[13] Karagoz O, Chimoto K, Citak S, Ozel O, Yamanaka H, Hatayama K. Estimation of S-wave velocity structure and site response characteristics by microtremors array measurements in Tekirdag región, NW Turkey. Earth, Planets and Space. 2015;**67**:176

[14] Lomax A, Snieder R. Finding sets of acceptable solutions with a genetic algorithm with application to surface wave group dispersion in Europe. Geophysical Research Letters. 1994;**21**: 2617-2620. DOI: 10.1029/94GL02635

[15] Ólasfsdóttir EA. Multichannel Analysis of Surface Waves, Methods for Dispersion Analysis of Surface Wave Data. Reykjavík: University of Iceland, School of Engineering and Natural Sciences; 2014. p. 70

[16] Arai H, Tokimatsu K. S-wave velocity profiling by joint inversion of

microtremor dispersion curve and horizontal-to-vertical (H/V) spectrum. Bulletin of the Seismological Society of America. 2005;**95**(5):1766-1778

[17] Sánchez-Sesma F, Pérez-Ruiz A, Luzón F, Campillo M, Rodríguez-Castellanos A. Diffuse fields in dynamic elasticity. Wave Motion. 2008;**45**: 641-654

[18] Sánchez-Sesma F, Rodríguez M, Iturrarán-Viveros U, Luzón F, Campillo M, Margein L, et al. A theory for microtremors H/V spectral ratio: Application for a layered medium. Geophysical Journal of International Banner. Express Letter. 2011;**186**(1): 221-225

[19] Perton M, Sánchez-Sesma FJ, Rodríguez-Castellanos A, Campillo M, Weaver R. Two perspectives on equipartition in diffuse elastic fields in three dimensión. Journal of the Acoustical Society of America. 2009;**1**26 (3):1125-1130

[20] Bouchon M. A simple method to calculate Green's functions for elastic layered media. Bulletin of the Seismological Society of America. 1981; **71**(4):959-971

[21] Kawase H, Matsushima S, Satoh T, Sánchez-Sesma F. Applicability of theoretical-to-vertical ratio of microtremors based on the diffuse field concept to previously observed data. Bulletin of the Seismological Society of America. 2015;**105**(6):3092-3103

[22] Bonnefoy-Claudet S, Cornou C, Bard P, Cotton F, Moczo P, Kristek J, et al. H/V ratio: A tool for site effects evaluation. Results from 1-D noise simulations. Geophysical Journal International. 2006;**167**:827-837

[23] Bodin P, Horton S. Broadband microtremor observation of basin resonance in the Mississippi embayment, central us. Geophysical Research Letters. 1999;**26**(7):903-906

[24] Crane JM. Effects of stress and water saturation on seismic velocity and attenuation in near surface sediments [doctor philosophy dissertation]. USA: Mississippi College; 2013. p. 146

[25] Campbell K. Estimates of shear-wave Q and κ_0 for unconsolidated and semiconsolidated sediments in eastern North America. Bulletin of the Seismological Society of America. 2009; **99**(4):2365-2392

[26] Watabe Y, Sassa S. Sedimentary stratigraphy of natural intertidal flats with various characteristics. Soils and Foundations. 2012;**52**(3):411-429

[27] Matsuoka M, Wakamatsu K, Fujimoto K, Midorikawa S. Average shear wave velocity mapping using Japan engineering geomorphologic classification map. Structural Engineering/Earthquake Engineering. 2006;**23**(1):57s-68s

[28] Allen T, Wald D. Topographic Slope as a Proxy for Seismic Site-Conditions (Vs30) and Amplification Around the globe. Open-File Report 2007–1357. Reston, Virginia: U.S. Geological Survey; 2007

[29] Zhao J, Xu H. A comparison of V_{S30} and site period as site-effect parameters in response spectral ground-motion prediction equation. Bulletin of the Seismological Society of America. 2013; **103**:1-18

[30] McVerry G. Site-effect as continuous functions of site period and Vs30. In: Proceedings of the Ninth Pacific Conference on Earthquake Engineering, Building and Earthquake-Resilient Society; 14–16 April; Auckland, New Zealand. 2011

[31] Nakamura Y. Seismic vulnerability indices for ground and structures using

microtremors. In: World Conference on Railway Research, Florence. 1997

[32] Kraft J. Development of liquefaction susceptibility and hazard maps for the Islands of Jamaica and Trinidad [master thesis]. USA: Georgia Institute of Technology; 2013. p. 109

[33] Holzer TL, Noce TE, Bennett MJ. Liquefaction probability curves for surficial geologic deposits. Environmental and Engineering Geoscience. 2011;**17**(1):1-21

[34] Rivet D, Campillo M, Sánchez-Sesma F, Shapiro N, Singh K. Identification of surface wave higher modes using a methodology based on seismic noise and coda waves. Geophysical Journal International. 2015; **203**:856-868

[35] Bozzoni F, Corigliano M, Lai C, Salazar W, Scandella L, Zuccolo E, et al. Probabilistic seismic hazard assessment at the eastern Caribbean Islands. Bulletin of the Seismological Society of America. 2011;**101**(5):2499-2521

Chapter 5

Long-Wave Generation due to Atmospheric-Pressure Variation and Harbor Oscillation in Harbors of Various Shapes and Countermeasures against Meteotsunamis

Taro Kakinuma

Abstract

First, the generation and propagation of long ocean waves due to the atmospheric-pressure variation have been simulated using the numerical model based on the nonlinear shallow water equations, where the atmospheric-pressure waves of various pressure-profile patterns travel eastward over East China Sea. Before the oscillation attenuation in Urauchi Bay, Japan, the incidence of long waves can continue owing to an oscillation system generated between the main island of Kyushu and Okinawa Trough. Second, the simple estimate equations are proposed to predict both the wave height and wavelength of long waves caused by an atmospheric-pressure wave, using atmospheric-pressure data above the ocean. Third, numerical simulation has been generated for the oscillation in the harbors of C-, I-, L-, and T-type shapes, as well as Urauchi Bay with two bay heads like a T-type harbor. Finally, we discuss disaster measures, including the real-time prediction of meteotsunami generation, as well as both the structural and the nonstructural preparations.

Keywords: meteotsunami, long wave, atmospheric pressure, harbor oscillation, secondary undulation, submarine trough, East China Sea, real-time prediction

1. Introduction

At Urauchi Bay of Kamikoshiki Island, situated in the western offing of Kyushu Island, Japan, as shown in **Figure 1**, heavy harbor oscillations occurred during February 24–26, 2009, where the maximum total amplitude of water level reached 3.0 m [1], resulting in that eight fishing boats were capsized and several houses were flooded, as shown in **Figures 2–4**. In terms of time, Japan Standard Time (JST) is used in this chapter. According to the Grid-Point-Value (GPV) pressure data, published by Japan Meteorological Agency (JMA), atmospheric-pressure waves propagated almost eastward over East China Sea, during this term.

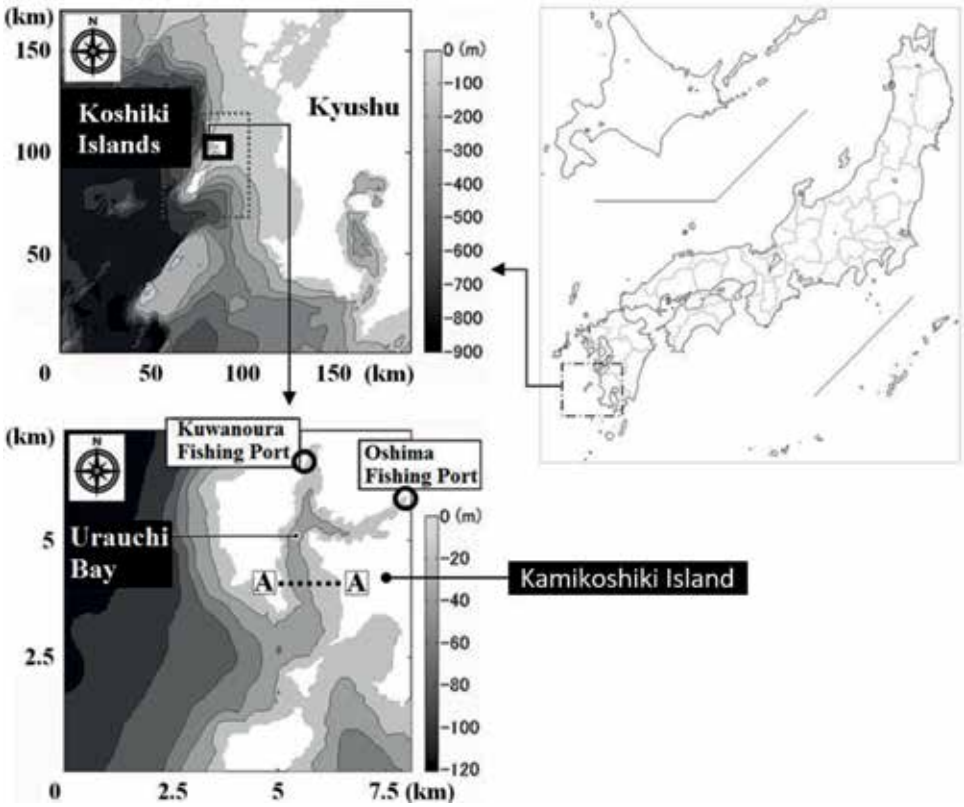

Figure 1.
The still water depth around both the main island of Kyushu, and Urauchi Bay in Kamikoshiki Island, Kagoshima Prefecture, Japan. East China Sea is spread to the west of these islands.

Figure 2.
The refloatation operation for the fallen fishing boats around 8:00 (the left-hand side), and eight flooded cars at 8:33 (the right-hand side), on February 25, 2009. These photos were taken by Satsumasendai City Office at Oshima Fishing Port, which is located at one of two heads of Urauchi Bay, as indicated in ***Figure 1****.*

Such atmospheric-pressure waves propagating over the sea surface have often generated significant long ocean waves, through an amplification mechanism, that is, the Proudman resonance [2], especially when the phase velocity of the atmospheric-pressure wave is close to that of the long ocean waves, as examined by, for example, Hibiya and Kajiura [3] and Vilibic et al. [4], where they numerically reproduced the large harbor oscillation in Nagasaki Bay, Kyushu, Japan, and that in Ciudadella Harbor, Balearic Islands, Spain, respectively. Once long ocean waves are generated by meteorological disturbance due to the instability of a wintry weather system, as well as a storm, and reach a nearshore zone, the wave height of the secondary undulation increases owing to the decrease of water depth, like a tsunami caused by a submarine earthquake (e.g., [5]), a land slide (e.g., [6]), etc., such that

Figure 3.
The receding flows through the seawall at 8:36 on February 25, 2009 (the left-hand side), and an inundated house fence (the right-hand side). These photos were taken by Satsumasendai City Office at and near Oshima Fishing Port, respectively.

Figure 4.
A damaged fishing boat (the left-hand side), and the basement of a jetty, where part of armor stones have been flowed out (the right-hand side). These photos were taken by the author at Oshima Fishing Port on February 28, 2009.

the long waves are called "meteotsunamis." Meteotsunamis amplified depending on the conditions of atmospheric-pressure waves [7] can become external forces to create huge oscillation, severe inundation, etc. to coastal areas. Long ocean waves supposed to be meteotsunamis have been discussed based on observed data for many coastal zones, considering local characteristics concerning both geographic features and meteorological phenomena (e.g. [8, 9]); Bailey et al. [10] reported meteotsunamis caused by storms, which attacked the east coasts of the United States, facing the continental shelf; recent meteotsunami cases around the world were summarized by Tanaka and Ito [11]. In nearshore zones, meteotsunamis are amplified through not only shoaling but also harbor oscillation in ports, harbors, and bays. Harbor oscillation, also called seiche, with the harbor paradox [12], depends on incident-wave period, harbor shape, and water depth. The oscillation in harbors of various horizontal shapes has been studied using linear theories [13], hydraulic experiments [14], nonlinear numerical models [15], etc.

In this chapter, first, we numerically simulate long ocean waves due to atmospheric-pressure waves with different pressure-profile patterns, including the atmospheric-pressure waves that caused the large harbor oscillation in Urauchi Bay on February 25, 2009. Second, simple estimate equations concerning both the wave height and wavelength of long waves generated by atmospheric-pressure variation are proposed using atmospheric-pressure data above the ocean, for easy prediction methods are required for disaster prevention by, for example, fisheries cooperatives and local authorities, although the numerical computation is necessary to research both the mechanisms and characteristics of meteotsunamis. Third, we apply a numerical model based on the nonlinear shallow water equations, to study oscillation in harbors of various shapes, including the types of "L," "I" with a narrow region, "I" with a seabed crest or trough, "C," and "T," as well as Urauchi Bay, which has two heads like a T-type harbor. Finally, we discuss disaster measures against meteotsunamis, generated to propagate toward the west coasts of Kyushu. Several methods for the real-time prediction of meteotsunami generation are

proposed, using an inverse analysis, as well as the proposed simple prediction equations, after which both the structural and the nonstructural preparations for meteotsunamis are summarized.

2. Numerical model and calculation conditions

A set of nonlinear shallow water equations, in consideration of atmospheric-pressure gradient at the sea surface, is solved in the horizontal two dimensions by applying a finite difference method. The fundamental equations are

$$\frac{\partial \eta}{\partial t} + \frac{\partial}{\partial x}\{(\eta + h)U\} + \frac{\partial}{\partial y}\{(\eta + h)V\} = 0, \tag{1}$$

$$\frac{\partial U}{\partial t} + \frac{\partial U^2}{\partial x} + \frac{\partial (UV)}{\partial y} = fV - g\frac{\partial \eta}{\partial x} - \frac{1}{\rho}\frac{\partial P}{\partial x} + A_h\left(\frac{\partial^2 U}{\partial x^2} + \frac{\partial^2 U}{\partial y^2}\right) - \frac{KU\sqrt{U^2 + V^2}}{\eta + h}, \tag{2}$$

$$\frac{\partial V}{\partial t} + \frac{\partial (UV)}{\partial x} + \frac{\partial V^2}{\partial y} = -fU - g\frac{\partial \eta}{\partial y} - \frac{1}{\rho}\frac{\partial P}{\partial y} + A_h\left(\frac{\partial^2 V}{\partial x^2} + \frac{\partial^2 V}{\partial y^2}\right) - \frac{KV\sqrt{U^2 + V^2}}{\eta + h}, \tag{3}$$

where U and V are horizontal velocities in the x and y directions, respectively; η, h, and P are water surface displacement, still water depth, and atmospheric pressure at the water surface, respectively; f and A_h are the Coriolis coefficient and horizontal eddy viscosity coefficient, respectively. In the present study, gravitational acceleration g = 9.8 m/s^2, seabed friction coefficient $K = 2.6 \times 10^{-3}$, and seawater density ρ = 1035.0 kg/m^3. The Sommerfeld radiation condition is adopted at the boundaries of the computational domain, while the boundaries between land and sea are assumed to be vertical walls with the perfect reflection of waves.

3. Long-wave generation due to atmospheric-pressure waves

3.1 The relationship between the parameters of atmospheric-pressure waves and long-wave generation

In the large area along the west coasts of Kyushu, as well as Yamaguchi Prefecture nearby Kyushu, secondary undulation, supposed to be caused by atmospheric-pressure disturbance above East China Sea, often increases from February to April, sometimes leading to disasters as mentioned above. In this section, we discuss the relationship between the parameters of atmospheric-pressure waves and long-wave generation in the ocean. The computational domain is part of East China Sea, where the longitude is from 123.0 to 131.0°E, and the latitude is from 30.0 to 32.5°N, with the actual seabed configuration. The still water depth in East China Sea near the main island of Kyushu is shown in **Figure 5**, where it is around 800 m at the deepest site in Okinawa Trough. The grid widths Δx and Δy are 790.0 and 925.0 m, respectively, while the time step Δt is 2.0 s. In this section, the Coriolis coefficient f and horizontal eddy viscosity coefficient A_h in Eqs. (2) and (3) are 7.3×10^{-5} s^{-1} and 100.0 m^2/s, respectively.

In the computation, it is assumed that the atmospheric pressure is uniform from north to south, and atmospheric-pressure waves travel eastward at a constant phase velocity over East China Sea. The distribution of atmospheric pressure along the latitude lines is classified into four patterns shown in **Figure 6**, based on the GPV

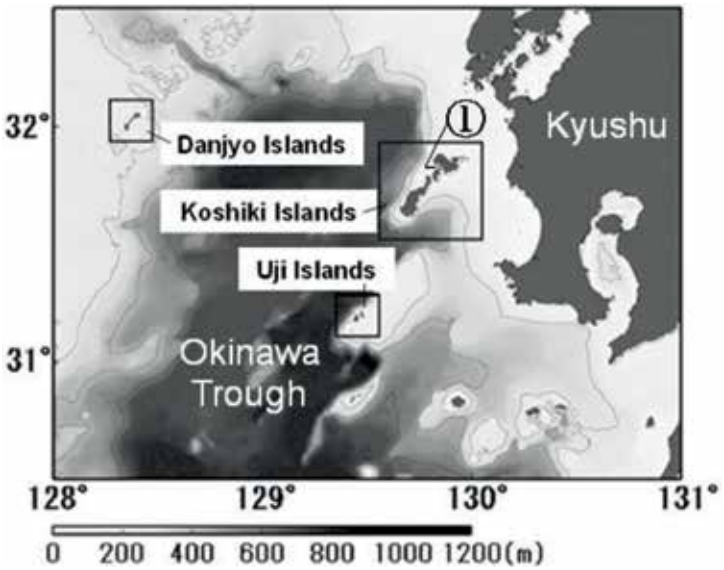

Figure 5.
The still water depth in East China Sea near the main island of Kyushu. The point indicated with ① is located off the mouth of Urauchi Bay, where the huge harbor oscillation of 3.0 m in total amplitude was observed. The still water depth is around 800 m at the deepest site in Okinawa Trough.

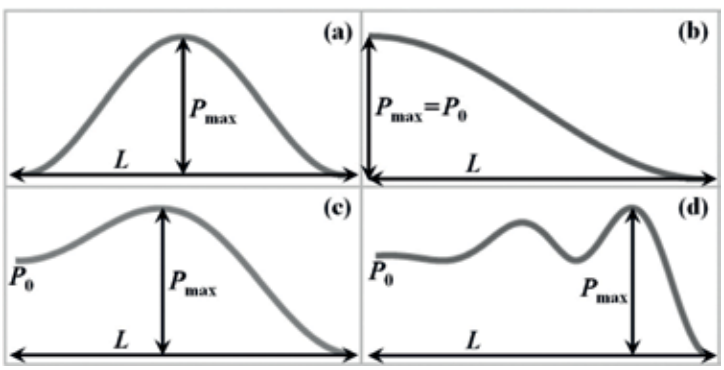

Figure 6.
Typical four patterns for the high-pressure profiles of atmospheric-pressure waves, propagating rightward. P_{max} is the maximum value of pressure, while P_o is a stable value of pressure, where $P_o = 0$ in (a), $P_o = P_{max}$ in (b), and $P_o < P_{max}$ in (c) and (d).

pressure data, where the atmospheric pressure P is a deviation from the value of pressure for an average atmospheric-pressure condition. It should be noted that an atmospheric-pressure wave is not a pressure wave in fluids, including a sound wave and a shock wave, but the propagation of an atmospheric-pressure profile.

An atmospheric-pressure wave of pattern (a), for example, has three parameters, that is, wavelength L, the maximum value of pressure, $P_{\max}$, and phase velocity C_p, where these values are kept constant before the wave stops in the numerical calculation. The pressure profile for an atmospheric-pressure wave of pattern (a) is described as

$$P(x,t_0) = \begin{cases} \dfrac{p_{\max}}{2}\left\{1+\cos\left[\dfrac{2\pi}{L}(x-x_c)\right]\right\} & (|x-x_c| \le L/2), \\ 0 & (|x-x_c| > L/2), \end{cases} \tag{4}$$

where the initial position of the pressure peak, x_c, is at the longitude of 124°E.

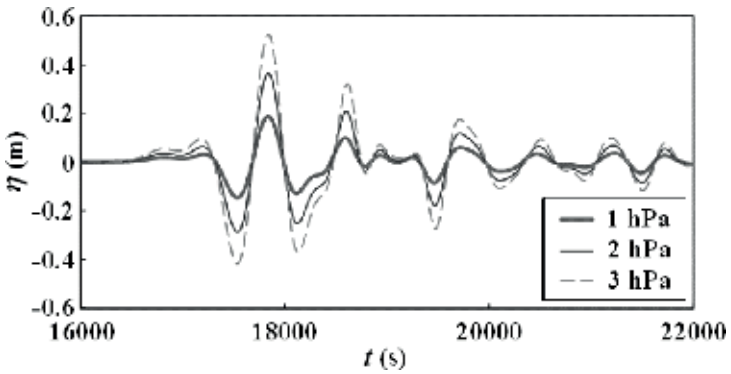

Figure 7.
*The water surface displacements at Point ① indicated in **Figure 5**, for various values of P_{max}. The wave profile of atmospheric pressure is pattern (a), where L = 10.0 km, C_p = 20.0 m/s, and P_{max} = 1.0, 2.0, or 3.0 hPa. The still water depth is about 22.0 m at Point ①.*

Figure 7 shows the numerical calculation results of water surface displacements at Point ① indicated in **Figure 5**, owing to an assumed atmospheric-pressure wave of pattern (a), where L = 10.0 km, C_p = 20.0 m/s, and $P_{\max}$ = 1.0, 2.0, or 3.0 hPa. Point ① is located off the mouth of Urauchi Bay, where the huge harbor oscillation of 3.0 m in total amplitude was observed, as mentioned above. The wave height of the generated long waves at Point ① is almost in proportion to $P_{\max}$, which has been also confirmed at the other monitoring points near Danjyo Islands or Uji Islands. According to **Figure 7**, many long waves propagate through Point ①, owing to the travel of one atmospheric-pressure wave.

Shown in **Figure 8** is the wave height and period of the long wave with the maximum wave height at Point ① indicated in **Figure 5**, for various values of C_p, where the wave profile of atmospheric pressure is pattern (a); L = 30.0 km and $P_{\max}$ = 1.0 hPa; the waves are defined using the zero-up-cross method. Inside the area from 125.5 to 127.0°E, and from 30.0 to 32.5°N, the average value of still water depth is 80 m, or 100 m, over the continental shelf, such that the Proudman resonance for long ocean waves can occur when the phase velocity of an atmospheric-pressure wave, C_p, is around the phase velocity of linear shallow water waves, that is, $\sqrt{gh}\approx 30$ m/s. According to **Figure 8**, the wave height of the long ocean waves increases as C_p is close to 32.0 m/s.

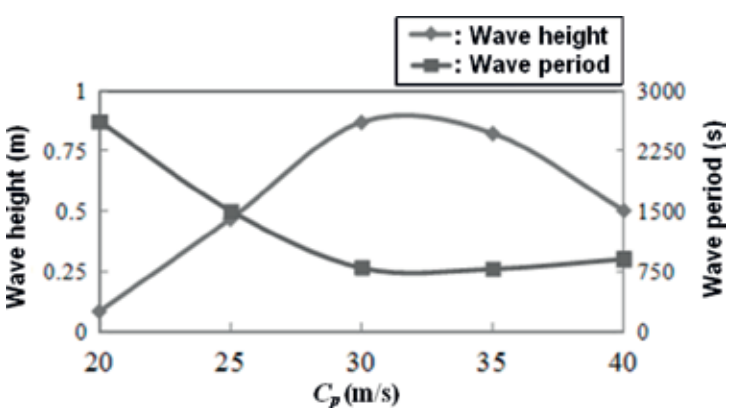

Figure 8.
*The wave height and period of the long wave with the maximum wave height at point ① indicated in **Figure 5**, for various values of C_p. The wave profile of atmospheric pressure is pattern (a), where L = 30.0 km and P_{max} = 1.0 hPa.*

3.2 The long waves on the days when large harbor oscillation occurred in Urauchi Bay

The pressure profiles for atmospheric-pressure waves of patterns (b), (c), and (d) shown in **Figure 6** are described for $|x - x_c| \leq L/2$ as

$$\text{(b)}: P(x,t_0) = P_0\{1 - \sin[\pi(x - x_c)/L]\}/2, \tag{5}$$

$$\begin{aligned}\text{(c)}: \quad P(x,t_0) &= P_0\{1 + \cos[2\pi(x - x_c)/L]\}/2 \\ &\quad + P_0\{1 - \sin[\pi(x - x_c)/L]\}/2,\end{aligned} \tag{6}$$

$$\begin{aligned}\text{(d)}: \quad P(x,t_0) &= 0.05e^{\kappa}P_0\{1 + \cos[6\pi(x - x_c)/L]\}/4 \\ &\quad + P_0\{1 - \sin[3\pi(x - x_c - x_d)/L]\}/2,\end{aligned} \tag{7}$$

respectively, while $P(x, t_0) = P_0(x < x_c - L/2)$ and $P(x, t_0) = 0.0$ $(x > x_c + L/2)$. In Eq. (7), x_d is the initial position of the second pressure peak, and the power κ is $0.02x$.

The parameters of each pattern are evaluated based on the GPV pressure data on the days when large harbor oscillation occurred in Urauchi Bay. For example, the time variation of GPV pressure distribution on February 25, 2009, when the largest harbor oscillation was observed in Urauchi Bay from 2009 to 2018, is shown in **Figure 9**.

Figure 10 shows the pressure profiles along three latitudes of 30.0, 30.5, and 31.0°N, at 3:00 on February 25, 2009, according to the GPV pressure data shown in **Figure 9**. An atmospheric-pressure wave, where the pressure gap was 4–5 hPa, and the total wavelength was 80–120 km, traveled almost eastward over East China Sea, at the phase velocity of around 140 km/h from 3:00 to 4:00, 120 km/h from 4:00 to 5:00, and 150 km/h from 5:00 to 6:00, such that the wave profile of the atmospheric pressure on the day is described with pattern (d), where the mean values of the parameters, that is, L, $P_{\max}$, and C_p, are 90.0 km, 4.0 hPa, and 38.6 m/s, respectively.

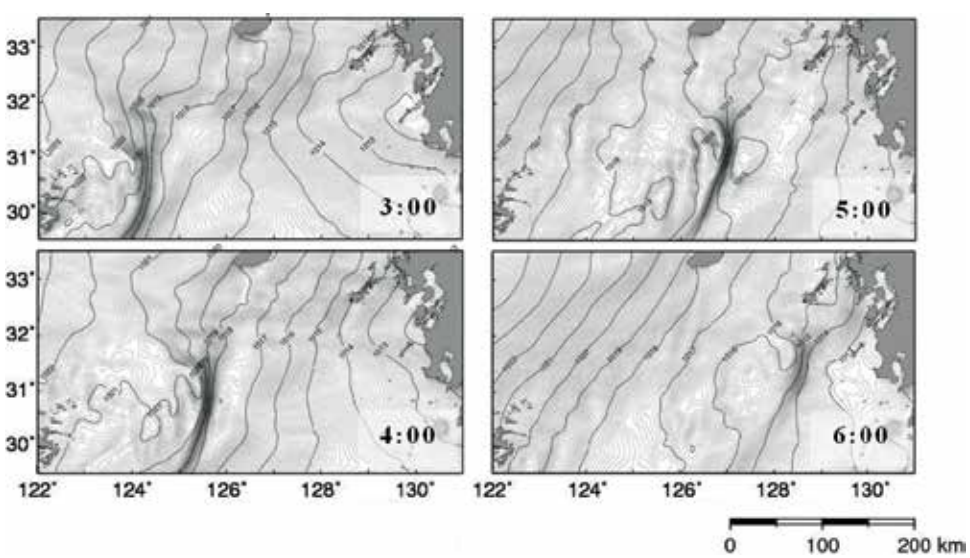

Figure 9.
The time variation of the GPV pressure distribution on February 25, 2009, when the huge harbor oscillation of 3.0 m in total amplitude was observed in Urauchi Bay. The GPV pressure data were published by Japan Meteorological Agency.

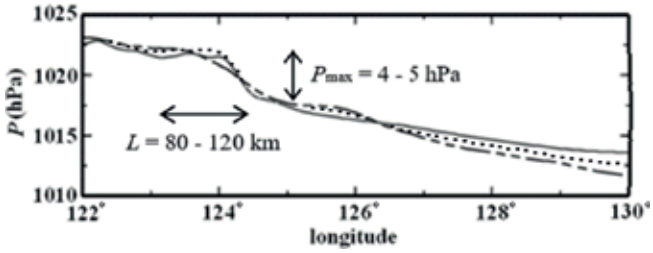

Figure 10.
The GPV pressure distributions along three latitudes of 30.0, 30.5, and 31.0°N, at 3:00 on February 25, 2009. The solid, dotted, and chain double-dashed lines show the pressure along the latitudes of 30.0, 30.5, and 31.0° N, respectively.

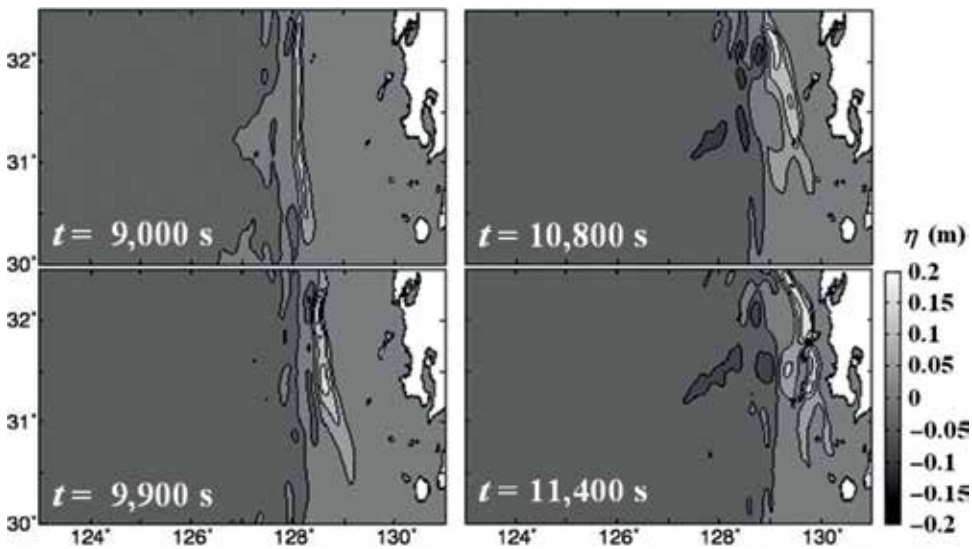

Figure 11.
The numerical result for the time variation of water level distribution on February 25, 2009. The wave profile of atmospheric pressure is pattern (d), where L = 90.0 km, P_{max} = 4.0 hPa, and C_p = 38.6 m/s.

Depicted in **Figure 11** is the numerical result for the time variation of water level distribution due to the atmospheric-pressure waves, where the pressure profile is pattern (d), and its parameters L, $P_{\max}$, and C_p are 90.0 km, 4.0 hPa, and 38.6 m/s, respectively. The waves show refraction over Okinawa Trough, for the phase velocity of the generated long waves decreases over the deep trough, after which they propagate to the northeast, as pointed out by Katayama et al. [16].

The numerical result for the water surface displacement at Point ① indicated in **Figure 5** is shown in **Figure 12**, where the wave height of the first three waves is over 1 m, and the wave period of the first to the fifth waves is about 1000, 750, 700, 760, and 660 s, respectively.

According to the observed data [9], large harbor oscillation also occurred in Urauchi Bay on March 3, 5, and 6, 2010, where the wave profiles of atmospheric pressure are described by patterns (b), (c), and (d), respectively, based on the corresponding GPV pressure data, and the mean values of the parameters (L, $P_{\max}$, and C_p) are (100.0 km, 3.0 hPa, 20.0 m/s), (100.0 km, 4.0 hPa, 33.0 m/s), and (90.0 km, 4.0 hPa, 25.0 m/s), respectively. Shown in **Figure 13** are the numerical calculation results for the water surface displacements at Point ① indicated in **Figure 5**, originating from the atmospheric-pressure waves of patterns (b), (c), and (d),

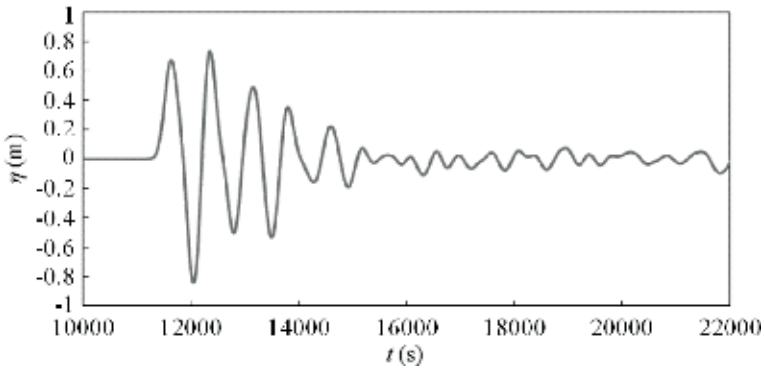

Figure 12.
The numerical result for the water surface displacement at point ① indicated in ***Figure 5****, on February 25, 2009. The wave profile of atmospheric pressure is pattern (d), where L = 90.0 km,* P_{max} *= 4.0 hPa, and* C_p *= 38.6 m/s.*

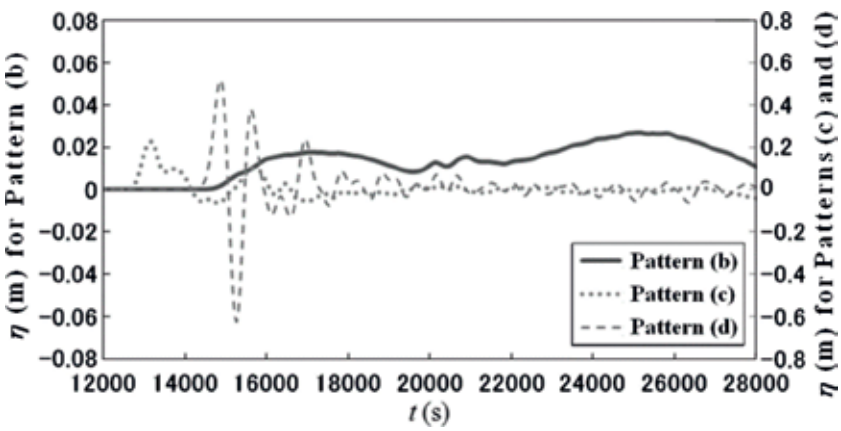

Figure 13.
The numerical results for the water surface displacements at Point ① indicated in ***Figure 5****. The wave profiles of atmospheric pressure are patterns (b), (c), and (d), where the parameters (L,* P_{max}*, and* C_p*) are (100.0 km, 3.0 hPa, 20.0 m/s), (100.0 km, 4.0 hPa, 33.0 m/s), and (90.0 km, 4.0 hPa, 25.0 m/s), respectively.*

with the abovementioned mean values of their parameters. The wave height of the long waves due to the atmospheric-pressure wave of pattern (b) is lower than that in the other cases, for the atmospheric pressure does not decrease after its increase. If the sea surface, which has been pressed down, is relieved owing to attenuation in atmospheric pressure, the balance between the atmospheric pressure and the water surface gradient is not maintained, resulting in the production and propagation of free-surface waves, and the Proudman resonance appears when the moving velocity of the recovery point of atmospheric pressure matches the phase velocity of long ocean waves. Although the reason why the harbor oscillation in Urauchi Bay was rather large on March 3, 2010, is thought to be linked to the instability in atmospheric pressure before the day, future work is required.

Conversely, the long waves generated by the atmospheric-pressure wave of pattern (d) show remarkable wave height of 1.1 m, where the atmospheric pressure decreases after its increase. The wave period of the first wave is about 1300 s, while that of the second and the third waves is about 1250 and 900 s, respectively. These values of wave period, as well as the numbers of exited long waves, concern the amplification of harbor oscillation, as discussed in the following sections. The long waves due to the atmospheric-pressure wave of pattern (c) also show the maximum

wave height of about 0.3 m, and the wave period of the long wave with the maximum wave height is around 2600 s.

4. Oscillation system between the main island of Kyushu and Okinawa Trough

The amplification of harbor oscillation requires continuous wave energy incidence into the harbor. **Figure 14** shows the water surface displacements at Point ①, off the mouth of Urauchi Bay, owing to the atmospheric-pressure wave of pattern (a), where L = 10.0 km, $P_{\max}$ = 1.0 hPa, and C_p = 20.0 m/s. In the figure, the numerical result, in consideration of wave reflection at the west coasts of the main island of Kyushu, is compared with that without wave reflection at the west coasts of the main island of Kyushu, where the target domain for the latter is a restricted area between 123°E and 130°E. In the former case, an oscillation system is generated off the southern Kyushu, between the main island of Kyushu and Okinawa Trough, resulting in the continuous motion of water surface, to make heavier harbor oscillation in, for example, Urauchi Bay. Another oscillation system off the northern Kyushu may also appear between the main island of Kyushu and other islands, without the submarine trough, as suggested by Hibiya and Kajiura [3].

In order to examine the generation of an oscillation system between Okinawa Trough and the main island of Kyushu, we perform numerical experiments for a hypothetical seabed configuration. **Figure 15(a)** shows the actual seabed configuration along the latitude of 31.8°E, where Urauchi Bay is located as shown in **Figure 5**, while **Figure 15(b)** shows the hypothetical seabed configuration, where the trough length is extended to make the distance between wave reflection points larger. In both cases, the perfect reflection boundary condition is adopted at the west coasts of the main island of Kyushu.

In the one-dimensional computation for long waves, the nonlinear surface wave equations based on a variational principle [17] is applied to consider both the strong nonlinearity and dispersion of long waves over the shallower areas, as well as the deeper trough, where the velocity potential is assumed to show a linear distribution in the vertical direction. The water surface profile is given by η (m) = -0.2 m sin $[2\pi(x - 790.0\text{ km})/27.7\text{ km}]$ (790.0 km ≤ x ≤ 817.7 km), and the velocity potential is zero everywhere, at the initial time. **Figure 16** shows the water surface displacements at Points P1–P5, for the hypothetical seabed configuration illustrated in **Figure 15(b)**, where the fundamental equations were solved using the implicit

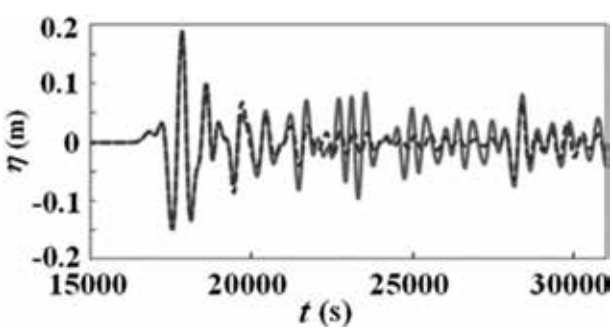

Figure 14.
*The numerical results for the water surface displacements at point ① indicated in **Figure 5**. The atmospheric-pressure profile is pattern (a), where L = 10.0 km, P_{max} = 1.0 hPa, and C_p = 20.0 m/s. The solid and broken lines represent the results with and without wave reflection at the west coasts of the main island of Kyushu, respectively.*

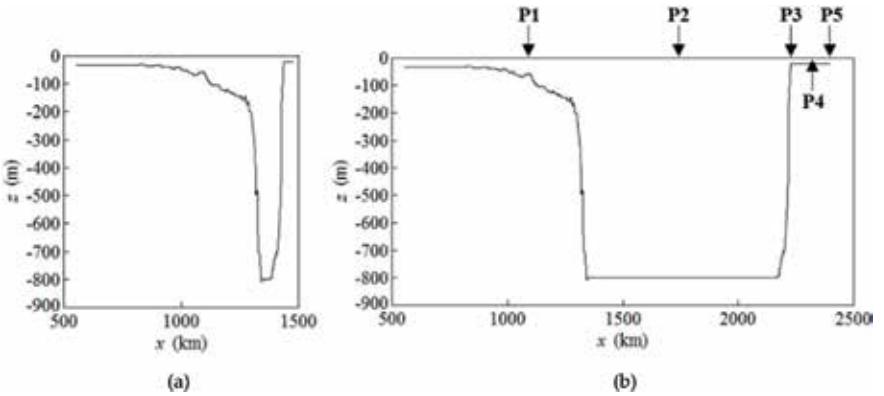

Figure 15.
The seabed configurations of East China Sea along the latitude of 31.8°E: The actual seabed configuration (a), and a hypothetical seabed configuration with an extended trough (b).

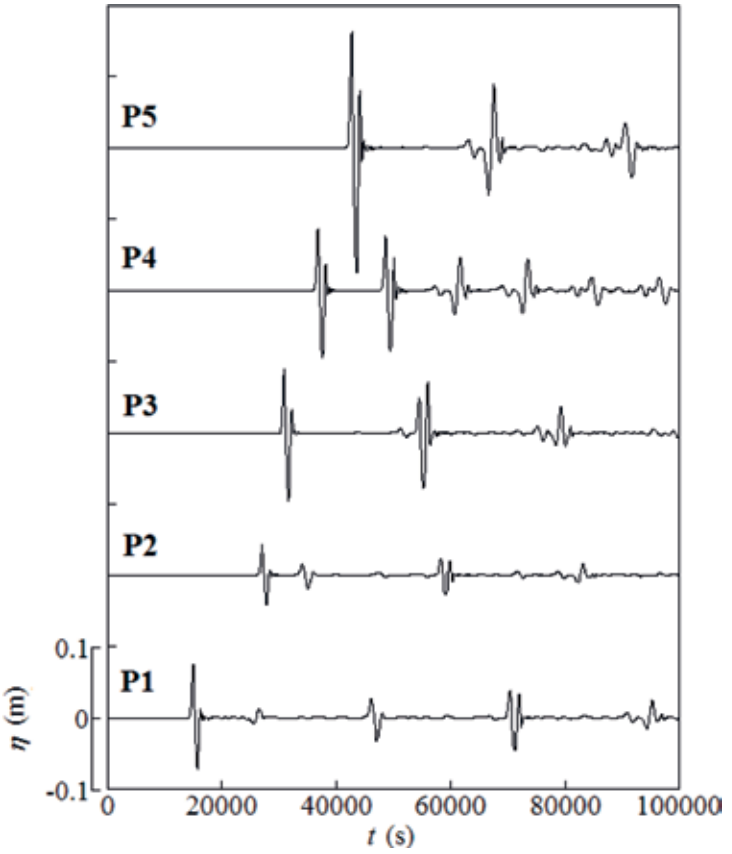

Figure 16.
The water surface displacements at the Points P1–P5 for the hypothetical seabed configuration illustrated in ***Figure 15(b)****.*

scheme [18]. An oscillation system with repeated reciprocation of long waves has been built up, resulting in the periodical oscillation at Point P4, where Koshiki Islands are situated. Such continuous undulation in water surface contributes to amplify harbor oscillation in bays and harbors at the west coasts of the southern Kyushu.

5. Simple method to estimate long waves due to an atmospheric-pressure wave

5.1 Estimate equations for the wave height and wavelength of generated long waves

As mentioned in Section 1, long waves due to atmospheric-pressure variation can cause large harbor oscillation, resulting in hazards including the damages of fish boats and the inundation of houses, such that it is necessary for fishing cooperatives, town offices, etc. to prevent such hazards. If a simple method to predict the generation of serious long ocean waves is available, then they can make provision against meteotsunamis, several hours before. In this section, we propose equations to estimate both the wave height and wavelength of coming long ocean waves, using the measured or GPV data of atmospheric pressure, without derivation, integration, or complex numerical calculation.

It is assumed that the distribution of atmospheric pressure p above the outer sea is trapezoidal at the initial time t = 0.0 s, as shown in **Figure 17**, where the profile for a low-pressure case is illustrated, after which the atmospheric-pressure wave propagates stably at a constant phase velocity, in the positive direction of the x-axis.

The water surface is assumed to rise 1.0 cm owing to the pressure decrease of 1.0 hPa, and then the initial profile of water surface is also trapezoidal as shown in **Figure 18**. The maximum value of water surface displacement is $-P/10{,}000$ (m) for $x_0 + D_P \le x \le x_0 + D_P + L_P$ at $t = t_0$, where P (Pa) < 0 is the minimum pressure value of the atmospheric-pressure wave shown in **Figure 17**, and L_P is the distance where its pressure value hardly shows variation.

After the initial condition shown in **Figure 17**, side AB of the low-pressure profile moves at a constant phase velocity, resulting in a gradual recovery of atmospheric pressure from the low-pressure condition. The moving velocity of point A, where the pressure recovery starts, that is, the phase velocity of the atmospheric-pressure wave, C_P, is assumed to equal the phase velocity of long ocean waves, C, to

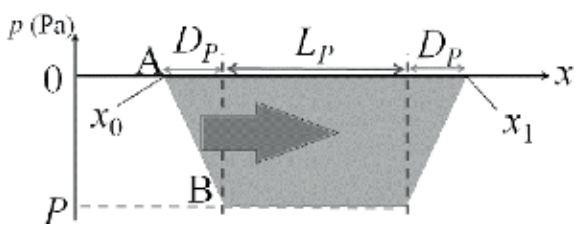

Figure 17.
The initial atmospheric-pressure distribution of a low-pressure wave. After the initial time, the pressure wave propagates at a constant phase velocity in the positive direction of the x*-axis.*

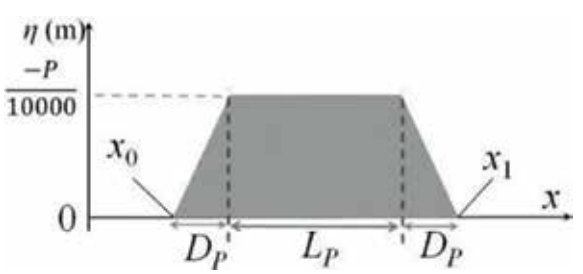

Figure 18.
The initial water surface profile due to the initial atmospheric-pressure distribution shown in ***Figure 17****.*

consider a sever case due to the Proudman resonance. It is also assumed that the wavelength of long ocean waves, λ, is much larger than the still water depth h, that is, $h/\lambda \ll 1$, such that $C_P = C = \sqrt{gh}$.

When $t = \Delta t$, the positions of points A and B become $x = x_0 + \Delta L$ and $x = x_0 + D_P + \Delta L$, respectively, where $\Delta L = C_P \Delta t$. The water body CDFE sketched in **Figure 19**, which is part of the raised water at the initial time, is relieved owing to the recovery of the low pressure during Δt.

The parallelogram CDFE, which we call S_0, shown in **Figure 19**, corresponds to the trapezoid S_1 shown in **Figure 20**, where the height and the length of lower base of the trapezoid S_1 are a (m) $= -P\Delta L/D_P/10{,}000$ and $L_1 = D_P + \Delta L$, respectively, for side EF shown in **Figure 19** is an isopotential energy level at $t = \Delta t$. The relieved water body S_1 transforms to two long ocean waves, propagating in the positive and negative directions of the x-axis, where the wave height, the wavelength, and the absolute value of phase velocity, of the two long waves, are approximately $a/2$, L_1, and C, respectively.

Through the recovery of low pressure after $t = \Delta t$, the relief of water body is repeated, such that the long ocean wave, propagating in the positive direction of the x-axis, is overlapped by other long waves generated continuously. Consequently, the wave amplitude H and wavelength λ of the long wave traveling in the positive direction of the x-axis are estimated by

$$H = (-PL_P/D_P)/20{,}000 \text{ (m)}, \tag{8}$$

$$\lambda = D_P, \tag{9}$$

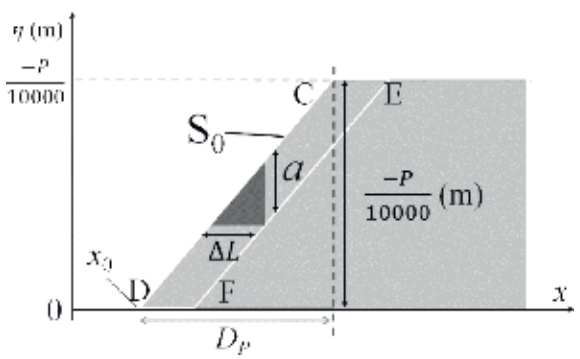

Figure 19.
An enlarged illustration of part of the water surface profile shown in ***Figure 18****. Side AB of the low-pressure profile shown in* ***Figure 17****, is above side DC of the water surface profile at* t = 0.0 s*, after which side AB comes above side FE at* t = Δt.

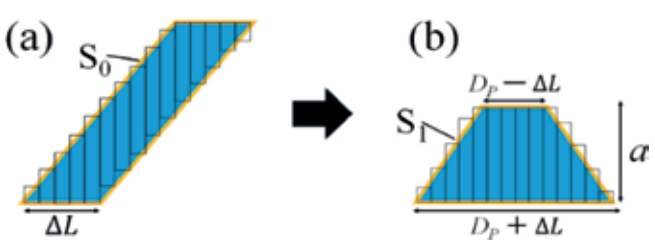

Figure 20.
An aggregation of water columns, S_0, relieved owing to the recovery of low pressure (a), and the corresponding trapezoidal water body S_1 (b).

respectively. When L_P is the moving distance of side AB, Eq. (8) corresponds to the prediction equation shown by Hibiya and Kajiura [3], using the method of characteristics. The parameters P, L_P, and D_P can be evaluated according to the observed or GPV pressure data for the wave profile of an atmospheric-pressure wave.

Conversely, if we observe the time variation of atmospheric pressure at several offshore sites, to obtain the recovery rate of pressure p, that is, r_P, which is defined by $\partial p/\partial t$, the estimate equation for H is

$$H = (r_P L_P / C_P)/20,000(\mathrm{m}), \tag{10}$$

for r_P corresponds to $-PC_P/D_P$ (Pa/s), according to **Figure 17**. It is noted that Eqs. (8)–(10) can be also applied to high-pressure cases, where the positive value P is the highest value of atmospheric pressure.

5.2 The validation of predicted values through the estimate equations

Several results through the proposed estimate equations, that is, Eqs. (8) and (9), are compared with the corresponding numerical results obtained using the numerical model based on Eqs. (1)–(3), for the one-dimensional generation and propagation of meteotsunamis. The still water depth h is assumed to be uniformly 100.0 m. In the numerical computation, the distribution of atmospheric pressure at the water surface is changed gradually from zero to a low-pressure distribution as shown in **Figure 17**, resulting in a water surface profile as shown in **Figure 18**. After obtaining the initial steady state, side AB shown in **Figure 17** moves at $C_P = C = \sqrt{gh}$. The Coriolis coefficient, seabed friction coefficient, and horizontal eddy viscosity coefficient are zero in Eqs. (1)–(3) for simplicity.

Figure 21 shows the numerical calculation results of water surface displacements at $x = x_1$ indicated in **Figure 18**, where $P = -400$ Pa and $L_P = 100{,}000$ m; $D_P = 12{,}500$, 25,000, and 50,000 m. The decrease in water surface displacement η for $t < 7{,}000$ s is due to the decrease in atmospheric pressure before the initial time, while the increase in η for $t > 11{,}000$ s is caused by the propagation of the

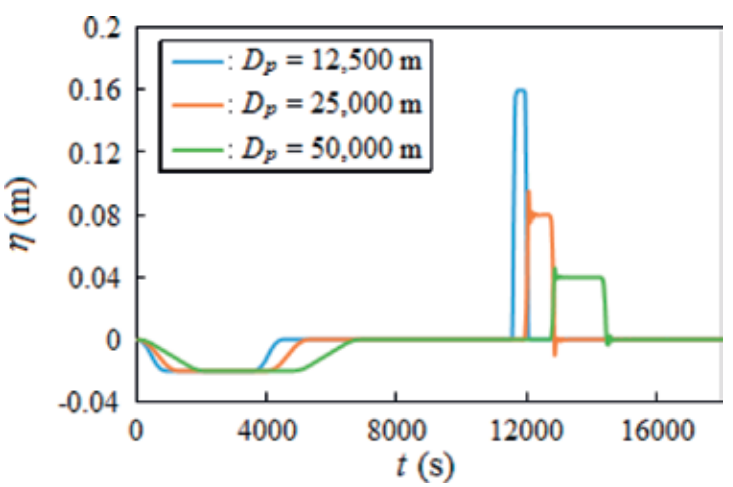

Figure 21.
*The numerical results of water surface displacements at $x = x_1$ indicated in **Figure 18**, obtained using the nonlinear shallow water model, for various values of D_P, where $P = -400$ Pa; $L_P = 100{,}000$ m; $D_P = 12{,}500$, 25,000, and 50,000 m.*

Values of pressure parameters				Numerical results obtained using Eqs. (1)–(3)			Estimated values from Eqs. (8) and (9)	
D_P (m)	r_P (Pa/s)	L_P (m)	P (Pa)	H (m)	λ (m)	T (s)	H (m)	λ (m)
12,500	1.00	50,000	−400	0.080	12,500	400	0.08	12,500
		100,000	−200	0.080			0.08	
			−400	0.160			0.16	
	−1.00	100,000	400	−0.160			−0.16	
25,000	0.50	50,000	−400	0.040	25,000	800	0.04	25,000
		100,000	−200	0.040			0.04	
			−400	0.080			0.08	
	−0.50	100,000	400	−0.080			−0.08	
50,000	0.25	50,000	−400	0.020	50,000	1600	0.02	50,000
		100,000	−200	0.020			0.02	
			−400	0.040			0.04	
	−0.25	100,000	400	−0.040			−0.04	

Table 1.
*The wave amplitude H, wavelength λ, and wave period T of the generated long ocean waves, at $x = x_1$ indicated in **Figure 18**, obtained using the numerical model based on the nonlinear shallow water equations, that is, Eqs. (1)–(3), as well as the estimated values of H and λ through Eqs. (8) and (9), where D_P, L_P, and P are defined in **Figure 17**; r_P is the recovery rate of atmospheric pressure.*

atmospheric-pressure waves. As D_P is decreased, the wavelength of the meteotsunamis decreases, but their wave height increases.

Shown in **Table 1** are the numerical results of wave amplitude H, wavelength λ, and wave period T, for the generated long waves propagating through $x = x_1$ indicated in **Figure 18**, in comparison with the corresponding estimated values of both H and λ from Eqs. (8) and (9), respectively. The estimated values show good agreement with the corresponding computational data, such that the proposed estimate equations are available to predict the approximate values of both the wave height and wavelength of severe meteotsunamis, using observed or GPV atmospheric-pressure data.

6. Numerical calculation for harbor oscillation in harbors of various shapes

6.1 Numerical calculation conditions

Meteotsunamis can be amplified to be heavier through harbor oscillation, as well as shoaling. In this chapter, we discuss oscillation in harbors of various shapes, by applying the numerical model based on the nonlinear shallow water equations, that is, Eqs. (1)–(3). The Coriolis coefficient f and horizontal eddy viscosity coefficient A_h are 0.0 s^{-1} and 30.0 m^2/s, respectively. Illustrated in **Figure 22** is an example of computational domains, where the harbor of a horizontally rectangular shape, we call, an I-type harbor. A train of incident regular waves, the wave height of which is 0.2 m, enters the computational domain through its leftward boundary and then propagates inside the harbor, leading to harbor oscillation.

The target harbors are model harbors of various shapes, as well as an actual bay, where the horizontal shapes of the model harbors are I-type, L-type, C-type, and

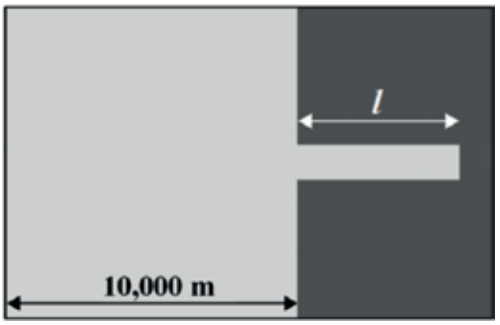

Figure 22.
The computational domain for harbor oscillation in an I-type harbor. The incident waves, the wave height of which is 0.2 m, enter the computational domain through its leftward boundary.

T-type, while the actual bay is Urauchi Bay. We examine numerical calculation results for the amplification factor of wave height due to oscillation in these harbors.

6.2 Amplification in the L-type harbors

Figure 23 shows L-type harbors, as well as an I-type harbor, where the harbor-axis length is 2000 m, while the bending position of the L-type harbors is different. The still water depth h is 20.0 m in the computational domains.

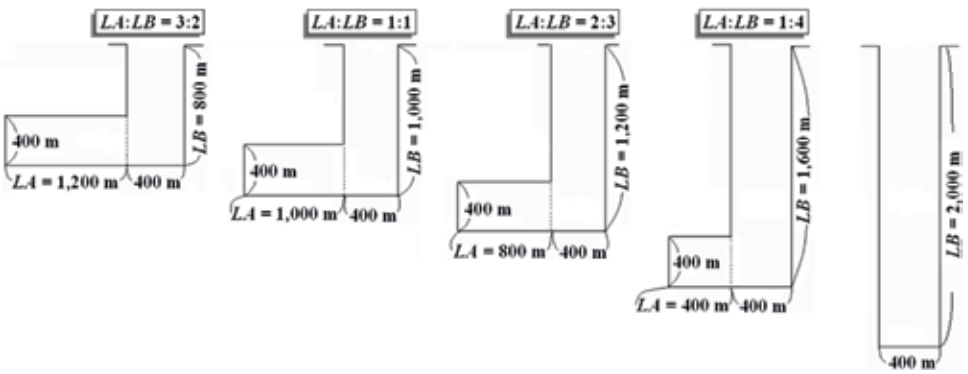

Figure 23.
The horizontal shapes of the L-type harbors with different bending positions, as well as the I-type harbor, where the harbor-axis length is 2000 m. The still water depth h is 20.0 m.

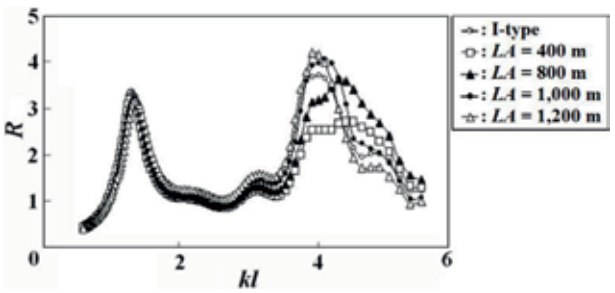

Figure 24.
The values of amplification factor R at the head of the L-type harbors with different bending positions LA, as well as that of the I-type harbor with the same harbor-axis length, shown in ***Figure 23****.*

Shown in **Figure 24** is the amplification factor R at the head of the L-type harbors with different bending positions, as well as the I-type harbor, shown in **Figure 23**, where R is defined by the ratio between the maximum wave height at each point, and the wave height of the incident waves, that is, 0.2 m; kl is dimensionless wave number, that is, $2\pi l/\left(T\sqrt{gh}\right)$. Although both the values of R and kl for the first mode in all the harbors are almost the same, the value of R for the second mode increases as the distance between the bending position and the harbor head, LA, is increased. It should be noted that when LA is 1000 and 1200 m, the value of R at the head of the L-type harbors is larger than that of the I-type harbor with the same harbor-axis length.

6.3 Amplification in the I-type harbors with a narrowed area

Figure 25 shows I-type harbors with a narrowed area, where the position, or the width, of the narrowed area is different. The still water depth h is 20.0 m in the computational domains.

Shown in **Figure 26** is the amplification factor R at the points indicated in **Figure 25** for the I-type harbors with a narrowed area, where the same symbols are used for the numerical results as that for the corresponding positions shown in **Figure 25**. The value of R at the head for the first mode is larger in harbor I_2 than that in harbor I_1, where the narrowed area is located at the harbor mouth, while the second mode shows the opposite phenomenon. The value of R at the head for the

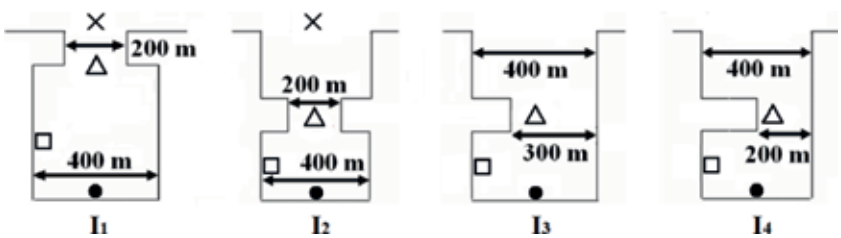

Figure 25.
The horizontal shapes of the I-type harbors with a narrowed area, where the position, or the width, of the narrowed area is different. The harbor length is 2000 m, and the still water depth h is 20.0 m.

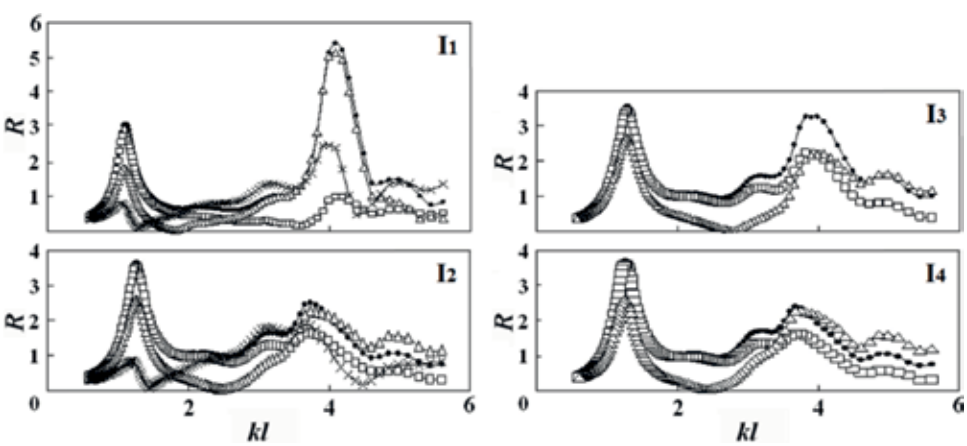

Figure 26.
*The values of amplification factor R at the points indicated in **Figure 25** for the I-type harbors with a narrowed area. The numerical results are represented with the same symbols as that used for the corresponding positions shown in **Figure 25**.*

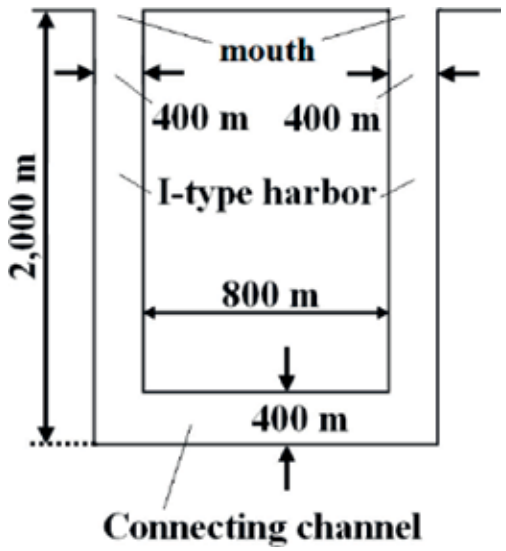

Figure 27.
The horizontal shape of the C-type harbor, where two I-type harbors are connected with a rectangular-section channel. The still water depth h is 20.0 m.

second mode is larger in harbor I_3 than that in harbor I_4, where the harbor width at the narrowed area is narrower than that in harbor I_3.

6.4 Amplification in the C-type harbor

Depicted in **Figure 27** is a C-type harbor, where two I-type harbors are connected with a rectangular-section channel, such that the C-type harbor has two mouths. The still water depth h is 20.0 m in the computational domain.

Figure 28 shows the amplification factor R in the C-type harbor shown in **Figure 27**. At the heads of the I-type harbors, the long waves coming through two mouths are in almost opposite phase, such that the value of R becomes lower than that at the head of the corresponding I-type harbor alone, as shown in **Figure 24**.

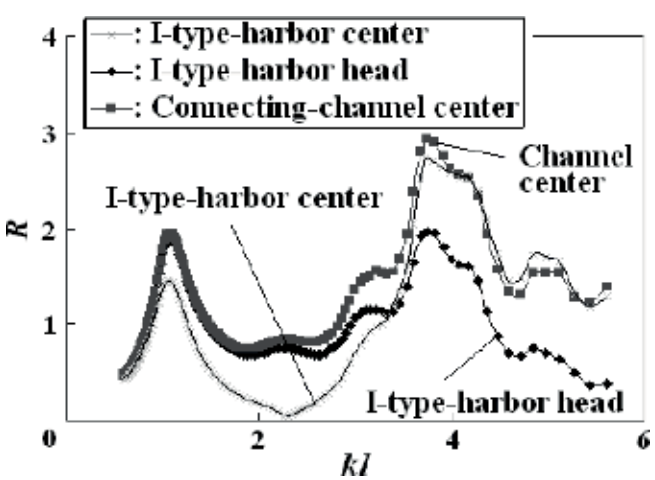

Figure 28.
The values of amplification factor R at the longitudinal centers of the I-type harbors, the heads of the I-type harbors, and the longitudinal center of the connecting channel, for the C-type harbor shown in ***Figure*** *27.*

Conversely, the amplification factor R for the C-type harbor shows large values at the longitudinal centers of the I-type harbors, as well as that of the connecting channel, for the value of R depends on the phase difference between the long waves coming through two mouths.

6.5 Amplification in the I-type harbors with a seabed crest or trough

Shown in **Figure 29** are the seabed configurations of I-type harbors with a seabed crest or a seabed trough, where the still water depth is 10.5 or 29.5 m at the longitudinal center, respectively; except at the longitudinal center, the seabed is uniformly sloping inside the harbors. The still water depth is 20.0 m at both the head and mouth of the harbors, as well as outside the harbors in the computational domains. The length and width of the harbors are 2000 and 400 m, respectively.

Figure 30 shows the amplification factor R at the head of the I-type harbors with a seabed crest or trough, shown in **Figure 29**, as well as that of the I-type harbor with a flat seabed, shown in **Figure 23**. In the I-type harbor with the seabed crest, the first and the second modes appear at lower values of kl than those with the seabed trough, respectively, for the average water depth is shallower in the former than in the latter. At the head of the I-type harbor with the seabed crest, the value of R for the first mode is larger than that for the second mode, while at the head of the I-type harbor with the seabed trough, the reverse is true.

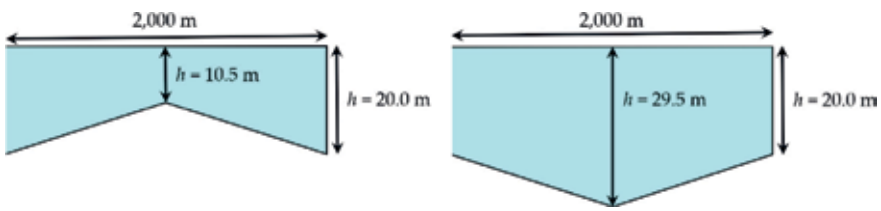

Figure 29.
The side views of the I-type harbors with a seabed crest (the left-hand side) and a seabed trough (the right-hand side). The length and width of the harbors are 2000 and 400 m, respectively. The still water depth is 20.0 m outside the harbors in the computational domains.

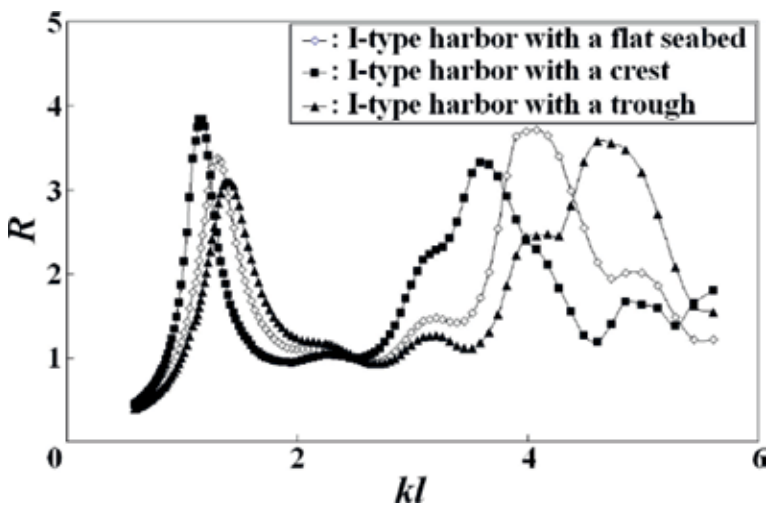

Figure 30.
The values of amplification factor R at the head of the I-type harbors with the seabed crest or trough shown in ***Figure 29****, as well as that with a flat seabed, shown in* ***Figure 24****.*

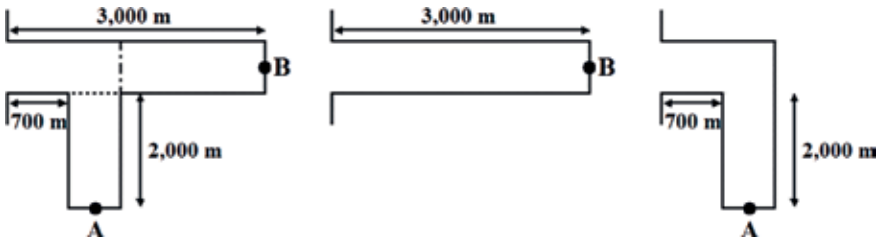

Figure 31.
The horizontal shapes of the T-type harbor (the left-hand side), the I-type harbor (the middle), and the L-type harbor (the right-hand side), where the T-type harbor includes both the I-type and L-type harbors. The harbor width is 600 m, and the still water depth h is 20.0 m.

6.6 Amplification in the T-type harbors

A T-type harbor has two heads, as shown in **Figure 31**, where an I-type and L-type harbors are also depicted for comparison. The harbor width is 600 m, and the still water depth h is 20.0 m in the computational domains.

Figure 32 shows the amplification factor R_m at the heads of the T-, I-, and L-type harbors shown in **Figure 31**, where R_m is defined by the ratio between the maximum wave height at each point and that at the harbor mouth. The second mode, specific to T-type harbors, appears when the wave period of the incident waves, T, is about 640 s, where the oscillation shows antinodes at two heads of the T-type harbor.

6.7 Harbor oscillation in Urauchi Bay

6.7.1 Amplification in Urauchi Bay

Urauchi Bay has two bay heads, as shown in **Figure 1**, such that the bay has a shape similar to that of a T-type harbor. **Figure 33** shows the amplification factor R_m at two fishing ports, that is, Oshima Fishing Port and Kuwanoura Fishing Port,

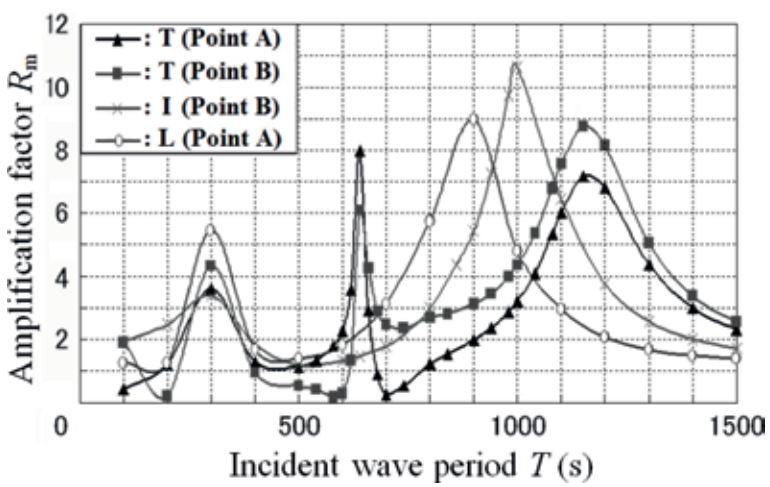

Figure 32.
*The values of amplification factor R_m at points A and B, which are located at the heads of the T-, I-, and L-type harbors shown in **Figure 31**, where R_m is defined by the ratio between the maximum wave height at each point and that at the harbor mouth.*

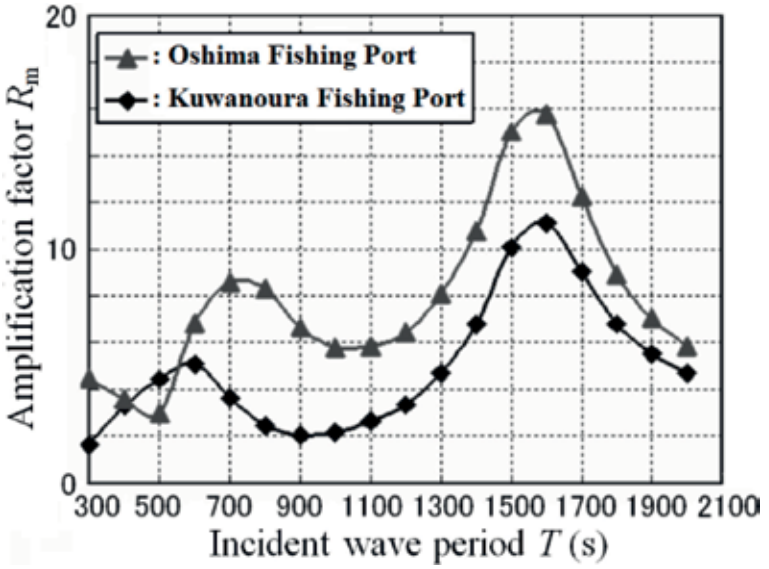

Figure 33.
The values of amplification factor R_m at Oshima and Kuwanoura Fishing Ports facing Urauchi Bay, as shown in ***Figure 1****, where the former is located at a bay head, while the latter in another branch is not at another bay head.*

facing Urauchi Bay, where the amplification factor R_m is defined by the ratio between the maximum wave height at each point and that at the bay mouth. It should be noted that Oshima Fishing Port is located at one of the bay heads, while Kuwanoura Fishing Port is at another bay branch, but not at its head. Although the oscillation period T for the first mode is 1580 s at both Oshima and Kuwanoura Fishing Ports, the period T for the second mode is 720 s at Oshima Fishing Port, while 600 s at Kuwanoura Fishing Port. The values of R_m for both the first and second modes at Oshima Fishing Port, where eight fishing boats capsized owing to the heavy harbor oscillation during February 24–26, 2009, as mentioned above, are larger than those at Kuwanoura Fishing Port, respectively.

6.7.2 Water surface displacements at the ports of Urauchi Bay

The time variations of the water surface displacements at Oshima and Kuwanoura Fishing Ports are shown in **Figure 34**, where those for T = 800 s, near the second modes, show large phase difference between these two branches, for

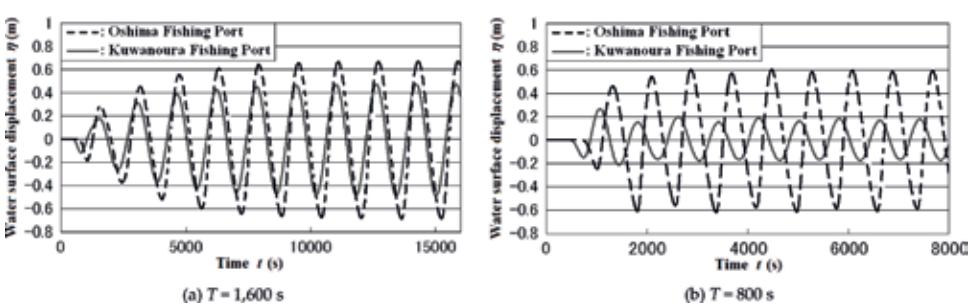

Figure 34.
The time variations of water surface displacements at Oshima and Kuwanoura Fishing Ports facing Urauchi Bay, where T is the wave period of the incident waves. (a) T = 1600 s; (b) T = 800 s.

Urauchi Bay shows the oscillation resemble to a T-type harbor, with antinodes at two heads and a node at near the bifurcation.

6.7.3 The damping processes of oscillations in the T-type harbor and Urauchi Bay

In order to study the damping process of oscillation in the T-type harbor shown in **Figure 31**, we continuously give incident waves to obtain a quasi-steady state of harbor oscillation, after which the incidence of waves is stopped when t = 0.0 s. **Figure 35** shows the time variations of the maximum water level at point A indicated in **Figure 31**, during the damping of harbor oscillation for the first, second, and third modes after t = 0.0 s. The wave period of the incident waves, T, for the first, the second, and the third modes are 1150, 650, and 300 s, respectively, based on **Figure 32**. The damping of the oscillation for the second mode is slower than that for both the first and the third modes, because part of wave energy is trapped in the second-mode oscillation between two harbor heads.

Conversely, **Figure 36** shows the time variations of the maximum water level at Oshima and Kuwanoura Fishing Ports facing Urauchi Bay shown in **Figure 1**. The wave period of the incident waves, T, is 1600 s for near the first mode, and 720 s for the second mode, based on **Figure 33**. The first-mode oscillation remains longer than the second-mode oscillation, which is not applicable to the T-type harbor mentioned above. Although future work is required to make this reason clear, we can tell the following difference between an actual bay and a typical T-type harbor:

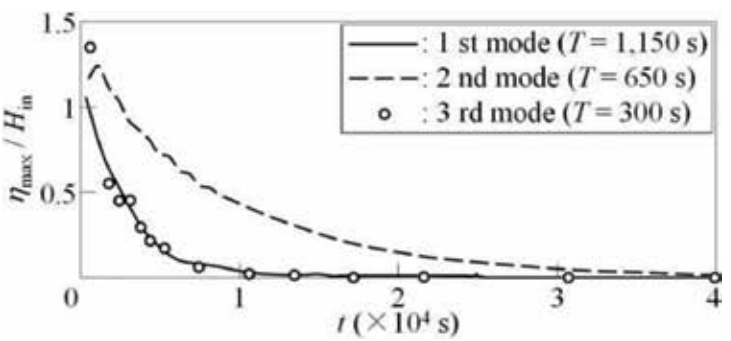

Figure 35.
*The time variations of the maximum water level at point A in the T-type harbor shown in **Figure 31**, for the harbor oscillation of the first, the second, and the third modes.*

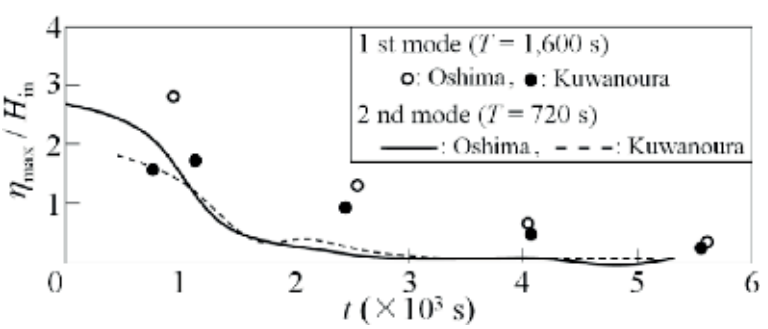

Figure 36.
*The time variations of the maximum water level at Oshima and Kuwanoura Fishing Ports facing Urauchi Bay shown in **Figure 1**. The wave period of the incident waves, T, is 1600 s for near the first mode, and 720 s for the second mode, based on **Figure 33**.*

the width, as well as the still water depth, of the actual bay is not uniform; the shape of the actual bay is curving at some angle.

7. Countermeasures against meteotsunamis

7.1 The real-time prediction of meteotsunami generation

7.1.1 The application of an inverse analysis

We discuss disaster measures against meteotsunamis, generated to propagate toward the west coasts of Kyushu. In order to predict the generation and propagation of meteotsunamis in real time, it is necessary to obtain atmospheric-pressure variation far from Kyushu. If we know the sites, concerning the generation of meteotsunamis through atmospheric-pressure variation, the valuable information on atmospheric pressure is restricted, such that the following inverse analysis is available:

a. We give some atmospheric-pressure variation at a site, to generate numerical simulation for atmosphere in a huge area including the Asian Continent, the Indian Ocean, and East China Sea, with a typical atmospheric condition for each season.

b. If an atmospheric-pressure wave appears over East China Sea, we give the atmospheric-pressure wave at the sea surface as an external force, to obtain the amplitude distribution of long waves along the west coasts, as well as the islands, of Kyushu, by applying the numerical model based on Eqs. (1)–(3).

c. We repeat the abovementioned calculation process for various conditions on atmospheric pressure, with atmospheric-pressure variation at different sites.

d. Using the results, we analyze inverse problems, where we give the distributions of long-wave amplitude, observed by, for example, the nationwide ocean wave information network for ports and harbors (NOWPHAS) conducted by the Ministry of Land, Infrastructure, Transport and Tourism, at the coasts of Kyushu, with the corresponding atmospheric-pressure conditions, to identify the sites in the Asian Continent and the Indian Ocean, which concerns the generation of meteotsunamis in East China Sea, through atmospheric-pressure variation.

According to the real-time variation in atmospheric pressure at the important sites, we can pick up bays and ports, which involve the risk of meteotsunami attack, to make adequate preparations for the meteotsunamis over a few days.

Conversely, we can also utilize a pattern recognition system for atmospheric-pressure distributions, instead of the inverse analysis, to exemplify dangerous atmospheric-pressure patterns.

7.1.2 Prediction for the amplitude of long waves using atmospheric pressure above East China Sea

We can predict approximate values for meteotsunami parameters, including long-wave amplitude, based on real-time variation in atmospheric pressure at several sites in East China Sea. If we obtain atmospheric-pressure data from barometers at plural islands, such as Danjyo Islands and Uji islands, shown in **Figure 5**, far from

the west coasts of Kyushu, we can imagine the propagation direction of atmospheric-pressure waves and predict the possible largest long-wave amplitude H in East China Sea, by applying the proposed Eq. (10). It is, however, difficult to place barometers at several islands, including uninhabited islands, far from the main island of Kyushu, and the maintenance of the barometers, with sustainable data transfer units, is a hard task. As long as we obtain time variation in atmospheric pressure only at one site, we can predict the possible largest amplitude H, by applying Eq. (10), although the accuracy of H is low, for the propagation direction of the atmospheric-pressure waves is not clear.

If fishing cooperatives and town offices obtain GPV atmospheric-pressure data, presented by JMA, to find out an atmospheric-pressure wave traveling east, they can predict the propagation direction, as well as the possible largest amplitude, of long-waves in East China Sea, where the accuracy of the predicted parameters is improved using Eqs. (8) and (9). It is important to catch every occurrence of large secondary undulation easily, even though both predictive accuracy and hitting ratio are relatively low. The fishing cooperatives and town offices, where the simple derivation process of Eqs. (8)–(10) is preferably understood, should be aware of the importance of the daily monitoring for variation in atmospheric pressure as a routine work.

7.2 Structural measures

The following structural measures against meteotsunamis are useful, depending on conditions including bay shape and water depth distribution:

a. Breakwaters are raised for ports with experience of large harbor oscillation, where several dozen centimeters may be enough. In case high breakwaters work against the loading of fishes and cargos, lockages of less than 1 m in height are suitable.

b. The bay width is narrowed with jetties, to protect ports and towns at bay heads, without inconvenience for daily steerage. It should be noted that the flow velocity, due to not only meteotsunamis but also tides, between the jetties may be larger, resulting in seabed scour, and that wave energy may be trapped behind jetties, leading to water surface oscillation prolonged in the bay. Furthermore, some device is required to advance seawater exchange, for part of the bay is occlusive. If the district to be protected is a narrow area, a water gate between two jetties is effective.

c. Permeable breakwaters with impounding reservoirs are constructed for coasts at high risk of overflow.

d. Fishery facilities are built, or moved, to adequate places, for corves etc., located near a node of harbor oscillation, may be flown away owing to flow of large velocity. The fish that got away is always big. The right places should be determined considering both water level and flow velocity, based on the characteristics of harbor oscillation in each bay or port.

e. Both drainage pipes and street gutters are designed to prevent inundation due to the intrusion of seawater into the residential area through the pipes and gutters. Although the walls of the castle, which is a world heritage, in Galle, Sri Lanka, rejected the tsunamis caused by the 2004 Indian Ocean earthquake, the seawater entered the inside of the walls through drainage pipes, leading to the flood.

f. River banks are constructed in consideration of meteotsunamis ascending rivers, as well as downflows due to heavy rain. The wave height of nonlinear tsunamis due to a submarine earthquake increases, when they travel upstream along a river with relatively narrow width, depending on the mouth shape of the river, according to the numerical results from the three-dimensional calculation [19].

7.3 Nonstructural measures

The coastal structures are permitted to be built considering cost effectiveness, nearshore environment, etc., such that nonstructural measures, including evacuation and preparation against meteotsunamis, are necessary as follows:

a. When a meteotsunami is predicted to be generated in the ocean, fishing boats and vessels are put offshore, if it is not stormy; if it is possible, they are put up on the land. Otherwise, mooring ropes should be tied firmly to prevent the flowage of fishing boats. If the ropes are too short, boats and vessels may be damaged when they collide with seawalls, or go on shore, owing to water level rise and onshore currents. Conversely, when the water level lowers, boats are hung by mooring ropes, as sketched in **Figure 37**, and they become upside-down, after which they are waterlogged as the water level rises. Note, however, that if mooring ropes are too long, boats are damaged owing to their collisions, such that bumpers should be attached to both boats and seawalls, unless the mooring positions are not moved to calm spots in harbor oscillation. Mooring facilities should be developed for temporary mooring at calm positions against meteotsunamis.

b. Waterproof tools, such as waterproof walls and sandbags, should be prepared for inundation of architectures including houses, shops, fishery facilities, factories, etc. **Figure 38** shows the examples of waterproof walls, equipped at Kinki Area Seaside Disaster Prevention Center in Osaka Prefecture, Japan.

Figure 37.
A fishery boat hung by a mooring rope, as the water level lowers owing to meteotsunamis.

Figure 38.
The waterproof walls equipped at Kinki Area Seaside Disaster Prevention Center in Osaka Prefecture, Japan. The wall panels can be carried and set at places where waterproof is supposed to be required. In case shown in the figure, the panels are piled up in front of the doors, using frames.

c. It is most important to notify inhabitants immediately that meteotsunamis are predicted to approach the coasts, using a community wireless system and speakers, or door-to-door visits. The prediction of disasters including meteotsunamis is probabilistic, commonly without high accuracy in their parameters, such that education to increase public awareness about disaster prevention is essential. It is crisis management that covers all the cases, whether the boy who cries wolf is right or not.

8. Conclusions

First, the generation and propagation of long ocean waves due to the atmospheric-pressure variation were simulated using the numerical model based on the nonlinear shallow water equations, where the atmospheric-pressure waves of four pressure-profile patterns traveled eastward over East China Sea, as well as the atmospheric-pressure waves that caused the large harbor oscillation in Urauchi Bay on February 25, 2009. The wave height of the long waves increased as the moving velocity of the pressure-recovery point was close to that of the long ocean waves. Before the oscillation attenuation in Urauchi Bay, the incidence of long waves can continue owing to an oscillation system generated between the main island of Kyushu and Okinawa Trough.

Second, the simple estimate equations were proposed to predict both the wave height and wavelength of severe meteotsunamis, using observed or GPV atmospheric-pressure data concerning the pressure profile of atmospheric-pressure waves or the recovery rate of atmospheric pressure in the ocean, without complicated calculation. The estimated values for both the wave height and wavelength of the long ocean waves showed good agreement with the corresponding computational data.

Third, numerical simulation was generated for the oscillation in the harbors of various shapes. The amplification factor at the head of the L-type harbor for the second mode increased, as its bending position was nearer to the harbor mouth. As

the narrowed area of the I-type harbor was located nearer to the harbor mouth, the amplification factor at the head for the first mode decreased, while that for the second mode increased. The C-type harbor showed the amplification depending on the position with the phase difference between the waves coming through two mouths. When the I-type harbor has the seabed crest, the amplification factor at the head for the first mode was larger than that for the second mode, while the reverse was true, when the I-type harbor has the seabed trough. Although the oscillation in Urauchi Bay had the second mode specific to T-type harbors, where antinodes appeared at their two harbor heads, future work is required to make clear the reason why the damping processes were different between Urauchi Bay and the T-type harbor.

Finally, the disaster measures were discussed against meteotsunamis, generated to propagate toward the west coasts of Kyushu. The methods of real-time prediction for meteotsunami generation were proposed using the inverse analysis, as well as the simple prediction equations, after which both the structural and the nonstructural measures against meteotsunamis were summarized.

Acknowledgements

Sincere gratitude is extended to Satsumasendai City Office for providing the photographs shown as **Figures 2** and **3**. I also express my gratitude to Mr. Kosuke Fukita, Mr. Soichiro Hidaka, Mr. Taisuke Inoue, Mr. Hiroyuki Matsukawa, Mr. Shota Minami, Mr. Yuki Suetsugu, Mr. Taishi Toyofuku, and Dr. Kei Yamashita, who contributed to the numerical simulation, etc., when they were student members of our laboratory. I am grateful to the reviewer for suggestive comments on countermeasures against meteotsunamis. This work was supported by JSPS Grant-in-Aid for Scientific Research (C) Grant Number JP17K06585.

Author details

Taro Kakinuma
Division of Ocean and Civil Engineering, Graduate School of Science and Engineering, Kagoshima University, Kagoshima, Japan

*Address all correspondence to: taro@oce.kagoshima-u.ac.jp

References

[1] Kakinuma T, Asano T, Inoue T, Yamashiro T, Yasuda K. Survey on February 2009 abiki disaster in Urauchi Bay, Kamikoshiki Island. Journal of Japan Society of Civil Engineers. 2009; **65**(B2):1391-1395. In Japanese

[2] Proudman J. The effects on the sea of changes in atmospheric pressure. Geophysical Journal International. 1929; **2**(s4):197-209

[3] Hibiya T, Kajiura K. Origin of the Abiki phenomenon (a kind of seiche) in Nagasaki Bay. Journal of the Oceanographical Society of Japan. 1982;**38**:172-182

[4] Vilibić I, Monserrat S, Rabinovich A, Mihanović H. Numerical modelling of the destructive meteotsunami of 15 June, 2006 on the coast of the Balearic Islands. Pure and Applied Geophysics. 2008;**165**:2169-2195

[5] Kakinuma T, Tsujimoto G, Yasuda T, Tamada T. Trace survey of the 2011 Tohoku tsunami in the north of Miyagi prefecture and numerical simulation of bidirectional tsunamis in Utatsusaki peninsula. Coastal Engineering Journal. 2012;**54**:28. Article Id 1250007

[6] Kakinuma T. Tsunami generation due to a landslide or a submarine eruption. In: Mokhtari M, editor. Tsunami. Rijeka, Croatia: InTech; 2016. pp. 35-58

[7] Niu X, Zhou H. Wave pattern induced by a moving atmospheric pressure disturbance. Applied Ocean Research. 2015;**52**:37-42

[8] Monserrat S, Vilibić I, Rabinovich AB. Meteotsunamis: Atmospherically induced destructive ocean waves in the tsunami frequency band. Natural Hazards and Earth System Sciences. 2006;**6**(6):1035-1051

[9] Asano T, Yamashiro T, Nishimura N. Field observations of meteotsunami locally called "abiki" in Urauchi Bay, Kamikoshiki Island, Japan. Natural Hazards. 2012;**64**(2):1685-1706

[10] Bailey K, DiVeglio C, Welty A. An Examination of the June 2013 East Coast Meteotsunami Captured by NOAA Observing Systems. NOAA Technical Report NOS CO-OPS 079. 2014. 42 p

[11] Tanaka K, Ito D. Multiscale meteorological systems resulted in meteorological tsunamis. In: Mokhtari M, editor. Tsunami. Rijeka, Croatia: InTech; 2016. pp. 13-33

[12] Miles J, Munk W. Harbor paradox. Journal of the Waterways and Harbors Division. 1961;**87**(WW3):111-130

[13] Hwang L-S, Tuck EO. On the oscillations of harbours of arbitrary shape. Journal of Fluid Mechanics. 1970; **42**:447-464

[14] Horikawa K, Shuto N, Nishimura H. Characteristic oscillation of water in an L-shaped bay. Coastal Engineering in Japan. 1969;**12**:47-56

[15] Derun AB, Kakinuma T, Isobe M. A nonlinear numerical model of harbor oscillations and its application to responses of harbors of various shapes. Proceedings of Coastal Engineering. 2003;**50**:231-235. In Japanese

[16] Katayama H, Kato H, Tanji Y, Nakayama A. Numerical analysis about disaster by abiki on February, 2009. Proceedings of Civil Engineering in the Ocean. 2010;**26**:837-842. In Japanese

[17] Kakinuma T. A set of fully nonlinear equations for surface and internal gravity waves. In: Brebbia CA, editor. Coastal Engineering V. WIT Press; 2001. pp. 225-234

[18] Nakayama K, Kakinuma T. Internal waves in a two-layer system using fully nonlinear internal-wave equations. International Journal for Numerical Methods in Fluids. 2010;**62**:574-590

[19] Kakinuma T, Kusuhara Y. A 3D Numerical Analysis for Tsunamis Ascending a River. RIMS Kôkyûroku. 2019 (in print)

Chapter 6

Identification and Assessment of Hazard of Development in Gypsum Karst Regions: Examples from Turkey

Sevda Özel

Abstract

This study includes natural hazards and environmental problems caused by gypsum on and near the soil, water, and structures. These are karst-specific deformations (caves, fractures, cracks) naturally occurring in gypsum areas, and the problems of salinization, corrosion, erosion, soil and water pollution that occur as a result of dissolution caused by the contact of gypsum with water. In particular, it has been determined that various transfer routes/lines that facilitate human life cause problems on substructures/superstructures resulting from their passage in gypsum areas or on substructures/superstructures (road, buried pipe, building) resulting from the spread of urbanization on this unit, and these have various risks. As a result of these events that have been proven by various studies, it has also been observed that gypsum causes natural hazards and has environmental impacts on human/plant/animal life and living environments and it has also been determined that the quality and sustainability of life/living environment decreased. Therefore, in this study, it has been put forward that gypsum areas pose a risk for the life of all kinds of living beings and that the choice of gypsum areas in the site selection for urbanization will always be risky with respect to natural hazards and environmental problems.

Keywords: gypsum, karst, Sivas (Turkey), natural hazard, environment

1. Introduction

The gypsum unit is one of the evaporite units that can be easily dissolved when it contacts with water in nature. Furthermore, gypsum units are geological environments with karstic characteristics as limestone unit, and all karstic structures can also develop in gypsum units. Therefore, gypsum areas are the sources for pollutants with inorganic characteristics, and geologically they also include geological structures that develop specifically to karstic areas. Moreover, gypsum areas are risky geological environments where natural hazards may occur in the case of the presence of settlement areas or human-made structures (building, road, substructure systems, etc.) on them [1–3]. For these reasons, gypsum is an important evaporite unit that should be taken into account in terms of both natural hazards and environmental problems and urbanization. Therefore, gypsum units cause negative effects on soil infertility and ground/surface water quality due to problems such as dissolution, salinization,

erosion, and corrosion that directly occur in nature [4–6]. On the other hand, the rapid construction that comes with urbanization requires new settlement areas. Therefore, there are also constructions on gypsum units [3]. The reason why it is considered that gypsum areas will cause significant environmental problems in the future is natural hazards and environmental problems that will arise in the event when gypsum is mainly surfaced or very close to the surface especially in new places opened for settlement, as required by karst geology. This also suggests that there will be risks for the life of humans and living beings and that these risks will increase, especially in these kinds of areas in the future, along with the opening of an area consisting of evaporite units for construction. Geological structures specific to gypsum karst lead to the formation of caves/areas causing the danger of collapse under the ground of the building and also collapses along with the fact that dissolution caves and dissolution channels are merged over time and create large galleries. As a result of these events, concrete materials, pipes, and cable systems of buildings and substructure systems are damaged. This also means that substances that may leak liquid and gas are mixed into the soil, water, and even into the atmosphere or that there are energy losses. Thus, there will also be economic losses. For this reason, it was considered necessary to draw attention to the problems originating from gypsum, while they are examined with environmental problems and soil and water pollutions on the issues for environmental monitoring purposes, and these problems should not be ignored [5].

When natural-origin environmental problems described above are considered, it is essential to reveal the geological, engineering, hydrogeological, and environmental impact models of the environment in the site selection for settlement purposes and in the site selection of other human-made constructional areas [7, 8]. Therefore, various maps on different topics and scales that define the gypsum area from all aspects and geological/geophysical sections of various sizes are prepared by the relevant experts and scientists [3, 9–16]. Thus, gypsum areas can be defined in detail by using mineralogical-petrographic and structural properties of geologically lithological units, their degree of weathering, geophysical-hydrological-physicomechanical properties, and meteorological status, and other surface and underground research methods. With these studies, risky areas at the horizontal-vertical or shallow-deep dimensions can be determined by preparing reports and maps to take precaution for natural hazards and environmental impacts. According to the results found, new and future sustainable planning and preparations can be made for these issues. Then, human/plant/animal health and their living environments can be maintained in a sustainable manner. Therefore, the problems of erosion and pollution may be reduced more effectively with the measures to be taken. In conclusion, all these issues were examined in this study.

2. Natural hazards environmental problems in gypsum karst regions

2.1 Regional features of gypsum karst morphology in the study area and its surroundings: examples from Sivas (Turkey)

Karst is a morphological term and it is important to analyze karst morphology in terms of natural hazards, because the gypsum unit is a type of karst and can be solved if it contacts water. Gypsum can transform to anhydride as a result of geological and atmospheric processes in near-surface karsts, or vice versa. In other words, with the introduction of water into the anhydrite structure through these processes, an anhydrite unit can transform into a gypsum unit. These transformations also occur in the Hafik Formation, in Sivas (**Figure 1a**). The Hafik Formation is an Oligo-Miocene aged unit presenting wide spread in the Sivas evaporite basin

and mostly consisting of massive gypsums [17–19, 20]. Upon examining **Figure 1a**, it is observed that the Sivas tertiary basin shows a northeast-southwest extension [21]. On the other hand, this basin starts from Gemerek in the southwest of Sivas and extends along the Sivas center, Hafik, Zara, and Imranlı. In **Figure 1a, b**, the study area is located in the Sivas basin and occurs from the Hafik Formation. This basin is one of the largest Central Anatolia basins, which was formed in the collision zone and is located in the most important gypsum karst area of Turkey. However, the areas of gypsum outcrops occur in Central and Eastern Anatolia, and gypsum formations are found mostly in Ankara, Çankırı, Çorum, Kırşehir, Kayseri, and Sivas regions (**Figure 1a**). In addition, dissolution dolines are found in the youthful karst areas between Sivas and Zara; some of the most important collapse dolines are found in the mature karst area between Hafik and Zara [15, 20, 22, 23, 26, 27]. The dolines on gypsum have solution and collapse characteristics, and it was observed that population rates were low in these areas [24]. According to the study by Hadimli and Bulut (2000) because of the dense surface karst in these gypsum areas is observed; these areas do not offer suitable environments for human life. Therefore, in Turkey, in areas where macrokarst structures (poly, uvala, doline) are observed, even despite a continuous population, it has been observed that the areas with microkarst structures (lapya) observed are used periodically [24]. Furthermore, in karstic fields, karstic structures (such as doline bases) are used for agricultural area needs (due to need), although they do not show high agricultural potential. In particular, large doline-based areas around

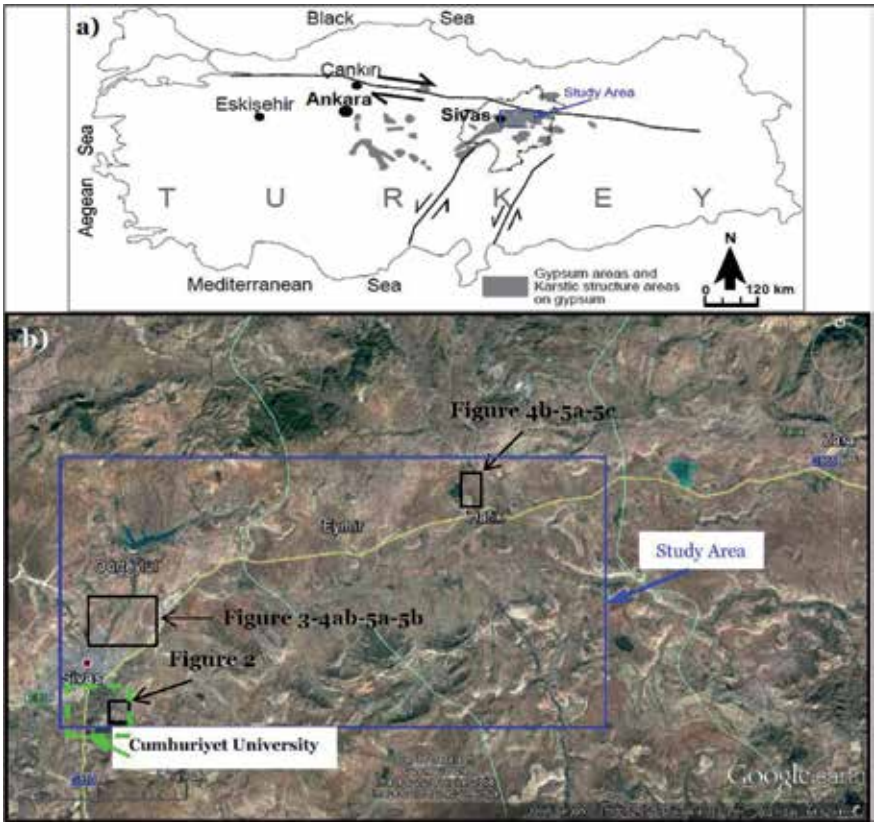

Figure 1.
(a) Study area (rearranged from [23, 25], and (b) the locations of figures (arranged from Google Earth, 2018, August 12, 2018)).

Hafik (Sivas) and Zara (Sivas), developed in different sizes and gypsum formation, are used for agricultural production [24, 25]. However, these lands are also used as settlement area, forest area, pasture area, natural parks, natural sports and tourism resort area, raw material acquisition (e.g., plaster, cement industry), and mining area [24].

The sudden generation of collapse dolines in areas underlain by gypsum constitutes great danger for both lives and property. Karst features, such as sinkholes, near-surface caves, and collapse structures, which are formed in water-soluble rocks, constitute potentially serious hazards. Groundwater in karst areas is an important resource, which needs to be developed and protected [23]. Water percolates over or through gypsum and dissolves the highly soluble rock; and this causes the formation of sinkholes, caves, natural bridges, disappearing streams, and springs. Thus, natural hazards include damage and/or collapse of houses, buildings (such as dams, bridges, highways, and farmlands) [26, 28]. Such events can cause great economic hardship, disruption of lives, and even loss of life. Conclusively, the study area is located on the gypsums on the Hafik Formation and geologic units with gypsum intercalation (**Figure 1a**). Therefore, karst structures such as fractures, cracks, dissolution caves, and deterioration areas specific to karstic areas are very extensive in these units. Moreover, the geological formation of the study area does not change, the Hafik Formation and karstic structures in this formation continue throughout the study area [3]. The full ranges of gypsum-karst features are present in the region, and there is a number of striking examples of karst hazards and environmental problems [26, 28, 40].

Therefore, collapses in karst terrains constitute very serious geological hazards and can damage engineering structures and cause groundwater contamination [29]. In these areas, very shallow soil could develop, or there is no soil development, and the outcropped karstic area is open to external factors and processes. Therefore, this unit mainly consisting of massive gypsum and gypsum interfingered fractured rocks has a structure that is easily dissolved under the impact of atmospheric processes [6]. Thus, cracks and intense joint systems in various directions have developed in gypsums of the Sivas basin. These are causing the fall of rocks (blocks) in parts where bevels are steep at rocks [13]. These natural hazards and their environmental problems are common in Sivas.

2.2 Natural hazards and environmental problems caused by gypsum areas

Natural hazards and environmental problems that occur in gypsum areas depending on the karstic characteristics of a gypsum unit and the geochemical, hydrogeological and atmospheric characteristics of its mineralogical composition may lead to different effective problems in human/plant/animal health and their living environments. Every detail is important in urban planning since the selection of gypsum areas as new settlement areas will cause problems in planning studies that increase with urbanization. These problems can be listed as foundation and drainage works in unplanned/out-of-plan construction works, constructions, which cannot be completed on time, safety problems that may arise due to the wrong material selection, and enabling the formation of new pollution areas [5, 30, 31]. While making site selection in these cases, if there is an area, which is zoned or will be zoned for construction, planning will be different according to them in the works to be done. Therefore, the reduction of costs and the correct orientation of investments can be ensured by examining the issues related to site selection and very large-scale events. Another important issue is related to carrying out scientific studies because different preparations will be made with different studies in site selection depending on the geological characteristics of

gypsum, the parcel size of the building to be constructed, and building types. First of all, since the size of the area where the structure will be placed is different or the load to be imposed on the ground will be different depending on the size/number of floors of the buildings to be constructed, methods are selected accordingly and survey studies are initiated. If works are completed with correct planning when it comes to site selection, the gains brought along by them will be too much. However, in gypsum areas, the following natural hazards and environmental problems are generally observed.

2.2.1 Leachate waters

Surface waters or groundwaters contacting with gypsum lead to the dissolution of gypsum. Thus, the concentration of ion dissolved in water increases, and the water transmitted threatens the soil fertility and the life of living beings by leaking into the soil in the areas where it transmits. Furthermore, the waters brought by precipitation through washing the surfaced gypsum impair the quality of potable or tap waters and soil quality by mixing into surface waters and leaking into underground waters. In urban areas, corrosion, salinization, mineral transformation, and dissolution cause damage to the ground and structures in places where building foundations and substructure systems exist. As a result of this, safety problems arise in buildings or on the ground (**Figures 2–5b,c**). For example, hazardous leachate waters or gases in buried pipes damaged by corrosion erosion may mix into the soil and then underground waters, which means the formation of a source of pollution [5, 6].

2.2.2 Subsidence/collapse/rock (block) fall

If site selection is made or construction areas are selected for settlement purposes without getting engineering service, the problems of ground subsidence in gypsum areas, and rockfall in collapse areas and slope areas can be observed (**Figures 2a, b, 3b** and **5b, c**) [3]. They have a negative impact on human life and lead to material and moral losses. For example, subsidence and cracks occur in foundation ground due to dissolution in the gypsum unit (with the contact of leachate water), and this may cause damage to buildings. However, the rockfall constitutes a safety problem (e.g., in road, highway, and railway routes) [13] (**Figure 3b**). Consequently, various structural damages (cracks, dissolution, collapse, sinkholes,

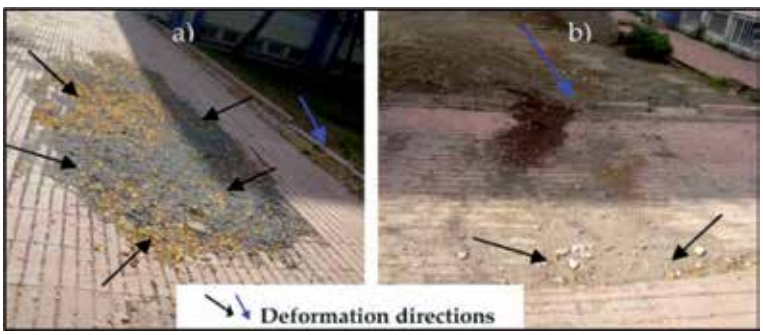

Figure 2.
Gypsum-based ground deformations in the southeast Sivas city (Turkey) (photos: Sevda Özel, 2018). (a) As the setting-collapse increases, the cavity (~1.0 × 2.5 m^2) is filled with fill material (as a temporary measure) and (b) a newly formed dissolution area under the pavement (~0.3 × 0.5 m^2).

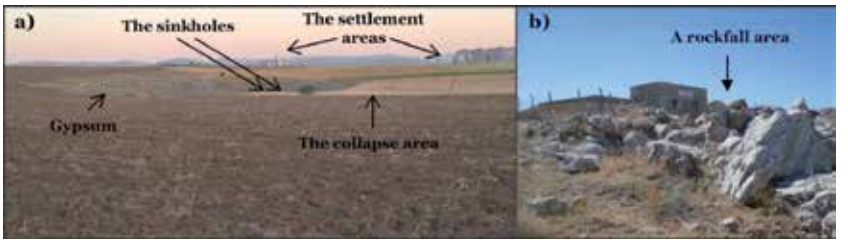

Figure 3.
Gypsum-based karst deformations in Sivas (Turkey) (photos: Sevda Özel 2013, 2015). (a) The collapse area, sinkholes, and the gypsum clastic soils in the east and northeast of Sivas. (b) The rockfalls in the northeast of Sivas.

doline, erosion, corrosion, rockfall, etc.) arise and are observed in the structures of the building (**Figures 2–5b, c**).

2.2.3 Health and living environment of living beings

Vegetation losses also occur with soil salinization occurring with leachate waters containing the high amounts of dissolved ions mixing into the water from gypsum as a result of the contact of gypsum with water in cover units on the edges or on gypsum. In this case, erosion may occur in these regions over time (**Figures 4a** and **5b, c**). Therefore, all living beings including humans, and their living environments are damaged by these losses. Hence, low water-soil quality decreases and destroys the nutritional sources of living beings; soil-water pollution, as well as inadequate nutrition conditions, affect the health of living beings, and plant species may become extinct or decreased due to erosion (**Figure 4a, b**). Similarly, living beings may have to migrate to living environments where healthier and better opportunities exist. The health and living environments of living beings are impaired with these exposures in the dimension of the environmental problem.

While discussing the dimensions of environmental impacts in terms of the settlement by reviewing the detailed characteristics of the environment, hydrogeological and hydrogeophysical investigations are important in this regard. In particular, it is necessary to perform well-planned field studies that determine shallow and deep geological/geophysical, hydrogeological and environmental impact characteristics of the gypsum karst region. Whether the Environmental Impact Assessment (EIA)/Strategic Environmental Impact Assessment (SEIA)

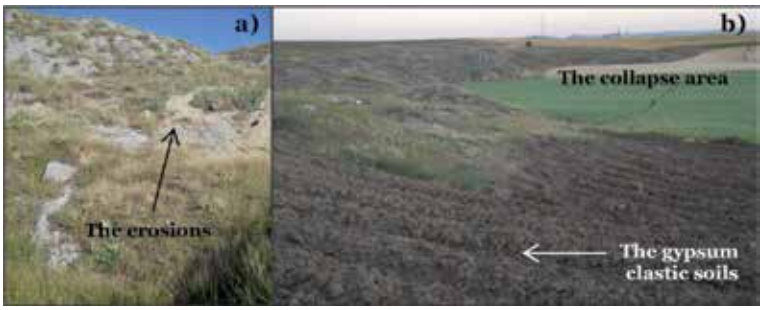

Figure 4.
(a) The erosions in the east of Hafik-Sivas (Turkey) (photo: Sevda Özel, 2013). (b) The gypsum clastic agricultural soils in the east and northeast of Sivas city (Turkey) (approximately 1–2 km away from the city) (photo: Sevda Özel, 2013).

is required, the identification of aquifers, the calculation of aquifer hydraulic parameters, and underground water-surface water information (feeding-discharge zones, the rate and direction of the flow of underground water, underground water level, the amounts of seasonal variations, hydrogeochemical properties of underground water and leachate waters, and underground water level maps) are necessary.

The geological stratification status (thickness, depth, slope, topographic changes of layer limits, geological and geophysical parameters) should be calculated. In the detailed investigation of karst geomorphology, the necessary attention should be paid to the seismic activity status, seismic activity history, and meteorological and morphological characteristics of the region. With these studies, the limits of hazardous areas and the risks can be determined after geological-hydrogeological-hydrogeophysical characteristics of the environment are determined in site selection. Therefore, it is important to define geological environments well and choose the right calculation method in terms of the environmental impact analysis and the measures to be taken. In addition to these, these regions are also monitored periodically by monitoring network and sampling methods designed based on the success and environmental impact of measures taken according to detailed engineering geology/geophysics and environmental geotechnical inputs, and engineering properties of the field, as a result of the environmental impact assessment [4–7, 32]. Thus, control mechanisms, management style, and other plans/projects can be prepared to take measures against risks and dangers within a scientific framework. Furthermore, site selection, natural hazards, environmental problems, and the monitoring studies of them show that it is necessary to maintain joint research with the relevant engineering and other disciplines and that the increase/improvement of environmental protection laws is important. Therefore, it will be important and useful to ensure that studies are not limited only with the top surface and subsurface studies and that necessary attention will be paid to shallow and deep investigations. Based on this idea, the examples of the creation of living environments that are less affected by gypsum-induced events will increase. Moreover, it should be taken into account that natural hazards and environmental impacts caused by gypsum are not only those that appear on the Earth's surface and that there may also be ongoing problems under the ground. Accordingly, when natural hazards and environmental impacts specific to gypsum areas are examined, environmental problems and natural hazard/risk situations caused by gypsum in the site selection for settlement purposes and in the site selection of other human-made construction structures are listed below:

2.2.3.1 Mineral transformations

These transformations constitute an important environmental problem for deformations resulting from volume expansion and especially for settlement areas (such as structural damage) and agricultural-water areas. In addition to gypsum ($CaSO_42H_2O$), which is one of the minerals of the evaporite group, anhydride ($CaSO_4$) and other minerals of the evaporite group are easily soluble when they contact with water (**Figure 5a–c**).

In the event of the loss of water in the environment, these minerals may be recrystallized, new minerals may be formed by the displacement of ions, or minerals may transform into each other. For example, as gypsum ($CaSO_42H_2O$) absorbs heat (as temperature increases) depending on climate conditions, it loses water and may transform into gesso ($CaSO_4½H_2O$) and anhydride ($CaSO_4$) units, respectively [3]. On the other hand, the melting temperature of gypsum is very high (about >100°C or about 700–1500°C), the dissolution temperature of gypsum

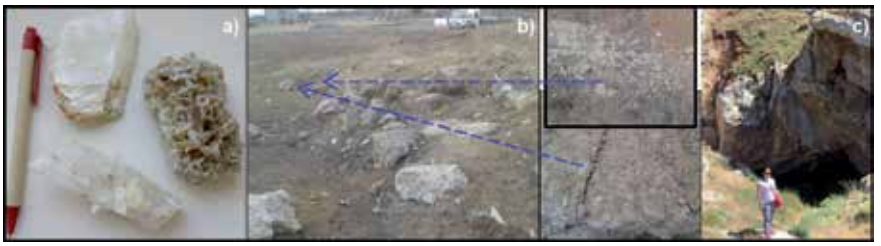

Figure 5.
(a) Gypsum samples collected from the northeast and south-southeast of Sivas (Turkey) (photo: Sevda Özel, 2005, 2007, and 2010). (b) Surfaced gypsum in the northeast of Sivas (Turkey) (photos: Sevda Özel, 2015) (c) Gypsum karstic deformation structures (cave, fracture, crack, collapse) from Hafik Formation in Sivas (Turkey) (photo: Sevda Özel, 2017).

is very low (about 0–50°C) [33–35]. For example, the solubility of gypsum in pure water at 20°C is 2.531 g/L [34, 36]. Gypsum is about 10–30 times more soluble than limestone, and it commonly has a lower mechanical strength [3, 15, 23, 33, 34]. However, between 0 and 30°C, the range encompassing most natural waters, the solubility of gypsum increases by 20%, reaching a maximum (about 2.66 g/L) at 43°C [34]. Therefore, sudden collapses in gypsum areas are a great danger for both life and property [3]. Therefore, the quality of water in the basins where the rock types formed by these minerals dominate is easily impaired, and surface and underground waters in which evaporite group minerals are dissolved are naturally polluted [4, 6, 38]. These polluted waters also pollute fertile soils if they leak into the soil.

Evaporite units tend to expand and swell depending on their origin, and these unites may also involve areas where underground waters are collected, and the sources where underground waters rise to the surface [3]. Upon examining **Figure 1** it is observed that, a shallow or deeper ground cover may develop or soil development may not occur at all in these areas. If the karstic area is surfaced, these areas are open to external factors (e.g. precipitation, wind, temperature) and processes (e.g. dissolution, erosion, deterioration). In this case, cracks in various directions, dense joint systems, melting areas, and various karstic structures begin to occur in gypsum areas. Moreover, larger fractures or new faults may occur as a result of seismic activity and collapse events. Furthermore, rock (block) fall events may also occur in rocks where slopes are perpendicular [12]. According to all these geological characteristics, significant ground problems are encountered in the existing buildings in the area or during and after new construction with the use or selection of gypsum areas as settlement areas (**Figure 1a,b**). These areas should be included in the class of areas with risky areas, especially if such areas continue to be selected as new settlement areas.

2.2.3.2 Pollution

There is always a risk of pollution in soil and underground/surface waters in gypsum areas. This pollution problem takes place as a result of salinization. Gypsum units may lead to salinization by ion decomposition resulting from the contact with water. Waters with the intense ion content formed during salinization threaten underground waters, surface waters, soil quality, and the life of plants, animals, and humans in the places of their passage, as leachate waters. In other words, leachates are the waters containing inorganic pollutants, and they also interact with other materials. This also reduces the existing underground/surface water quality and decreases the soil fertility, plant diversity, and the

acquisition of fertile product [5, 6, 24, 27, 29]. The pollutants mixed in the soil also affect living beings in the soil, plants that grow/are grown in the soil, or living beings fed with these plants.

2.2.3.3 Ground damage

Since gypsum units geologically have swelling-expansion characteristics due to their mineralogical structure, they cause swelling in the ground. Thus, ground and structure deformations caused by the swelling of gypsum grounds, and material damages occur on superstructure grounds and in substructure systems (**Figures 2a,b** and **5b**). In these situations that endanger the safety of buildings, the life of human and living beings will also be under risk due to the safety problem (**Figure 2**). On the other hand, gypsum units may also be covered with alluvial units in some places. In this case, similar ground swelling problems may occur if units with swelling properties like clay are found in the alluvial filling material. Therefore, it is necessary to control leachate and underground waters in the construction areas in both cases.

2.2.3.4 Corrosion

Corrosion may occur on the grounds of gypsum areas and in the immediate vicinity of them, and in structures (**Figure 5b**). In particular, there is a corrosive effect on installation, building foundation, and substructures. It leads to rapid deterioration, and rusting and corrosion of materials in buildings and substructure pipe systems. Underground corrosion results from chloride (Cl) dissolved from the evaporite units in the caves in the soil, sulfate salts (SO_4), and dissolved gaseous oxygen (O). As a result of the fact that these dissolved ions cause stress difference in metal and electrolyte, they are oxidized to the metal ion in the anode or realize the corrosion (on the micro- or macroscale) event by passing into the solution as a metal ion [39]. Therefore, corrosion is one of the environmental problems arising from the gypsum unit since it causes damage to structures, building systems, and soil.

2.2.3.5 Karst structures

They pose a threat to people and structures or to agriculture and water areas in and near settlement areas in places where karst-type structures such as fractures/cracks, dissolution caves, and dissolution channels develop [28, 40] (**Figures 2–5b,c**). In the regions with intense collapses, hazardous areas that cause a safety problem for human and other living things emerge. Furthermore, agricultural areas, water resources, road routes, as well as settlement areas are also damaged. Therefore, a safety problem exists not only in settlement areas and in the immediate vicinity of them but also outside of them, and it affects the lives of all living beings. Furthermore, these problems also pose risks to national economies.

2.2.3.6 Seismic activity

It is also important to monitor seismic activity in and around these areas. In a region which is active in terms of seismicity, fractures, faults, and subsidence dissolution caves/areas in gypsum units, and changes in underground water levels should be monitored because new deformations may develop over time and new dissolution caves/areas may also occur (**Figures 1a** and **5b, c**).

New problems will be added to the existing problems if all these natural and environmental factors that have an impact on the sustainability of the environment and the quality of life of all kinds of living beings are not determined, and hazards, risks and other problems that may arise are not kept under control in time. Therefore, the attempts of regional or local authorities to maintain environmentalist works, as well as at the dimension of countries, and the compliance with the EIA/SEIA reports in constructions are important for the sustainability of the quality of life.

3. Conclusions

In this study in which geological and geomorphological and natural and environmental risks in gypsum areas were examined, natural hazards, environmental problems, and risk situation were dissociated and discussed. In other words, upon evaluating the available data, it was suggested that the problems arising from the gypsum karst may occur and may increase over time with the contributions of the intense seismic activity, geological units specific to karstic environments, heavy rainfall due to erosion, and occasional human interventions. On the other hand, all events such as soil and water pollution caused by gypsum in evaporite areas, salinization in the soil, and underground/surface waters as a result of the dissolution of gypsum, corrosion on the ground and structures, swelling and collapses on the ground, and the development of various karstic structures (dissolution/erosion/collapse areas, caves, fractures, cracks, etc.) underground were described as environmental problems. The hazards, environmental problems, and risks that may arise in gypsum areas, in the site selection of settlement areas due to urbanization and population growth were also emphasized.

In conclusion, it was strongly emphasized that gypsum areas with all types of features specific to karstic areas are risky areas in terms of natural hazards and environmental problems and that they would also maintain various environmental problems in the future. Accordingly, it was proposed for countries and regional and local authorities to prepare various risk maps showing the limits of hazardous and safe areas for the prevention of economic losses and the sustainability of all living things, to be always sensitive to environmental hazards within these limits, and to carry out monitoring studies. Furthermore, since the amount of dissolution and damaged area in gypsum may increase under the effect of water over time, these areas are defined as risky areas for settlement in geological engineering studies. Therefore, it will be useful always to pay the necessary attention to foundation engineering because, in the future, corrosive areas that will cause damage to the structure and ground in the foundation of the structure may occur and decompose concrete and building systems, and grounds may collapse by dissolution. Therefore, it would be useful to be cautious in geologically gypsum areas since natural hazards and environmental problems will always pose risks in these areas.

Author details

Sevda Özel
Department of Geophysical Engineering, Cumhuriyet University, Sivas, Turkey

*Address all correspondence to: sozel@cumhuriyet.edu.tr

References

[1] Sevil J, Gutiérreza F, Zarrocab M, Desira G, Carbonela D, Guerreroa J, et al. Sinkhole investigation in an urban area by trenching in combination with GPR, ERT and high-precision leveling. Mantled evaporite karst of Zaragoza city, NE Spain. Engineering Geology. 2017;**231**:9-20. DOI: 10.1016/j.enggeo.2017.10.009

[2] Carbonel D, Rodríguez-Tribaldos V, Gutiérrez F, Galve JP, Guerrero J, Zarroca M, et al. Investigating a damaging buried sinkhole cluster in an urban area (Zaragoza city, NE Spain) integrating multiple techniques: Geomorphological surveys, DInSAR, DEMs, GPR, ERT, and trenching. Geomorphology. 2015;**229**:3-16. DOI: 10.1016/j.geomorph.2014.02.007

[3] Darıcı N, Özel S. Examination of the structural characteristics arising in gypsums by the GPR and MASW methods (Sivas, Turkey). Natural Hazards. 2018;**93**:1-16. DOI: 10.1007/s11069-018-3320-1

[4] Atmaca E. Examination and replanning of solid waste manegement of Sivas citiy center [thesis]. Sivas, Turkey: Cumhuriyet University Graduate School of Natural and Applied Sciences Department of Engineering; 2004

[5] Özel S. Investigating with Geophysical Methods of Spreading Inside the Underground of the Leachates of the sivas city solid waste disposal area [thesis]. Sivas, Turkey: Cumhuriyet University, Graduate School of Natural and Applied Sciences Department of Geophysical Engineering; 2010

[6] Özel S, Yılmaz A, Candansayar ME. The Examination of the spread of the leachates coming out of a solid waste disposal area on the ground with geophysical and geochemical methods (Sivas, Turkey). Journal of Applied Geophysics. 2017;**138**:40-49. DOI: 10.1016/j.jappgeo.2017.01.013

[7] Yılmaz A. Çevre Jeolojisi. Sivas, Turkey: Cumhuriyet Üniversitesi Mühendislik Fakültesi Yayın; 2008.Vol. 107. 379 p

[8] Yılmaz A. Çevre Jeotekniği. Sivas, Turkey: Cumhuriyet Üniversitesi Mühendislik Fakültesi Yayın; 2009a.Vol. 116. 276 p

[9] Duvarcı E. Rejyonal Jeoelektrik Haritaları Projesi: Sivas Tersiyer Havzası Özdirenç Etüdü. Report no: 9701, 20. Ankara, Turkey: General Directorate of Mineral Research and Exploration (MTA) Publications; 1994

[10] Toshioka T, Tsuchida T, Sasahara K. Application of GPR to detecting and mapping cracks in rock slopes. Journal of Applied Geophysics. 1995;**33**:119-124

[11] Tanıdır R, Karlı R. Türkiye Rejyonal Elektrik Haritalar Projesi. Report no: 9868. Ankara, Turkey: General Directorate of Mineral Research and Exploration (MTA); 1996

[12] MTA. Sivas ve civarının mühendislik jeolojisi haritası. Sivas, Turkey: General Directorate of Mineral Research and Exploration (MTA) Publications, MTA Orta Anadolu I. Bölge Müdürlüğü; 1996

[13] MTA. Sivas kentinin çevre jeolojisi ve doğal kaynakları. Sivas, Turkey: General Directorate of Mineral Research and Exploration (MTA) Publications, MTA Orta Anadolu I. Bölge Müdürlüğü; 1997

[14] Xavier D, Odile A. GPR and Seismic imaging in a gypsum quarry. Journal of Applied Geophysics. 2000;**45**:157-169

[15] Waltham T, Cooper A. Features of gypsum caves and karst at Pinega (Russia) and Ripon (England). Cave and Karst

Science. Transactions of the British Cave Res Assoc. 1998;**25**(3):131-140

[16] Xu C, Butt SD. Evaluation of MASW techniques to image steeply dipping cavities in laterally inhomogeneous terrain. Journal of Applied Geophysics. 2006;**59**:106-116. DOI: 10.1007/s12665-018-7660-7

[17] Yılmaz A. Tokat (Dumanlıdağı) ile Sivas (Çeltekdağı) dolaylarının temel jeoloji özellikleri ve ofiyolitli karışığın konumu. Maden Tetkik ve Arama Dergisi. 1984;**99**(100):1-18. Ankara, Turkey

[18] Yılmaz A, Yılmaz H. Characteristic features and structural evolution of a post collisional basin: The Sivas Basin, Central Anatolia, Turkey. Journal of Asian Earth Sciences. 2005;**27**:164-176

[19] Aktimur T, Atalay Z, Ates S, Tekirli ME, Yurdakul ME. Geology of Area in the Between Çavuşdag ile Munzur Mountains. Ankara, Turkey: MTA (Mineral Research & Exploration General Directorate) Report; 1988. Vol. 8320 p. 102

[20] Dinçer H, Zeybek Hİ. Doline topography on the northeast of Sivas city. SOBİDER. Journal of Social Sciences. 2017;**17**(4):531-542

[21] Ayaz E. Sivas yöresinin karmaşık jeolojik yapısına bağlı olarak gelişen önemli maden yatakları ve MTA'nın Sivas yöresindeki yeni bulguları. MTA Doğal Kaynaklar ve Ekonomi Bülteni. 2013;**16**(13):65-87, General Directorate of Mineral Research and Exploration (MTA) Publications, Ankara, Turkey

[22] Doğan U, Özel S. Gypsum karst and its evolution east of Hafik (Sivas, Turkey). Geomorphology. 2005;**71**:373-388. DOI: 10.1016/j.geomorph.2005.04.009

[23] Hadimli H, Bulut İ. The land use, its problems and organisation in karstic areas. Ankara University TUCAUM 5. National Geography Symposium), 16-17 October 2008, Proceedings Book, Ankara, Turkey. 2009:39-48

[24] Doğan U, Yeşilyurt S. Gypsum karst south of İmranlı, Sivas, Turkey. Cave and Karst Sciences. 2004;**31**:1

[25] Günay G. Gypsum karst, Sivas, Turkey. Environmental Geology. 2002;**42**:387-398. DOI 10.1007/s00254-002-0532-0

[26] Karacan E, Yılmaz I. Collapse dolines in miocene gypsum: an example from SW Sivas (Turkey). Environmental Geology. 1997;**29**:(3/4)

[27] Ulugergerli E, Akca I. Detection of cavities in gypsum. Journal of Balkan Geophysical Society. 2006;**9**:8-19

[28] Darıcı N. Investigation of in gypsum developing structural features with ground penetrating radar (GPR) and multi channel analysis of surface waves (MASW) methods [Master Thesis]. Sivas, Turkey: Cumhuriyet University, Institute of Science, Department of Geophysical Engineering; 2015

[29] Yılmaz I. GIS based susceptibility mapping of karst depression in gypsum: A case study from Sivas basin (Turkey). Engineering Geology. 2007;**90**:89-103

[30] Martínez-Moreno FJ, Galindo-Zaldívar J, Pedrera A, González-Castillo L, Ruano P, Calaforra JM, et al. Detecting gypsum caves with microgravity and ERT under soil water content variations (Sorbas, SE Spain). Engineering Geology. 2015;**193**:38-48. DOI: 10.1016/j.enggeo.2015.04.011

[31] Zini L, Calligaris C, Forte E, Petronio L, Zavagno E, Boccali C, et al. A multidisciplinary approach in sinkhole analysis: The Quinis village case study (NE-Italy). Engineering Geology. 2015;**197**:32-144. DOI: 10.1016/j.enggeo.2015.07.004

[32] Gutiérrez F, Parise M, DeWaele J, Jourde H. A review on natural and human-induced geohazards and impacts in karst. Earth-Science Reviews. 2014;**138**:61-88. DOİ: /10.1016/j. earscirev.2014.08.002

[33] Yılmaz A. Çevresel Etki Değerlendirme. Cumhuriyet Üniversitesi Mühendislik Fakültesi Yayın No: 110, 275p,Sivas, Turkey; 2008b

[34] Bögli A. Karst hydrology and physical speleology. Springer, Berlin, p284; 1980

[35] Klimchouk A. The dissolution and conversıon of gypsum and anhydrite. Int J Speleol. 1996;**25**(3-4):21-36. DOI: 10.5038/1827-806X.25.3.2

[36] Brandt F, Bosbach D. Bassanite ($CaSO_4$ $0.5H_2O$) dissolution and gypsum ($CaSO_4$ $2H_2O$) precipitation in the presence of cellulose ethers. Journal of Crystal Growth. 2001;**233**:837-845

[37] Gutiérrez F, Parise M, DeWaele J, Jourde H. A reviewon natural and human-induced geohazards and impacts in karst. Earth-Science Reviews. 2014;**138**:61-88. DOI: /10.1016/j. earscirev.2014.08.002

[38] Waltham T, Cooper A. Features of gypsum caves and karst at Pinega (Russia) and Ripon (England). Transactions of the British Cave Res Assoc, Cave and Karst Sci. 1998;**25**(3)

[39] Yılmaz A, Atmaca E. Environmental geological assessment of a solid waste disposal site: a case study in Sivas, Turkey. Environ Geology. 2006;**50**:677-689. DOI: 10.1007/s00254-006-0241-1

[40] Candansayar ME, Demirel C. Boru hatları ve korozyon etütlerinde jeofizik çalışmalar. Antalya, Turkey. TMMOB Jeofizik Mühendisleri Odası Ali Keçeli Jeofizik-Jeoteknik Çalıştayı Bildiriler Kitabı; 2015

Chapter 7

Dam Retirement and Decision-Making

Zhao Xueying, Zhang Shunfu and Zhao Xiaoqiu

Abstract

Reservoir is an important part of water conservancy engineering system and an important infrastructure for economic and social development. However, with the increase of operating time, as well as the change of social demand and operating environment, the safety, function, benefit, cost, and other characteristics of the reservoir are also changing. Like living things, reservoirs also have a life cycle of "birth, old age, illness, and death." The retirement of a dam is an inevitable stage in the life cycle management, as well as a means of resource readjustment and rational utilization. Combined with dam retirement cases that caused severe impacts in history, generalized dam removal eco-environment influence factors are obtained from aspects of materializing, ecology, society, and economy. Based on economic rationality theory and flood consequence assessment, two decision-making methods of dam retirement are put forward. The flood consequence method is applied on the case of Heiwa reservoir; key evaluation indexes are compiled from the aspects of ecology, economy, and society; and the evaluation system based on single index is constructed.

Keywords: risk assessment, risk reduction, dam retirement decision, dam removal

1. Introduction

After the dam removal, the ecosystem balance formed by the long-term storage of the reservoir will be broken, which is not a simple adverse process of the ecological environment impact of the dam construction, and may pose a new threat to the river ecosystem. Therefore, it is of great theoretical significance and practical value to establish a method to assess the impact of removal decision. In order to achieve that, key factors need to be identified first.

2. Comprehensive impact of reservoir removal

After a period of operation, the lake ecosystem formed by reservoir storage tends to be stable. After the reservoir was scrapped and the dam was dismantled, the river was reconnected, the hydrological situation was restored to the natural state, and the lake ecology gradually returned to the river ecology. However, this is not a simple reverse process. After the balance is broken again, if scientific control measures are not taken, the natural evolution may generate new stresses on the ecological environment.

In history, some cases have made delightful improvement; some of the others have led to irreparable impacts. Avoid going astray by reviewing the past, which is significant to generalized dam removal eco-environment influence factors.

2.1 Impact characteristics

The research on the impact of reservoir removal on ecological environment involves engineering technology, ecological environment, social economy, human history, and other fields. This paper summarizes the research results and practical cases of reservoir removal around the world. The characteristics of reservoir removal impact on ecological environment are comprehensiveness, contradiction, time-space continuity, and uncertainty.

2.1.1 Comprehensiveness

As with other water resource management behaviors, the impact of dam demolition is comprehensive. This characteristic is reflected in the comprehensive impact of physical, biological, ecological, social, economic, and cultural factors on the ecological environment after the dam is dismantled.

2.1.2 Contradiction

The contradiction reflects the two sides of the impact of dam demolition, that is, while it is beneficial to one element, it is harmful to the other. For example, the removal of dams to restore the connected state of rivers is conducive to the breeding of migratory fish but also easy to cause species invasion.

2.1.3 Space-time continuity

The impact caused by reservoir removal can be spatially from the upstream to the downstream of the dam site, from the river where the dam site is located to the river, and even from the river basin. The time span can be days, months, or even decades. Short-term effects have been generated in the process of dam removal, such as sediment release from the reservoir area, pollution caused by sediment output, water oversaturation, etc. Long-term effects include natural water recovery, the reservoir area becoming a flowing river again, the change of river temperature, the gradual recovery of sediment movement, and so on.

2.1.4 Uncertainty

As a result of subjective and objective reasons, the impact of reservoir removal is uncertain. The subjective reason is that relevant researches are not in-depth and comprehensive enough, and many problems are difficult to be accurately explained from the mechanism. For example, there are still many disputes about the evolution process and mechanism of river channel in the reservoir caused by sediment output, and how to scientifically determine the goal of ecosystem restoration after dam removal is still an academic problem. The objective reason is mainly the impact of global climate change, which is also a difficult problem faced by all water resource management activities.

2.2 Reservoir removal impact classification

Reservoir removal may reshape or even destroy rivers and coastal ecosystems, causing a series of new problems. In this section, hydrological sediment,

topography, water quality, ecological environment, social and economic aspects, and the impact of reservoir removal are classified and analyzed.

2.2.1 Hydrological influence

The construction of the dam will lead to changes in the flow rate, change frequency, duration, occurrence timing, and change rate of the hydrological situation of the river. After the dam is dismantled, the flow rate and water level of the river will change with the seasons, get rid of human intervention, and return to the natural hydrological situation, which will completely reverse the hydrological situation of the river.

After the dam is removed, the river will be reconnected, and the lower reaches of the river will be continuously restored. The shrinking condition of the lower reaches of the river will be alleviated, and the groundwater supply in the lower reaches of the river will be basically restored to nature. However, if the downstream channel has insufficient sediment transport capacity, sediment deposition, and riverbed elevation, the downstream section flow capacity decreases, the channel specific decline becomes slow, the flood discharge capacity weakens, and the reservoir regulation and storage protection are lost; the downstream river level is raised during the flood period, increasing the flood risk in the downstream region.

2.2.2 Sediment impact

Sedimentation is one of the main causes of reservoir removal in China. After the dam is removed, the sediment in the reservoir area will move again. Sediment deposition is the result of the decrease of water flow carrying capacity which is controlled by the backwater effect and velocity of reservoir. If the operation time of reservoir dam is short or the impact of dam on sediment transport is small, the impact of removal on sediment transport is relatively small. On the contrary, the law of sediment transport will change greatly after the reservoir is scrapped. When a small radial reservoir is abandoned, the silt deposited may be mostly carried downstream by the current. After the reservoir with large capacity is scrapped, there may still be a large amount of sediment in place.

Sediment in reservoir area is transported downstream with current, which not only increases turbidity of downstream river segment but also usually leads to sediment deposition in downstream river segment and changes topography of downstream river channel. Fine sediment may cover the original habitat, block the gap between the bed matrices, and destroy the spawning habitat of fish, resulting in the death of fish. It may also block downstream waterways and water intakes, which will adversely affect human production and life.

When pollutants are contained in the sediment, the sediment carrying pollutants to the downstream diffusion after dam removal is bound to have a significant impact on the downstream river habitat. The content of fine sediment and the way of land use upstream are the important factors influencing the pollutant load in the reservoir. This is because fine-grained sediment has a large specific surface area and can absorb more pollutants than coarse sediment. In addition, the upper reaches of the reservoir land use mode can directly affect the reservoir sedimentation, sediment gradation, and pollutant content. Studies have shown that in the basins dominated by agricultural production, the riparian soil is eroded, and the nonpoint source pollution of the river is serious, resulting in a large amount of fine sand and rich nutrients in the silt in the reservoir area. For the watershed dominated by forest land, the sedimentation amount of reservoir is usually small, and the nutrient content of sediment is low [1, 2].

Fort Edward Dam, New York, the United States, was dismantled in 1973. No measures were taken to remove sediment from the reservoir before the dam was dismantled. After the dam was dismantled, serious problems occurred in downstream water quality and navigation. Pollutants—polychlorinated biphenyls (PCBs)—spread with sediment transport and had catastrophic effects on downstream river ecosystems, leading directly to New York state's ban on fishing in the Hudson River in 1976 and posing risks to downstream public health. In addition to pollution, most of the Hudson's waterways, docks, and industrial parks are blocked, reducing the river's ability to cross water, increasing the risk of flooding downstream towns, and causing millions of dollars in economic losses to fishing and shipping [3].

2.2.3 Impact of topography and landform

2.2.3.1 Erosion in the reservoir

The reconnection of rivers, the restoration of natural state of river flow, the reservoir area, and the sediment deposited upstream by the erosion of water to the downstream lead to erosion in the reservoir. The main factors influencing sediment transport in the reservoir include channel flow, sediment particle size and its type, deposition amount, and dam removal mode [4].

This is a slow process of development, at the site of the dam, to form a clear groove head, constantly expanding upstream. From the longitudinal perspective, the depth of topographic erosion in the reservoir area gradually increases, and the specific drop of the river course is greatly adjusted until it encounters impervious obstacles or the specific drop reaches a stable state, and finally the upper and lower reaches of the dam site reach a new dynamic balance [5]. The new balance is sometimes similar to that before the dam was built, but in most cases, some of the sediment remains in place, unwashed downstream by the current.

2.2.3.2 Downstream adjustment

The increase of river sediment content and sediment carrying load forces a series of new adjustments in the lower reaches of the river. At present, it is generally believed that sediment release after dam removal will determine the change of riverbed elevation and sediment transport in the lower reaches, and the process of sediment release can be approximately simulated by sand wave model.

In the early stage after dam removal, the downstream channel adjustment results in the change of bed matrix and channel morphology, and the final result is the evolution of river floodplain system. After a long time, the sediment content of the river reverts to the natural level, which may lead to the transverse movement of the river and the erosion of the floodplain surface.

2.2.4 Impact on water quality

With the increase of water retention time, the reservoir water has adverse effects of low oxygen content, changes in water temperature and pH value, serious eutrophication, and high pollutant concentration. After the dam is dismantled, the continuity of the river is restored, and the adverse effects on the water quality above are alleviated. However, the removement of sediment deposited in the reservoir will lead to the increase of turbidity of the downstream river body, especially when the sediment adsorption has pollutants, which may seriously affect the water quality of the downstream river.

2.2.5 Habitat impact

2.2.5.1 Aquatic habitats

As one of the important characteristics of habitat, bed matrix will change with the adjustment of channel morphology and the change of sediment erosion and deposition after the dam is removed.

The study found that the fine sediment in the reservoir is eroded by the current, exposing the underlying gravel and pebble layers, thus improving the habitat quality of fish and increasing the biodiversity. After the dam is removed, the habitat quality of fish will be improved, the barrier of fish migration will be removed, fish can reach the upstream spawning area, the number of migratory fish often rises, and the number and diversity of aquatic insects and other organisms may increase [6]. The salmon population, which had been sharply reduced, has been recovered to 80% of what it was before the dam was built, after four dams on the Snake River in the United States were dismantled [7].

There are studies showing that, for downstream regions, fine sediment deposition in the downstream reduces riverbed permeability; affects the spawning and breeding habitats of fish; reduces the survival rate, diversity, and abundance of aquatic organisms; and brings adverse effects on downstream habitats [8]. After the removal of the Colorado Dam in the United States, a large amount of sediment released was deposited in the deep pool of the river within 12 km downstream, blocking the gap between coarse particles of sediment, resulting in the death of thousands of fish and the reduction of population density and composition change of large invertebrates. Some scholars have found that the above adverse effects can be eliminated naturally and the rate and recovery degree are related to the biological characteristics. For example, organisms with long life cycle and fixed growth are deeply disturbed and slow in self-recovery. On the contrary, species with short life cycles can recover quickly in a short time [9].

2.2.5.2 Wetlands

Reservoir removal will change the hydrological state of surface water and groundwater as well as the law of river sediment transport, thus leading to a variety of changes in upstream and downstream riverside wetlands. The type and scale of this impact vary from place to place.

The changes of surface and groundwater hydrological state are the main influencing factors of upstream wetlands after dam removal. Some of these influences are seasonal, while others are long-term. For the downstream wetlands, the law of sediment transport and the change of groundwater hydrological state are the main influencing factors. Reservoir removal causes silt deposition in the lower reaches of the river, which may lead to the invasion of wetland plants in the silt area, thus forming a new wetland habitat.

2.2.6 Social impact

The loss of reservoir function, and no other projects to make up for it, may cause serious social problems. For example, if water supply or agricultural irrigation is the main reason for the removal of reservoirs and if the water supply and irrigation needs of residents cannot be effectively solved, serious social problems will arise. In addition, the scour of reservoir area silt may cause the similar problem enters downstream river course along current, silt up downstream channel or channel take water entrance, affect safety of local traffic carriage and production and domestic

use seriously. All these impacts need to be analyzed during the demonstration and planning and design of reservoir removal, and appropriate measures should be taken, such as building alternative projects, dredging river channels, rebuilding or building new water intakes, etc., so as to reduce the adverse impact on society [10].

The right to use the land in the reservoir area and the change of the value of the original lakeside land also belong to the social impact that may be caused by the removal of the reservoir, but compared with the above problems, the social impact of this problem is relatively small.

2.2.7 Economic impact

In China, the primary consideration of reservoir removal is public safety, followed by economic problems. Economic impact analysis is helpful for reservoir stakeholders and their management agencies to compare and choose dam removal schemes and posttreatment measures and optimize schemes [11]. While not every reservoir to be scrapped will undergo a formal cost-benefit analysis, basic economic assessments are needed.

Generally, the economic impact of reservoir removal is divided into two categories: cost and benefit. Cost is regarded as negative impact and benefit as positive impact. The saving of reservoir operation and maintenance cost is often regarded as the positive impact of removal, while the loss of reservoir social and economic benefits is considered as the negative impact of removal. In principle, economic value assessment can be carried out for all kinds of impacts mentioned above, which can be finally reflected through economic impact. However, it is difficult to accurately define the impact category for a small part of the influences, and quantitative and quantitative assessments are difficult for existing influences. Therefore, at current stage, it is difficult to accurately analyze the economic impact of reservoir removal.

3. Decision-making method for reservoir removal

Although many cases have proved that reservoir removal can play a positive role in ecological environment restoration, due to the limitations of people's cognition of the impact of dam demolition and the complexity and unpredictability of the impact of reservoir removal, we cannot blindly be optimistic about the ecological consequences of dam demolition.

Scientific decision analysis and systematic evaluation of the impact of dam removal should be carried out before dam removal. With the help of science and technology and case data, the feasibility of scrapped schemes will be studied by conducting analysis or comprehensive evaluation on the ecological environment, social economy, dam demolition consequences, and other aspects. General, mature, and simple methods, such as mathematical model, physical model, analogue analysis, and professional judgment, should be used when making decisions.

Due to the unpredictability of social, economic, and ecological environment, it is difficult to comprehensively evaluate the impact of reservoir removal on ecological environment. In addition, multi-criteria system decision-making focuses on reflecting external interference as a whole, and it is difficult to reflect the mechanism of influencing factors on decision-making objectives, and the interaction between influencing factors is not conducive to managers to improve the decision-making scheme [12]. In contrast, in-depth study of the sensitivity of a single criterion to a specific pressure response can not only strengthen the comparative study of various schemes but also improve the sensitivity [13]. Therefore, the reservoir removal decision based on a single criterion is highly operable and sensitive.

The selection of removal criteria shall reflect the characteristics of reservoir dam. If the reservoir disease risk is serious and the function atrophy, the economic theory can be used to analyze whether it is reasonable to reinforce the reservoir economically. If attention is paid to the impact of changes in the scrapped reservoir flood situation on the flood safety of downstream towns, it is necessary to conduct targeted flood risk analysis of downstream regions and evaluate the impact of river inflow on downstream towns after the scrapped reservoir. Similarly, if serious reservoir siltation is concerned about the sediment transport process after dam removal, a model can be established to simulate the development process of river sediment transport after dam removal and evaluate the impact of sediment transport with water flow.

At present, reservoir removal is composed mainly of the small reservoir in China. The social and economic benefits of reservoir, operation and maintenance, risk removal, and reinforcement costs can be measured when making decisions. From the perspective of dam economics, the rationality of risk removal and reinforcement plans and dam removal and reinforcement plans can be evaluated. In addition, some small reservoirs may still play a certain role in the urban flood control system. Although the removal of the reservoir can eliminate the risk of dam break, it will increase the risk of flood downstream if it leaves the regulation and storage function of the reservoir.

3.1 Economic decision-making methods

This method is suitable for reservoirs which lost main function and high maintenance costs.

Generally speaking, in the early stage of reservoir operation, only a small amount of cost is needed to meet the needs of operation, maintenance and daily management, during this period, the economic benefits of the reservoir are obvious, and greater social and economic benefits can be obtained. However, with the increase of dam age and the aging of materials and facilities, the cost of operation and maintenance increases. In contrast, long-term operation of the reservoir leads to problems such as deposition, which reduce the social and economic benefits of the reservoir. In a word, the relationship between reservoir cost input and benefit output varies from time to time with reservoir state and operation age.

Peng Hui proposed to establish the evaluation model of dam removal with the help of economic theory and according to the annual economic loss and benefit of the dam [14]. The economic loss and benefit were measured by this model, and the decision was not made from the perspective of reservoir disease risk. Based on its research, this paper proposes the economic decision-making method of reservoir removal. By analyzing the payback period of investment in reservoir restoration project, this method evaluates whether the reservoir restoration project is economically reasonable or not.

The annual cost of reservoir includes daily operation and management costs (V_o), maintenance costs of dam and facilities (V_m), etc. The annual costs of reservoir can be expressed as follows:

$$C = V_o + V_m \tag{1}$$

The annual benefits of the reservoir include the economic benefits from the functions of water supply, irrigation, power generation and shipping (V_e), the social benefits from flood regulation and storage (V_s), the recreational benefits from the reservoir landscape (V_r), etc. The annual income of the reservoir can be expressed as follows:

$$B = V_e + V_s + V_r \tag{2}$$

According to the annual cost (Eq. (1)) and income (Eq. (2)), the annual cost-benefit map of the reservoir is drawn, and the change process of the cost and benefit of the reservoir is obtained. Generally speaking, the input cost of the reservoir increases gradually with the operation time, while the benefit of the reservoir is on the contrary, decreasing year by year with time. Regression analysis is carried out on multi-year data to fit the time functions c(t) and b(t) of annual cost and benefit, as shown in **Figure 1**.

With the increase of operation time, the annual input cost increases. When the reservoir is considered to make decision of retirement, the annual input cost shall be the historical maximum, denoted as the t1 in that year and the input cost as C1. Assuming that the benefits and costs only change over time, the time function of the benefit and cost can be estimated according to the actual cost and benefit function, remember c′(t) and b′(t). When the cost of the c′(t) reservoir in the t t2 year reaches C1 again, it will be deemed that the reservoir state returns to the initial decision state, and the interval from t1 to the t2 is the service life of the reservoir restoration measures. Within the interval of [t1, t2], the multi-year net income A (i.e., the shaded area in **Figure 2**) and the multi-year average net income R can be calculated as follows.

$$A = \int_{t_1}^{t_2} \left[b'(t) - c'(t) \right] dt \tag{3}$$

$$R = \frac{A}{(t_2 - t_1)} \tag{4}$$

At t1 time point, one-off investment cost for consolidation F was input, which needs to be compensated by net income A obtained over many years during the period of time Δt = t2−t1. According to the payback period method of investment, the payback period of reinforcement investment F is set as T.

$$F(1+i)^T = R(1+i)^{T-1} + R(1+i)^{T-2} + \cdots + R(1+i) + R \tag{5}$$

$$T = \frac{\lg R - \lg(R - iF)}{\lg(1+i)} \tag{6}$$

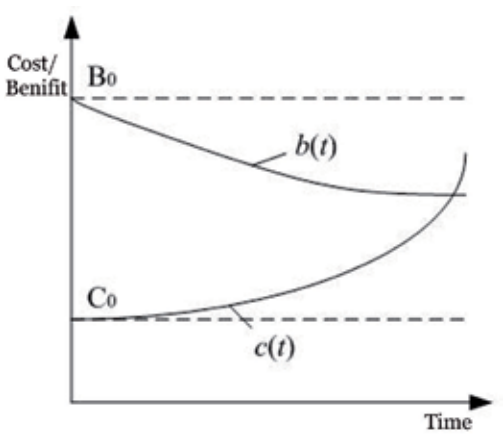

Figure 1.
Time function diagram of annual cost and annual income of a reservoir.

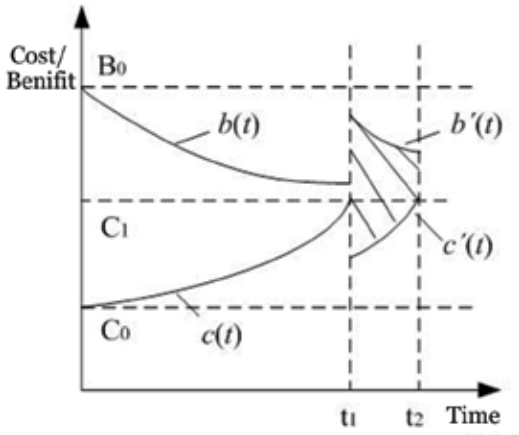

Figure 2.
Time t2 calculation diagram of occurrence of new disease risks of the dam after reinforcement.

In the equations above, i stands for social discount rate.

The extended service life of the reinforcement project is less than the recovery life of the project cost, which indicates the project is economic irrationality and disposal can be considered; in the same way, if $T \leq \Delta T$, indicates the project is economically feasible

3.2 Consequence decision method

Flood impact is an important evaluation content of reservoir removal decision under the urban background, and simulating the impact of reservoir removal on flood situation is conducive to proposing targeted reduction measures and improving the decision-making scheme.

The assessment framework for the consequences of reservoir removal covers six steps, namely, the formulation of a plan, the establishment of an assessment index system, the determination of flood loss indicators, the establishment of a flood risk model, the calculation of flood loss, and the program assessment.

At least two schemes are selected for evaluation, and the evaluation results are compared with each other. Two schemes of reservoir current flood control and reservoir removal are usually used to evaluate the flood changes of reservoir removal scheme based on the current flood control of reservoir.

The evaluation index system criterion layer constructed in this paper consists of economy, society, and environment.

Flood economic losses are divided into direct economic losses and indirect economic losses. Direct economic loss refers to the total loss of physical damage caused by flood, usually including loss of farmland production, damage to housing and facilities, and financial losses [15]. Indirect economic losses are considered to be other losses caused or implicated by direct economic losses, specifically, the stoppage and production reduction losses caused by flood disaster, the economic losses caused by the increase of intermediate investment backlog, and the loss of investment premium [16].

The inundation of downstream cities caused by the flood will affect human normal activities to varying degrees, which is the embodiment of the social impact of the flood. The degree of the impact can be measured by the number of people affected by the flood and the inundation range.

The impact of flood on urban environment is divided into landscape damage and soil erosion. On the one hand, the water will carry the bare soil in the erosion

area, causing a large amount of soil loss; on the other hand, the vegetation of flood areas is damaged by floods, causing losses to the urban landscape.

Take Heiwa reservoir as an example. Heiwa reservoir, located in the southwest of Chuzhou city, Anhui province, was spontaneously built and operated by villagers. It was completed and started operation in 1977 with a capacity of 560,000 m^3. The maximum height of the dam is 12.2 m. With the advancement of urbanization, the farmland in the lower reaches turned into urban area. The spillway goes straight through the new campus of Chuzhou College, which is less than 2 miles away. Buildings and population are numerous and dense, as shown in **Figure 3**. The reservoir has been identified as dangerously weak, due to poor construction quality and capacity of management, which makes downstream region a high-risk zone. Besides that, the reservoir's main function has changes from agricultural irrigation as designed to urban flood control.

In general, Heiwa reservoir, which has lost design function, needs continuously huge investment in improving dam state to prevent dam break. It is a typical case for dam removal discussion.

The lower reaches of the reservoir pass through the main urban area of Chuzhou city from the southwest to the northeast (see **Table 1** for details). Along the way, residential areas, schools, medical care, administrative institutions, and commercial shops are distributed. As shown in **Figure 4**, in case of dam break danger, huge economic loss and significant social impact will be caused.

To improve the city's flood control system, the Chuzhou water conservancy department has established an urban flood control plan by intercepting the flood in the western mountainous area of Chuzhou and protecting the central urban area and the industrial zone between the Qingliu River west and the Beijing-Shanghai railway. The key point of this plan is to discharge the reservoir water from the southwest hilly region into the Qingliu River via the newly built flood interception ditch, around the west side of the main urban area to the south side (see **Figure 4**). The western flood interception ditch intersects the reservoir channel at point B. If the flood interception ditch is completed, the flood discharge pressure of river section will be relieved. The designed maximum discharge at point B of the flood interception ditch is 50 m^3/s. There is a flood gap on the left bank of point B, and the flood exceeding the designed flow rate will be discharged into the Qingliu River by the spillway at a maximum flow rate of 8 m^3/s through the urban river channel.

Figure 3.
Satellite map of Heiwa reservoir location.

No.	River section	River section information
1	The reservoir—A	The reservoir spillway
2	A—B	South campus of Chuzhou University
3	B—C	Residential landscape section
4	C—D	Underground drainage ditch section
5	D—E	Joining the drainage flow of Yujiawa reservoir and flowing into the open channel section
6	E—Qingliu River	Joining Qingliu River

Table 1.
Downstream channel information of reservoir.

Figure 4.
Regional distribution and river channel diagram of the lower reaches of the reservoir.

3.2.1 Evaluation scheme

In this section, three evaluation schemes are proposed for Heiwa reservoir under the condition that it encounters a flood once every 50 years: (1) flood regulation scheme for the reservoir. Under the current situation of Heiwa reservoir, the peak discharge from the reservoir to the discharge from the reservoir is 34.1 m^3/s; (2) the scheme of reservoir removal, and the peak inflow of the reservoir, is 54.9 m^3/s, and point D of the river meets the incoming water from Yujiawa reservoir; and (3) the reservoir was scrapped, and the city's flood control system was improved. The flood interception ditch shared the discharge of some of the water from Heiwa reservoir and Yujiawa reservoir, and the excess discharge still flowed from the river section into Qingliu River. The flow data of each scheme are shown in **Table 2**.

Based on the flood consequence criteria, a two-dimensional hydrodynamic mathematical model was established to simulate the flood evolution process, result as below.

Without the effective urban flood control planning, the city's flood discharge capacity of the urban channel system is insufficient, and the city was seriously affected by the flood return period of 50 years. As shown in Figure **Figure 5**. Especially, due to confluence of Heiwa reservoir flood drainage and Yujiawa reservoir flow at the open channel of Huifeng Road, both sides of the road were flooded; the average water depth was about 0.25 m, maximum depth of 1.72 m; and Chuzhou Development Zone was affected seriously, with submerged depth of the water at about 0.7 m. The low-lying depression area on the east side of Beijing-Shanghai

Scheme number	Scheme description	Flow rate (m^3/s)		
		Point A	River section BD	River section DE
1	Reservoir flood routing	34.1	34.1	71.6
2	Reservoir removal	54.9	54.9	92.4
3	Reservoir removal + flood control planning	54.9	33.7	33.7

Table 2.
Flow point data of flood simulation scheme.

railway was the most seriously flooded with a maximum depth of 3.77 m. This area is located outside the main urban area of Chuzhou and has a low population density.

Under the scheme of reservoir removal, the discharge rate of the lower discharge increases from 34.1 to 54.9 m^3/s, and the flood discharge pressure of the drainage ditch system increases; the average submerged depth is about 0.84 m, and the maximum submerged depth is 4.02 m. The submerged range increases from 1.63 to 1.83 km^2; the newly added flooded area is mainly located in the housing area downstream of the dam site, as shown in **Figure 6**.

Under the new flood control system, the flooded area and water depth of the reservoir scrapping scheme are significantly less than that of the reservoir flood control before the implementation of the plan, as shown in **Figure 7** for details. After the implementation of flood control planning, the Xipie flood interception ditch can accommodate the flow rate of 21.2 m^3/s, and the flow rate of the flood flowing into the urban river course is 33.7 m^3/s, slightly lower than the regulated flood volume of the reservoir 34.1 m^3/s. Although the flow rate is similar, the submerged area of the former is only 35% of that of the latter. The inundation area of the downstream risk area is 0.58 km^2, mainly concentrated in underground drainage ditch CD river section. The maximum depth was reduced from 4.02 to 2.66 m; the water depth of the Beijing-Shanghai railway decreased from 1.72 to 0.30 m.

The simulation results show that, after the removal of Heiwa reservoir, the reservoir completely loses the capacity of regulating and storing. Although the discharge volume under the channel will increase by 56%, the inundation range and average inundation depth will increase by only 11 and 12%, which is relatively small compared with the flood control scheme of the reservoir. This is because the downstream

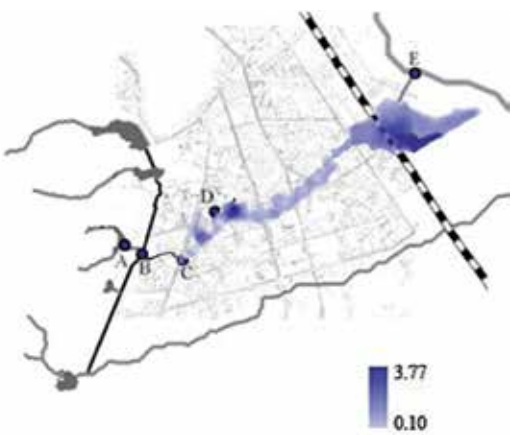

Figure 5.
Flood depth of the lower reaches of the reservoir flood control scheme in case of a flood once every 50 years.

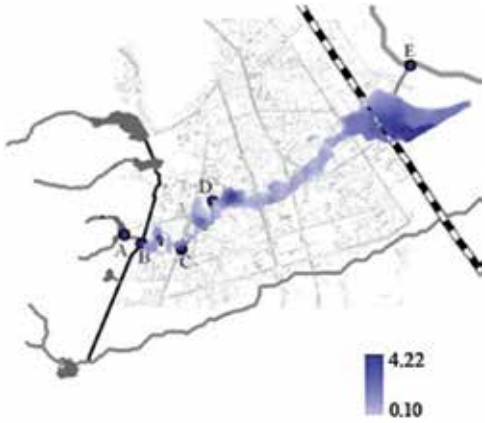

Figure 6.
Flood depth downstream of reservoir abandonment scheme in case of a flood once every 50 years.

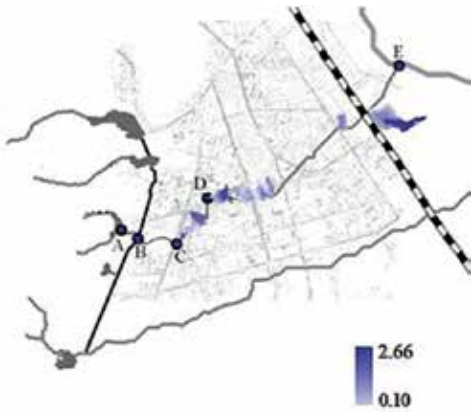

Figure 7.
Flood depth in the lower reaches of the joint flood control planning scheme for flood once encountered every 50 years.

discharge volume of the reservoir far exceeds the flood discharge capacity of the downstream urban channel system. In other words, the flood control effect of the reservoir is not significant, and even if the reservoir is removed, it will not significantly increase the inundation range and water depth. In comparison, although the reservoir has been scrapped and lost its flood control capacity, the flooded area of the lower reaches of the reservoir has been significantly reduced after combining with the urban flood control planning. Compared with the reservoir scrapped plan before the implementation of the planning, the flooded area of the latter has been reduced by 69%.

3.2.2. Flood impact assessment

According to the characteristics of the calculation region and the loss data of agricultural and commercial assets in typical flood disasters in history, the loss rate was determined, and the corresponding relationship between the loss rate and water depth was finally determined, as shown in **Table 3**.

According to the flood analysis and results of three schemes, combined with the regional feature distribution, to measure socio-economic indicators including

the flood area population, submerged area, submerged residential area, affected length of road and railway, affected population and GDP of each scheme. Results are shown in **Table 4**.

See **Table 5–7** for the flood loss values under different water depth levels of each simulation scheme.

The result of loss assessment shows that the building loss is between RMB 3.04 million and 26.48 million, the landscape loss is from RMB 933,300 to 8.39 million, the road loss is from RMB 14,000 to 86,100, the railway loss is from RMB 0 to 1.36 million, and the total loss is from RMB 3.99 million to 3.63 million. Among the three schemes, the total loss of scrapped reservoir is the largest, among which the loss of buildings is the largest, followed by the loss of landscape.

Depth (m)	Building	Vegetation	Railway	Roads
0.05–0.5	0	5	1	2
0.5–1.0	1	10	2	3
1.0–2.0	5	19	6	10
2.0–3.0	18	50	22	28
> = 3.0	24	68	32	39

Table 3.
Ground object loss rate: water depth relationship (unit, %).

Scheme number	Submerged area (km^2)	Submerged area of buildings (km^2)	Affected road length (km)	Affected railway length (km)	Affected landscape area (km^2)	Total GDP affected (RMB 10,000)	Total population affected (person)
1	1.63	0.97	3.15	0.70	0.58	6337	2798
2	1.83	1.12	3.52	0.76	0.66	7100	3184
3	0.58	0.24	0.97	0	0.21	2250	997

Table 4.
Calculation of the statistical table of flooded surface features in the region.

Depth grade (m)	Building loss	Landscape loss	Railway loss	Road loss	Total
0.05–0.5	0.00	154.66	126.00	4.41	285.07
0.5–1.0	208.00	186.66	0.00	4.20	398.86
1.0–2.0	520.00	30.40	0.00	0.00	550.40
2.0–3.0	144.00	53.33	0.00	0.00	197.33
≥3.0	192.00	72.53	0.00	0.00	264.53
Total	1064.00	497.57	126.00	8.61	1696.18

Table 5.
Scheme 1: flood loss table of water depth at all levels unit: RMB 10,000.

Depth grade (m)	Building loss	Landscape loss	Railway loss	Road loss	Total
0.05–0.5	0.00	175.99	136.80	4.41	317.20
0.5–1.0	296.00	213.32	0.00	4.20	513.52
1.0–2.0	720.00	324.25	0.00	0.00	1044.25
2.0–3.0	1440.00	53.33	0.00	0.00	1493.33
≥3.0	192.00	72.53	0.00	0.00	264.53
Total	2648.00	839.41	136.80	8.61	3632.82

Table 6.
Flood loss table of water depth at all levels in Scheme 2 unit: RMB 10,000.

Depth grade (m)	Building loss	Landscape loss	Railway loss	Road loss	Total
0.05–0.5	0.00	56.00	0.00	1.40	57.40
0.5–1.0	80.00	37.33	0.00	0.00	117.33
1.0–2.0	80.00	0.00	0.00	0.00	80.00
2.0–3.0	144.00	0.00	0.00	0.00	144.00
≥3.0	0.00	0.00	0.00	0.00	0.00
Total	304.00	93.33	0.00	1.40	398.73

Table 7.
Flood losses of all levels of water depth in Scheme 3 unit: RMB 10,000.

4. Conclusion

Due to the aging, poor construction quality, and maintenance, water damage and other adverse factors make it a prominent risk for the Chinese reservoir management institution. In the face of the long-term challenges of the disease-risk reservoirs, it is an effective way to solve the problems of the disease-risk reservoirs by disposing of the ones with serious disease risk, shrinking function, and technically unfeasible and economically unreasonable danger reservoirs while taking engineering measures to remove and reinforce them.

Based on economic rationality theory and flood consequence assessment, two decision-making methods of dam retirement are put forward. The flood consequence method is applied on the case of Heiwa reservoir; key evaluation indexes are compiled from the aspects of ecology, economy, and society; and the evaluation system based on single index is constructed. Comparing the plans of current dam situation, dam removal, and dam removal combined with urban flood control measure, the flood risk influence is evaluated. The evaluation results show that the reservoir scrapping will not have significant effects on the flooding situation in downstream cities. Besides, the urban flood control regulation measures could greatly mitigate the urban flood risk.

Acknowledgements

My deepest gratitude first goes to Dr. Sheng Jinbao and Dr. Wang Zhaosheng, my supervisors, for their constant encouragement and guidance. My thanks would go

to workmates in Dam Safety Management Center of MWR at Nanjing for discussing ideas presented here. Contributions from Pro. Qian Xing at Nanjing University are greatly appreciated.

This chapter is supported by National Key R&D Program of China (2017YFC1501202).

Author details

Zhao Xueying[1,2*], Zhang Shunfu[1,2] and Zhao Xiaoqiu[3]

1 China Institute of Water Resources and Hydropower Research, Beijing, China

2 Center of Flood and Drought Disaster Reduction of Ministry of Water Resources, Beijing, China

3 Changjiang Institute of Survey, planning, Design and Research Limited CO, Wuhan Hubei, China

*Address all correspondence to: zhaoxy@iwhr.com

References

[1] Ahearn DS, Dahlgren RA. Sediment and nutrient dynamics following a low head dam removal at Murphy Creek, California. Limnology and Oceanography. 2005;**50**:1752-1762

[2] Hart DD, Pizzuto JE, et al. An integrative approach towards understanding ecological responses to dam removal: The Manatawny Creek study. Journal of the American Water Resources Association. 2002;**38**(6):1581-1599

[3] Dam-Breaking and River-Rescuing in the United States [Internet]. 2014. Available from: http://www.bjny.gov.cn/nyj/231595/603501/232647/5531535/index.html [Accessed: 11-11-2016]

[4] Doyle MW, Stanley EH, Harbo JM. Channel adjustments following two dam removals in Wisconsin. Water Resources Research. 2000;**39**(1):1-15

[5] Riggsbee JA, Julian JP, Doyle MW, et al. Suspended sediment, dissolved organic carbon, and dissolved nitrogen export during the dam removal process. Water Resources Research. 2007;**43**(9):W09414

[6] Bednarek AT. Undamming rivers: A review of the ecological impacts of dam removal. Environmental Management. 2001;**27**(6):803-814

[7] Hui P, Defu L, Bin T. Analysis on the current situation of international dam demolition. China Rural Water Conservancy and Hydropower. 2009;**5**:130-135

[8] Thomson JR, Hart DD, Charles DF, et al. Effects of removal of a small dam on downstream macroinvertebrate and algal assemblages in a Pennsylvania stream. Journal of the North American Benthological Society. 2005;**24**:192-207

[9] Stanley EH, Doyle MW. Trading off: The ecological removal effects of dam. Frontiers in Ecology and the Environment. 2003;**1**(1):15-22

[10] Internet. Available from: http://www.waymarking.com/waymarks/WMXN4 [Accessed: 07-08-2015]

[11] Heinz Center. Dam Removal: Science and Decision Making. Washington, DC: H. J. Heinz Center for Science, Economics and the Environment; 2002

[12] Xiaochun W, Tangbin H, Hongjun Z, et al. Study on ecological evaluation and ecological red line of Huma River. Chinese Journal of Fisheries. 2014;**27**(6):59-65

[13] Shangbo Z, Xingzhong Y, Hong L, et al. Advances in river health assessment based on different indicator organisms. Chinese Journal of Ecology. 2013;**32**(8):2211-2219

[14] Hui P, Defu L. Dam Aging and Retirement. China Water and Power Press; 2015

[15] Baohua W, Qiang F, Yonggang X, et al. An overview of flood disaster economic loss assessment methods at home and abroad. Journal of Catastrophology. 2007;**22**(3):95-100

[16] Yuxiang H, Zongyue Y, Yinghong S. Measurement of indirect economic losses of disasters. Journal of Catastrophology. 1994;**9**(3):7-11

Chapter 8

Seismic Hazard of Viaduct Transportation Infrastructure

Wael Zatar

Abstract

Prestressed concrete viaduct structures are used for the construction of many highways and railways. The objective of this study was to clarify the inelastic response behavior of partially prestressed concrete viaduct structures during severe earthquake excitations. A study that includes experimental and analytical phases was carried out. Small-scaled models were employed so as to represent actual viaduct structures. Specimens representing the PC girders of the viaduct structures were tested experimentally. The first technique was statically reversed cyclic loading test to study the inelastic response behavior of the PC girders and to obtain the hysteretic-load deformational characteristics. The sub-structured pseudo-dynamic testing technique was implemented as the second testing technique. During the sub-structured pseudo-dynamic test, the PC girder was tested experimentally, and the RC columns of the viaduct structure were simulated analytically. An amplified excitation of the 1995 Hyogo Ken Nanbu earthquake was used. Response analyses for the viaduct model were carried out. A comparison between the experimental results and results obtained from response analyses was made. An agreement between the experimental and analytical results was found. The study revealed that not only the RC columns but also the PC girders may undergo extensive damage during severe earthquake excitations.

Keywords: earthquake-resistant structures, viaduct structures, sub-structured pseudo-dynamic tests, statically reversed cyclic loading tests, partially prestressed concrete, dynamic analysis

1. Introduction

Viaduct structures and elevated bridges are becoming more common for railways and highways. During the past few decades, partially prestressed concrete has been used for the construction of viaduct structures. Earthquakes have a habit of identifying structural weakness and concentrating the damage at these locations. Elevated bridges and viaduct structures have little or no redundancy in structural systems, and failure of one structural element or connection is thus more likely to result in collapse [1]. Therefore, it is of a great importance to carefully understand the seismic response behavior of viaduct structures. Experimental investigations have been carried out in the past to study the deformation and cracking of partially prestressed concrete beams under static and cyclic fatigue loading [2]. Various loading tests have been carried out to study the inelastic response behavior of the elevated bridges when subjected to ground motions. Since the girders of these bridges are generally hinged to the piers, only the piers are subjected to earthquake

forces. Moreover, few research studies have been carried out to study the effect of prestressing the reinforced concrete piers of highway bridges [3, 4].

On the other hand, because of the monolithic moment-resisting connection between the superstructure and the columns of the viaduct structures, less bending moments were expected in the bottom ends of the columns, and other plastic hinges at the tip of the columns may result to allow for some energy dissipation at these locations. Additionally, not only the columns but also the girders might have some damage. Yet not enough tests have been performed to study the inelastic response behavior of the partially prestressed concrete (hereafter known as PC) girders of the viaduct structures [5–7]. The objective of this study was to obtain the inelastic response behavior of such PC viaduct structures due to severe earthquake excitation.

A study that includes experimental and analytical phases was carried out. Specimens representing the PC girders of the viaduct structures were tested experimentally. Statically reversed cyclic loading and sub-structured pseudo-dynamic testing were conducted. The objective of the statically reversed cyclic loading test was to study the inelastic response behavior of the PC girders and to obtain the hysteretic-load deformational characteristics. During the sub-structured pseudo-dynamic test, the PC girder was tested experimentally, and the RC columns of the viaduct structure were simulated analytically. Response analyses for the viaduct model in terms of hysteretic moment-rotation curves and time histories were carried out. The plastic deformability expressed in terms of the ductility factor and the dissipated energy was examined. A comparison between the experimental results and results obtained from response analyses was made.

2. Outlines of tests

2.1 Test specimens

The viaduct model (**Figure 1**) was constructed at a 1/10 scale of a full-size viaduct structure. The PC girder of the viaduct structure was considered as the experimental substructure. It was reasonably assumed that the viaduct girder was symmetric with respect to the center of each bay. This assumption was made for simplicity and due to the difficulty of implementing members with different inflection points, and because of the linearly varying moment distribution. Consequently, the PC girder was assumed to be composed of two identical cantilever members satisfying compatibility and equilibrium conditions at the center. Only half of the PC girder was considered as the experimental member (**Figure 1a**). The model numbering scheme, dimensions, and degrees of freedom are shown in **Figure 1b**.

Two partially PC specimens representing the experimental PC girder members of the viaduct models and named B-1 and B-2 were tested. The specimens have the same dimensions, reinforcing bars, and prestressing tendons arrangement. Specimen B-1 was tested using a statically reversed cyclically loading, while specimen B-2 was tested using a sub-structured pseudo-dynamic test. The upper part of each specimen (**Figure 2**) represents the PC girder part. The PC girder part was placed monolithically with a lower part. The lower part represents the moment-resisting connection and the upper part of the reinforced concrete column of the viaduct model. The lower part has sufficient rigidity to allow the observation of the damage of the PC girders during testing.

The PC girder part has a depth of 25 cm, a width of 20 cm, and a length of 200 cm. The lower part of the specimen has a depth of 50 cm, a width of 50 cm, and a length of 120 cm. The girder part has two reinforcing bars with 13 mm diameter at each side of the section. The girder part has one D11 mm prestressing

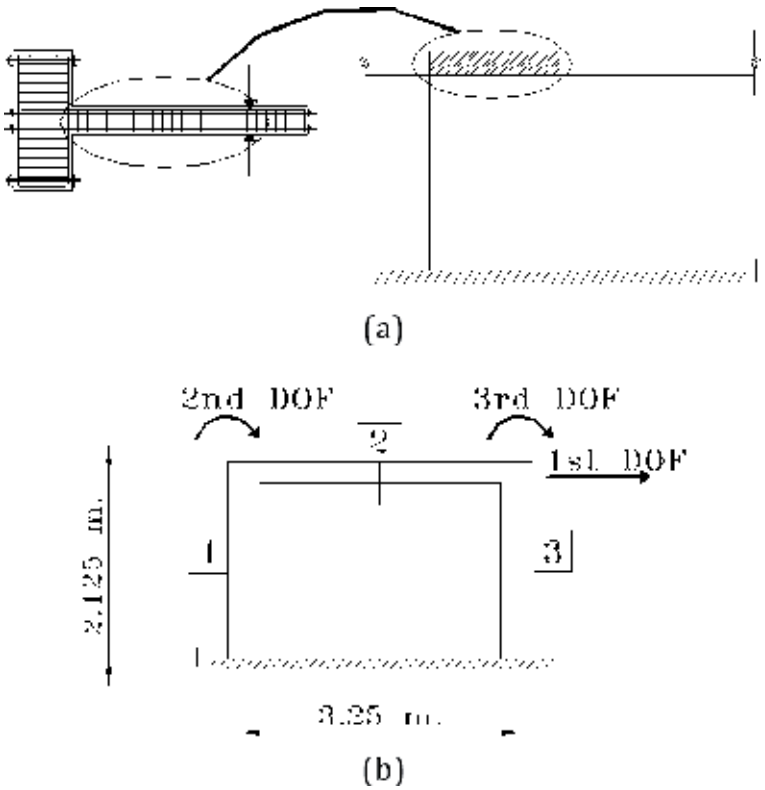

Figure 1.
Experimental test specimen and model used during the sub-structured pseudo-dynamic testing: (a) Experimental test specimen; (b) model used in the sub-structured pseudo-dynamic testing.

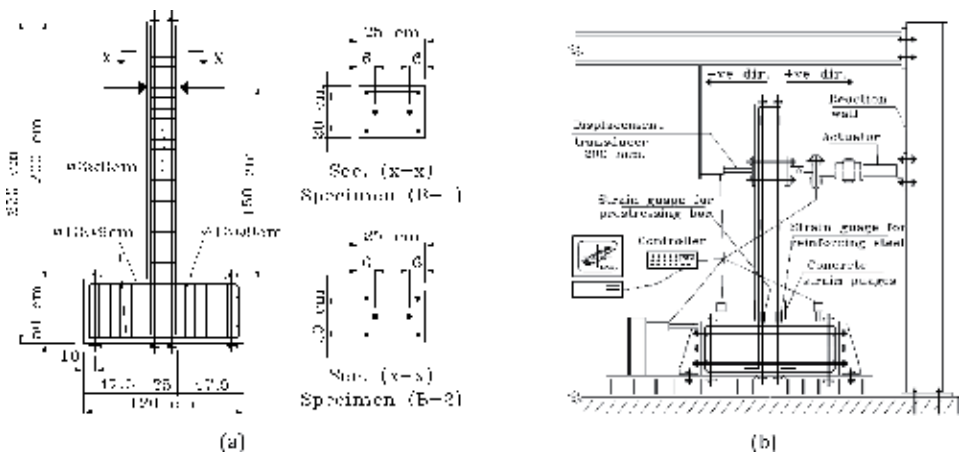

Figure 2.
Test specimens and loading setup: (a) test specimens; (b) loading setup.

tendon at each side of the cross section (**Figure 2**). The mechanical prestressing ratio of the specimens is 0.55. The design philosophy implicitly requires that shear failure be prevented or delayed so that the member under consideration may dissipate, by flexure, energy larger than required for the applied earthquake. Therefore, relatively close-spaced transverse hoops were arranged for the entire length of the girder part. The rectangular hoops were 3 mm in diameter and were spaced at 8 cm.

The specimens were fixed to a testing floor by the use of side supports, prestressed rods, and high-strength bolts. The loading was applied through an actuator that was fixed at a height of 150 cm from the bottom end of the PC girder of each specimen (**Figure 2**). The corresponding a/d ratio is 6.8. The average compressive cylindrical concrete strength is 400 kgf/cm^2. The yield strength of the reinforcing bars is 3400 kgf/cm^2, and the yield strength of the prestressing tendons is 12,200 kgf/cm^2. Details of the specimens are shown in **Figure 2**.

2.2 Statically reversed cyclic loading testing

Statically reversed cyclic loading test was carried out for specimen B-1. The objective of conducting this test was to clarify the load-displacement characteristics of the PC girders. The specimen was tested using the setup shown in **Figure 2b**. The setup consisted of the specimen, actuator, reaction wall, testing floor, data loggers, computer for data acquisition, and displacement measuring devices. The yield displacement was the measured displacement corresponding to the recorded yield load. The imposed displacements to the specimen through the actuator were multiples of the prestressing tendons yielding displacement. Ten repetitions of each cycle were considered. Typically, ten repetitions cannot be attained during a real severe earthquake, but they were planned to fully clarify the load-displacement characteristics. **Figure 3** shows the input displacements that were applied to specimen B-1.

2.3 Sub-structured pseudo-dynamic testing

2.3.1 Structural model

Many numerical and experimental studies have been carried out to clarify the inelastic behavior of RC columns. However, very few experimental studies have been carried out to date on the response behavior of the full structures in which few members may undergo extensive inelastic deformations. The inelastic deformations of the few members may significantly affect the overall response behavior and the structure integrity of the full structure. The unavailability of test records for the full viaduct structures can be attributed to the high cost and scale of conducting the associated large tests.

Sub-structured pseudo-dynamic test is a computer-controlled experimental technique in which direct numerical time integration is used to solve the equation of motion. By incorporating the sub-structuring concept, it is possible to test only the critical member effect on the inelastic seismic response of the whole structure.

The PC girder of the viaduct structure was considered as the experimental substructure. The PC girder was assumed to be composed of two identical cantilever

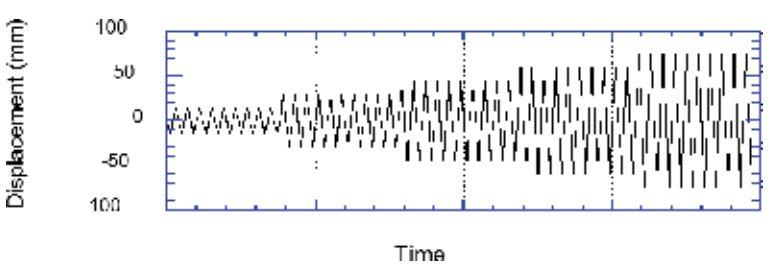

Figure 3.
Input displacements applied to specimen B-1 during the statically reversed cyclic loading test.

members satisfying compatibility and equilibrium conditions at the center, and thus having only half of the girder as the experimental member (**Figure 1a**).

2.3.2 Experimental procedures

The sub-structured pseudo-dynamic testing technique was used for testing specimen B-2 of the viaduct model shown in **Figure 1b**. The load was applied quasi-statically during the test, and the dynamic effects were simulated numerically [8]. An analytical inelastic mechanical model and its restoring force-displacement model were used for all the RC members of the viaduct structure except for the PC girder [9]. The restoring force for the PC girder was measured directly from the loading test system [10].

One component model [11] was employed for the inelastic member model. The one component model consists of a linearly elastic member with two equivalent nonlinear springs at the member ends (**Figure 4a**). The rotational deformation of the member due to the bending moment was expressed as the sum of the flexural deformation of the linear elastic member and the rotational deformation of the two equivalent nonlinear springs. The spring constants are known as KPA and KPB (**Figure 4a**) and are determined using Otani's method [12]. The inelastic moment-rotation relationship of the spring was calculated by means of the ordinary flexural theory based on the assumption that the point of contra flexure was located at the center of each member. Furthermore, the rotations due to bond slip of the reinforcing bars as well as the prestressing tendons from the connecting joint were taken into consideration using Ohta's method [13] for all the members of the viaduct model.

Takeda's et al. trilinear model [14] was used as the hysteretic restoring force model for the RC members (**Figure 4b**). Takeda's et al. model includes the characteristic behavior of concrete cracking, yielding, and strain hardening of the main reinforcement. Takeda's et al. model is a realistic and conceptual model that recognizes the continually degrading stiffness due to bond slip, shear cracks, and energy absorption characteristics of the structure during an earthquake excitation. The stiffness of Takeda's model during unloading (K_r) was defined by Eq. (1):

$$K_r = \left(M_c + M_y\right) / \left(\theta_c + \theta_y\right) \left|\theta_y / \theta_m\right|^{\alpha} \tag{1}$$

where α was the unloading stiffness parameter that was considered equal to 0.4 for the RC columns. The earthquake excitation during the sub-structured pseudo-dynamic test was the modified Hyogo-Ken Nanbu 1995 earthquake excitation (NS direction). The Hyogo-Ken Nanbu earthquake excitation was selected to represent a near-field excitation. The time scale was amplified to half the original time scale that was recorded during the original Hyogo-Ken Nanbu excitation. The maximum ground acceleration that was considered during the sub-structured pseudo-dynamic test was kept as the original acceleration (818 gal) that was recorded during the original excitation [15, 16] (**Figure 4c**).

The so-called mixed (explicit-implicit) integration method that was originally developed for finite elements analysis was found to be suitable for the sub-structured pseudo-dynamic test [10]. However, Nakashima et al. [17] found out that for the sub-structured pseudo-dynamic test, the constitutive operator splitting (OS) method is the most effective method in terms of both stability and accuracy. Consequently, the OS method was implemented in this study for the numerical integration of the equation of motion. The integration time interval was 0.0005 second, and the earthquake time interval was 0.005 second.

Two percent damping was assumed for each mode of the modal damping until the member under consideration experience a rotation angle equal to the yield

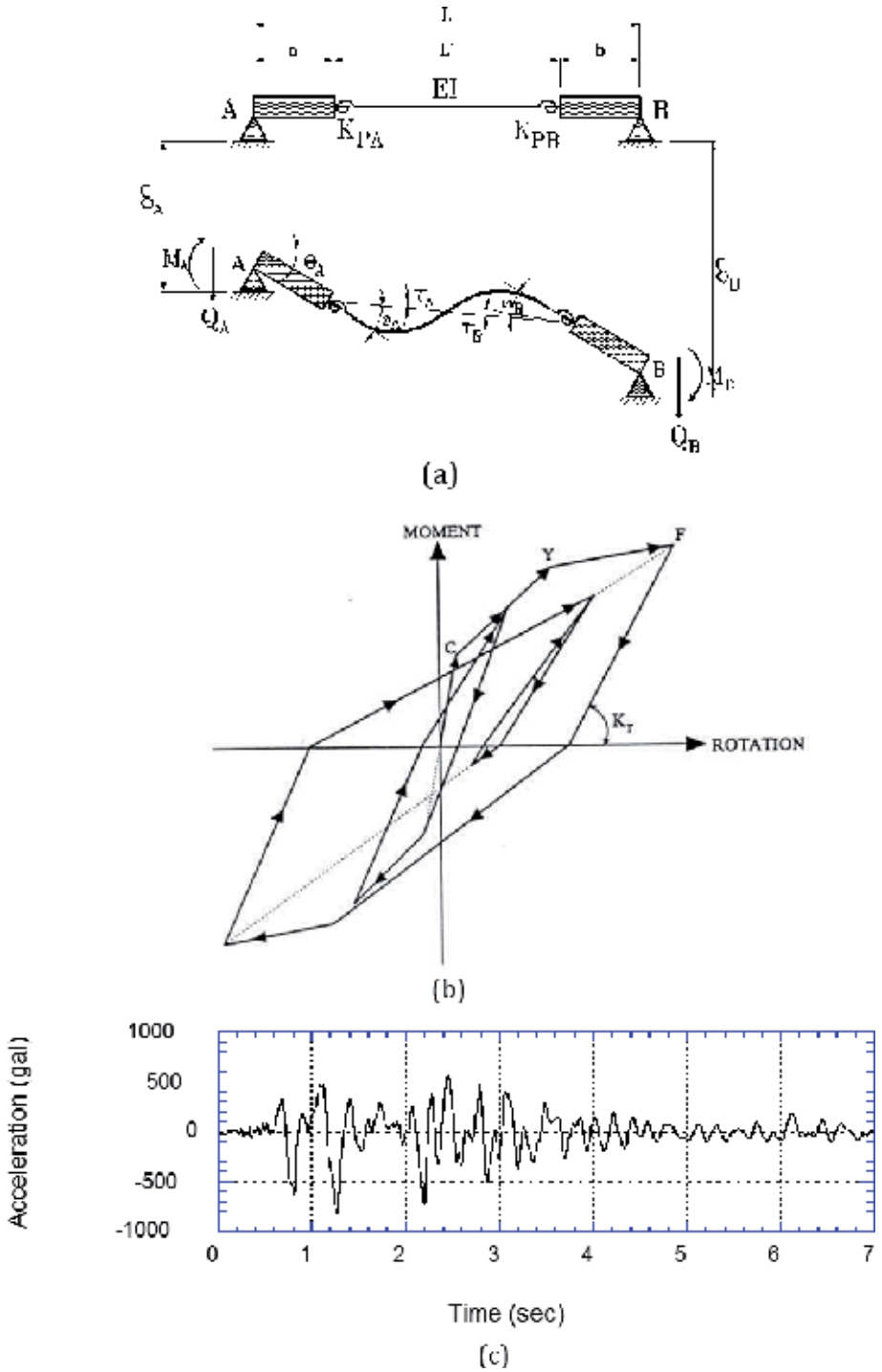

Figure 4.
One component model, Takeda's hysteretic restoring force model, and input ground excitation: (a) One component model, (b) Takeda's hysteretic restoring force model; (c) input ground excitation (Hyogo-Ken Nanbu Earthquake, 1995, Kobe city, NS direction).

rotation angle. After reaching the yield rotation angle, the damping was assumed to become zero due to the fact that only the hysteretic damping is dominant after the displacement reaches the yield displacement. The system that was used in the

sub-structured pseudo-dynamic test consists of the specimen, loading actuator, reaction wall, data loggers, personal computer for analyzing the inelastic response of the viaduct model and for controlling the input/output data, measuring devices, another personal computer for data acquisition, digital/analog (D/A) converter, and analog/digital (A/D) converter. The test procedures were as follows:

1. The displacement of the girder at the first step was calculated analytically by the response analysis program that was based on Takeda's trilinear model.

2. By means of the digital/analog converter, the calculated displacement was converted from a digital value into an analog value that can be applied to the specimen through the actuator.

3. Immediately after the actuator applies the required displacement to the specimen, the restoring force was directly measured from the loading system. The computer records this restoring force after converting the data from analog to digital through the A/D converter.

4. The previous restoring force was used for the calculation of the displacement in the next step.

5. The previous steps (steps 1–4) were repeated for the entire duration of the input excitation.

3. Test results

3.1 Statically reversed cyclic loading test

The input cyclic wave, shown in **Figure 3**, was employed during the statically reversed cyclic loading testing of specimen B-1. **Figure 5a** shows the load-displacement curve for specimen B-1. The test was continued, after reaching the ultimate load, till a decrease of the load to 80% of the ultimate load was noticed. The 80% is a common acceptance criterion stipulated in the New Zealand standards [18] and has been adopted by many prominent researchers [1].

The maximum displacement, in the two directions of loading, was about five times the yielding displacement of the prestressing tendons. The skeleton (backbone) curve for the specimen was experimentally obtained and shown in **Figure 5b**. The anticipated bond slip of the reinforcement and prestressing tendons was considered while predicting the analytical skeleton curve. A good agreement between the analytical and the experimental skeleton curves was found (**Figure 5b**).

The flexural cracks were opened and closed, while almost no shear cracks were observed during the test. The hysteretic loops shown in **Figure 5a** show stiffness degradation and a change in stiffness during reloading which is known as pinching [19]. The pinching can be attributed to opening and closing of the cracks during the cyclic loading. Shear, which is generally responsible for the pinching of the load-deformation curve, was not the cause of the pinching.

Prestressed concrete members usually show marked elastic recovery even after considerable inelastic deformations, and thus leading to the occurrence of the pinching of the hysteretic loops. Energy dissipation capacities of the prestressed concrete members were less than those of reinforced concrete members because of the elastic recovery after considerable inelastic deformations.

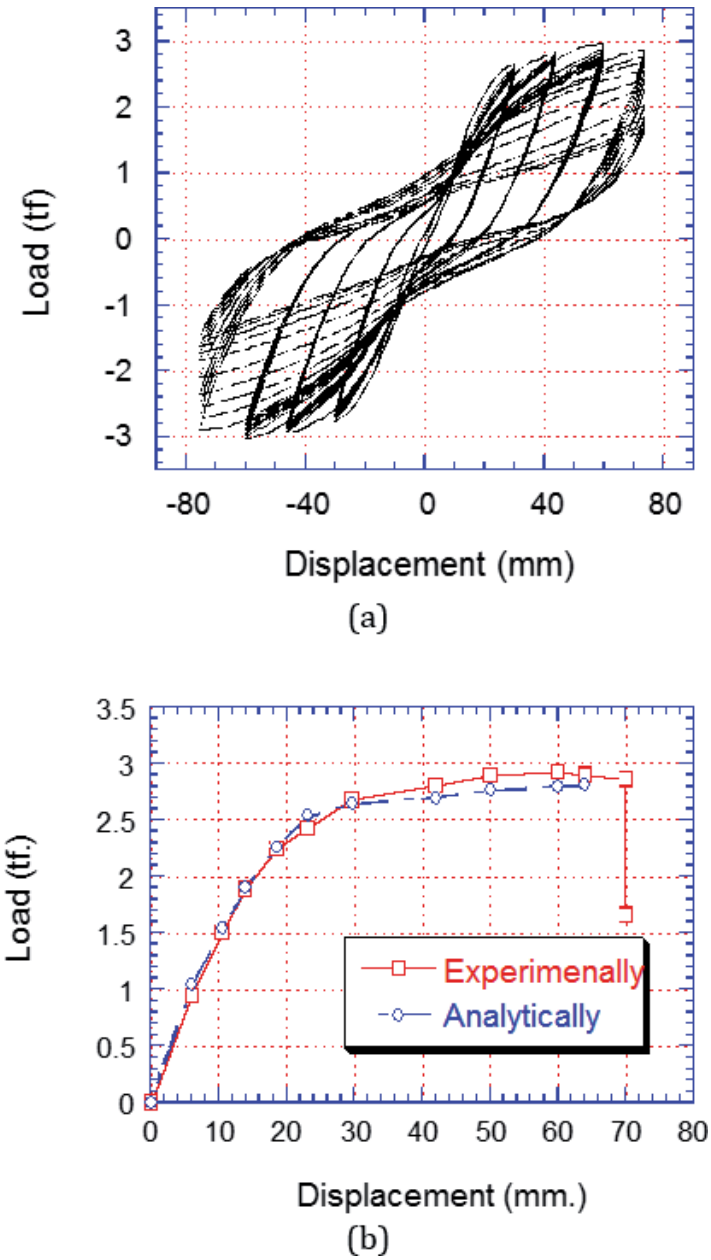

Figure 5.
Hysteretic load-displacement and backbone curves for specimen B-1 during the statically reversed cyclic loading test: (a) Hysteretic load-displacement curve; (b) experimental and analytical backbone curves.

Specimen B-1 was a partially prestressed concrete specimen, and therefore the pinching was not significant. Consequently, a higher energy dissipation capacity than that of a fully prestressed concrete member was attained. The hysteretic load-displacement curve (**Figure 5a**) shows a stable behavior with a comparatively minor strength enhancement.

At early stages of loading and until a displacement of three times the yield displacement of the PC tendons, the residual tensile forces in the PC tendons were adequate to close previously opened cracks. At a displacement equal to four times the yielding displacement of the PC tendon, the concrete compression strains in the plastic hinge

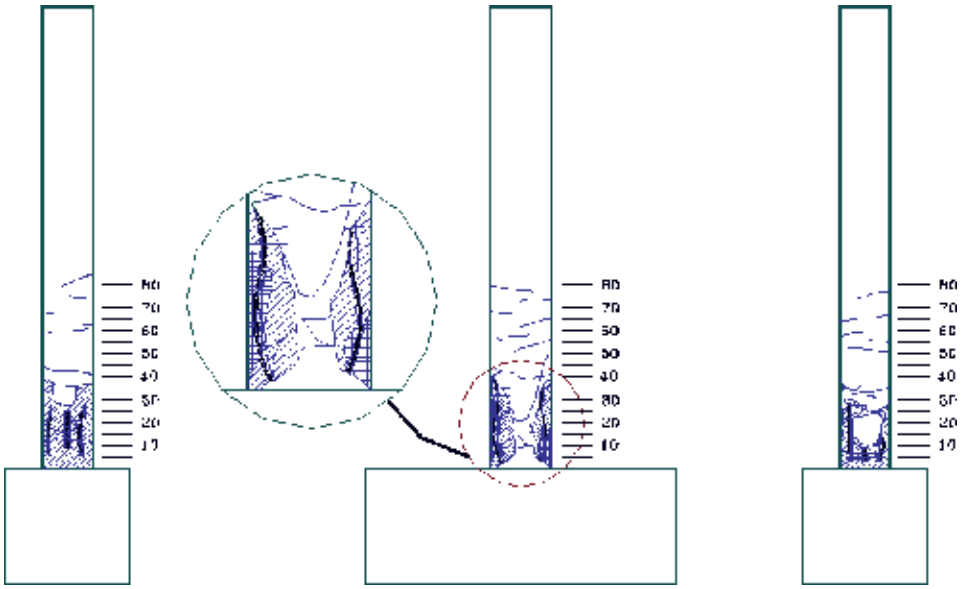

Figure 6.
Cracking pattern of specimen B-1 at the end of the statically reversed cyclic loading test (heights are given in centimeters).

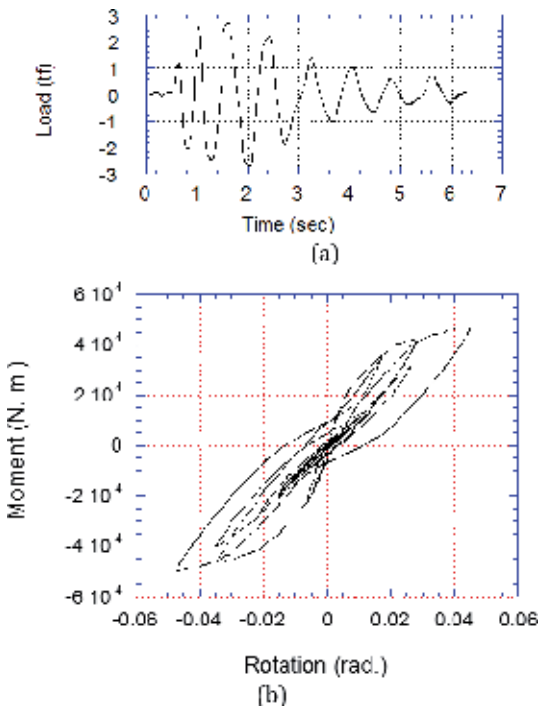

Figure 7.
Load-time history of the actuator and experimental hysteretic moment-rotation curve of the left end of the PC girder: (a) Load-time history of the actuator; (b) experimental hysteretic moment-rotation curve of the left end of the PC girder.

region exceeded the unconfined compression strain capacity, and concrete cover spalling was noticeable. Because of the existence of relatively close-spaced transverse hoops, crushing was delayed inside the concrete core as they act to restrain the lateral

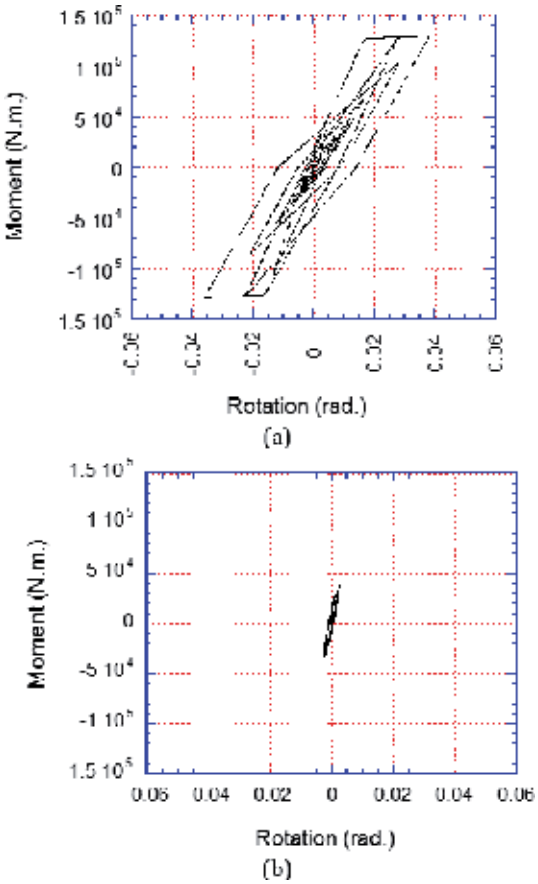

Figure 8.
Experimental hysteretic moment-rotation curves of the bottom and top ends of the RC column during the sub-structured pseudo-dynamic testing: (a) Experimental hysteretic moment-rotation curve of the bottom end of the RC column; (b) experimental hysteretic moment-rotation curve of the top end of the RC column.

compression of the concrete that accompanies the onset of crushing, thus maintaining the integrity of the concrete core. It was not until a displacement of five times the yield displacement when the crushing began to penetrate inside the core concrete due to the large number of repetitions of the cycles. Additionally, the reinforcing bars experienced large increase in the tensile strains and buckling after cover spalling in the plastic hinge region. The cracking pattern of specimen B-1 after the test is shown in **Figure 6**.

3.2 Sub-structured pseudo-dynamic test

The used time history of the actuator load during the test is shown in **Figure 7a**. The resulting hysteretic moment-rotation curve for the left end of the PC girder is shown in **Figure 7b**. Pinching of the hysteretic loops is clear in **Figure 7b**. A maximum rotation angle of 0.045 rad. was observed and, the figure also indicates a considerable damage of the PC girder due to the input excitation.

Figure 8a shows the hysteretic moment-rotation curve of the bottom end of the left column of the viaduct model. It can be noticed from the curve that a considerable damage occurred during the input excitation. A maximum rotation of 0.036 rad. was observed. **Figure 8b** shows the hysteretic moment-curvature curve of the top end of the left column of the viaduct model. It can be observed from the curve that limited energy was dissipated in the plastic hinge that was expected

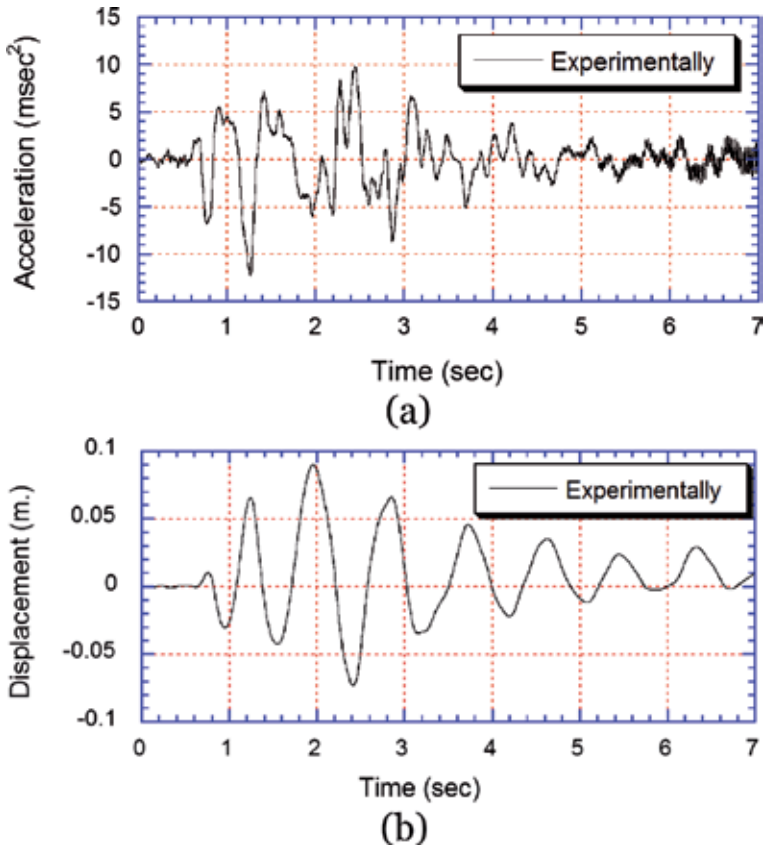

Figure 9.
Experimental acceleration time history and displacement time history during the sub-structured pseudo-dynamic testing: (a) Acceleration time history; (b) displacement time history.

to form at the top of the left column of the viaduct model. Similar results were obtained for the bottom and top ends of the right column of the viaduct model. A comparison between the hysteretic moment-rotation curves in **Figures 7b** and **8a** shows that not only the reinforced concrete column but also the PC girder may undergo extensive damage during an earthquake excitation. As a consequence, adequate care should be given to the PC girder design to satisfy the requirements of a seismic-resistant structure.

The time history of the response acceleration (**Figure 9a**) shows that the maximum observed acceleration was 12.2 m/sec^2 that occurred at a time equal to 1.25 second. The time and direction of the maximum acceleration were consistent with the time and direction of the maximum input ground acceleration (**Figure 4c**). The time history of the response displacement (**Figure 9b**) shows that the maximum displacement was 8.5 cm, which occurred at a time equal to 1.95 second.

4. Response analysis results

The results that were obtained from the reversed cyclic loading tests and the sub-structured pseudo-dynamic tests for the tested viaduct models show that not only the RC piers but also the PC girders may be damaged during earthquake excitations. This conclusion cannot be generalized without investigating to what extent changes in the viaduct model can influence the resulting response behavior and ductility

factor. A parametric study that includes parameters such as the yielding ratio (P_y/mg), the elastic natural period, and the strength ratio between the PC girder and the RC columns is required to verify the conclusion.

The accuracy of any parametric study is dependent on the accuracy of the available analytical hysteretic restoring force models for prestressed and reinforced

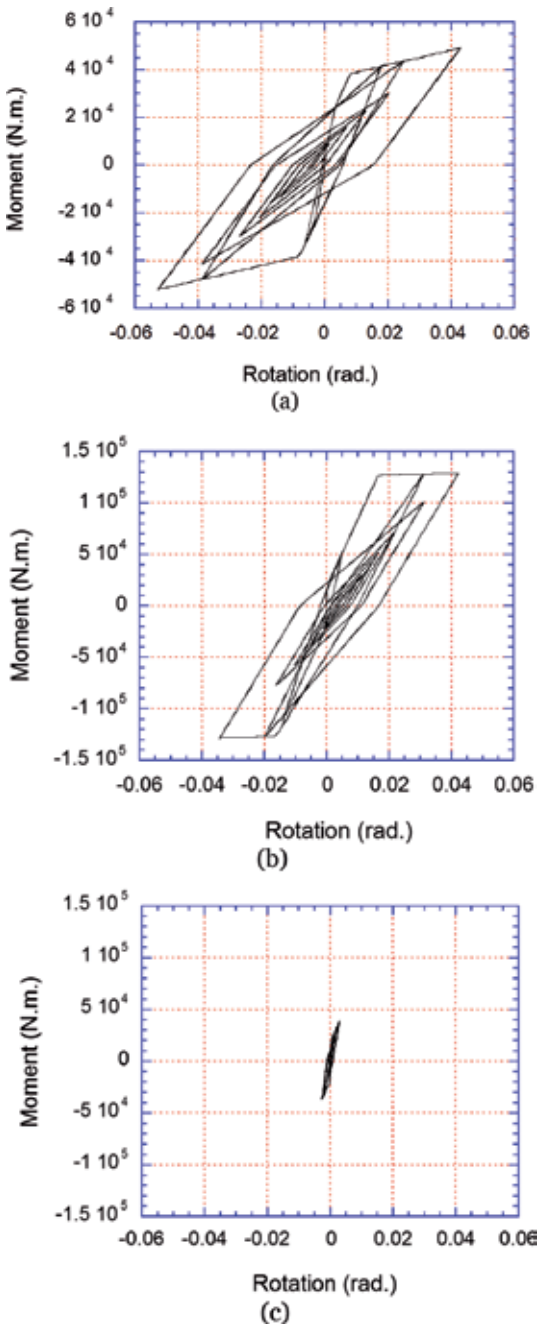

Figure 10.
Analytical hysteretic moment-rotation curve of the left end of the PC girder and the bottom and top ends of the RC column: (a) Analytical moment-rotation curve of the left end of the PC girder; (b) analytical moment-rotation curve of the bottom end of the RC column; (c) analytical moment-rotation curve of the top end of the RC column.

concrete members of the viaduct model. Therefore, response analyses were carried out for the same viaduct model that was tested using the sub-structured pseudo-dynamic test in the previous section. The response analysis results were compared with the experimental results of the sub-structured pseudo-dynamic test.

The one component model proposed by Giberson [11] was employed during the response analyses. Takeda's trilinear restoring force model was used for the RC columns, and the modified Takeda's model was used for the PC girders. The modified Takeda's model [7] accounts for the partial prestressing that was applied to the girders. Zatar et al. [20, 21] presented and verified the accuracy of another restoring force model for prestressed and partially prestressed members. The model by Zatar et al. incorporated modifications for Takeda's restoring force model.

Figure 10a shows the hysteretic moment-rotation curve analytically obtained for the left end of the PC girder. The maximum moment was -5.15×10^{-4} Nm, and the corresponding rotation was -0.043 rad.

Figure 10b and **c** shows the hysteretic moment-rotation curves for the bottom and the top ends of the RC column, respectively. Little energy was dissipated at the top end of the column. Conversely, considerable damage was observed at the plastic hinge that existed at the bottom end of the RC column. The maximum moment in the bottom end of the column was 1.3×10^5 Nm, and the corresponding rotation was -0.042 rad.

A comparison was made between the experimental and analytical hysteretic moment-rotation curves for the left end of the PC girder and for the bottom and

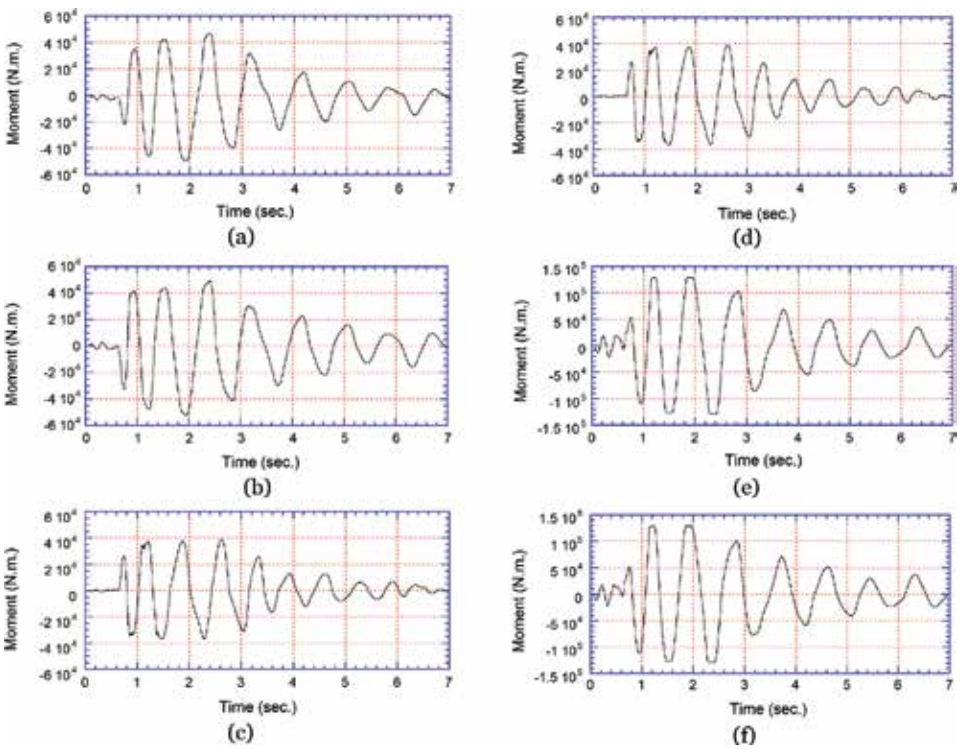

Figure 11.
Experimental versus analytical moment time history for the left end of the PC girder and the top and bottom ends of the RC column: (a) Experimental moment time history for the left end of the PC girder; (b) analytical moment time history for the left end of the PC girder; (c) experimental moment time history for top end of the RC column; (d) analytical moment time history for top end of the RC column; (e) experimental moment time history for the bottom end of the RC column; (f) analytical moment time history for the bottom end of the RC column.

the top ends of the RC column, respectively (**Figures 7**, **8**, and **10**). The comparison included the observed damage, the hysteretic behavior, the maximum moment, and the associated rotation. An overall good agreement was found between the sub-structured pseudo-dynamic test and the response analysis results. The unloading stiffness of the hysteretic moment-rotation curve of the PC girder that was obtained from the response analyses was different from the unloading stiffness that was found during the sub-structured pseudo-dynamic test. However, the total dissipated energy that was obtained from the response analyses was found to be almost similar to the experimentally dissipated energy during the excitation.

The moment time history curves that were obtained from the sub-structured pseudo-dynamic test for the left end of the PC girder and the bottom and the top ends of the RC column are shown in **Figure 11a**, **c** and **e**, respectively. The corresponding moment time history curves that were obtained from the response analyses are shown in **Figure 11b**, **d** and **f**, respectively. The comparison between the experimental and analytical moment time histories shows good agreement, thus verifying the accuracy of the used analytical hysteretic restoring force models for both the prestressed and the reinforced concrete members of the viaduct model. Consequently, the restoring force models can be further employed in a parametric study that includes the yielding ratio (P_y/mg), the elastic natural period, and the strength ratio between the PC girder and the RC columns. A parametric study that included these parameters is carried out in order to verify the study conclusions as well as to fully understand the response behavior of the viaduct structures during severe earthquake excitations. Because of space limitations, the results of the parametric study are not included in this paper. However, all the results can be found elsewhere [22].

5. Conclusions

The objective of this study was to clarify the inelastic response behavior of partially prestressed concrete girders of viaduct structures during severe earthquake excitations. A study that includes experimental and analytical phases was carried out. Small-scaled models were employed so as to represent actual viaduct structures. Specimens representing the PC girders of the viaducts were tested experimentally. Two testing techniques were employed in the experimental phase of the study. The first technique was a statically reversed cyclic loading test. The objective of the statically reversed cyclic loading test was to study the inelastic response behavior of the PC girders and to obtain the hysteretic-load deformational characteristics. The sub-structured pseudo-dynamic testing technique was implemented as the second testing technique. During the sub-structured pseudo-dynamic test, the PC girder was tested experimentally, and the RC columns of the viaduct structure were simulated analytically. Response analyses for the same viaduct model in terms of hysteretic moment-rotation curves and time histories were carried out. From the test results, it can be concluded that:

1. Not only the RC columns but also the PC girders are subjected to inelastic deformations that may cause a considerable damage during earthquake excitations. As a consequence, adequate care should be given to the PC girder design to satisfy the strength and ductility requirements of a seismic-resistant structure.

2. A comparison between the experimental and analytical results in terms of the resulting skeleton curves, time histories, hysteretic curves, and the dissipated energy was made. A good agreement between the experimental and analytical results was found. Therefore, the analytical model can be utilized

in further parametric studies that aim to fully clarify the response behavior of prestressed concrete viaduct structures.

3. A parametric study that is based on the calibrated hysteretic analytical restoring force model is conducted and shall result in having design guidelines for the partially prestressed concrete girders under earthquake excitations.

Acknowledgements

The author would also like to acknowledge the members of the structural laboratory at Saitama University who provided assistance during the experimental phase of the study. The author would like to acknowledge Dr. Hiroshi Mutsuyoshi, a structural engineering professor at Saitama University, for his valued assistance, full support, and appreciated comments.

Author details

Wael Zatar
Marshall University, Huntington, West Virginia, United States

*Address all correspondence to: zatar@marshall.edu

References

[1] Priestley MJN, Seible F, Calvi GM. Seismic Design and Retrofit of Bridges. New York: John Wiley & Sons Inc; 1996

[2] Harajli M, Naaman AE. Deformation and Cracking of Partially Prestressed Concrete Beams under Static and Cyclic Fatigue Loading. Report No. UMEE 84R1. Ann Arbor, Michigan: Department of Civil Engineering, the University of Michigan College of Engineering; 1984

[3] Zatar W, Mutsuyoshi H. Residual displacements of concrete bridge piers subjected to near field earthquakes. American Concrete Institute Structural Journal. 2002;**99**(6):740-749

[4] Zatar W, Mutsuyoshi H, Koizumi H. A restoring force model for partially prestressed concrete. Transactions of the Japan Concrete Institute. 1999;**21**:247-254

[5] Zatar W, Mutsuyoshi H. Earthquake Damage of Prestressed Concrete Viaduct Structures. International Association of Bridge and Structural Engineering (IABSE) Symposium of Long-Span and High-Rise Buildings, 1998

[6] Zatar W, Mutsuyoshi H. Dynamic response behavior of prestressed concrete viaduct under severe earthquake. In: Proceedings of the Workshop on Earthquake Engineering Frontiers in Transportation Facilities, Technical Report NCEER-97-0005. 1997

[7] Hosaka I, Mutsuyoshi H, Zatar W, Tanzo W. Behavior of concrete viaduct structures. Transactions of the Japan Concrete Institute. 1997;**19**:171-177

[8] Yamada Y, Iemura H, Tanzo W. Sub-structured hybrid loading of structural members under combined axial, shear, and bending loads. *8th Symposium of Earthquake Mechanics* in Japan. 1990. pp. 1503-1508

[9] Mutsuyoshi H, Machida A, Sadasue K, Oba S. Earthquake response behavior of first-level girder in R/C frame structure based on pseudo-dynamic test method. Transactions of the Japan Concrete Institute. 1992;**14**:289-296

[10] Mutsuyoshi H, Tanzo W, Machida A. Influence of member ductility on the total seismic response of RC piers using sub-structured pseudo-dynamic tests. Transactions of the Japan Concrete Institute. 1993;**15**:353-360

[11] Giberson MF. Two nonlinear beams with definitions of ductility. Journal of the Structural Division. 1969;**95**(2):137-157

[12] Otani S. Inelastic analysis of R/C frame structures. Journal of the Structural Division. 1974;**100**(7):1433-1449

[13] Ohta M. A study on earthquake resistant design for reinforced concrete bridge piers of single column type. Report of the Ministry of Construction Japan, 153; 1980

[14] Takeda T, Sozen MA, Nielsen NN. Reinforced concrete response to simulated earthquake. Journal of the Structural Division. 1970;**96**(12):2557-2573

[15] Preliminary Report on the Great Hanshin Earthquake, January 17, Proceedings of the Japan Society of Civil Engineers; 1995

[16] Ghasemi H, Otsuka H, Cooper JD, Nakajima H. Report on the Aftermath of the Kobe Earthquake. Vol. 60. United States Department of Transportation-Federal Highway Administration, TFHRC; 1996. p. 2

[17] Nakashima, Ishida, Ando. Numerical integration methods for substructure pseudo-dynamic test method. Transactions of the

Architectural Institute of Japan, Structural Engineering Series, No. 417, 1990, pp.107-117. (In Japanese)

[18] NZS 4203. New Zealand Standard, Code of Practice for General Structural Design and Design Loadings for Buildings. Standard Association of New Zealand; 1976. p. 80

[19] Saatcioglu M. Modeling hysteretic force-deformation relationship for reinforced concrete elements, earthquake resistant concrete structures, inelastic response and design. Journal, American Concrete Institute, ACI Special Publication. 1991;**127**(5):153-198

[20] Zatar W, Mutsuyoshi H. Logical on-line hybrid computer actuator and quasi-static testing schemes of PC columns. International Journal of Information Technology in Architecture, Engineering and Construction. 2003;**1**(3):209-224

[21] Zatar W, Mutsuyoshi H. Control of Residual Displacements of RC Piers by Prestressing. Washington D.C.: American Society of Civil Engineers (ASCE) Publication; 2001. ISBN: 0-7844-0553-0, Library of Congress Catalog Card No. 2001-018922

[22] Zatar W. Seismic Behavior of Prestressed Concrete Bridge Piers and Viaducts. D. Eng. Dissertation. Japan: Department of Civil and Environmental Engineering, Saitama University; 1999

Section 3

Grasping Response: Contending with Consequences

Chapter 9

Determinants of Coping Strategies to Floods and Droughts in Multiple Geo-Ecological Zones

Theobald Mue Nji and Roland Azibo Balgah

Abstract

Floods and droughts—the most frequent water-related hazards are negatively impacting livelihoods across the world, particularly in Sub-Saharan African countries, where poverty remains endemic. Naturally, victims adopt different coping strategies against burgeoning hydro-meteorological hazards. Contemporary research on determinants for coping decisions in SSA has been largely driven by isolated case studies, of little relevance for broad-based policy making. We analyze the determinants for coping with floods and droughts across multiple geo-ecological zones in Cameroon. Quantitative data primarily obtained from 2024 flood and drought household victims in the Western Highlands and Sudano-Sahelian Upland geo-ecological zones are analyzed alongside qualitative data obtained through 31 FGDs and 99 IDIs using descriptive statistics and regression analysis in MS Excel 2013 and SPSS 20 for the questionnaires and content analysis in Nvivo 11 for the unstructured interviews. Results reveal government policy, socio-cultural, economic and educational factors, and hazard experience as major shapers of coping decisions, irrespective of hazard type, timing and geo-ecology ($P = 0.05$). In contrast to the state-of-the-art, we observed livelihoods improvement after some hazardous events. The policy implications for long-term coping and resilience building are then discussed.

Keywords: determinants, coping strategies, hazards, floods and droughts, multiple geo-ecological zones, broad-based policy making

1. Introduction

Drought and flood-related disasters have been more devastating than other natural hazards (volcanoes, earthquakes, landslides, etc.), as far as deaths, sufferings and economical and cultural destructions are concerned. Apart from destructive direct effects, flood and drought events have been followed by secondary, indirect tragedies, such as famine, epidemics, fire, destruction of social networks, etc. [1]. Despite the progress in science and technology, man has remained very susceptible to extreme drought and flood events. Their escalation is facilitated by the continuous development of costly but inappropriate infrastructures, increase in population density, and a rather decrease in the buffering capacities (deforestation, urbanization, drainage wetlands, etc.). Understanding the way people in such areas, especially in SSA perceive these hazards, their experiences and interpretations

of patterns of occurrence, coping mechanisms, characteristic factors that drive household and community modus operandi when such anomalies strike are of great imperativeness for the design and implementation of household and community based strategies to curb the effects of floods and droughts; and build more resilient communities.

Bhavnani and colleagues for instance opine that droughts and floods alone account for up to 80% of the loss of life and 70% of the economic losses in SSA [2]. Frequent floods and droughts conditions have reduced the GDP growth of many African countries [1, 3, 4]; and have as well endangered their development advances [5]. Both water-related phenomena have direct and indirect impacts. Over the last 5 decades, floods and droughts have evolved to become major problems in SSA; causing depletion of assets, environmental degradation, impoverishment, unemployment and forced migrations [2, 5, 6]. Flood has been variously defined but for the purpose of this study we have operationally defined flood as a body of water which rises to overflow land which is normally not submerged [7, 8]. There are mainly five types of floods: river flood, flash flood, inland flood, storm surge, coastal flood [8, 9]. Floods are considered as one of the most frequent global hazards [10]. Floods account for approximately 40% of natural disasters and will possibly become more recurrent and severe due to global warming [11].

Unlike floods, droughts are characterized by a slow development, long duration, affects vast areas, and high severity [12]. Furthermore, droughts are expected to become more severe and frequent. This is expected to lead to more water demand, global climate change, and a limited water supply [13]. Based on the nature of water shortages, droughts can be classified into the following four types: meteorological, hydrological, agricultural, and socioeconomic [14]. Among these types, meteorological droughts occur more frequently and regularly than the other three drought types and normally trigger other types of droughts [13].

Floods and droughts are now the most frequent types of major disasters. The impacts of climate change are likely to increase their occurrence as they happen to be the most frequent types of major disasters nowadays especially in SSA. In the era of climate change, the reliability on predictability in rainfall patterns has been reduced significantly [15]. The frequency and severity of weather-related events such as floods and droughts have increased unpredictably and shall continue over time.

Cameroon is one of the SSA countries most hit by these climatic extreme anomalies. It is a country in Equatorial Africa, located on the Gulf of Guinea in Central Africa. It lies between latitude 1°40′ and 13°05′ north and between longitude 8°30′ and 16°10′ east; its area is 475, 412 km^2. Cameroon's beauty and relevance in SSA stems from her extremely diversified landscapes, rich natural resources (petroleum, bauxite, timber and many tropical crops), cultural and ethnic diversity and a multiplicity of climatic and geomorphologic zones. It is not surprising therefore that Cameroon has been nicknamed *Africa in Miniature*.

Cameroon's geo-physical location, tectonic history and climate makes her one of the most susceptible countries affected by natural hazards in Africa. The regularity and devastation caused by such hazards along the active Cameroon Volcanic Line (CVL) are becoming more frequent and even more disastrous, affecting livelihood assets including human, social, financial, natural, physical capital [10, 16]. The country is becoming more prone to and persistently hit by floods and droughts but also by mud flows, rock fall, lahars, volcanic eruptions, toxic gas emissions, earth tremors and landslides which occur on a regular annual pattern.

Despite her diversity and abundant natural resources, Cameroon is also a victim of several hazards and disasters which have accompanied global climate change. Average temperatures have risen since 1930 [17] and average rainfall has reduced by

more than 2% per decade since 1960 [17]. Projected changes in rainfall range from −12 to +20 mm per month (−8 to +17%) by the 2090s [18]. Furthermore, average annual temperatures are predicted to increase between 1.5° and 4.5° by 2100, with a 1.6° to 3.3° rise in coastal zones; and a 2.1° to 4.5° rise in the Sudano-Sahelian region [17]. Average rainfall is predicted to continue to decrease, leading to a prolonged dry season in the Sudano-Sahelian ecological zone. Desert conditions are expected to dominate this area by 2100. It is predicted that Lake Chad will be nearly completely dried up by 2060 [19].

IPCC has established that a 2° rise globally will result in a sea-level rise of between 69 cm and 1 m across the world [20]. Cameroon, given its location along the coast is also expected to experience the impacts of sea level rise over the next century. The above-mentioned statistics indicate that Cameroon is highly vulnerable to floods and droughts. Tiefenbacher et al. [21] have argued that such vulnerability presents a serious threat to the development of the leisure sector and in this case would pose serious problems in attaining sustainable development and generates new challenges for achieving the SDGs; and jeopardizes progress already made. The analysis of climate variability impacts in Cameroon indicates consequences in almost all sectors of development, with huge negative impacts on livelihoods especially at household level [19, 22].

Burgeoning floods and droughts are expected to inflict adverse effects on many Cameroonian households, given their heavy reliance on agriculture for livelihoods dependence of most households on agriculture [23]. Current agricultural contribution to the country's GDP could drop by 14% points from 20% now to an estimated 6% in 2025 [16, 22, 24]. This drop will resolve mainly from increased desertification (drought) in the north and higher incidence of flooding in the south and in the north of the country.

A fundamental step towards reducing the effects of floods and droughts in Cameroon lies in identifying risk management strategies whose validity supersedes specific geo-ecological zones [16, 24]. In this paper we therefore undertake the agency to understand the array of household determinants of coping with the threats of floods and droughts, the shapers of the peoples' perceptions, interpretations and experiences to these risks within their daily lives and how all of these tend to shape the way they respond to the threats presented by floods and droughts in their households across the western highlands and the Sudano-Sahelian geo-ecological and socio-cultural areas of Cameroon with the intention to identify drivers that are robust over space and time.

2. Study area and population, data collection and analysis

2.1 Study area

Cameroon is characterized by five geo-ecological zones with varied landscapes and climates. These are described as Zone I (Sudano-Sahelian); Zone II (High Guinea Savannah); Zone III (Western Highlands); Zone IV (Humid Forest with monomodal rainfall pattern); and Zone V (Humid Forest with bimodal rainfall pattern) [25] (**Table 1**).

The current study was carried out in two of the 5 geo-ecological zones; the Sudano-Sahelian upland and the Western highlands. The Sudano-Sahelian zone is located between latitude 7 and 13° north thus covering more than 21% of the national territory. It has a rippling relief with plateaus that have varying altitudes between 500 and 1000 m and plains with altitudes ranging from 200 to 300 m. The area is also characterized by mountains and flood valleys. In addition to the

SN	Geo-ecological zones	Regions	Surface areas (km^2)
I	Sudano-Sahelian Upland	North and Far North	100,353
II	High Guinean savannah	Adamawa Region, Mbam Division and Lom and Djerem Division	123,077
III	Western Highlands	West and North West	31,192
IV	Humid Rainforest with monomodal rainfall pattern (maritime coast)	Littoral and South West Regions	45,658
V	Humid Forest with bimodal rainfall pattern (Tropical forest)	Centre, South and East Regions	165,770
Total			466,050

Table 1.
Cameroon geo-ecological zones and surface areas.

geographical position of the zone, it has a distinctively dry climate as compared to the rest of the country with a single and short rainy season of about 4 months reaching its peak in August and a very severe and lengthy dry season of up to 7 months or more as one progresses up north from the Mandara Mountains. The annual mean rainfall ranges from 400 mm in the northern part to 1100 mm in the southern part of the zone with an average temperature of up to 28° [25].

On the other hand, the Western Highlands is located between latitudes 5°40′ and 7° north and between longitudes 9°45′ and 11°10′ east. The zone is characterized by relief of massifs and mountains. It features several dormant volcanoes, including Mt. Oku and Mt. Bamboutos. A cool temperate-like climate, influenced mainly by mountainous terrain and rugged topography also characterizes the region. Average rainfall is about 2400 mm, temperatures averaging between 23 and 32° [19]. There are two main seasons; the rainy season which starts from mid-March and ends in mid-November and dry season from Mid-November to mid-March. The dry season is characterized by the harmattan with dry air. Forests once largely covered the Western Highlands but because of the influence of anthropomorphic activities the forests were progressively cleared for farmland and grazing, and today, only patches remain. Although small, these patches are recognized as globally important sites for conservation.

2.2 Study population

Study participants were limited to the study areas; were of both sexes (male and female), aged 20 years and above and had been in the area for at least 10 years; and must have witnessed at least one flood and/or drought event. Data were collected from flood victims in 14 communities of the Western Highlands; and 17 drought-only communities, and 10 floods and droughts affected communities in the Sudano-Sahelian geo-ecological zone.

2.3 Data collection

Three Social Science instruments were used for data collection to ensure accurate and reliable data in order to attain the study objective. The combined approach was used in collecting the data. Three instruments (individual questionnaires, Focus Group Discussion (FGDs) guides and In-depth interview guides) were employed in collecting both quantitative and qualitative data to investigate the research question.

2.4 Individual questionnaire

This was a structured questionnaire used to collect quantitative data from 2024 different floods and droughts household heads or their representatives. It was developed to understand victims' perceptions and to identify the factors that influence their adoption of specific coping strategies in situations of floods and/or droughts. Socio-demographic information was collected as well. Questionnaires were administered to respondents on a face to face basis after obtaining their consent. We had two sets of questionnaires designed for the purpose of this study: one for floods victims and the other for drought victims.

2.5 Focus Group Discussions (FGDs) and In-depth Interviews (IDIs)

To generate qualitative data, 31 FGDs and 99 IDIs were conducted in different floods and droughts communities with household members to capture the general opinion and perception of household members on the hazards and disasters, the consequences of such phenomena in their households and the determinants of their preferred coping strategies. We also sort to understand how experience, cultural factors and location within a certain geo-ecological zone could influence the adoption of formal or informal coping strategies. The data collection instruments in this case were also designed separately to distinctively collect data for droughts and floods.

2.6 Data analysis

All quantitative data generated from the questionnaires were entered into a template designed in the Statistical Package for Social Sciences (SPSS version 20.0) (IBM Corp., Armonk, NY, USA). The data were cleaned and later on analyzed using both SPSS and Microsoft Excel 2013.

For qualitative data (FGDs and IDIs), they were recorded in the field using dictaphones (voice recorder) and later on transcribed and typed into a word processing program (Microsoft Word 2013). The transcribed data were analyzed using Nvivo version 11, and themes were established in relation to research objectives. This was to ensure a standardized analysis and interpretation of the qualitative data generated across tools.

3. Results and discussions

3.1 Socio-economic description of sampled population

This section presents and discusses the socio-economic characteristics of the sample. The discussions are done by comparing results from the Sudano-Sahelian region with those from the Western Highlands. It is worth mentioning that the distribution of respondents across geo-ecological zones indicates that 60% of the from the Sudano-Sahelian zone while 40% was from the Western Highlands. In addition, the sample comprises of victims of both droughts and flood events (45.2% drought victims, 40.7% flood victims and 14.1% both drought and flood victims). More so, while all the respondents in the Western Highlands were flood victims, in the Sudano-Sahelian region, only 0.7% of the respondents witnessed floods alone. 75.7% of the respondents were drought victims, 23.6% had witnessed both droughts and floods.

3.2 Education

In general, most of the respondents had attained only primary level of education (65%), seconded by those with secondary level education (21.9%), third by those with no formal education (7.2%) and lastly by those with High school level of education (5.9%). The results are presented in **Table 2**.

Most respondents had attained only primary school education, irrespective of geo ecological zone. This amounted to 69.8% of droughts victims, 55.6% of flood victims and 81% of both flood and drought victims in the Sudano-Sahelian region ($P < 0.001$); and 54% of the flood victims in the Western highlands.

3.3 Sex

Over 60% of the entire sample are male, while <40% are female. The distribution in the different geo-ecological zones is presented in **Figure 1**. In the Sudano-Sahelian region, the males also had the higher proportion as compared to the females among those who witnessed droughts (69.1 and 30.9% respectively, $P = 0.085$) and those who witness both floods and droughts (63.9 and 36.1% respectively, $P = 0.085$). The Sudano-Sahelian region is in the northern part of Cameroon and most of the people here a Muslims living in a closed society. Access to women is generally more challenging than is the case for men. Interestingly, the majority of those who witnessed floods in the Sudano-Sahelian region were females (55.2 and 44.8% respectively, $P > 0.05$). This stems from the fact that women are the ones mostly involved in farming activities and fetching of water thereby exposing them to the daily realities of the environment. In the Western Highlands, majority of the respondents were males (55.2%) as compared to 44.8% who were females.

3.4 Marital status

The distribution in the entire sample according to the marital status of the respondents showed that majority of them were married (76.1%) while 17.7% were still single. In addition, while 4.8% of the respondents were widow(ers), a very small proportion of the respondents (1.3%) had divorced their spouses. Results from the geo-ecological zones are presented in **Table 3**. These are traditional societies where both boys and girls marry very young and divorce is almost viewed as a taboo. Since it is considered that a woman is married to a family, she is generally considered stilled married to the successor of her husband even after the dead of her real husband. Moreover, men generally remarry upon the dead of their wives because the wives facilitate their household chores which men are essentially not familiar with.

Geo-ecological zone	Disaster type	Primary (%)	Secondary (%)	High school (%)	No formal education (%)	X^2 (*P*-value)
Sudano-Sahelian	Drought	69.8	18.8	3.4	8	32.423 ($P < 0.001$)
	Floods	55.6	22.2	0	22.2	
	Both	81	6	2.1	10.9	
Western Highlands	Floods	54	31.1	10.1	4.8	11.547 ($P < 0.001$)

Table 2.
Educational attainment of respondents.

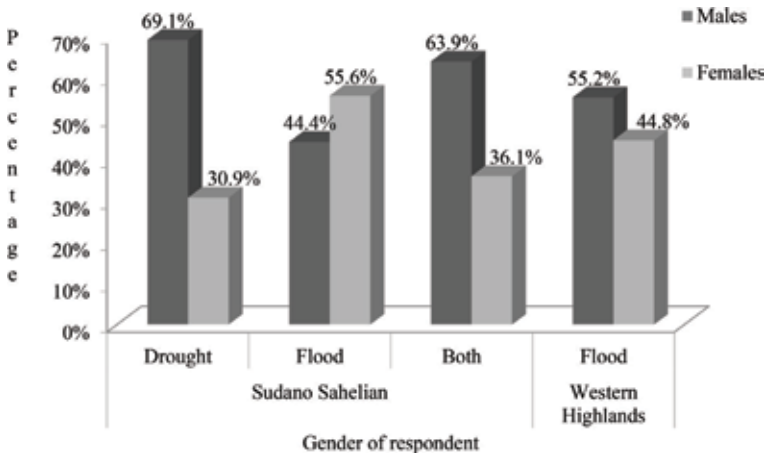

Figure 1.
Sex distribution of respondents.

Geo-ecological zone	Disaster type	Divorced (%)	Married (%)	Single (%)	Widow(er) (%)	Chi-square
Sudano-Sahelian	Drought	0.8	81.9	15.3	2.2	4.6841, $P = 0.585$
	Floods	0.7	77.8	22.2	0.0	
	Both	0.4	86.7	11.2	1.8	
Western Highlands	Floods	1.8	66.4	0.2	22.7	10.308, $P > 0.05$

Table 3.
Distribution according to marital status.

The results indicate that majority of the respondents in both geo-ecological zones as well as for the different disasters were married (66.4% in the Western Highlands and 81.7% for drought, 77.8% for flood and 86.7% for both flood and drought victims in the Sudano-Sahelian region, $P > 0.05$).

3.5 Main occupation

As a livelihood source, most of the respondents were involved in farming activities to sustain their families (60%). However, while 32.1% were business persons, 8.8% of the respondents had salaried jobs. The comparative analysis as presented in **Figure 2** also show that most of the respondents rely on farming for their household livelihoods (56.7% in the Western Highlands and 67.9% for drought and 77.8% for flood victims in the Sudano-Sahelian region, $P = 0.001$).

For those who witness both floods and droughts, the majority of them were found to rely on their respective businesses for their livelihoods (52.4%) as compared to 43.7% who rely on farming.

3.6 Religious affiliations

In our sample, only a slight difference was observed between Christians and Muslims (48.1 and 48.4% respectively). However, a small proportion of the respondents (3.5%) were African Traditionalists. **Figure 3** presents the distribution in the two geo-ecological zones.

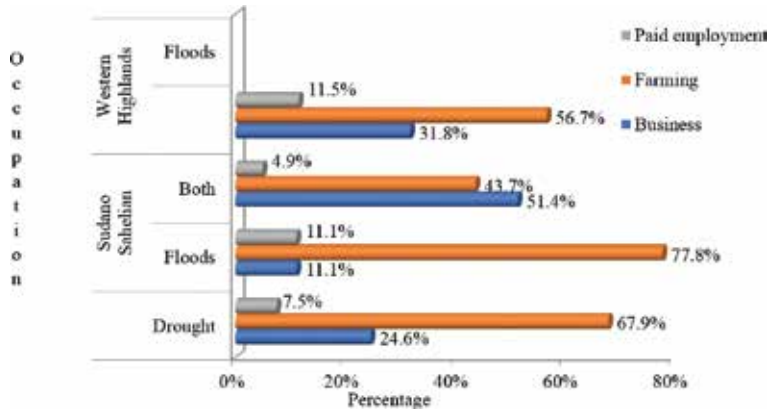

Figure 2.
Main occupation of respondents.

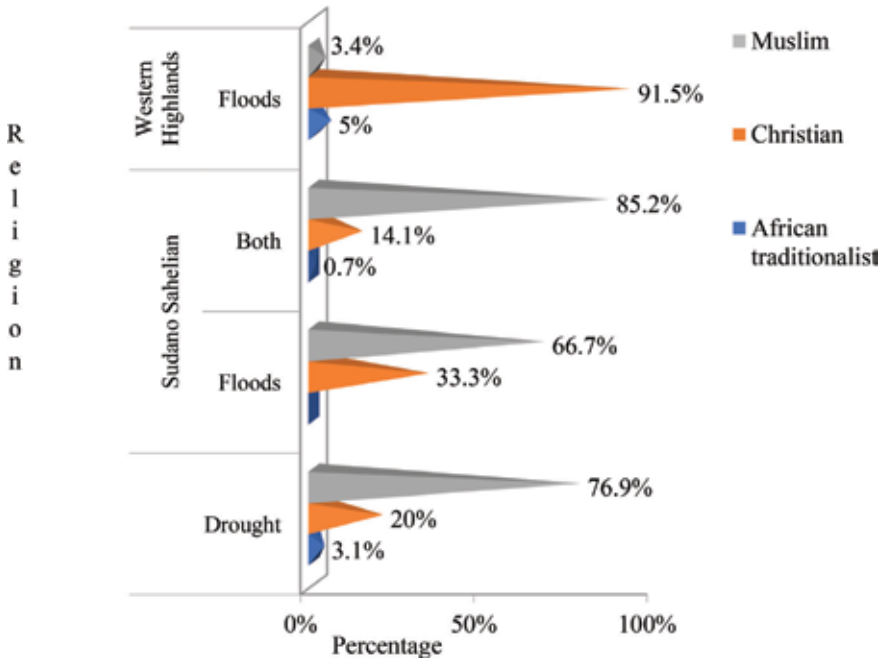

Figure 3.
Religious affiliation of respondents.

From **Figure 3**, we can infer that most of the victims in the Western Highland region are Christians (91.5%). On the contrary, majority of the respondents in the Sudano-Sahelian region for all disaster types were Muslims (85.2% for both drought and flood victims, 66.7% for flood victims and 76.9% for drought victims, $P = 0.02$). This is logical as the Western highlands and the Sudano-Sahelian Zones are both Christian and Muslim communities respectively. More description of the sample population has been presented in **Table 4**.

It can be inferred from **Table 3** that the age of the respondents was significantly higher among respondents in the Sudano-Sahelian zone than those in the Western Highlands (45.41 ± 16.617 years and 43.4 ± 13.739 years respectively, $P = 0.004$). Similar result was also observed with respect to the number of years the respondents have been living in their communities, as it was significantly higher among

Geo-ecological zone	Variable	Sample mean	Disaster type	Mean	Std. dev	Std. error
I	Age/years	45.41**	Floods	43.22*	22.532	7.511
			Droughts	44.13*	16.757	0.554
			Both	49.59*	15.284	0.905
	Number of years living in the village	26.35***	Floods	28	8.139	2.713
			Droughts	25.16	11.99	0.396
			Both	30.14	8.922	0.529
	Total household size	7.41	Floods	8.33	3.122	1.041
			Droughts	7.6	2.933	0.097
			Both	6.77	2.444	0.145
	Income before disaster/FCFA	64,990***	Floods	87,780	125,300	41,770
			Droughts	66,950	72,440	2390
			Both	57,975	46,650	2760
	Income after disaster/FCFA	34,050***	Floods	46,330	75,290	25,090
			Droughts	32,290	48,220	1590
			Both	26,480	23,930	1420
II	Age/years	43.40**	Floods	43.40*	13.739	0.481
	Number of years living in the village	24.5***	Floods	24.5	11.575	0.405
	Household size	7.62	Floods	7.62	3.024	0.106
	Income before disaster/FCFA	113,390***	Floods	113,390	173,040	6060
	Income after disaster/FCFA	63,670***	Floods	63,670	95,555	3350

**Significant at 10% level.*
***Significant at 5% level.*
****Significant at 1% level.*
I = Sudano-Sahelian; II = Western Highlands.

Table 4.
Age, household size, years in the community and income of respondents.

respondents in the Sudano-Sahelian zone than those in the Western Highlands (26.35 ± 11.507 years and 24.5 ± 11.575 years respectively, $P = 0.001$). On the other hand, the estimated household income before and after the disasters were significantly higher among the respondents in the Western Highlands over those from the Sudano-Sahelian zone (FCFA113, 390 and FCFA64, 990 respectively before, $P = 0.001$ and FCFA63, 670 and FCFA34, 050 respectively after, $P = 0.001$). Only the total household size was found not to differ significantly between the two geo-ecological zones (7 ± 3 persons for the Sudano-Sahelian and 8 ± 3 persons for the Western Highlands, $P = 0.105$). Details across the different disaster types have also been provided in **Table 3**.

3.7 Characteristics of floods and droughts in the study areas

This sections first of all looks at the number of times the respondents have witness disaster events in the last decade, before exploring their perceptions with respect to

damage of the disasters as well as the severity of the damage. From **Table 5**, we can infer that more floods have been witnessed in the last decade in the Sudano-Sahelian Zone than in the Western Highlands (5 and 3 respectively, $P < 0.001$).

These disasters are known to bring about damages to the asset portfolio of their victims. Presented in **Table 6** are some of the negative impacts of the disasters faced by the victims both at household and community levels. The results show mix impacts. For instance while damage to natural environment and livestock at the household level was higher in the Sudano-Sahel region than in the Western Highlands (reported by 91 and 43.8% respectively) loss of property was higher in the Western Highlands than in the Sadano-Sahel region (reported 72.6 and 59.9% respectively).

For the Sudano-Sahel region, the highest three damages are incurred through increase in sickness and diseases (reported by 96.9%), destruction of crops (reported by 93.4%) and damage to natural environment and livestock (reported by 91%). For the Western Highlands, the highest three damages are incurred through the destruction of crops (reported by 97.3%) increase in sickness and diseases (reported by 93.7%) and damage to ancestral links (reported by 89.1%). Details of these as well as the perceptions with respect to damages at the community level can be obtained from **Table 5**.

3.8 Severity of disaster damage

Base on the level of damage experienced by each household, the respondents provided information on the severity of the damages caused by the disasters both at household and community levels. The results have been summarized in **Figures 4** and **5**.

At the household level, a significantly higher proportion of the victims from the Sudano-Sahel region acknowledged the severity of the damage from the disasters to be very high than those from the Western Highlands (74.2 and 30.2% respectively, $P < 0.001$). On the other hand those who said the severity of the damage was high was significantly higher in the Western Highlands than in the Sudano-Sahelian region (36.4 and 13.4% respectively, $P < 0.001$).

The results at the community level with respect to the severity of the damages caused by the disasters are similar with those at the household level. For instance just as was the case at the household level, at the community level a significantly higher proportion of the victims from the Sudano-Sahelian region acknowledged the severity of the damage from the disasters to be very high than those from the Western Highlands (71.8 and 28.6% respectively, $P < 0.001$). Similarly, a significantly higher proportion of those who said the severity of the damage was high was from the Western Highlands than in the Sudano-Sahelian region (39.8 and 13.5% respectively, $P < 0.001$).

Disaster	Geo-ecological zone	Mean	Std. deviation	Std. error mean	F-test
Both	Sudano-Sahelian	6.68	1.300	.077	Not applicable
Drought	Sudano-Sahelian	5.99	2.917	.096	Not applicable
Flood	Sudano-Sahelian	4.89	3.060	1.020	0.000
	Western Highlands	3.43	1.615	.057	

Table 5.
Number disasters faced in the last 10 years.

Asset	Geo-ecological zone	Household level		Community level	
		No (%)	Yes (%)	No (%)	Yes (%)
Damage to natural environment and livestock	Sudano-Sahelian	9	91***	8.1	91.9***
	Western Highlands	56.2	43.8***	19.4	80.6***
Loss of human life	Sudano-Sahelian	98.2**	1.8	90.9	9.1
	Western Highlands	97.5*	2.5	92.3	7.7
Loss of property	Sudano-Sahelian	40.1	59.9***	17.7	82.3**
	Western Highlands	27.4	72.6***	21.1	78.9**
Destruction of crops	Sudano-Sahelian	6.6	93.4***	0	100
	Western Highlands	2.7	97.3***	0	100
Destruction of public infrastructure	Sudano-Sahelian	31	69*	0	100
	Western Highlands	33.5	66.5*	0	100
Destruction of worship grounds	Sudano-Sahelian	50.8	49.2	39.5	60.5***
	Western Highlands	36.6	63.4***	7.9	92.1***
Damage to ancestral links	Sudano-Sahelian	39.7	60.3***	71.1***	28.8
	Western Highlands	10.9	89.1***	36.8	63.2
Physical injury	Sudano-Sahelian	61.2	38.8***	19.9	80.1
	Western Highlands	79***	21	17.8	82.2
Increase in sickness and diseases	Sudano-Sahelian	3.1	96.9**	8	92***
	Western Highlands	6.3	93.7**	14.4	85.6***

*Significant at 10% level.
**Significant at 5% level.
***Significant at 1% level.

Table 6.
Analysis of perceptions of damages caused by disasters.

3.9 Disaster management strategies adopted by respondents

This section presents the different strategies explained to be used by the respondents following disasters and especially the last event. As presented in **Table 6**, there were some similarities as well as differences in the disaster management strategies employed by the respondents in the Sudano-Sahelian and Western Highlands regions both at household and community levels. For instance it can be inferred that the respondents in both geo-ecological zones did not rely very much on insurance (0% all round) and borrowing from the Bank (1.6% for Sudan-Sahel and 1.3% for Western Highlands at household level and 0% for Sudan-Sahel and 1% for Western Highlands at community level). On the other hand, they reduced their household savings (94.5% for Sudano-Sahelian and 99.1% for Western Highlands at household

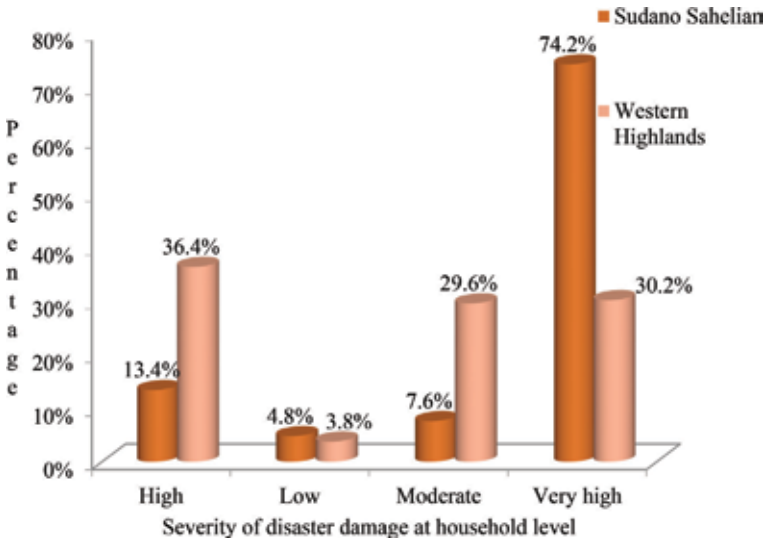

Figure 4.
Severity of damage at household level.

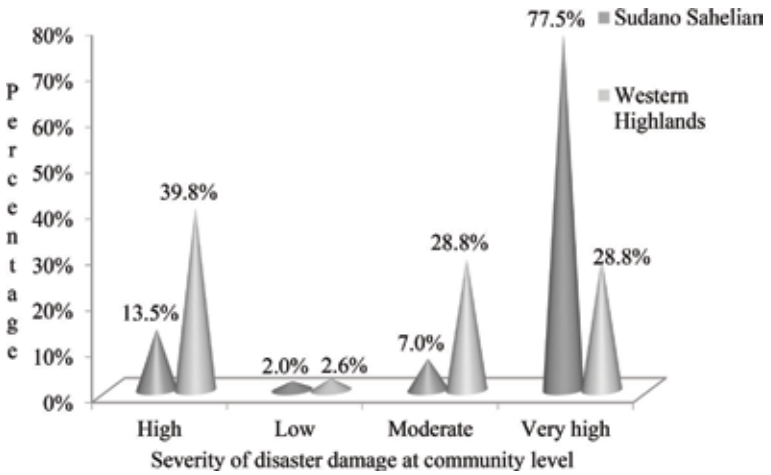

Figure 5.
Severity of damage at community level.

level and 98.1% for Sudano-Sahelian and 98.5% for Western Highlands at community level), rely on stored food (80.3% for Sudano-Sahelian and 87.2% for Western Highlands at household level), and also rely heavily from help from friends and relatives (77.6% for Sudano-Sahelian and 83.6% for Western Highlands at household level and 62.3% for Sudano-Sahelian and 61.6% for Western Highlands at community level). Details of these and more are presented in **Table 7**. It is worth mentioning that of all the strategies captured, only insurance premiums was not used by any of the respondents in the study area.

Presented in **Figure 6** is a summary of the above captured strategies. It can be observed from **Figure 6** that the respondents in both the Sudano-Sahelian Region and the Western Highlands adopted and implemented mainly informal disaster management strategies in order to cope with the negative effects of the disasters (95.6 and 98.9% respectively, $P < 0.001$).

Strategy	Geo-ecological zone	At household level (%)	At community level (%)
Borrow money from Bank***	Sudano-Sahelian	1.6	0
	Western Highlands	1.3	1
Borrow from neighbors***	Sudano-Sahelian	48.2	0.1
	Western Highlands	68.7	19.4
Relocation***	Sudano-Sahelian	40.3	41.9
	Western Highlands	56.6	52
Assembled at central location***	Sudano-Sahelian	30.8	33.2
	Western Highlands	3.6	0
Evacuated by the government***	Sudano-Sahelian	11.8	24.9
	Western Highlands	11.4	3.6
Got help from NGOs***	Sudano-Sahelian	44.2	63.9
	Western Highlands	31.2	44.9
Reduce household savings***	Sudano-Sahelian	94.5	98.1
	Western Highlands	99.1	98.5
Receive help from social groups***	Sudano-Sahelian	39	19.4
	Western Highlands	80.9	49.9
Receive help from Church*	Sudano-Sahelian	8	53.2
	Western Highlands	10.1	49.9
Receive help from friends and relatives**	Sudano-Sahelian	77.6	62.3
	Western Highlands	83.3	61.6
Receive help from Central government***	Sudano-Sahelian	66.5	0
	Western Highlands	17.5	0.2
Receive help from individuals***	Sudano-Sahelian	12	0.2
	Western Highlands	64.7	21.1
Insurance support	Sudano-Sahelian	0	0
	Western Highlands	0	0
Received free medication***	Sudano-Sahelian	67	51.8
	Western Highlands	12.1	25.3
Sold family labor***	Sudano-Sahelian	10.1	69.4
	Western Highlands	27.3	92.4

Strategy	Geo-ecological zone	At household level (%)	At community level (%)
Sold household assets***	Sudano-Sahelian	66	0.1
	Western Highlands	74.2	18.7
Sold household livestock***	Sudano-Sahelian	82.2	0.1
	Western Highlands	36	21.5
Rely on stored food***	Sudano-Sahelian	80.3	0.1
	Western Highlands	87.2	17.1
Building of embankment***	Sudano-Sahelian	62.4	0.4
	Western Highlands	6.1	48.7

*Significant at 10% level.
**Significant at 5% level.
***Significant at 1% level.

Table 7.
Disaster coping strategies.

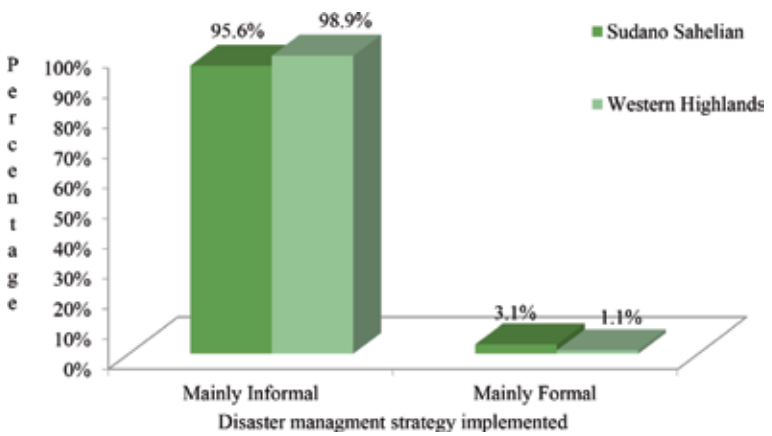

Figure 6.
Main disaster management strategy used by respondents.

We also analysed to identify trends in similarities and differences in the disaster management strategies employed by the respondents from the different disasters faced. The results have been presented in **Table 7**. Mixed results were also observed here at the household and community levels. For instance the distribution according to insurance (0% all round) show that the respondents did not rely very much on it irrespective of the disaster faced. On the other hand, the distribution in terms of reduced household savings indicate strong reliance among the victims of the different disasters (98.9% for flood victims, and 97.5% for drought victims and 100% for both floods and drought victims at the household level, 99.2% for flood victims, and 93.9% for drought victims and 96.5% for both floods and drought victims at community level). Another important strategy used by the disaster victims is to rely heavily on help from friends and relatives (83.3% for flood victims, and 71.8% for drought victims and 96.1% for both floods and drought victims at the household level, 61.4% for

Strategy	Disaster type	At household level (%)	At community level (%)
Borrow money from Bank**	Floods	1.3	1
	Droughts	2.1	0
	Both	0	0
Borrow from neighbors***	Floods	68.8	19.2
	Droughts	62.6	0
	Both	1.1	0.4
Relocation***	Floods	51.6	47.9
	Droughts	25	43.4
	Both	96.8	0
Evacuated by the government***	Floods	11.5	4
	Droughts	15.2	32.5
	Both	0.7	0
Got help from NGOs***	Floods	31.3	45.3
	Droughts	38.3	57.7
	Both	63.2	83.9
Reduce household savings**	Floods	98.9	99.2
	Droughts	97.5	93.9
	Both	100	96.5
Receive help from social groups***	Floods	80.6	49.8
	Droughts	44.8	24.5
	Both	20	2.8
Receive help from Church	Floods	10.1	50
	Droughts	10.2	52.9
	Both	1.1	54.7
Receive help from friends and relatives***	Floods	83.3	61.4
	Droughts	71.8	62.4
	Both	96.1	62.5
Receive help from Central government***	Floods	17.8	0.2
	Droughts	57.6	0
	Both	95.8	0
Receive help from individuals***	Floods	64.2	21.1
	Droughts	14.9	0.2
	Both	2.5	0
Insurance support	Floods	0	0
	Droughts	0	0
	Both	0	0
Received free medication***	Floods	12.6	25.7
	Droughts	58.1	47.4
	Both	95.8	65.3

Strategy	Disaster type	At household level (%)	At community level (%)
Sold family labor***	Floods	26.9	92
	Droughts	13.1	75
	Both	0.7	51.9
Sold household assets***	Floods	74	18.4
	Droughts	56.4	0
	Both	97.2	0.4
Sold household livestock***	Floods	36.3	21.2
	Droughts	77.5	0
	Both	97.9	0.4
Rely on stored food***	Floods	80.3	17.1
	Droughts		0
	Both	87.2	0.4
Building of embankment***	Floods	6.7	48.2
	Droughts	53.6	0.5
	Both	91.2	0

**Significant at 5% level.
***Significant at 1% level

Table 8.
Disaster management strategies adopted by disaster type.

flood victims, and 62.4% for drought victims and 62.5% for both floods and drought victims at community level). Details of these and more are presented in **Table 8**.

The Binary Logistic Regression was adopted for this analysis. In this analysis, the dependent variable (Disaster coping strategies) took 1 for Mainly Informal Strategies and 0 for Mainly Formal strategies. 16 explanatory variables were used in the analysis. The attributes of our models as presented in **Table 9** and show strong relationships between the dependent and independent variables in the analysis ($X2 = 109.423$, $P < 0.001$).

In addition, the attributes of **Table 10** show that our model explains 23.3% of the factors that affect coping strategies among the drought and flood victims in the two geo-ecological zones.

The factors that affect the coping strategies among the drought and flood victims in the two geo-ecological zones are presented in **Table 11**. The results show that the type of disasters faced, belonging to a social group or network, number of disaster faced, the main occupation of the household head and the number of years living in the community (residence time) positively affected the decisions of the disaster victims to adopt mainly informal disaster coping strategies. On the other

		Chi-square	df	Sig.
Step 1	Step	110.948	15	.000
	Block	110.948	15	.000
	Model	110.948	15	.000

Table 9.
Omnibus tests of model coefficients.

Step	−2 Log likelihood	Cox & Snell R square	Nagelkerke R square
1	416.685a	0.053	0.233

Table 10.
Model summary.

	B	S.E.	Wald	df	Sig.	Exp(B)
Age*	−.058	.012	22.708	15	.000	0.943
Type of disaster	0.190	0.325	0.341	15	0.559	1.209
Educational level*	−1.523	0.602	6.401	15	0.011	0.218
Geo-ecological Zone	−2.114	1.147	3.394	15	0.065	0.121
Household size	−0.040	0.055	0.539	15	0.463	0.961
Marital status	−0.046	0.333	0.019	15	0.890	0.955
Belong to a group or network	18.098	7067.871	0.000	15	0.998	23.64
Number of disasters faced*	0.210	0.064	10.835	15	0.001	1.234
Main occupation of household head	0.116	0.274	0.181	15	0.671	1.123
Religious affiliations	0.675	0.406	2.767	15	0.096	1.965
Residence time*	0.044	0.014	9.708	15	0.002	1.045
Sex	−0.536	0.319	2.831	15	0.092	0.585
Household income before disaster	.000	.000	0.894	15	0.344	1.000
Household income after disaster	.000	.000	1.701	15	0.192	1.000
Per capita income before disaster	.000	.000	2.851	15	0.091	1.000
Per capita income before disaster	.000	.000	1.544	15	0.214	1.000
Constant	−18.243	7067.872	.000	15	0.998	.000

**Significant at 10% level*

Table 11.
Regression determinants.

hand, the age, educational level, household size, marital status and the sex of the respondents showed negative relationships with adopting mainly informal disaster coping strategies. In addition, both incomes before and after the disasters as well as the per capita income before and after the disasters seem not to be important variables that could be used to differentiate households in terms of disaster coping strategies (B = 0.000 for all four variables). These therefore indicate that the financial/economic status had no influence on the decisions of the disaster victims to adopt one form of disaster coping mechanisms over the other [16, 20, 26, 27].

Of significance to this study is the number of disasters faced (B = 0.210, $P < 0.001$), religious affiliations (B = 0.675, $P = 0.096$) and the residence time (B = 0.044, $P = 0.002$).

The number of disasters experienced by households (B = 0.210, $P < 0.001$) is therefore seen to be an important variable influencing household decisions to adopt mainly informal disaster management strategies. This is normal, considering that experiencing too many disasters often affect the ability of households to bounce back. Consequently, these households tend to lean on community based informal response mechanisms to deal with aftermaths of disasters [28, 29]. This is probably why [30] explained that if people are made aware of any potential disasters they might face and their collective responsibility in preventing or minimizing the

effects of the disasters, it will help them to make preparedness part of their lives according to the disaster management options available to them. Over time, experience in managing (especially long term) shocks becomes an asset, as victims plough back these experiences into strategies aimed at preventing, mitigating, coping or resisting similar (and even dissimilar) shocks in the future. Similar contentions have been raised in the topical literature by [31, 32]. One can therefore conclude that experience with disasters can be quite robust in determining the management practices that victims (especially in developing countries) adopt to deal with natural hazards.

In an area where people roughly share the same way of life, occupation and are subjected to similar shocks, they are likely to employ similar coping strategies when hazards strike as response opportunities and available coping mechanisms are relatively homogeneous [27]. This probably explains why in the research area, the main occupation of the household head affected their household coping strategies. Improving agricultural techniques can therefore enhance the coping capacities of our sampled households to future floods. Improving education to enhance access to off-farm income activities should also be contemplated.

Though not significant, belonging to a social group or network showed the strongest contribution to the use of mainly informal disaster coping strategies in this study (B = 18.098, $P > 0.05$). Therefore, the more networks a household head belongs to, the more the household is going to rely mainly on disaster coping strategies to handle disaster effects. This therefore suggests that households who belong to groups or networks are likely to dissipate risks through livelihood diversification. This aligns with the findings of [31] who explained appropriate forms of social capital especially belonging to networks usually appear to have the potential to aid rural income generation as well as reduce vulnerability to livelihood shocks of poor households. Thus for any additional group that the household head joins, the probability that the household will employ mainly informal disaster coping strategies increases by 23.64 times.

The probability of the Wald statistics for the variables age and educational level for instance (22.708 and 6.401 respectively) suggests that the disaster victims who are older and more educated are likely to move away from using mainly informal risk management mechanisms to both informal and formal mechanisms. The negative coefficient on education leads us to hypothesize that the more educated a household head is, the more he/she is likely to use formal than informal instruments in managing disasters. These results however contradict the findings in the topical case studies [26, 27, 32]. About 34 for instance in his work in India found education to be a very cost-effective strategy for influencing and implementing schooling decisions in poor households in India. A probable explanation for this is the generally low levels of education observed in the Cameroon case study.

4. Conclusion

Our research demonstrates that Cameroon has diverse geo-ecological zones with climate-related hazards and disasters that are specific to some while others cut across. Through a comparative analysis, we differentiate that the Sudano-Sahelian zone is characterized by severe droughts and very deadly floods in both the urban and rural settings while the Western highlands are typified by floods in both the urban and rural settings as well. Further, we gained insights into the different drivers of household determinants of coping with droughts and floods in both geo-ecological zones. Respondents identified Informal coping mechanisms as their major fallback positions and include amongst others; reducing their household

savings, relying on stored food and heavy reliance on assistance from friends and relatives. Formal coping strategies were not identified as major drivers at both household and community levels in any of the zones. This explains that building social networks is a very important component in building policies that aim at making households more resilient in these zones.

We also observed that socio-cultural factors and experience with previous disasters influenced the type of strategies people would adopt in subsequent events. The nomadic nature of the Muslim households in the Sudano-Sahelian area elucidates why temporal or permanent migrations will easily be an option in coping with droughts and/or floods. This was not the case with most of the sedentary population of the Western Highlands where most people reported the wish to maintain their residence even after experiencing the floods except in the neighborhoods that have been completely and permanently inundated.

In addition, this was the first of a kind to have witnessed a positive change in income levels of some household members, especially in the Western Highlands where the huge floods have given the opportunity for change in socio-economic activities. Most have now engaged in lumbering and illicit sale of fuel which are considered more economically rewarding than the farming activities they formerly practiced. The presence of water routes now facilitates the transportation of timber from the hinterland to the coast as well as the transportation of fuel from neighboring Nigeria to Cameroon. The energetic male about the ages of 35 and 45 are gainfully employed in this new found economic sector.

Above all, this study is a first step in developing a robust methodology for comparing household determinants for coping with climate-related vagaries within and across multiple geo-ecological zones and within and across hazards/disasters. It serves as a platform for broad-based policy making and implementation not only within Cameroon but across SSA where similar realities abound.

Author details

Theobald Mue Nji[1] and Roland Azibo Balgah[2*]

1 Department of Sociology and Anthropology, Faculty of Social and Management Sciences, University of Buea, Cameroon

2 College of Technology, The University of Bamenda, Cameroon

*Address all correspondence to: balgahroland@gmail.com, balgazib@yahoo.com

References

[1] Jury MR. Economic impacts of climate variability in South Africa and development of resource prediction models. Journal of Applied Meteorology. 2000;**41**:46-55

[2] Bhavnani R, Vordzorgbe S, Owor M, Bousquet F. Report on the Status of Disaster Risk Reduction in the Sub-Saharan Africa Region. Commission of the African Union, United Nations and the World Bank. 2008. Available from: http://www.unisdr.org/files/2229DRRinSubSaharanAfricaRegion.pdf [Accessed November 28, 2018]

[3] World Bank. Managing Water Resources to Maximize Sustainable Growth: A Country Water Resources Assistance Strategy for Ethiopia. Washington DC: The World Bank; 2005. pp. 8-10

[4] Brown C, Meeks R, Hunu K, Yu W. Hydroclimate risk to economic growth in sub-Saharan Africa. Climate Change. 2011;**106**:621-647

[5] Hellmuth ME, Moorhead A, Thomson MC, Williams J, editors. Climate Risk Management in Africa: Learning from Practice. New York, USA: International Research Institute for Climate and Society (IRI), Columbia University; 2007. pp. 15-29

[6] Scheffran J, Marmer E, Sow P. Migration as a contribution to resilience and innovation in climate adaptation: Social networks and co-development in Northwest Africa. Applied Geography. 2012;**33**:119-127

[7] Yevjevich V. Floods and society. In: Proceedings of the NATOASI Conference on "Coping with Foods", Erice; 3-15 November 1992. 1992. pp. 11-17

[8] Zbigniew WK, Saisunee B, Axel B, Holger H, Lettenmaier D, Menzel L, et al. Natural Resources Forum. 2002;**26**:263-274

[9] Marfai MA. Potential vulnerability implications of coastal inundation due to sea level rise for the coastal zone of Semarang City, Indonesia. Environmental Geology. 2008;**54**:1235-1245

[10] Bang H, Miles L, Gordon R. The irony of flood risks in African dryland environments: Human security in North Cameroon. World Journal of Engineering and Technology. 2017;**5**:109-121

[11] Reacher M, McKenzie K, Lane C, Nichols T, Iversen A, Hepple P, et al. Health impacts of flooding in Lewes: A comparison of reported gastrointestinal and other illness and mental health in flooded and non-flooded households. Communicable Disease and Public Health. 2004;**7**(1):1-8

[12] Hao L, Zhang XY, Liu SD. Risk assessment to China's agricultural drought disaster in county unit. Natural Hazards. 2012;**61**:785-801

[13] Fontaine MM, Steinemann AC. Assessing vulnerability to natural hazards: Impact-based method and application to drought in Washington state. Natural Hazards Review. 2009;**10**:11-18

[14] Wilhitea DA, Sivakumarb MVK, Pulwartyc R. Managing drought risk in a changing climate: The role of National Drought Policy. Weather and Climate Extremes. 2014;**3**:4-13

[15] Doris F, Edward W, Caroline T, Mary A. Assessment of the coping strategies of flood victims in the Builsa District. Environment and Sustainability. 2018;**2**(1):17-25

[16] Azibo BR, Ateh FS, Nji TM, Azibo NK. Determinants for strategies to cope with climate related flood hazards in Cameroon. Climate Change. 2017;**3**(12):2-10

[17] Molua EL, Lambi C. The economic impact of climate change on agriculture in Cameroon. Policy Research Working Papers. 2007;**1**:4364

[18] McSweeney C, New M, Lizcano G. UNDP Climate Change Country Profiles: Cameroon. Oxford: United Nations Development Programme and University of Oxford; 2008. pp. 8, 30-32

[19] IPCC. Climate Change 2007: Impacts, Adaptation and Vulnerability. Cambridge, Cambridge University Press: Intergovernmental Panel on Climate Change; 2007

[20] Helgeson JF, Dietz S, Hochrainer-Stigler S. Vulnerability to weather disasters: The choice of coping strategies in rural Uganda. Ecology and Society. 2013;**18**(2):2

[21] Tiefenbacher JP, Day FA, Walton JA. Attributes of repeat visitors to small tourist-oriented communities. The Social Science Journal. 2000;**37**(2):299-308

[22] Innocent NM, Bitondo D, Balgah RA. Climate variability and change in the Bamenda highlands of North Western Cameroon: Perceptions, impacts and coping mechanisms. British Journal of Applied Science & Technology. 2016;**12**(5):1-18

[23] Nguh BS, Kimengs JN. Land use dynamics and wetland Management in Bamenda: Urban development policy implications. Journal of Sustainable Development. 2016;**9**(5):1-11

[24] Yenshu VE. Knowledge systems, agricultural practices/farming systems and the challenges of climate change. Revue de L'Academie des Sciences du Cameroun. 2013;**11**(1):85-91

[25] Ndi HN. Environmental change and malaria in Maroua, Far North Cameroon. In: Paper Presented at the 2nd International UGEC Conference on "Urban Transitions and Transformations: Science, Synthesis and Policy"; 6-8 November; Taipei. 2014. 27 pp

[26] Berman R, Quinn C, Paavola J. Identifying drivers of household coping strategies to multiple climatic hazards in Western Uganda: Implications for adapting to future climatic change. Climate and Development. 2014;**1**:1-26

[27] Jensen R. Do labor market opportunities affect young Women's work and family decisions? Experimental evidence from India. The Quarterly Journal of Economics. 2012;**127**:753-792

[28] IPCC. Climate Change 2014: Impacts, Adaptation, and Vulnerability. Geneva: Intergovernmental Panel on Climate Change; 2014

[29] Holzmann R, Hinz RP, Dorfman M. Pension Systems and Reforms Framework: Social Protection and Labour. Discussion Paper No. 0824. 2012. Retrieved from: Sitersources.worldbank.org/Socialprotection/resources/2805581225731593400/spl_at_WB_2000-08.pdf [Accessed: 20/11/2017]

[30] Balgah RA. Managing Natural Risks and Shocks. Informal Response Dynamics and the Role of Non-profit Organization. Stuttgart, Germany: Grauerverlag; 2011

[31] Pathirage C, Seneviratne K, Amaratunga D, Haigh R. Knowledge Factors and Associated Challenges for Successful Disaster Knowledge Sharing. United Nations Office for Disaster Risk Reduction and Global Assessment Report on Disaster Risk Reduction. 2014. Available from: www.preventionweb.net/hyogo//inputs/Pathirage [Accessed February 15, 2018]

[32] Njome M, Chuyong G, de Wit M. Volcanic risk perception in rural communities along the slopes of Mt. Cameroon, west Central Africa. Journal of African Earth Sciences. 2010;**58**:608-622

Chapter 10

Emergency Communications Network for Disaster Management

Carlos Alberto Burguillos Fajardo

Abstract

In recent years, from the majority of field experiences, it has been learned that communications networks are one of the major pillars for disaster management. In this regard, the exploitation of different space technology applications to support the communications services in disasters plays an important role, in the prevention and mitigation of the natural disasters effects on terrestrial communications infrastructures. However, this chapter presents the design and implementation of an emergency communications network for disaster management, based on a topology that integrates communications satellites with remote sensing satellites into an emergency communications network to be activated in disaster events, which affect public or private terrestrial communications infrastructures. Likewise, to design the network, different technical and operational specifications are considered; among which are: the emergency operational strategies implementation to maneuver remote sensing satellites on orbit for optimal images capture and processing, as well as the payload and radio frequencies characterization in communications satellites to implement communications technology tools useful for disaster management. Therefore, this emergency communications network allows putting in operation diverse communications infrastructures for data and images exchange, making available the essential information to accomplish a fast response in disasters or to facilitate the communications infrastructures recuperation in emergencies situations.

Keywords: disaster management, space technology applications, emergency communications network, communications satellites, remote sensing satellites, communications technology tools, images and data exchange

1. Introduction

At the present time around the world, the use and integration of different space technology applications that contribute to planning and designing alternative communications networks for the relief of the disaster's impact, on the terrestrial communications infrastructures, have gained great importance in the disaster management scenario. In each one of the disaster stages, the information flow between the disaster management organizations, the population, and other actors, in general, is a critical and fundamental factor to provide a quick and opportune response to all aspects linked to a disaster event. Frequently in diverse disasters situations, the terrestrial communications infrastructures are affected by the disaster impacts, phenomena that cause the communications services unavailable to support in the disaster management. In most cases, the disasters impact mainly communications services, such as the mobile phone networks, fiber optic systems, terrestrial

microwave systems, fixed telephone services, private and public TV networks, commercial radio networks, and also the Internet services infrastructures. Scenarios that have a considerable impact in all processes are related to the preparedness, response, and recovery in disaster conditions, since the communications services have an important function in the disaster management tasks.

Regarding current space technologies applications, a remote sensing satellite is a space technology whose operations make possible the analysis and understanding of the damages caused by nature's disaster. It is also a technology that has the ability to provide valuable information to assist in all the disaster management phases. From this perspective, the integration of the remote sensing satellites and communications satellites in a novel and practical topology with the purpose of implementing an emergency communications network to manage disaster events represents an important and necessary resource to enhance the abilities to monitor, manage, and control the critical data flow associated with the occurrence of one or more disasters in a specific region. In the same way, this operational integration offers a suitable and versatile resource to improve the emergency response time, and it is helpful to formulate the different indispensable measures to reduce the consequences and impacts of the disaster on the terrestrial communications infrastructures as well as on other public and private properties.

As a result, extensive works have been done over the last few years, proposing the integration of the space technology applications for disaster management, for example, studies about the role of the mobile satellite services and the remote sensing satellites in disaster management, with the aim to decrease the human casualties in natural events through the utilization of both technologies [1]. Similarly, various space technology applications and their utility to prevent the causes or mitigate the disaster's consequences have been investigated and analyzed. Concluding through this analysis, space technologies, such as active and passive remote sensing satellites, communications satellites systems, global navigation satellite systems, and weather satellites platforms, among others space technology applications, have a significant usage and importance in the processes or activities of risks reduction and disaster management, due to the flexibility in their operation characteristics [2]. In the same way, diverse organizations linked to the space sector around the world have focused their studies on the use and applications of space technology in the different stages involved in the disaster management. For instance, in pre-disaster planning, during disaster, and also in post-disaster phase, an integrated approach of using remote sensing and communications systems, disaster warning radar systems, the portable communications systems, and many others combined with satellite links to carry out the disaster management tasks is considered [3].

Nevertheless, the work presented in this chapter addresses the design and implementation of an emergency communications network for disaster management. A network designed is based on a topology developed through the analysis and formulation of operational and technical strategies that allow combine the capacities and resources available in the communications satellites and remote sensing satellites inside a topology which facilitates the implementation of diverse communications technology solutions and different schemes or medias for images exchange between the entities or organizations involved in the disasters management tasks, during each stage that comprise the disaster management in case of disaster events that affect the public and private communications infrastructures.

Equally, the emergency communications network, designed and developed methodically through this chapter, is an operational scheme useful and reliable to carry out the disaster management in different scenarios of hazard, considering the operational resources available through the integration of the communications satellites and remote sensing satellites on orbit and also their infrastructures at ground segment level. Operational schemes that provide the capabilities to put into operation services or technology solutions are as follows: Communications architectures for disaster

warning/management, radio and TV broadcasting services by satellite, cellular phone services over satellite, video conference services, very small aperture terminal (VSAT) networks, broadband satellite Internet services, and distinct architectures to images exchange, among other technology resources useful in the disaster management field.

2. Emergency communications networks role in disaster management

Most organizations recognized globally with the active participation in the communications technology area and their applications, including the International Telecommunication Union (ITU), propose that "when a disaster strikes, telecommunications save lives." Therefore, the Information and Communication Technology (ICT) has been recognized as a powerful instrument for the national economic, social, and cultural development, since they have the objective to increase the countries production levels and enhance the quality of life of people in the world [4]. In this regard, numerous studies and field systematic experiences have shown the great importance of preserving the communications services operation and also ensuring, at all times, the operability of their associated infrastructures; as the main challenge is presented throughout the disaster events or in hazard scenarios that must be faced by the entities and the personnel responsible for disaster management, since the communications services are a key resource and indispensable to carry out the disaster management tasks in numerous risk situations.

It is important to highlight the high demand that exists during the disaster events for several types of communications services available, and also for keeping fast access and effective update of the information. In the same way, standardized communications and information processes have increased the reliability of communications traffic, besides easy access to the communications services through a fast and reliable system integration and interoperability, to keep the communications flow in operation in all disaster events stages. These are the primary functions and requirements to be guaranteed by the communications networks with the aim to support continuously the communications services operation during a disaster. In **Figure 1**, some disaster events that can affect the communications services operation are pointed out; the

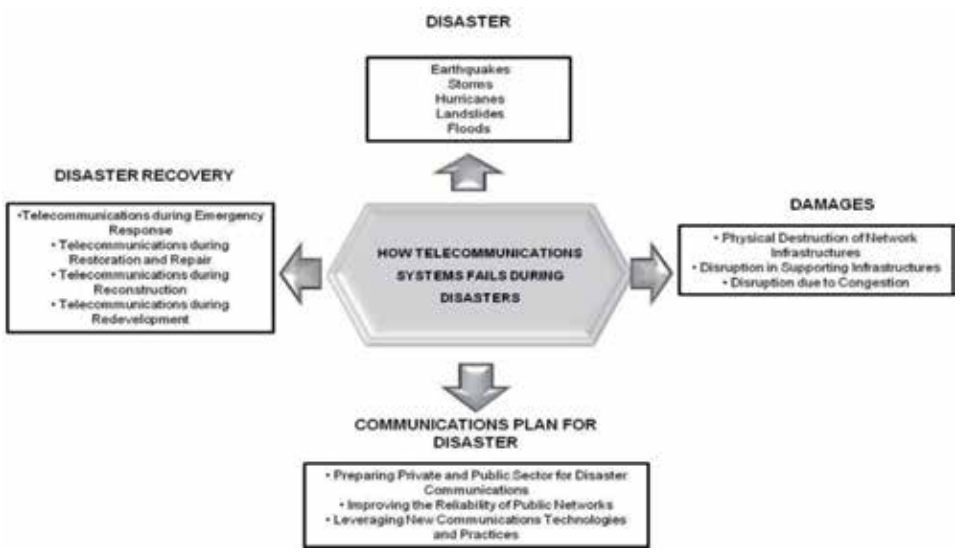

Figure 1.
Communications systems damages and recovery in disasters.

figure details the likely damages on the communications networks infrastructures caused by disasters, the potential communications planning required to guarantee the communications services operation, and the actions that must be taken to recover the communications services in the event of a disaster.

Since the communications terrestrial infrastructures may be damaged partially or totally in disaster events, the communications satellite systems' exploitation in disasters has been increased in the last years, because this technology is fast and reliable to restore the terrestrial communication infrastructures affected by disasters. This is especially due to the flexibility that offers the communications satellite systems hardware to be installed easily in disaster zones, facilitating the fast communications services recovery.

In fact, the importance of the emergency communications networks in disaster events has been proved in many countries; for instance, the Dominican Republic, Central America, is ranked as one of the 10 countries most affected by climate risks worldwide, because it is exposed to diverse recurrent natural phenomena such as hurricanes, tropical storms, floods, earthquakes, landslides and forest fires according to the Global Climate Risk Index of the last years. Large recurrence of disaster events have originated in the Dominican Republic, and the creation of a national plan for emergency communications in disasters is not only based on the use and management of the communications infrastructure existing in the country but also in the implementation of alternative communications infrastructures and technologies to mitigate the impact of the disaster in this region. Emergency communications network combines the use of the communications satellites with the exploitation of different data set coming from the remote sensing satellites, meteorological satellites, telemetry systems, and specialized equipment with the objective to manage the real-time information exchange in disaster as well as provides a technological platform useful for early warning, mitigation, and forecasting disasters events. Therefore, this emergency communications network in the practice has contributed to the coordination of relief operations carried out by national entities and the international community in the Dominican Republic, becoming an effective resource in the management of the disasters occurred in this country.

Identically, another practical experience shows the significance of the emergency communications networks in disasters management; it was noticed in the Sichuan Earthquake occurred in the People Republic of China on May 12, 2008, at 14:28 Hrs, with 8.0 magnitude on the Richter scale, causing the death of numerous people and damages in many critical infrastructures of this province. In particular, due to this earthquake, the telecommunications systems were seriously affected, losing half of the wireless communications in Sichuan province and telecommunications services in Wenchuan and in four nearby counties. Nonetheless, to evaluate the infrastructure and system damages caused by this earthquake, the Chinese government used the remote sensing data (multisensor data) captured from 13 remote sensing satellites through the activation of the International Charter for "Space and Major Disasters"; equally utilized remote sensing data from Chinese institutions were linked to this field and images were downloaded from the Chinese remote sensing satellites.

In the same way, to mitigate the damages caused by the earthquake on the telecommunications infrastructures and services, the International Telecommunication Union (ITU) deployed 100 satellite terminals to help restore vital communications links in the regions affected by the earthquake. Additionally, the Chinese government activated the use of the national communications satellites network to recover the communications services in all affected areas, through the satellite communications services implementation to recover the terrestrial communications services affected in the earthquake. In this sense, not counting China for the earthquake date with an emergency communications network structured formally, both technologies, remote sensing satellites and communications satellites, were used simultaneously to manage the Sichuan earthquake consequences or impacts.

General speaking, in the Sichuan earthquake, the remote sensing satellites helped to analyze diverse damages, including the damages to communications systems. Moreover, they facilitated the formulation of measures to mitigate potential hazard situations, and provided the images with diverse resolutions required. In this same context, the communications satellites were employed to recover the communications services and also to support the alternatives technologies solutions implementation for different data types exchange between the entities in charges to management of the Sichuan earthquake. All the applications and tasks described above, covered by the remote sensing satellites and communications satellites combination in the Sichuan earthquake, are the most practical and compelling evidence to establish the design and operation philosophy of the emergency communications network developed in this chapter; and also they make clear the communications networks importance in disaster management.

3. Emergency communications network design strategy

The design and implementation of the emergency communications network for disaster management integrated by communications satellites and remote sensing satellites and also their ground stations can be divided systematically into six (06) main tasks: In first place, an operational procedure is formulated to maneuver the remote sensing satellites in orbit for optimal images capture in disaster events, considering the spatial and spectral resolution; then a model to images management and processing at ground segment level in emergency is designed, following which the technical characterization of the communications satellites transponders and radio frequency spectrum is carried out, with the aim to design the communications services necessaries for disasters management labors; subsequently, diverse communications applications and technology solutions are formulated, essentials for images and data exchange in disaster events, and the communications satellites transponders technical specifications to carry out the planning and design of the communications links budgets for priority services in emergency are analyzed afterward; lastly, the design of the topology and infrastructure required to integrate the communications satellites and remote sensing satellites to operate in an emergency communications network for disaster management, functional to be activated in events that affect the communications services facilities, is developed.

Nevertheless, to exemplify the emergency communications network design and describe the strategies proposed to maneuver the remote sensing satellites and communications satellites in emergency scenarios, two remote sensing satellites (Remote Sensing Satellite-1 and Remote Sensing Satellite-2) and one communications satellite (Satnet-3) were selected to integrate the network. More satellite platforms could also be integrated into the network, according to the availability thereof in disaster events. **Figure 2** describes the six tasks defined to design the emergency communications network for disaster management proposed in this chapter.

3.1 Operational procedure to maneuver the remote sensing satellites spatial resolution in disaster events

The remote sensing satellites spatial resolution refers in specific to the capacity that has the sensor installed on the satellite platform to distinguish or characterize the resolving power captured, with the aim to identify and also categorize the characteristics of two or more objects observed on the area scanned. This resolving capacity is related to the instantaneous field of view (IFOV) size of the sensor and intrinsically associated with the sensor geometrical characteristics, the sensor capacity to

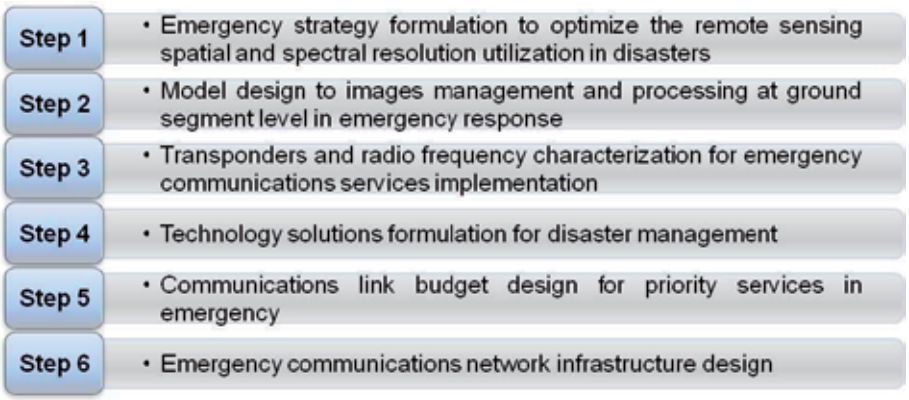

Figure 2.
Emergency communications network design strategy.

discriminate the targets tracked, the sensor capacity to calculate the periodicity of distinct targets tracked, and also to the sensor ability to determine the small targets spectral properties to obtain their spectral signatures. It is important to point out that the remote sensing spatial resolution has significant use in disaster events; its adequate application allows the sensor capturing images with details or specific characteristics required of the area tracked, affected by one or more disasters.

Especially, different spatial resolutions are necessaries that depend on the disaster occurred to ensure the images acquisition accuracy of diverse objects or of the earth surface characteristics through the sensor. In disaster management or emergency response, the spatial resolution is used principally to distinguish the diverse damages on the infrastructures affected by disasters, to establish the adequate measures for fast recovery of damages, to determine the respective scale for images analysis, and to characterize or define the location and areal precision on a surface given. In this way, to scan small areas and capture the more precise features thereof, it is necessary to use high resolution, but for wide areas, the smallest resolutions are frequently enough to recognize the features desired. On the other hand, the remote sensing satellite has a spatial coverage, an operational characteristic that defines the remote sensing satellite's geographical coverage in an interval of time; aspect that must be analyzed altogether with the sensors spatial resolution, since the different satellite land coverage variations, produced by the sensor scanning angles changes, will influence the sensor spatial resolution performance.

Figure 3 illustrates the remote sensing satellite terrain coverage and its field of view (FOV) angle. In this respect, at the first place, the sensor field of view (FOV) angle is represented on the figure; this angle corresponds to the whole area viewed by the sensor at a specific period of time and in particular is referred to the sensor radiometric resolution ability to capture the energy from the surface scanned. Equally, the same figure shows the sensor instantaneous field of view (IFOV), which represents the smallest solid angle subtended by the sensor opening from a specific height in orbit at one interval of time during a scanning period. However, the sensor observing area size can be obtained from IFOV angle multiplied by the distance, that is, from ground to the sensor in orbit, and the result represents the ground resolution cell viewed by the sensor, specifying the maximum sensor spatial resolution on the surface scanned. Finally, the figure describes the satellite trace direction and the sensor scan trajectory on the terrain. Both the sensor spatial resolution and the pixels size have a relation between them since the pixels size are modified by the sensor sweep on the earth surface due to the curvature thereof, which is more prominent at the border of the earth's surface scanned.

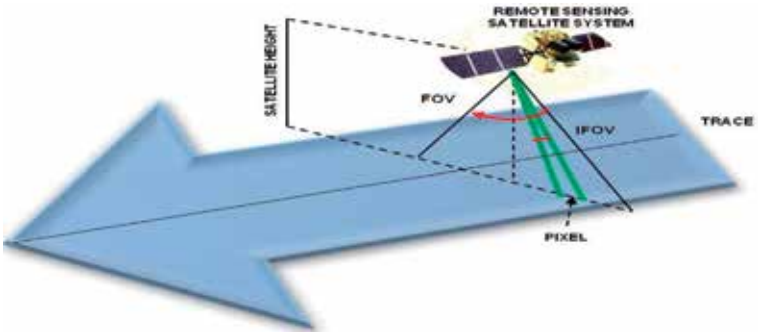

Figure 3.
Remote sensing satellite terrain coverage and field of view (FOV).

Satellite	Camera	Resolution	FOV (nadir)
Remote Sensing Satellite-1	PMC	PAN: ≤2.5 m MS: ≤10 m	5.15°
Remote Sensing Satellite-1	WMC	≤16 m	16.44°
Remote Sensing Satellite-2	HRC	Pam ≤1 m MS ≤ 4 m	2.93°
Remote Sensing Satellite-2	IRC	30 m (SWIR) 60 m (LWIR)	2.8°

Table 1.
Remote Sensing Satellite-1 and Remote Sensing Satellite-2 cameras resolution and field of view (FOV) angles.

Regarding the previous considerations, about the remote sensing satellites spatial resolution and its application in disaster management, the remote sensing satellites sensors have operational technical specifications that influence the images capturing performance. These specifications are considered during the emergency communications network design and proposed to be managed with the objective to optimize the sensors spatial resolution performance in disasters events. Such technical specifications are specified following: remote sensing sensor terrain swath coverage estimation, potential remote sensing sensor terrain swath coverage in nadir and at off-nadir angle, remote sensing sensor pixels size estimation at nadir and off-nadir angle, and remote sensing sensor dwelling time for an along track scan; strategies are useful to achieve the best remote sensing satellite platforms performance inside the emergency communications network during the disaster management.

In **Table 1**, as examples are shown, the cameras resolutions and their fields of view (FOV), for the two (02) remote sensing satellites, are proposed to be part of the emergency communications network in disasters. In this regard, the Remote Sensing Satellite-1 has PAN and multispectral cameras (PMC) and also wide swath multispectral cameras (WMC) and the Remote Sensing Satellite-2 has high-resolution cameras (HRC) and infrared cameras (IRC).

3.1.1 Remote sensing sensors terrain swath coverage estimation in disaster events ($RSTSC_e$)

The remote sensing satellites on orbit operation have the capacity to change the view pointing angle of their sensors through the roll maneuvers; operational strategy implemented with the aim to allow the sensors to observe in different positions in direction to the vertical trajectory view angle on the terrain; from the nadir angle,

until some degrees above this angle. In consequence, by mean of this operational characteristic, the remote sensing satellites have the ability to change their coverage on the terrain, which allows the sensors to cover a greater terrain extension in each satellite pass, through the different pointing angles. Principally, the pointing angles variation of the remote sensors view on orbit from nadir, achieved through the roll maneuver, is useful in disasters management to scan from two different view angles identical areas involved in disaster events, with the aim to obtain images in different perspectives of the areas affected by disasters. Also it is useful to images analysis in a three dimensional model for the best understanding of damages in disasters; in the same way, the sensors pointing angle change is effective to accomplish the mapping and interpretation of the zones affected by disasters with the purpose to create simulations model for damages to facilitate the emergency response task and recovery.

For this reason, a proposal based on a methodology following a reliable operational procedure to manage the remote sensing sensors terrain swath coverage estimation ($RSTSC_e$) in emergency or hazard events is formulated. Accordingly, first, a procedure to determine the remote sensing sensors terrain swath coverage estimation ($RSTSC_e$), minimum in nadir pointing angle and maximum off-nadir pointing angle is established, considering the remote sensing sensors field of view (FOV) specifications for this estimation as a reference. Subsequently, the remote sensing sensor potential terrain swath coverage in nadir angle and off-nadir angle ($RSTSC_p$) using the spherical trigonometry mathematical method considering the law of sines for this aim is determined. In this sense, Eq. (1) specified below is proposed to calculate the remote sensing sensors terrain swath coverage estimated (LSC_s) minimum in nadir pointing angle and maximum off-nadir pointing angle in emergency response.

$$RSTSC_e = 2 \cdot S_r \cdot (tan\ FOV_s) \tag{1}$$

where $RSTSC_e$ is the remote sensing sensors terrain swath coverage estimation; S_r is the satellite ranging or altitude; *tan* tangent; and FOV_s is the sensor field of view angle.

For instance, to demonstrate the application of Eq. (1), the computation to estimate the terrain swath coverage ($RSTSC_e$) minimum in nadir pointing angle, and the terrain swath coverage ($RSTSC_e$) at maximum off-nadir pointing angle for the PAN and multispectral camera (PMC) of the Remote Sensing Satellite-1, as well as to the high-resolution camera (HRC) of the Remote Sensing Satellite-2, is executed; in this case, for both remote sensing satellites, an average ranging or altitude on-orbit operation around 640 km is considered. In **Table 2**, the results obtained once the corresponding calculations have been done are specified.

It is notable, through the results obtained and specified in **Table 2** using Eq. (1), that the Remote Sensing Satellite-1 and Remote Sensing Satellite-2, using their

Satellite platform	Satellite camera	Camera FOV in nadir angle	Camera FOV max-off nadir angle	RSTSCe in nadir angle	RSTSCe max-off nadir angle
Remote Sensing Satellite-1	PMC	5.15°	31°	115.328 km	768 km
Remote Sensing Satellite-2	HRC	2.93°	29°	65.51 km	709 km

Table 2.
Remote Sensing Satellite-1 and Remote Sensing Satellite-2 cameras terrain swath coverage estimation.

operational abilities to re-pointing the cameras in direction to the vertical trajectory of the view angle on the terrain from the nadir, can reach a wide swath coverage on the terrain. Operational capacity is useful to plan and develop diverse remote sensing satellite missions in disasters, with the aim to cover one or more specific terrain extensions affected during disasters in less time through different cameras view angles' characteristic that allows providing quick response in disasters events.

3.1.2 Remote sensing sensors potential terrain swath coverage in disaster events ($RSTSC_p$)

In emergency scenarios, the remote sensing sensors potential terrain swath coverage estimation, in nadir angle and off-nadir angle ($RSTSC_p$), as an operational procedure implemented on the satellite platform through the roll maneuvers, is an effective and reliable operational strategy to forecast in diverse disaster events, the expected terrain swath width to be scanned with the remote sensing sensors in the future satellite passes, using different view angles of the sensors over the terrain or areas that will be covered in a planned mission. In consequence, it is an important strategy in the disaster management, because it makes possible the prediction and planning in advance the terrain extensions affected by the occurrence of disasters that possibly will be explored by the satellite sensors. Fundamentally, three mathematical approaches can be used to calculate the remote sensing sensor potential terrain swath coverage in nadir angle and off-nadir angle ($RSTSC_p$). These mathematical formulations or methods are the next: oblique spherical triangle method, the spherical method using intersecting lines, and the planar surface projection method [5]. In specific, the oblique spherical triangle method based on the earth model illustrated in **Figure 4** is the method selected to predict the remote sensing sensor potential terrain swath coverage in nadir angle and off-nadir angle ($RSTSC_p$), because it is the most reliable and accurate method to perform the aforementioned operational calculation.

The oblique spherical triangle method previously mentioned and selected to predict the remote sensing sensor potential terrain swath coverage in nadir angle and off-nadir angle ($RSTSC_p$) is taken into account; It is specified that this methodology is based on a mathematical approach or solution by which is projected a straight line from the remote sensing satellite on-orbit operation until a perpendicular plane

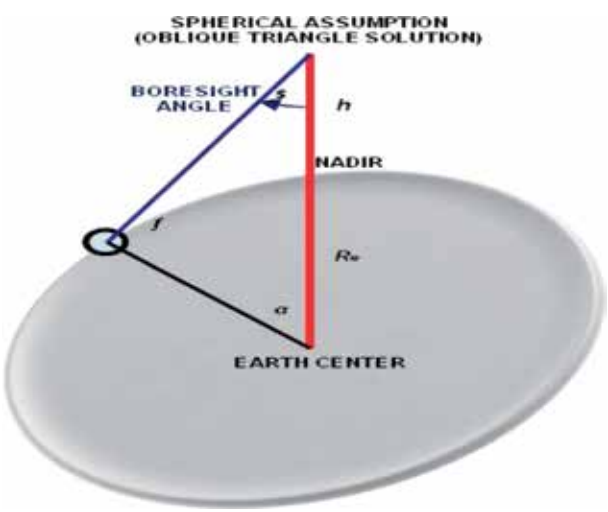

Figure 4.
Oblique spherical triangle method to predict the remote sensing sensor potential terrain swath coverage in nadir angle and off-nadir angle (RSTSC p*).*

with reference to the earth's surface, creating in this intersection point between the projected line and the earth surface an angle denominated non-included angle, designated with the letter (f), as it is shown in **Figure 4**; this angle corresponds to the remote sensing sensors' instantaneous field of view (IFOV) and represents the smallest solid angle subtended by the sensor opening from a specific height in orbit at one interval of time given on the earth surface. Generally speaking, the instantaneous field of view (IFOV) is the area on the ground viewed by the sensor at a given instant of time, an area that specifies the dimension on the ground of each pixel over the surface scanned. Additionally, in reference to an oblique triangle, three more angles characterized like included angles, described also in **Figure 4**, are created by imaginary lines represented for the remote sensing satellite ranging or height (h) in orbit, the earth radius (r_e), and the boresight angle or sensor FOV (s), forming altogether all these angles a triangle [6]. As result, considering the oblique spherical triangle method and the law of sines implementation to solve the triangle formed in **Figure 4**, it is feasible to calculate the remote sensing sensor potential terrain swath coverage in nadir angle and off-nadir angle ($\mathrm{RSTSC_p}$). Therefore, the mathematical formulation using the law of sines to estimate the $RSTSC_p$ is next discussed.

Since the three angles (α, ø, s) described in **Figure 4** must sum 180°, so f = 180 – α –s, solving (α) through the law of the sines, we have Eq. (2):

$$\alpha = sin^{-1} \cdot \left(\frac{\sin(s) \cdot (r_e + h)}{r_e} \right) - s \tag{2}$$

where α is the non-included angle (IFOV); s is the boresight angle (FOV); r_e is the radius of the earth; and h is the satellite height.

However, to compute the remote sensing sensor potential terrain swath coverage in nadir angle and off-nadir angle ($\mathrm{RSTSC_p}$) Eq. (3) is used.

$$RSTSC_p = \left(\frac{\alpha}{2\pi} \right) \cdot r_e \tag{3}$$

where $RSTSC_p$ is the remote sensing sensor potential terrain swath coverage; α is the non-include angle (IFOV); and r_e is the radius of the earth.

For instance, with the purpose of demonstrating the previous mathematical formulation for the high-resolution camera (HRC), of the Remote Sensing Satellite-2, a field of view angle after roll maneuver on orbit operation is considered: FOV (s) = 17° (12 degrees under the maximum FOV reached by this camera through the roll maneuver strategy). In the same way, to this satellite, an average ranging or height on orbit = 645 km and for the earth's radius, a value = 6378.137 km, is précised. Nevertheless, taking as a reference the triangle illustrated in **Figure 4**, which geometrically describes the oblique spherical triangle method to predict the remote sensing sensor potential terrain swath coverage in nadir angle and off-nadir angle ($\mathrm{RSTSC_p}$), from Eq. (2), α is solved and obtained for the High-Resolution Camera of the Remote Sensing Satellite-2, an IFOV = 1.78°, and then with Eq. (3), it is computed for this High-Resolution Camera, a potential terrain swath coverage off-nadir angle ($\mathrm{RSTSC_p}$) = 1807.81 km. Through this result, it is noticed that the high-resolution camera (HRC) of the Remote Sensing Satellite-2 in successive passes in different adjacent orbits due to the roll maneuver strategy implementation has the capacity to cover an extension equal to 1807.81 km of land over a defined territory.

Therefore, given that the maximum swath coverage of the high-resolution camera (HRC) off-nadir to 29° of inclination (maximum off-nadir angle) is = 709 km (information specified in **Table 2**) and the potential terrain swath coverage off-nadir angle ($\mathrm{RSTSC_p}$) = 1807.81 km calculated from Eq. (3), it is estimated a period of time: 1,807,810/709,000 = 2.5 days, through successive passes of the Remote Sensing

Figure 5.
Remote Sensing Satellite-2 high-resolution camera (HRC) potential view capacity with field of view at +29°.

Satellite-2 in different adjacent orbits with the high resolution camera (HRC) using a FOV (s) angle of: 17°, to cover the terrain extension obtained from the calculation of the potential terrain swath coverage off-nadir angle ($RSTSC_p$). In **Figure 5**, the Remote Sensing Satellite-2 high-resolution camera (HRC), potential view capacity with a field of view maximum at +29° achieved through the roll maneuver to cover a territory of 916,445 km^2 in consecutive passes is shown.

In resume, the prediction of the remote sensing sensor potential terrain swath coverage in nadir angle and off-nadir angle ($RSTSC_p$) is a strategy or operational procedure useful for planning the images collection opportunities on the diverse areas that are required to be scanned immediately after disaster events or on those zones that are involved in imminent hazard situations. It is possible to obtain results that are more accurate about the potential sensor terrain swath coverage in nadir angle and off-nadir angle ($RSTSC_p$) in real operation by the use of the satellite ranging data, measured and obtained periodically from its ephemerides predictions. Information provided through the operational software packages is installed in the remote sensing satellites ground control stations, since the satellite fly height on orbit influences the sensors' field of view (FOV) performance, which also affects the sensor swath coverage on the surface explored and the images resolution captured by the sensor. At the same time, besides to the strategies or operational procedures implemented for management the remote sensing satellites roll maneuvers on orbit, with the aim to change the cameras field of view (FOV) angles to enhance the cameras' coverage and also their revisit capability on the distinct areas affected by disaster events, there also exist other important technical aspects mentioned before in this chapter related to the cameras spatial resolution, and that must be considered to improve the remote sensing satellites operational performance inside the emergency communications network. Technical cameras or sensors parameters such as remote sensing sensor pixels size at nadir and off-nadir angle and the remote sensing sensor dwelling time for an along track scan are considered; and operational parameters taken into account are to be estimated as part of the strategies proposed to accomplish a better coverage and images capturing on the areas required in the course of emergency response in disasters.

3.1.3 Remote sensing sensors pixels size estimation at nadir and off-nadir angles to disaster management

The images captured for the remote sensing sensor have a particular structure based on a format integrated by a matrix of organized rows and columns or cells (pixels), denominated altogether, all these rows and columns, as raster imagery. In

this sense, one pixel constitutes the smallest physical point sampled of a raster image, and the pixels size in the raster image represents the smallest point size on the surface captured by the remote sensing sensor in function to the sensor instantaneous field of view (IFOV). Especially, the sensor pixel resolution is affected by the change in sensor scan angles due to the roll maneuver strategy between others operational aspects, which originates variations in the pixels dimensions, becoming increasingly distorted away from the nadir as view zenith angles increase. For this reason, the remote sensing sensor resolution looks distorted along the track and also across track direction at the extreme edges on the surface scanned [7].

However, the images pixels size captured by the remote sensing sensor is an important sensor performance characteristic necessary to be estimated, when the sensor scan angle is changed through the satellite roll maneuvers, with the objective to increase their potential swath coverage off-nadir angle to cover a specific extension of terrain in a region previously planned; since the pixel size estimation at nadir and off-nadir angles in disaster events is a useful method to define how much the sensor resolution can vary through the pixels spatial size variation along track scan and across track scan. It will also help to define the relation between the sensor resolution variation with reference to the different scan angles or FOV, as well as the influence of different FOV angle on the resolution of the images captured over the terrain in the diverse remote sensing satellites roll maneuvers required on orbit in case of emergency. The remote sensing pixels size geometrical characterization in nadir and off-nadir angles is described in **Figure 6**, where it is explained through a graphical representation the sensor FOV angles changes and their influence on the pixels size variation on the ground resolution cells.

In particular, the Remote Sensing Satellite-1 and Remote Sensing Satellite-2, satellites platforms considered to integrate the emergency communications network proposed in this chapter, are designed with cameras whose resolution is adequate to observe the geometry of diverse objectives and the characteristics related to the phenomena associated with the disasters events. In this respect, the sensors resolution belonging to these satellites platforms is represented by the ground sampling distance (GSD) and for each pixel with a defined spatial size in function to the sensor pointing angle or field of view (FOV) in nadir or off-nadir angle; next, for the aforementioned satellites platforms, their camera resolution characteristics are specified with the respective spatial pixels size to each one: the Remote Sensing Satellite-1 payload is integrated for two (02) PAN and multispectral cameras (PMC) designed with PAN and MS detectors to operate using both functions at the same time in the images capturing process; the panchromatic (PAN) sensor has a ground

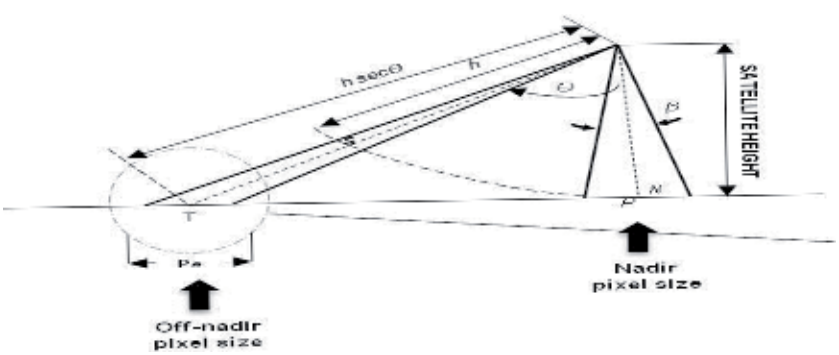

Figure 6.
Pixels size geometrical characterization in nadir and off-nadir angles.

sampling distance (GSD) in nadir ≤ 2.5 m and a pixel spatial size ≤ 6.25 m^2; in multispectral (MS) function, the sensor has a ground sampling distance (GSD) in nadir ≤10 m with a pixel spatial size ≤ 100 m^2; also, this satellite platform is designed with two (02) wide swath multispectral cameras (WMC) which operate in four (04) spectral bands with a ground sampling distance (GSD) in nadir ≤ 16 m and pixel spatial size ≤256m^2.

On the other hand, the Remote Sensing Satellite-2 has one (01) high-resolution camera (HRC) with optical sensors to produce panchromatic (PAN) and multispectral (MS) data simultaneously. In panchromatic (PAN) operation, this sensor has a ground sampling distance (GSD) in nadir ≤ 1 m with pixel spatial size ≤1m^2, and in multispectral (MS) operation, the sensor has a ground sampling distance (GSD) in nadir ≤ 4 m with a pixel spatial size ≤16 m^2. Likewise, in this satellite platform, the shortwave infrared (SWIR) sensor in nadir has a ground sampling distance (GSD) ≤ 30 m and pixel spatial size ≤900 m^2 and the long wave infra-red (LWIR) sensor has a ground sampling distance (GSD) ≤ 60 m in nadir with a pixel spatial size ≤3600 m^2. Overall, the camera's resolution performance characteristic of the satellites platforms that integrate the emergency communications network is a critical aspect that must be managed in an accurate way, with the aim to optimize the resolution of the images captured depending on the type of disaster events. Each step of the mathematical formulation to estimate the pixels size in nadir and off-nadir angle is introduced which is as follows:

Step 1: first, Eq. (4) is specified and next, the sensor field of view (FOV) swath width is estimated.

$$\boldsymbol{SFOV_{sw}} = \mathbf{2} \cdot \boldsymbol{h} \cdot \mathbf{tan}\left(\frac{\beta}{\mathbf{2}}\right) \tag{4}$$

where $SFOV_{sw}$ = sensor field of view (FOV) swath width; h = satellite height; tan = tangent; and β = sensor field of view (FOV).

Step 2: Using Eq. (5), the sensor effective resolution is computed.

$$\boldsymbol{SE_r} = \frac{\boldsymbol{SFOV_{sw}}}{\boldsymbol{SP_n}} \tag{5}$$

where SE_r = sensor effective resolution; $SFOV_{sw}$ = sensor field of view (FOV) swath width; and SP_n = sensor pixels number.

Step 3: Finally, solving Eq. (6), the pixel size captured by the sensor is estimated.

$$\boldsymbol{SP_{se}} = (\boldsymbol{SE_r})^2 \tag{6}$$

where SP_{se} = sensor pixels size estimation; and SE_r = sensor effective resolution.

To explain the application of the previously mathematical approach formulated to estimate the pixels size in nadir and off-nadir angle in the remote sensing sensors, as an example, wide swath multispectral camera (WMC) as a remote sensor is taken which is installed in the payload of the Remote Sensing Satellite-1. This WMC is a medium-resolution push broom sensor with time delay integration (TDI) and capability to observe, in the visible range, a field of view (FOV) = 16.44° in nadir and maximum field of view (FOV) = 31° off-nadir achieved through the roll maneuver in orbit operation. Also, as additional information to develop this example is regarded for the Remote Sensing Satellite-1 on-orbit operation an average altitude or height = 650 km. Therefore, in first place, from Eq. (4), the computation of the WMC field of view (FOV) swath width in nadir is carried out, whose value is ≤187.796 km; afterward using Eq. (5) and given that this sensor has 12,000 pixels with 6.5 μm of size, the sensor effective resolution, (SE_r) =

≤187,796/12,000 = ≤15.64 m in nadir, and with Eq. (6), the pixels size in nadir to this sensor, (SP_{se}) = ≤245 m^2, are estimated. In the same way, by Eq. (4), at the WMC maximum off-nadir pointing angle (31°), a field of view (FOV) swath width ≤ 360.521 km is also calculated. As already known, this sensor has 12,000 pixels with 6.5 μm of size, and considering these specifications with Eq. (5), the sensor effective resolution, CE_r = 354,975/12,000 = 29.58m SE_r = ≤360,521/12,000 = ≤30 m with an off-nadir pointing angle in 31° of FOV is calculated; finally, through Eq. (6), a pixels size at the same pointing angle off-nadir for this sensor is computed, (SP_{se}) = ≤902 m^2. In summary, through the analysis of the above results, it is easy to deduct that the ground area represented by each pixel in nadir pointing angle has a better resolution than the pixels at off-nadir pointing angles. Such a phenomenon is due to the spatial resolution, which varies from the image center to the swath edge, and hence, also the pixels spatial size. Technical aspects are considered in those maneuver situations in which the changes of pointing angles of the sensors are necessaries to management of diverse disaster events in a shortest possible time.

3.1.4 Remote sensing sensors dwell time estimation in disaster events

At the present time, there are principally two (02) types of passive sensor technologies for optical cameras used frequently in the remote sensing satellites applications to images scanning and collection over the earth surface; such technologies are the whisk broom scanning sensors and the push broom scanning sensors. In this regard, the whisk broom scanning sensors, also known as spotlight in the across-track scanners, is a technology that uses a mirror to scan across the satellite's path over the ground track, reflecting the light captured into a single detector which collects the pixels of the images one at a time through the movement of the mirror back and forth [8]. In this type of sensor, the mechanism used to move the mirror makes this technology vulnerable to rapid degradation in function of the working hours to which the mechanism is subjected. It is also an expensive technology since it demands a special design of the movement mechanism parts. **Figure 7** describes the whisk broom sensors scanning working principle, where the remote sensing satellite camera sweeps in a direction perpendicular to the satellite flight path.

Likewise, the whisk broom sensors have the following operation characteristics: each line over the earth surface is scanned from one side of the sensor to the other through a rotating mirror, while the satellite platform moves forward over the earth's surface. Different successive scans of the mirror build up a two-dimensional image of the earth's surface, and by means of a bank of internal detectors in the

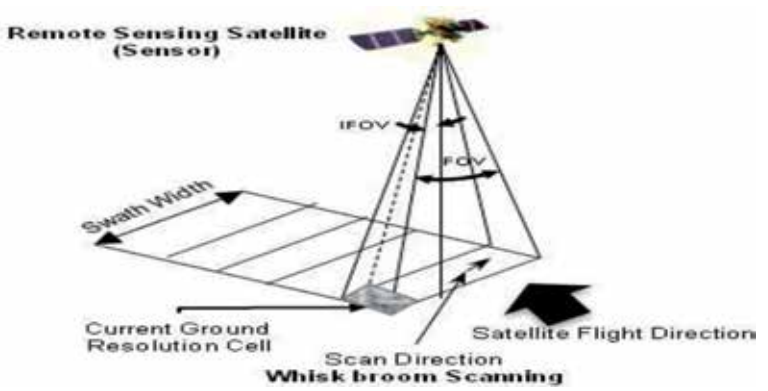

Figure 7.
Whisk broom sensors technology scanning principle.

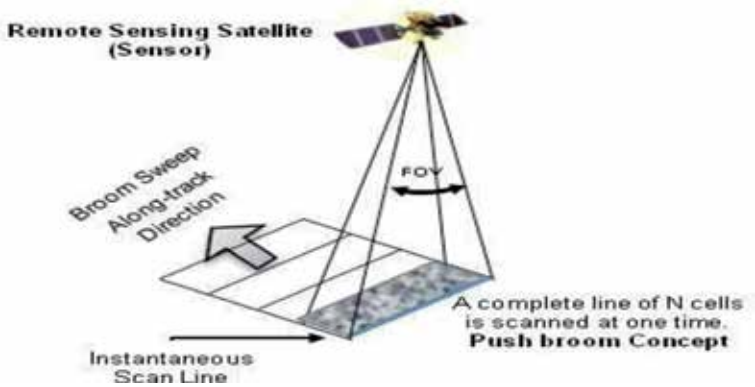

Figure 8.
Push broom sensors technology scanning principle.

cameras, each one sensitive to a specific range of wavelengths is detected and the energy for each spectral band is measured; after the energy is captured by each detector like an electrical signal, it is transformed into a digital data and stored on the remote sensing satellite. In the whisk broom scanning, the IFOV and the satellite height in orbit define the sensor spatial resolution, whereas the images swaths are in function to the mirror sweep that is represented by the sensor angular field of view; angle measured in degrees and used to record the pixels of the scan lines of the images. All the whisk broom sensor data are collected on the land surface within an arc below the satellite system usually of around 90–120°.

On the other hand, the push broom scanning is also referred to as along-track scanning; the sensors used here is a linear array of detectors, arranged perpendicular to the flight direction of the satellite to cover all the pixels in the along-track dimension at the same time. In consequence, as the spacecraft flies forward, the image is collected one line at a time, with all pixels in a line being measured simultaneously [9, 10]. It is important to highlight that the push broom sensors have a drawback in its sensitivity which is very varying; if they are not perfectly calibrated, this can cause stripes in the data acquired. **Figure 8** shows the push broom sensors scanning working principle.

The push broom sensors have the next working principle: these optical sensors are designed with a linear matrix of detectors situated at the focal plane of the image. In specific, this matrix is formed by a lens system, which is pushed along track in direction to the satellite flight track projection over the scanning surface; the detectors matrix movement is similar to the displacement of the sows of a broom being pushed along a floor; during this displacement, each detector captures or measures the energy of every land resolution cells on an individual basis; after the energy has been detected, it is sampled electronically and digitally stored on the satellite platform. The push broom sensor's spatial resolution is determined by the size of its instantaneous field of view (IFOV) angle. Also, the push broom sensors are integrated by an independent linear matrix in charge to measure each spectral band or channel. In this sense, the linear matrixes normally consist of numerous charge-coupled devices (CCDs) positioned end to end.

A push broom sensor receives a stronger signal than a whisk broom scanner since it looks at each pixel area for longer; this provides a much longer detector dwell time than the across-track scanner on each surface pixel, thus allowing much higher sensitivity and a narrower bandwidth of observation, operation characteristic that improves the radiometric resolution. General speaking, the sensor dwell time is the amount of time the scanner has to collect photons from a ground

resolution cell. However, the dwell time depends on some factors, such as satellite speed, the width of the scan line, time per scan line, and time per pixel. Therefore, it is a sensor performance parameter that requires to be estimated, when the remote sensing satellite sensors view angle is changed through the satellite roll maneuvers, to scan areas affected by disasters from different scan angles, due to its impact on the sensors radiometric resolution.

Since the remote sensing satellites with push broom sensors are the proposed platforms to integrate the emergency communications network planned, the mathematical approach applicable to calculate the dwell time, considering the push broom sensors through its along-track scanning, is specified in Eq. (7):

$$\boldsymbol{DT_{ats}} = \left(\boldsymbol{GR_{ce}} | \boldsymbol{Sat_v}\right) \tag{7}$$

where DT_{ats} = dwell time for along-track scan; GR_{ce} = ground resolution cell; and Sat_v = satellite orbital velocity.

From the above mathematical approach, considering the Remote Sensing Satellite-2 High-Resolution Camera (HRC) specifications in Multispectral (MS) band, with a ground resolution cell of: ≤4 m •≤4 m, information specified in section 3.1.3, a Remote Sensing Satellite-2 mean orbit velocity of 7.8 km/s; using Eq. (7), the dwell time computation for Satellite-2 High Resolution Camera (HRC) along-track scanning is carried out, $DT_{ats} = \left(\leq 4\text{m} \cdot cell \mid 7.8\frac{\text{km}}{\text{s}}\right) = \leq 0.51\text{ms} \cdot \text{cell}$; average time projected to be used by this High Resolution Camera (HRC), to collect photons from a ground resolution cell over the earth surface; technical specification must be taken into consideration to maneuver the remote sensing satellite in orbit with the aim to change the cameras scanning angles, in order to know the cameras photons acquisition time on each ground resolution cell for each satellite pass over an specific area affected by disasters using different cameras scanning angles; sensor operating characteristic that influences its radiometric resolution. To optimize the cameras dwell time calculation for the along-track scanning, it is recommended to use the satellite ephemerides data to obtain its speed projection on orbit, since the satellite speed is not constant and varies according to the satellite position on the orbit, phenomena that impact the cameras dwell time estimation.

3.2 Operational procedure to manage the remote sensing sensors spectral resolution in disaster events

The electromagnetic spectrum is integrated for a range of different wavelengths or spectral energy divided into regions defined as bands, and each object or target on the ground responds to a spectral reflectance inside this spectrum or has a spectral signature. In this context, the remote sensing sensors' spectral resolution describes the ability presented for these sensors to discriminate or capture wavelengths' intervals of the electromagnetic spectrum. While finer is the spectral resolution, narrower will be the wavelength range for a particular channel or band resolved by the sensor.

For instance, there are panchromatic sensors designed particularly, the with a single channel detector and capacity to capturing or resolving spectral data in a broad wavelength range of the visible electromagnetic spectrum. Therefore, the black and white bands of the spectral data are only solved by these sensors and the physical properties are measured in the apparent brightness of the targets. In specific, the spectral information related to the colors of the objectives is not captured in the panchromatic band. Furthermore, there are multispectral sensors designed with multichannel detectors to capture spectral data in different narrow wavelength bands inside a spectral band defined, resolving multilayer images that contain both the brightness and spectral

colors information of the targets captured. On the other hand, the hyperspectral sensors can collect 50 or more narrow bands. Particularly, the multispectral bandwidths are quite large, generally from 50 to 400 μm, frequently covering an entire color; for example, a whole red portion, while the hyperspectral sensors measure the radiance or reflectance of an object in many narrow bands, often from 5 to 10 μm.

From this point of view, there are remote sensing sensors with different spectral resolutions; for instance, panchromatic band for medium spectral resolution with a center wavelength located at 0.675 μm; panchromatic band for high spectral resolution with a center wavelength situated at 0.65 μm; multispectral band with center wavelengths in: B1/blue at 0.485 μm, B2/green at 0.555 μm, B3/red at 0.66 μm, and in B4/NIR at 0.83 μm; and also infrared spectral resolution with wavelengths in short-wave infrared (SWIR), covering the next spectrum: 0.9 ± 0.05 μm ~ 1.1 ± 0.05 μm, 1.18 ± 0.05 μm ~ 1.3 ± 0.05 μm, 1.55 ± 0.05 μm ~ 1.7 ± 0.05 μm, and in long wave infrared (LWIR), with wavelengths in the following range: 10.3 ± 0.1 μm ~ 11.3 ± 0.1 μm and 11.5 ± 0.1 μm ~ 12.5 ± 0.1 μm [11, 12].

Regularly, the remote sensing sensors are designed with a specific purpose focused on the applications of their spectral bands, whose objective is to collect different types of images, taking advantage of the microwave spectrum and its incidence angle on the earth's surface; operation characteristics allow establishing the appropriated exploitation or application for each sensor, since it was before mentioned that each target and ground characteristic presents a particular spectral signature or spectral response to the different wavelengths of the electromagnetic spectrum. Reflectance behavior provides the sensors the adequate spectral information to discriminate the different details of the targets measured. In this regard, due to the importance of the spectral resolution application in disaster events considering the diverse phenomena with specific features that may occur, a methodology inside the emergency communications network to management of the remote sensing sensors spectral resolution capabilities is proposed, in order to optimize and achieve a proper performance for each spectral resolution band of the remote sensing sensors in disaster events.

Methodology based on the operational technical strategies implementation, such as: databases design and management to store the images pixels considering their spectral derivation with the aim to create the spectral signatures thereof (tagging) inside the sensors field of view, technical criterion formulation to management of the wavelengths specifications handled for each sensor in reference to the targets spectral features to be captured and the technical procedure implementation to accomplish the real-time spectral data analysis with the objective to discriminate and evaluate the diverse scenes colors that potentially can be presented in diverse images

Spectral band	Remote sensing sensors potential spectral applications in disaster management
Multispectral (MS)	For monitoring and assessment: deforestation scenarios, water mass courses, fuels leak or oil spill limits, ice block coverage, terrain geological patterns, wildfire threats and spread, droughts, vegetation classes, coastal characteristics evolution, bathymetric trends, sediment-laden waters behavior, landslide, floods, urban damages differentiation and recreation, epidemic diseases behavior, emissions of diverse gases in particular and aerosols components, between others polluting elements.
Infrared (IR)	For monitoring and assessment: volcanoes eruptions and their associated events, moisture content of soil and vegetation, earthquake damages magnitude, surfaces thermal trends, hotspots, lava lakes formation, gas emission and propagation, land desertification and deforestation evolution, coastal erosion development, wildfires progress, damages in fires scenarios by the observation through the smoke, climate behavior and floods scenarios behavior.

Table 3.
Remote sensing sensors potential spectral applications in disaster management.

based on the design of a library with the known spectral signatures of the targets previously studied or analyzed. In **Table 3**, an overview of the applications of remote sensing sensors' potential spectral resolutions in the multispectral (MS) band and infrared (IR) band is provided, taking into consideration diverse disaster scenarios.

3.3 Operational procedure to manage the remote sensing sensors images in disasters events

In each disaster event or hazard situations, the demand levels and uses of the remote sensing sensors images increase exponentially, since a large number of institutions, public or private, are responsible to coordinate all the activities' necessaries for management of different disaster events, requiring a wide variety of images with features and specifications necessaries for assessing in a reliable and expeditious way the damages caused by one or more disaster events, with the aim to identify and categorize the potentials vulnerabilities or hazards that may be present in the disaster relief phase or in other disaster management stages. It is well known that each disaster event has its own characteristics; for such reason during the disaster management, different types of images with details or features in specific of the zones affected by disasters are required in order to evaluate and have a well understanding of the phenomenon produced, and so, this way formulates the more suitable strategies to carry out the disaster management tasks according to the scenarios presented. In essence, the accessibility to different images levels or products from the remote sensing sensors is a significant resource in the various stages of disaster management. Currently, the remote sensing satellites and their ground segments have the capability to provide a variety of images levels or products fundamental to manage disasters events in the phases of preparedness, assessment, and mitigation. However, in **Table 4** regarding the Remote Sensing Satellite-1 and the Remote Sensing Satellite-2 selected to be integrated into the emergency communications network developed in this chapter, the products and the general characteristics of the images captured and processed in the ground segments of these satellites platforms are specified. Essential images products need to be managed by taking into consideration the specifics of operational requirements involved in each disaster events.

Also in all the activities executed along the disaster management, the response time to the different hazard scenarios is the paramount element to optimize the actions that will be adopted during the disaster events management. In this sense, the remote sensing sensors' images products provide the necessary information to give a quick response to an extensive variety of disaster events, and even to their consequences by

Products levels	Images products specifications
Level 0: Data set in series or rows	Synchronized data frame, compatible with computerized data protocols and software packet
Level 1: Products with radiometric correction	Matrix of data radiometrically corrected, without geometric correction
Level 2: Products with systematized geometric correction	Data with radiometric and geometric correction using systematic models, without the use of terrestrial control points (GCP)
Level 3: Products with precise geometric correction	Radiometric and geometric correction using terrestrial control points (GCP)
Level 4: Products corrected through digital elevation terrestrial models	Data with radiometric and geometric correction using terrestrial control points and digital elevation terrestrial models in order to remove the terrain displacement effects, produced by the relief deformations

Table 4.
Remote Sensing Satellite-1 and Remote Sensing Satellite-2 images products specifications.

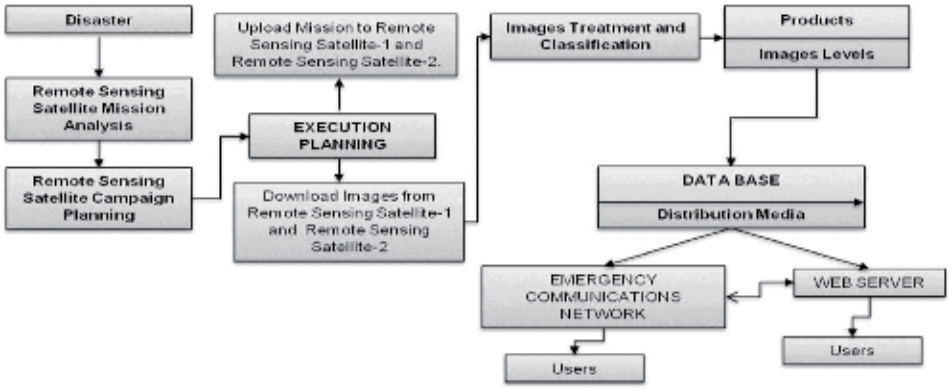

Figure 9.
Remote sensing sensors model to images management and processing at ground segment level in emergency scenarios.

means of the analysis and assessment of the factors tied to the phenomena occurred and recreated in the images captured through the remote sensing sensors using different spatial and spectral resolutions; taking into consideration, every sort of disaster has its own physical characteristics or particularities that require be evaluated through the analysis of images whose properties describe the details related to a particular disaster event or natural phenomena under study. As described in **Table 4**, the Remote Sensing Satellite-1 and Remote Sensing Satellite-2 typical raw data are treatment and processing using the software applications and methods available in the ground station of both platforms to obtain images products by levels. A process is carried out with the aim to reduce the radiometric and geometric errors in the images obtained and also to create images with the necessaries information to evaluate and understand the different disaster events based on their characteristics.

In specific, the radiometric correction in the remote sensing satellite images processing consists in removing from the images captured by the sensors all the errors effects created by the sun incidence angles and then added to the images from different atmospheric factors during their capturing; whereas the images geometric correction is a process that has the objective to remove from the images the geometric distortion errors, through the relation established between the images coordinate system and the geographic coordinate system used as reference. This correction is achieved using the sensor calibration data, the position and attitude measured data of the satellite in orbit, the terrain control points and the information about the atmospheric conditions that may affect the images captured. In consequence, due to the notable value of the remote sensing sensors images products in the disaster management, images with particular characteristics and suitable to analyze diverse type of disasters and even to support in the decision-making during the disasters management, there is the necessity to implement fast and accurate systematic processes for management of the sensor's images products at the ground segment in disaster scenarios. Hence, a systematic model is proposed in **Figure 9** for managing and processing the remote sensing satellites images at the ground segment in emergency response; considering the Remote Sensing Satellite-1 and Remote Sensing Satellite-2 ground segment infrastructures.

3.4 Communications satellites transponders and radio frequencies characterization for emergency services in disaster events

Due to the dizzying evolution of space technology, nowadays there are communications satellites with different payload characteristics and communication capacities and also ground stations, teleports, and hardware for communications

with a large variety of operation characteristics; whereby in disaster management, the analysis and characterization of the communications satellites payload and their capacities are crucial at the time to plan the communications services required in each disaster phase, and even it is an operational procedure necessary to recover the terrestrial communication services when their infrastructures are affected by the disaster events. In the same way, the communications satellites payload analysis provides the essential information to implement services and design communications links reliable and adjusted to the scenarios demanded in all the disaster management cycle. In the satellite communications field, there are a number of radio frequencies ranges used for communications links, such as C-band, X-band, Ku-band, Ka-band, and Q/V-band, each of them having their own propagation characteristics in the space, which makes one frequency more or less vulnerable with respect to other one when they propagate through the free space and are affected by diverse phenomena that take place at the earth atmosphere.

Generally, the most used frequencies bands in commercial communication satellites are the C-band, Ku-band, and Ka-band. Equally, many are the services and applications that can be implemented using the aforementioned frequencies bands. From this point of view, in this chapter, the transponders and radio frequencies characterization for emergency services in disasters is focused directly in the C-band, Ku-band, and Ka-band communications payload, with the objective to define the adequate use of these frequencies bands, at the time to implement technologies solutions in disasters scenarios.

However, with the purpose to describe in practical way the transponders and radio frequencies characterization methodology to implement useful and reliable emergency communications services in disasters, the communications payload of the satellite platform Satnet-3 is selected; communications satellite proposed to operate in the emergency communications network, designed with ben-pipe transponders technology type, is also known as transparent payload, and mainly integrated for the next devices: sixteen (16) transponders in C-band with 36 MHz of bandwidth and uplink frequency range from 6050 to 6350 MHz and downlink frequency range from 3825 to 4125 MHz. Fourteen (14) Ku-band transponders with 54 MHz of bandwidth and an uplink frequency range from 14,080 to 14,500 MHz and downlink frequency range from 11,280 to 11700 MHz. Three (03) Ka-band transponders with 120 MHz of bandwidth and frequency range for the uplink from 28,800 to 29,100 MHz and frequency range for the downlink from 19,000 to 19,300 MHz, one (01) antenna in C-band, one (01) antenna in Ku-band for the north beam and one (01) antenna in Ku-band for the south beam, likewise one (01) antenna in Ka-band [13].

Fundamentally, the Satnet-3 payload operates in three (03) frequencies ranges or bands, such as C-band, Ku-band, and Ka-band. Each of these bands is located inside the microwave spectrum frequencies range; electromagnetic waves sensitive to multiple attenuations factors when they propagate through free space are affected by the moisture of the atmosphere and others atmospheric conditions. For instance, for frequencies above 10 GHz, phenomena as rain, clouds, fogs, and diverse particles in the space have an important impact on their propagation and attenuation. In this regard, considering the communications satellite Satnet-3, as well as its payload operation frequency bands, and the phenomena or atmospheric factors that can affect the propagation of these frequency bands in the free space due to the attenuation caused by the phenomena that take place in troposphere, the characterization of the Satnet-3 frequencies spectrum is carried out, and illustrated in **Table 5**, their potential applications in order to implement communications links and emergency services reliable in diverse disasters scenarios or hazard existing.

Frequency band	Potential uses in disaster events	Frequency vulnerability
C-band	Earthquakes, Landslide, Volcanic eruptions, Subsidence of earth, Storms, Tornado, Hurricane, Wildfires, Typhoons, Tsunami, Floods, Coastal Erosion, Desertification, and Deforestation	This rage of frequency works properly without significant perturbation in adverse atmospheric conditions
Ku-band	Earthquake, Landslide, Volcanic eruptions, Subsidence of earth and Wildfires	Frequency range that cannot be used in adverse atmospheric conditions
Ka-band	Earthquake, Landslide, Volcanic eruptions, Subsidence of earth and Wildfires	Frequency range that cannot be used in adverse atmospheric conditions

Table 5.
Satnet-3 frequencies bands characterization for emergency services implementation in disasters.

Characterization takes into account the following technical aspects: for C-band frequencies spectrum used for Sanet-3 from 6050 to 6350 MHz (uplink frequencies) and from 3825 to 4125 MHz (downlink frequencies), in heavy rain around 16 mm/h, the signal attenuation is 0.03 dB/km, in moderate rain close to 4 mm/h, the C-band signals attenuation is nearly to zero, and the attenuation due to clouds and fog is very low. In the same way, for Ku-band Sanet-3 frequencies from 14,080 to 14,500 MHz (uplink frequencies) and from 11,280 to 11,700 MHz (downlink frequencies), in heavy rainfall around 150 mm/h, the signal attenuation is approximately 5 dB/km and in moderate rainfall, it is close to 0.5 dB/km. Equally for Ka-band from 28,800 to 29,100 MHz (uplink frequencies) and from 19,000 to 19,300 MHz (downlink frequencies), in heavy rainfall around 150 mm/h, the signal attenuation is just about 14.5 dB/km and in moderate rain, the signal attenuation is near to 0.9 dB/km; for both Ku and Ka-band, the signals attenuation per clouds and fog must not be neglected [14].

As result, in **Table 5**, it is noticed that the Satnet-3 C-band payload and radio frequencies offer more reliability, taking into account their less vulnerability against adverse atmospheric conditions in case of disasters, while the Ku and Ka frequencies bands are more vulnerable to the unfavorable atmospheric conditions, limiting the use of them only to specific disaster situations.

3.5 Technology solutions formulation for disasters management

The space information products and services are essential to build strong and effective response mechanisms that enhance the media and tools required for emergency response in disasters. Moreover, information technology and different communications services are the backbone in all the phases of the disaster management, due to the wide variety of data from diverse sources that must be gathered, organized, and displayed logically for decision-making in events of disasters. From this perspective, the space technology and in specific the communications satellites inside the emergency communication network play an important role, because they have the function of handling all the communications traffic and also provide the technology solutions in reference to the communications services required in the areas affected by one or more events of disaster.

In the same way, the communications satellites in combination with the remote sensing satellites in the emergency network have the ability to transmit and receive different types of images in function to the technologies solutions implemented. For such aim, the communications satellites teleport and also their associated infrastructures must meet different technical specifications to cover the

communications services requirements and the technology solutions operation specifications required for emergency response. It becomes important to point out that the technology solutions implementation process in disasters is based on the analysis of diverse aspects; some of them are mentioned as follow: disaster scenario determination, disaster classification and magnitude determination, space technology resources availability identification, communications satellites and remote sensing satellites operation technical specifications analysis, analysis of the demand for information and communication services, data flow analysis, terrestrial communications networks assessment and critical emergency communications network planning, among others, related with the characteristics of each disaster type.

However, the satellite link budget software Satmaster is the tool used in the emergency communications network to design the communications links and implement the services required in disaster. This software is widely used for satellite service providers to carry out the satellites links budget calculation since it is supported for specific communications standards and atmospheric models used to calculate the communications links budget, considering the services requirements and hardware specifications that had been defined to implement different technology solutions of services.

On the other hand, to exemplify the technology solutions implementation methodology in the emergency communications network, the communications satellite Satnet-3 and its teleport is regarded and selected to be integrated in the emergency communications network, both with the ability to support the implementation of different technology solutions to satisfy the diverse communications services required in the areas affected by disasters. The Satnet-3 teleport counts with satellite HUBs to provide a large variety of services, also with various communications infrastructure resources and connection to the national communication terrestrial network, among other capacities for communications services.

In consequence, as example, various communications services solutions that can be implemented through the Satnet-3 platform and its teleport infrastructure, integrated to the emergency communications network for disaster management, are described as follows: broadband satellite internet services, remote access for video conference services, radio and TV broadcasting services by satellite, dynamic databases to manage and store human or material losses due to disasters, remote access for video camera connections, cellular phone services over satellite, facilities with the technology required at the disaster site to manage hazard events or download and processing images, infrastructures for cloud computers and physical networks, unmanned aerial vehicle (UAV) networks, command and control center for land surveillance or assessment, technology platforms for exchange and images processing

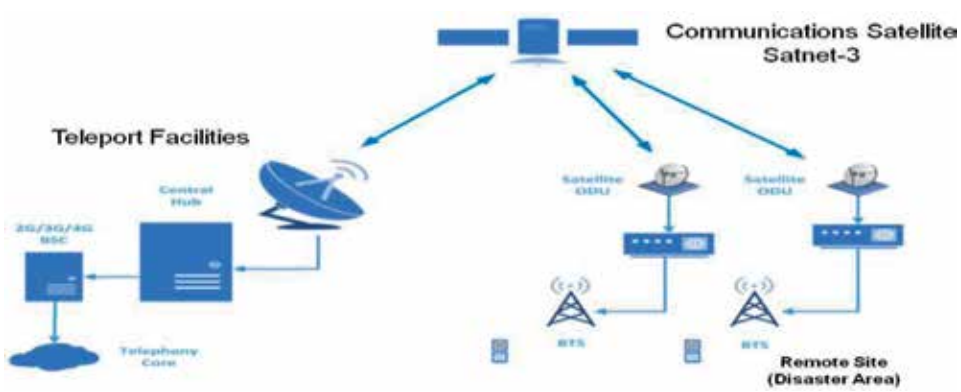

Figure 10.
Technology solutions for disasters management cellular backhaul-SCPC over satellite.

Cellular backhaul-SCPC teleport site to radio base station in remote site (outbound link)	
Uplink and downlink operation parameters	
Transponder (TP): Ku-1A	Teleport EIRP: 68.41 dBW
Carrier type: digital modulation	Teleport SFD: −95.55 dBW/m^2
Teleport antenna TX gain: 63.90 dBi	Carrier Modulation: QPSK
Teleport antenna RX gain: 62.18 dBi	Carrier Bandwidth: 1.9575 MHz
Uplink frequency: 14167.60 MHz	TP Carrier Occupied BW: 1.9800 MHz
Downlink frequency: 11367.60 MHz	TP Carrier Downlink EIRP: 22.58 dBW
Carrier polarization: horizontal/vertical	Carrier to Noise: 17.52 dB
Teleport HPA power required: 4.51 dBW	E_b/N_0: 5.4 dB

Table 6.
Cellular backhaul-SCPC outbound link budget.

Cellular backhaul SCPC radio base station in remote site to teleport site (inbound link)	
Uplink and downlink operation parameters	
Transponder (TP): Ku-1A	Remote site EIRP: 51.47 dBW
Carrier type: digital modulation	Remote site SFD: −111.64 dBW/m^2
Remote site antenna TX gain: 47.2 dBi	Carrier modulation: QPSK
Remote site antenna RX gain: 44.5 dBi	Carrier bandwidth: 1.9575 MHz
Uplink frequency: 14166.37 MHz	TP carrier occupied BW: 1.9800 MHz
Downlink frequency: 11366.37 MHz	TP carrier downlink EIRP: 21.56 dBW
Carrier polarization: horizontal/vertical	Carrier to noise: 16.95 dB
Remote site HPA power required: 4.27 dBW	E_b/N_0: 4.9 dB

Table 7.
Cellular backhaul-SCPC inbound link budget.

at different levels, star or mesh topologies for very small aperture terminal (VSAT) networks, among other technology resources, useful in the disaster management field. In this sense, the general architecture of a cellular backhaul single channel per carrier (SCPC) implemented over satellite in case of emergency is shown in **Figure 10**, utilizing the communications satellite Satnet-3 and its teleport.

Likewise, considering **Figure 10**, which describes the architecture of a cellular backhaul by satellite in star topology, using the software Satmaster (tool for communications links design), the link budget calculation for the single channel per carrier (SCPC) service correspondent to the implantation of a cellular backhaul was carried out, using the Satnet-3 Ku band transponders and its teleport, for disaster events that demand this type of services. **Tables 6** and **7** present the results obtained through the Satmaster communications tool for the uplink and downlink of the aforementioned service.

3.6 Emergency communications network topology for disaster events management

After the formulation and analysis of diverse operational strategies with the aim to optimize the processes necessary to integrate the communications satellites platforms and remote sensing satellites platforms and their ground stations inside

a network useful to manage different disaster events, in **Figure 11**, the structural topology of the emergency communications network for disaster events management designed in this chapter is presented. Network has a main function to serve as an operational structure to back up the conventional communications networks infrastructures affected by disasters, and in the same way, be an alternative infrastructure that can provide the capacities to implement diverse technology solutions and communications services to support in the tasks inherent to the disasters management in each of their phases.

Nevertheless, the communications satellites platforms in the emergency communication network has the principal function to handle all communications traffic between the areas affected by disasters and the entities in charge to manage the recuperation tasks in disasters, and also provide the necessary channels through their payload to implement the required technology solutions and the communications services demanded in disaster scenarios. Equally, the communications satellites platforms in combination with the remote sensing satellites in the emergency network have the function to transmit and receive different types of images captured for the remote sensing satellites and processed in their ground stations, through the technology solutions implemented for such aim.

In this sense, regarding the communications satellite Satnet-3 and the Remote Sensing Satellite-1 and Remote Sensing Satellite-2, satellites platforms are selected to design and implement the emergency communications network presented in this chapter; Satnet-3 in the emergency network has the main function to handle all the communications traffic and also provide the capacity to implement the communications technology solutions required in the areas affected by the disasters according to its payload capacity and teleport infrastructure. In combination with the Remote

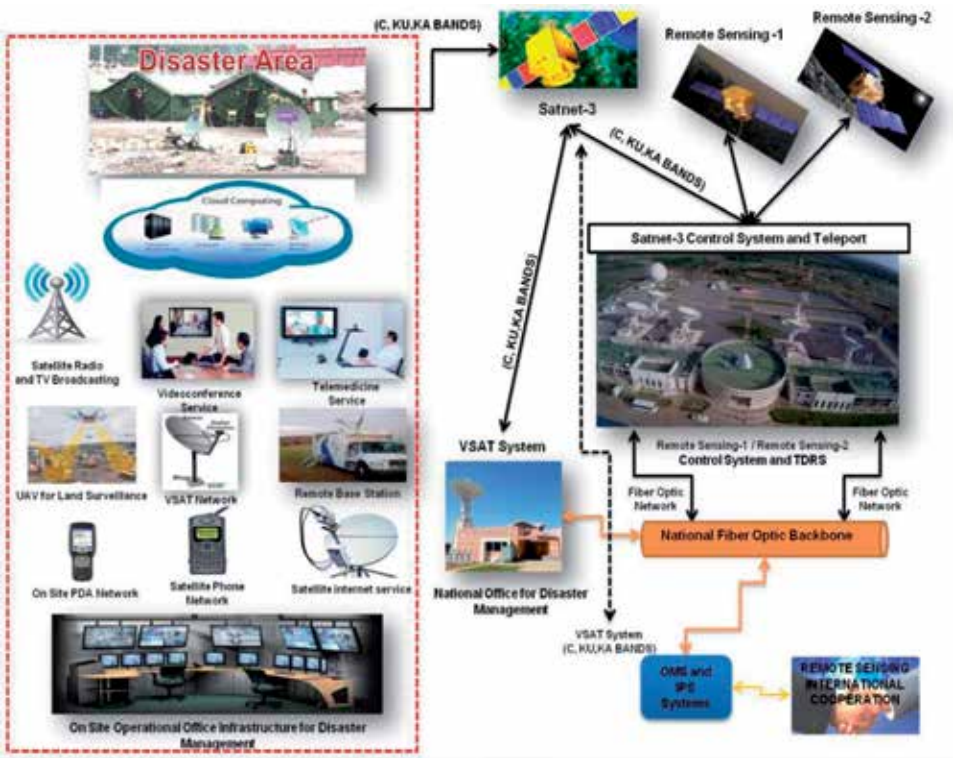

Figure 11.
Emergency communications network topology for disaster events management.

Sensing Satellite-1 and the Remote Sensing Satellite-2, Satnet-3 has the aim to receive images from the ground station of both remote sensing satellites and then transmit thereof through the technologies solutions implemented to the different affected areas in disaster events. The main task of the Remote Sensing Satellite-1 and Remote Sensing Satellite-2 is to capture images over the affected areas according to the different missions loaded from the ground station, following the operational strategies designed to manage both platforms in emergency situations for a quick and reliable response. Additionally, the communications network designed is integrated to a fiber optic backbone which provides to the network the capacity to transmit and receive images and other data types through terrestrial communications infrastructure that are also available in disaster scenarios.

In this way, the emergency communications network for disaster management allows to put in operation the next technology solutions: broadband satellite internet services, remote access for video conference services, radio and TV broadcasting services by satellite, dynamic databases to manage and store human or material losses due to disasters, remote access for video camera connections, cellular phone services over satellite, facilities with the technology required at the disaster site to manage hazard events or download and processing images, infrastructures for cloud computers and physical networks, unmanned aerial vehicle (UAV) networks, command and control center for land surveillance or assessment, technology platforms for exchange and image processing at different levels, star or mesh topologies for very small aperture terminal (VSAT) networks, among other technology solutions or services necessary to manage the disaster events scenarios where the terrestrial communications infrastructures have been damaged or may be at risk of failure due to the disaster's impacts. Likewise, in **Figure 11**, some of these technologies solutions or communications services that can be implemented through the emergency communications network are described as well.

4. Conclusions

Diverse organizations in charge to develop disasters management activities at a worldwide level focus on numerous studies for the improvement and formulation of new technologies to facilitate the execution of the procedures necessaries to carry out the disasters management processes in multiplicity hazard scenarios. Technologies can be novels and reliable to manage and plan the preparedness, mitigation and recuperation tasks in disasters. From this perspective, nowadays, the space technology makes available different satellite platforms on-orbit operation that provides the technology resources necessaries to increase and optimize the response capacities to manage the disaster events in their distinct phases. Therefore, the design of the infrastructure, such as emergency communications networks for disaster management by means of the communications satellites and remote sensing satellites integration, inside an operational topology operates in emergency scenarios; it is a novel communications and remote sensing applications platform useful to manage disaster events in all their phases. This type of emergency communications networks is an essential and adequate communications model to enhance the preparedness, mitigation, and recovery of the communications systems which can be affected by disasters, and besides, it is a reliable infrastructure to images capturing and processing in disaster scenarios.

However, the importance and application of the emergency communications networks in disasters are invaluable as it is noticed in the practical cases described through this chapter. For instance, in the Dominican Republic case, the country has often affected by natural disasters, which has an emergency communications

network designed to take advantage of the different data types received from communications satellites, remote sensing satellites, meteorological satellites, telemetry systems, and specialized equipment to manage a technological platform useful for forecast, early warning, and disaster events mitigation that may take place in this country.

Likewise, from the field experiences learned in the Sichuan earthquake, phenomenon occurred in the People Republic of China on May 12, 2008, the use of the remote sensing satellites and communications satellites simultaneously to manage this disaster was a resource useful to carry out diverse tasks of evaluation, mitigation, and recovery of the areas affected by the aforementioned earthquake. In specific, during the Sichuan earthquake, the remote sensing images with different spectral and spatial resolution were helpful to analyze the multiple damages caused by this disaster event, as well as to establish the measures needed to initiate the infrastructures damaged during recovering process. In relation to the communications satellites role in the Sichuan earthquake, these platforms were used to recover the communications services and to support the alternatives technologies solutions implementation for different data types exchanges between the entities in charge to manage the disaster. All the mentioned tasks developed by both satellite technologies in the Sichuan earthquake are the clearest basis of the operational philosophy implemented in the emergency communications networks for disaster management designed through the integration of the communications satellites and remote sensing satellites and, fundamentally, the operational perspective approached in the work presented.

In this sense, the emergency communication network for disaster management designed and described in this chapter is an infrastructure that provides the resources adequate to put in operation different communication technologies solutions and a variety of options or schemes to the images exchange between the actors involved in the disasters management tasks, and so as for the population in general affected by disasters directly. In the same way, the emergency network design is supported by a series of operational strategies formulated to enhance the communications services implementation in disasters through the adequate characterization of the communications satellites payload frequencies bands, as well as by operational procedures to optimize the remote sensing satellites spatial and spectral resolution during their operation inside the emergency communications network with the aim to improve the images capturing and management in events of disasters. In summary, the emergency communications network topology developed provides the capacities or functional resources to make possible the effective response to recover the public and private terrestrial communications infrastructures and services in disasters scenarios. Alternatively, the network may operate at an international scale, since it has the capacity to be managed in order to support other countries affected by disasters with damages on their terrestrial communications infrastructures. Considering only for such aim, the coverage region of the communications satellites that integrates the network, because of their beams coverage change by regions according to the satellite orbit position, unlike to the remote sensing satellites whose coverage is global.

Acknowledgements

I would like to thank Engineer Liliana de la Cruz Alvarez de Burguillos for her advice and encouragement throughout this project; her continued support and willingness to help me were of great value to develop this work.

Author details

Carlos Alberto Burguillos Fajardo

1 Regional Centre for Space Science and Technology Education in Asia and the Pacific, International School Beihang University, Beijing, China

2 Bolivarian Agency for Space Activities (ABAE), Simón Rodríguez Technology Complex, Caracas, Venezuela

*Address all correspondence to: shincomlabvene@hotmail.com; cburguillos@abae.gob.ve

References

[1] ESCAP, Hasan S, editors. Information and Communications Technology, Sound Practices in Space Technology Applications for Disaster Risk Reduction and Inclusive and Sustainable Development. Bangkok, Thailand: Disaster Risk Reduction Division, ESCAP Space Applications Section; December 2013, p. 3

[2] Mehdi A. The role of the mobile satellite services and remote sensing satellite in disaster management. International Journal of Modern Engineering Research (IJMER). 2012;**2**(6):4010-4013. DOI: AD2640104013

[3] Narain A. Space technology in disaster management. International Journal of Scientific & Engineering Research. December 2013;**4**(12):200-208. ISSN: 2229-5518

[4] ITU. Telecommunications SAVE LIVES. The Role of Information and Communication Technologies in Disaster Response, Mitigation and Prevention. Collection of the Basic Texts of the International Telecommunication Union Adopted by the Plenipotentiary Conference: ITU; 2003. pp. 3-4. BDT-01/2005

[5] Hodgson M, Bandana K. Modeling the potential swath coverage of nadir and off-nadir pointable remote sensing satellite sensor systems. The Cartography and Geographic Information Science. 2008;**35**:147-156. DOI: 10.1559/152304008784864668

[6] Mather. Developments in Water Science, Resolution of Remote Sensing Data. 1st ed. Amsterdam, Netherlands: Elsevier Science; 2003. 131 p. ISBN: 0-444-51429-5, 1987, cited by Jain SK, Singh VP

[7] Canada Center for Remote Sensing, editors. Tutorial: Fundamentals of Remote Sensing. Natural Resources Naturelles. NRCAN; 2016. p. 39

[8] Push Broom and Whisk Broom Sensors [Internet]. 2017. Available from: https://www.harrisgeospatial.com/Support/Self-Help-Tools/Help-Articles/Help-Articles-Detail/ArtMID/10220/ArticleID/16262/Push-Broom-and-Whisk-Broom-Sensors [Accessed: 2017-06-20]

[9] What is the difference between a Whisk Broom Scanner and Push Broom Technology [Internet]. 2017. Available from: https://www.quora.com/What-is-the-difference-between-a-whisk-broom-scanner-and-push-broom-technology [Accessed: 2017-07-01]

[10] Hartley RI, Gupta R. Linear push broom cameras. In: Eklundh JO, editor. Computer Vision— ECCV '94. ECCV 1994. Lecture Notes in Computer Science, Vol. 800. Berlin, Heidelberg: Springer; 2005. pp. 555-566. DOI: 10.1007/3-540-57956-7_63

[11] VRSS-1 Venezuelan Remote Sensing Satellite-1/Francisco de Miranda [Internet]. 2013. Available from: https://directory.eoportal.org/web/eoportal/satellite-missions/v-w-x-y-z/vrss-1 [Accessed: 2017-05-15]

[12] ABAE, CGWIC. Handbook VRSS-2 Performance Specifications. Section 1 Spacecraft. Annex 2, Revision 1. Contract Annex for VRSS-2 Program. Beijing, China: China Great Wall Industry Corporation; Jan 2014. p. 15-24

[13] Burguillos C, Deng H. Mathematical model to estimate the Venesat-1 transponders anode voltage evolution in-orbit operation. In: Proceedings of the 69th International Astronautical Congress (IAC), Space Communications and Navigation Global Technical Session; 01-05

October 2018; Bremen, Germany: 2018. pp. 2-3. DOI: IAC-18, B2, 8-GTS.3, 2, x47429

[14] Chai J. Handbook System Design of Satellite GCS. Radiofrequency Atmospheric Attenuation, BITTT Ground Segment Training. Venesat-1 Program. Beijing: Beijing Institute of Tracking and Telecommunication Technology; July 2007. p. 25

Chapter 11

Interview of Natural Hazards and Seismic Catastrophe Insurance Research in China

Jian Zhu

Abstract

In order to solve the increasingly serious threat of natural disasters in western Pacific coastal region, a new life-cycle cost analysis method is presented to evaluated the possible loss of natural disasters in the future in China. At the same time the research also lays a foundation for the promotion and establishment of earthquake catastrophe insurance in China. The estimation of earthquake losses for example RC buildings and industrial buildings based stochastic method models is the focus of the research. An assembly-based mixture fragility framework is firstly adopted for modeling and seismic loss estimation. The damage of the structural and non-structural which connected into response of the structures under given stochastic motions use nonlinear incremental time-history analysis to estimate in a detailed. Description of the uncertainty of all parameters in life-cycle cost (LCC) research through appropriate probability distributions to reach quantification of the LCC expected value. Moreover, the study is also to give the expected seismic catastrophe insurance premium (CIP) for two types of typical buildings in high seismic intensity areas of China based probabilistic seismic risk assessment in its service lifetime.

Keywords: natural hazard, life-cycle analysis, seismic catastrophe insurance premium, multi-storey RC buildings, single-storey industrial buildings, seismic fragility analysis, Monte Carlo samplings, stochastic simulation

1. Introduction

Recent the natural disasters such as earthquakes and hurricanes worldwide, especially those in the Pacific rim region such as Wenchuan Earthquake (2008), Nepal Earthquake (2015) and Indonesia Earthquake & Tsunami (2005, 2018), have demonstrated that the insufficient structural performance of buildings may lead to high disaster vulnerability on human society. Post-disaster recovery and reconstruction also test a country's disaster response capacity and economic strength. The direct loss of Wenchuan Earthquake in Western China (Ms8.0) was 845.1 billion Yuan in 2008, and only 1.66 billion Yuan was paid out by insurance, which can only rely on the huge amount of free economic assistance from the central government. But people in other Asian disaster regions are not always so lucky, Earthquake and tsunami heavily hit local society and economy in some Asian countries such as

Nepal or Indonesia which has no catastrophe insurance, and often leading to long-time local economic decline.

Most of Asian-Pacific regions located around the Pacific Rim seismic activity zone. High seismic intensity leads more high vulnerability to natural disasters due to particular geographic location. Since current building technology cannot avoid the negative effects of natural disasters such as earthquake, typhoons tsunami and atmospheric corrosion on the engineering economic loss, environment loss and human fatalities in whole society. It is necessary to evaluate the severity of the effects of various natural disasters. Such assessment study is not only aimed at the impact of a single disaster, but also should be based on the impact of long-term factors such as the life-cycle performance of engineering products.

Building structures are important places for human to work and live. Its durability, safety and comfort need to be guaranteed during life-cycle service. Building structure is located in the earth's natural environment, so during the service of the inevitable from the nature of wind, sunshine, rain, smog and other external factors. Some of the influences of these external environmental factors on civil engineering structures are beneficial. For example, mild air is beneficial to the strength growth of concrete in the long run, but most of the environmental influences from nature are harmful to the performance of buildings. Some external factors on the impact of buildings are potential and long-term adverse effects, such as due to global greenhouse gas emissions caused by the carbonization of concrete, acid gas corrosion of reinforcement, waves corrosion of Marine engineering structures. Which influence the modern civil engineering life-cycle sustainability. Other natural hazardous factors such as earthquake, typhoon, flood and tsunami are more dangerous and sudden affection. Human have defines such natural hazard as natural disasters. Now with the rapid development of economy in Eastern Asian coastal land, more population flow into metropolis, where infrastructures and buildings face huge pressure to long-term safe service in resisting natural hazards. For example the East Japan Earthquake (Ms9.0) on March 11, 2011 and the tsunami caused the damage of Fukushima nuclear power. The extremely serious accident of nuclear leakage, which caused extremely serious nuclear pollution to the Marine water environment of the western Pacific Ocean, caused long-term immeasurable loss.

According to U.S. risk analyst AIR Worldwide, direct earthquake insurance losses from Tohoku Earthquake caused by industrial and civil buildings, infrastructure amount to nearly $35 billion, which is almost equal to the total disaster losses of the global insurance compensation in 2010.

Now three procedures have be titled to minimize their devastating effects by enhancing resilience in communities, that is, by reducing (1) system failure probability, (2) consequences of system failures, and (3) fee and time to recovery. So in the past several decades Load-and-resistance-factor design (LRFD) was used as the framework under which many new and existing structures are analyzed for seismic adequacy. This approach seeks to assure performance primarily in terms of failure probability of individual structural component, such as strong-column-and-weak-beam requirement. But unfortunately past seismic disasters revealed that LRFD design could not meet the above need for minimizing system failures probabilities and decreasing life and economic losses.

Performance-based earthquake engineering (PBEE) methodology finally was be developed in 2000 by Pacific Earthquake Engineering Research (PEER) shown in **Figure 1**. This approach involves combined numerical integration of all the conditional probabilities to propagate the uncertainties from one level of analysis to the next, resulting in probabilistic prediction of performance. The PBEE frame work consist of four steps, respectively is Hazard analysis, Structural analysis, Damage analysis and Loss analysis, The PBEE now has become future research basis spirit in

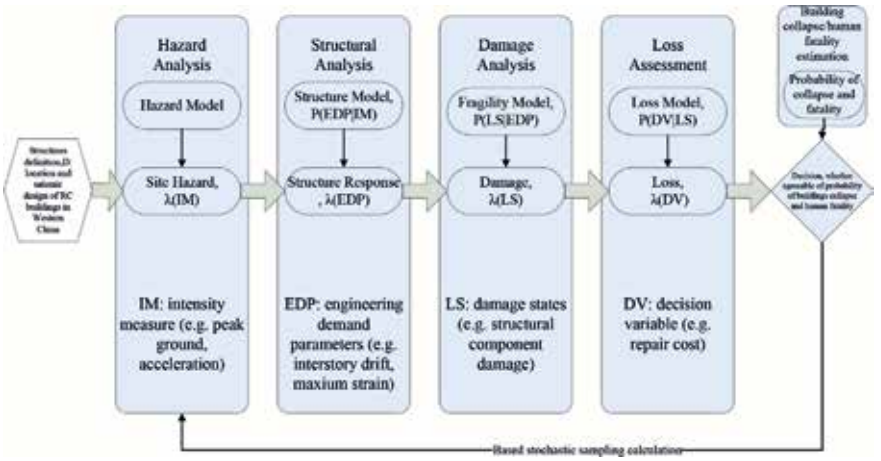

Figure 1.
PBEE framework methodology by PEER.

civil engineering all of the world. Uncertainties are included and propagated through each step of the PBEE process [1].

At present for better approach above targets, many researchers further push the research performance-based engineering forward a great step over the entire life-cycle of the buildings. That is definitely exciting prospect but there also have several obstacles must be fronted at same time.

Seismic life-cycle research requires proper integration of following three factors: (i) probability approaches for treating the uncertainties related to the seismic hazard and to the structural dynamic behavior including structural and non-structural components in the buildings, (ii) recovery time and seismic loss estimation methodologies for evaluating the structural performance based random probability and socioeconomic criteria, (iii) algorithms for efficient evaluation of the resultant multidimensional integrals completely quantifying seismic fragility and loss are shown in **Figure 2**.

In 2013 December super typhoon Haiyan landed in Philippines, and resulted in 6300 life losses, millions people without shelter and $2 billion in damage. So the most important mechanism is to rescue the refugees and compensate seismic loss from insurance companies. But how to determine buildings insurance premium ratio based seismic or typhoon loss estimation is a key problem in many Asia

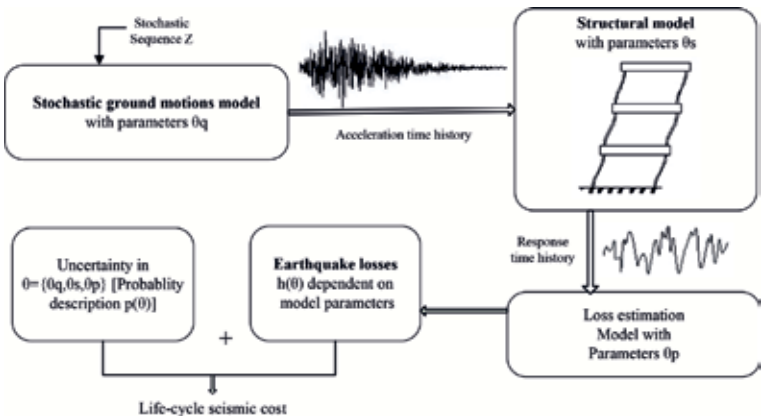

Figure 2.
Stochastic parameters of PBEE framework methodology.

countries. Refugees' buildings loss could not effective estimation because of absence reliable based research of life-cycle loss estimation. That is core reason why many Asia countries have not published normal disasters insurance policy at moment.

Earlier methodologies for seismic loss estimation mainly expressed seismic losses in terms of the global reliability characteristic of the structural system. Recent advances in PBEE quantify more appropriately repair cost, casualties, and downtime in relation to the structural or even on a detailed, component level (such as partitions, beams and columns) response [1], using seismic fragility curves to develop such a relationship. Nonlinear time-history as an more powerful analytical tool now accepted by many researchers in calculating seismic damage under a given earthquake excitation.

Nonlinear incremental time-history analysis is most popular methodology, which can facilitate such a description according local hazard levels through Intensity Measures (IMs) that represents the dominant features of the seismic excitation, and subsequent scaling of ground wave records to different IM values, as prescribed by a probabilistic seismic hazard analysis. Stochastic ground waves are chosen by fitting for response spectrum based China seismic code (GB50011-2010, 2] through online searching and selecting tool of PEER ground motion database, which represent samples of possible future ground waves for each hazard level of different regions in China. Additionally recent concerns related to ground motion scaling also in consideration into the stochastic ground wave model. The parameters of these ground wave, for example, duration of strong motion, can be related to earthquake (type of fault, moment magnitude and rupture distance) and site characteristics (shear wave velocity, local site conditions) by appropriate predictive relationship. Description of the uncertainty for the earthquake characteristics (moment and rupture distance) and for the predictive relationships, through appropriate probability models, to show a complete and detailed probabilistic description of potential future ground motion time waves. Therefore, the emphasis of primarily research is located in development of stochastic ground motion models.

In consideration of complexity and different regional characteristic about life-cycle seismic loss analysis, a whole set of innovated life-cycle analysis procedures based stochastic probability have been raised in this article based past PBEE research results.

The methodology indeed expand research time to life-cycle of buildings based PBEE, so basically it also consist of four steps same as PBEE framework. **Figure 3** shows the optimized methodology in research based PBEE.

This article is focus on a simulation-based, comprehensive research framework that aims to put the life-cycle loss estimation analysis into reality. Firstly life-cycle

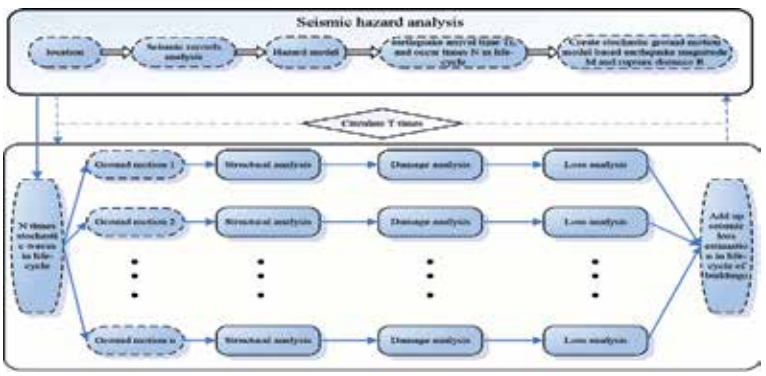

Figure 3.
Optimized framework of life-cycle loss estimation in research.

stochastic ground motion models including occurrence time point of every earthquake are adopted for the seismic hazard description in terms of detailed and versatile characteristic of seismic risk as well as balance in computation efficiency. Assembly-based vulnerability method is also used in evaluating seismic response of structural components based random probability in damage analysis. Therefore, life-cycle seismic cost is qualified by its expected value over the probability models and stochastic simulation is suggested for its evaluation. In the end, an revised probability life-cycle sensitivity analysis for identification of important risk factors for the life-cycle loss concept is also reviewed based former research results and stochastic sampling concepts. The analysis aims to identify the importance of the various risk-factors towards the overall performance of the structural system.

2. Seismic hazard analysis

Predictable ground motions in the special site firstly are considered in research as outer excitation to test structural system's performance. Yinchuan city which locate in high seismic hazard region in Western China was selected as sampling site in the research. A terrible earthquake (Ms8.0) was happened in Yinchuan district in 1739 and thousands of people died and earthquake disaster loss is very huge in record of local history. There are many NE-trending fault zones in the area. The local area is 180 km from north to south and 60 km from east to west. It is roughly 30 degrees northeast and has a total area of 7790 Km^2. According to the Chinese Building Seismic Code (GB50011-2010) [2], the area is 8 degree seismic intensity design area, and the basic seismic acceleration value is 0.2 g. The area is a fault basin formed by the Cenozoic. The exposed strata are dominated by Quaternary sediments. The soil foundation is dominated by soft sand soil and is classified as II sites group, the site basic design period is 0.4 s. The thickness of the soil layer is generally between several hundred meters and 1 km, and the shear wave velocity of the soil layer $V_{s30} = 150 - 300\text{m/s}$.

Life-cycle model of a seismic hazard specifies (1) the random arrival times, $T_1, T_2, \cdots$, of individual events at a site during a reference period τ, and (2) the random properties of the ground motion hazards under considerations at $T_1, T_2, \cdots$. The random properties involves: stochastic quantification of the earthquake intensity measure based precious activity matrix at the site and creating stochastic ground motions consistent with the intensity hazard.

Monte Carlo sampling algorithms can be used for generating samples of lifetime seismic hazard at a given site during a reference period τ. Therefore, a life-cycle hazard sample consists of the arrival times of individual events and the properties defining their probability law.

Near-fault ground strong pulse is also considered into research based earthquakes survey recent years in many places of the world. So the final stochastic ground motion consist of low-frequency (long period) and high –frequency components and be combined to form the acceleration time history.

2.1 Activity matrix and event arrival

The activity matrix of seismic hazard at a given site delivers the annual rate of occurrence for events of the hazard corresponding to earthquake magnitude, M, and rupture distance, r. We can plot activity matrices against the properties which completely define the probability law of the hazard at the site. The plot of mean annual rate of occurrence of earthquake for all (M, r) at the site is called the site seismic activity matrix [3].

The average number of events per year irrespective of the values of $(M, r)$is

$$\nu = \sum_{i=M,\, r} v_{i_M, i_r} \tag{1}$$

We assume that the events in time according to a homogeneous Poisson counting process $\{N(\tau), \tau \geq 0\}$ of intensity ν so that

$$P(N(\tau) = n) = \frac{(\nu\tau)^n}{n!} \exp(-\nu\tau), n = 0, 1, 2, \ldots \tag{2}$$

We note several properties of homogeneous Poisson counting process $\{N(\tau), \tau \geq 0\}$. First, the inter-arrival time $T_k - T_{k-1}$, $k = 1, \ldots, N(\tau)$, $T_0 = 0$, are independent exponential random variables with rate ν since $P(T > \tau) = P(N(\tau) = 0) = \exp(-\nu\tau)$. Second, conditional on $N(\tau) = n$, the unordered Poisson events $\{s_1, s_2, \cdots, s_n\}$ occurring in $(0, \tau)$ have the probability density function $1/\tau^n$. Therefore, the unordered Poisson events are independent and uniformly distributed on $(0, \tau)$ conditional on $N(\tau) = n$.The calculation method is based on the above properties to program. Samples of inter-arrival times are generated consecutively using their conditional distributions as long as the generated Poison events remain in $(0, \tau)$.

2.2 High-frequency component

For the higher frequency component of ground motions in the seismic hazard model means the frequency of wave larger than 0.1–0.2 Hz here. The approach corresponds to a 'source-based' stochastic ground motion model, developed by considering the type of the fault rupture at the source as well as of the propagation of seismic waves through the underground soil site till the structural foundation. It is based on a parametric description of the ground motion's radiation spectrum $A(f; M; r)$, dependent on the earthquake magnitude, M, and rupture distance, r, and expressed as a function including the frequency f of seismic wave. This spectrum consists of many factors that account for the spectral effects from the source (source spectrum) as well as propagation through the earth's crust. The duration of the ground motion is addressed through an envelope function $e(t; M; r)$, which is also depends on M and r. More details on them are shown in article [3]. These frequency and time domain function $A(f; M; r)$ and $e(t; M; r)$, completely describe the earthquake motion model and their characteristics are provided by predictive relationships that relate them directly to the seismic hazard such as M and r.

The time history for a specific event magnitude, M, and rupture distance, r, is obtained according to this model by modulating a white-noise sequence $Z_\omega = [Z_\omega(i\Delta t) : i = 1, 2, \ldots, N_T]$ by $e(t; M; r)$and subsequently by $A(f; M; r)$ through the following steps:

1. The sequence Z_ω is multiplied by the time envelope function $e(t; M; r)$.
2. This modified sequence is then transformed to the frequency domain.
3. It is normalized by the square root of the mean square of the amplitude spectrum.
4. The normalized sequence is multiplied by the radiation spectrum $A(f; M; r)$.
5. It is transformed back to the time domain to yield the desired acceleration time history.

The model parameters include two seismological parameters M and r, describing the seismic hazard, the white-noise sequence Z_ω and predictive relationship for function $A(f;M;r)$ and $e(t;M;r)$. **Figure 4** shows $A(f;M;r)$ and $e(t;M;r)$ based functions for different values of M and r. It can be seen that as the moment magnitude increases the duration of the envelope function for strong component in motions also increases and the spectral amplitude becomes larger at all frequencies with a shift of dominant frequency content towards the lower frequency regime. As the epicenter distance increases, the spectral amplitude decreases uniformly and the envelope function also decreases, but at a relatively smaller amount.

Figure 5 shows the detailed process of seismic wave fitting in view of different earthquake magnitude M and rupture distance r. And near-fault rupture influence

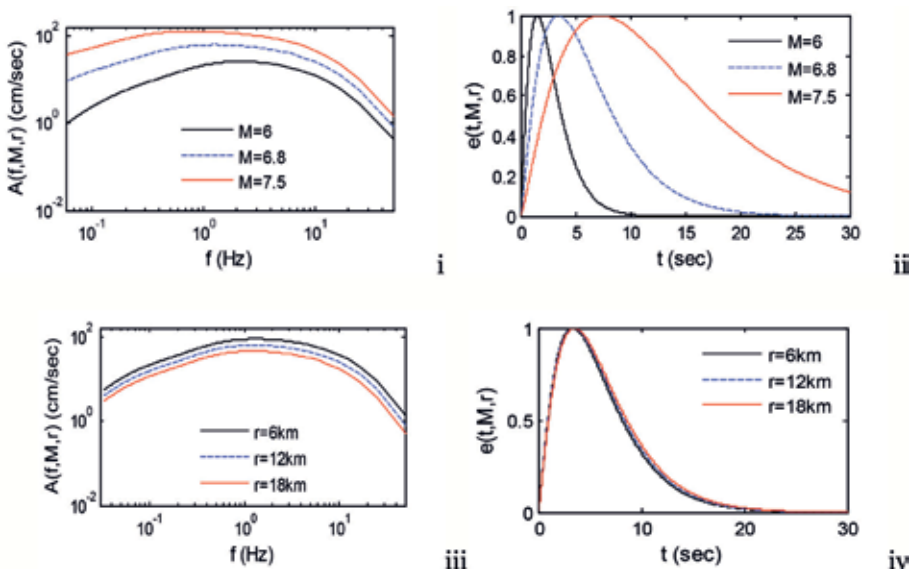

Figure 4.
Time and frequency envelope with different M and R.

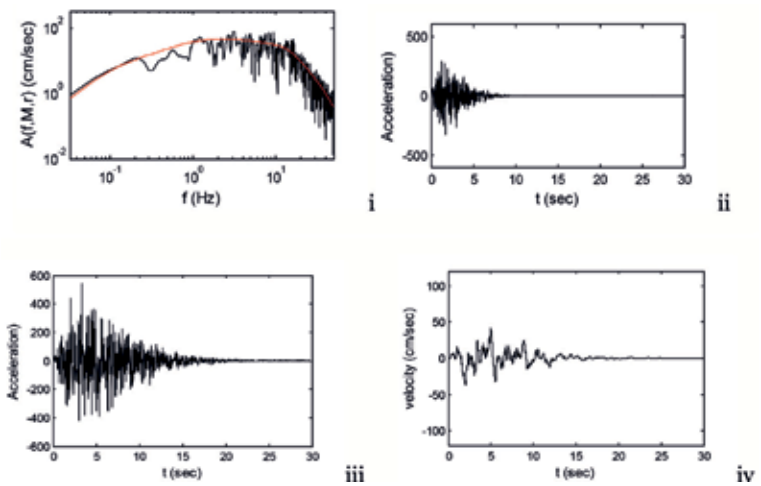

Figure 5.
Fitting process of stochastic time history wave.

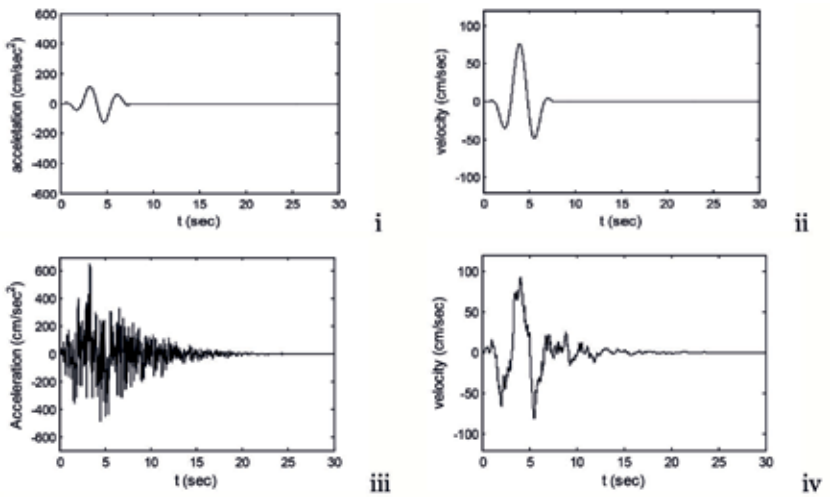

Figure 6.
Optimized wave in consideration of near-fault pulse.

also be considered so as to reflect actual situation in most high seismic intensity areas in China as shown in **Figure 6**.

3. Classic buildings modeling

China is known as the country of the most population and the world's factory, so industrial construction plays an important role in China's economic growth. Two kinds of classic buildings were be considered in the research including public buildings and industrial buildings in the research.

3.1 Multi-storey RC public buildings

A classic six storey reinforced concrete (RC) moment resisting buildings have been constructed in order to obtain the seismic insurance ratio and influence of various sources of uncertainties on the life-cycle cost in select Western China region. Steel of class with yield stress of 335 Mpa and modulus of elasticity equal to 210 Gpa has been considered, while concrete of cubic strength of 25 Mpa and modulus of elasticity equal to 30 Gpa. The structural layout of the building represents six bay in longitudinal direction with 6–8 m span lengths and three bay in transverse direction with 6–2.5–6 m span lengths respectively. The storey height is 3.3 m. The column elements size is 0.5 m $\times$ 0.5 m $\sim$0.5 m $\times$ 0.7 m. The beam size is 0.25 m $\times$ 0.6 m. The slab thickness is equal to 12 cm, while in addition to the self-weight of the beams and the slabs, a distributed permanent load of 2 kN/m^2 due to floor-finishing partitions and live load of 1.5 kN/m^2. For the analysis a three dimensional fiber model is created in Seismostruct software shown in **Figure 7**.

3.2 Single-storey industrial buildings

A regular, single-storey industrial digital finite element model is chosen in **Figure 8** to represent the system. The model is designed according China seismic code [2] to the prescriptions for loading, material, member dimensioning and detailing of the seismic design and gravity load.

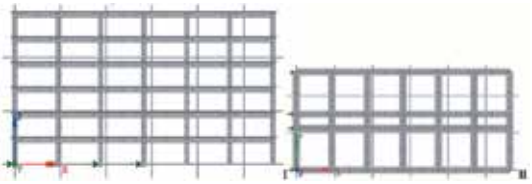

Figure 7.
The representative RC frames- (i) front view (ii) plan view.

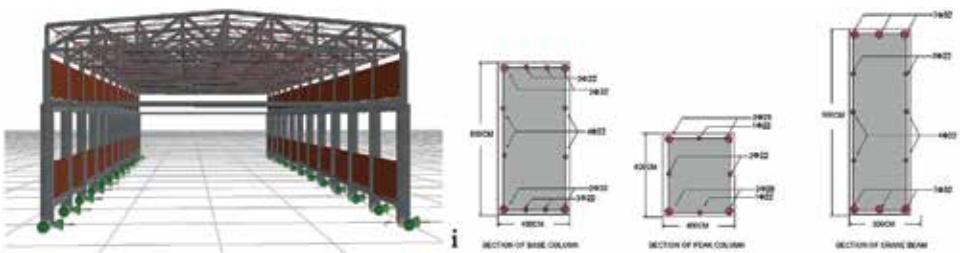

Figure 8.
Industrial building model (i: Overview, ii: Section detail reinforcement).

The structure consists with general configuration of bent widths and bay widths of 6 m and 24 m respectively, so the construction area of whole building is 1584 m^2 and which has 66 m long with 12 columns and 24 m width, structure is symmetrical in plan and elevation, and rectangular reinforced concrete track beam (0.30×0.90 m^2) on the bracket of two side longitudinal columns of the building. At the same time RC bent frame columns are variable cross-section columns, reinforcement ratio of down columns (0.40×0.80 m^2) is 1.86% ($4\phi32 + 8\phi22$) which is under the bracket and up-columns (0.40×0.40 m^2) is 1.96% ($4\phi25 + 4\phi22$) which is on the bracket. Track beams are confined frame element array on the brackets along the interior side of the building between bent frame columns. The roof of building which height is 9.6 m consist in reinforced concrete truss, the truss length is changed from 2.4 m in center to 1.5 m of two sides, moreover there are four kind of circular hollow steel bar be using with diameter from 0.03 m to 0.05 m, and thickness of bar' section is also verify from 2 to 3 mm.

The building's wall between columns generally consist of load-bearing infill masonry walls in China, confined by reinforced concrete bent frame columns and thickness of wall is 0.37 m commonly according China masonry code. Columns must have four 32 and 25 mm diameter longitudinal reinforcements, 8 mm diameter stirrups must be spaced 100 mm apart at the terminal and 200 mm at the center of the elements.

The masonry brick strength must at least MU15 and the mortar strength must at least M10 according to China masonry code, so typical masonry shear strength is 0.27–1 Mpa. Bilinear stress-strain relationships with strain hardening were used for reinforced members which yield strength is 335 Mpa [4] .Concrete axial compressive strength is 20–25 Mpa in considering of that many industrial frames in Western China regions. And coefficient with variation of 0.3 has been considered for steel and concrete respectively. Uniaxial nonlinear constant confinement concrete model that constant confining pressure is assumed throughout the entire stress-strain range is proposed by Mander to apply to element of concrete [5].

The roof live load of industrial frame usually was 1.0 kN/m^2, which is typical for an industrial building including snow load. And dead load is 2.0 kN/m^2 which considering worst condition.

4. Incremental dynamic damage analysis

In the seismic assessment of buildings a wide range stochastic ground motions from PEER strong motion database and seven seismic hazard level (HL) be considered in order to take into account the uncertainties. The main objective of IDA method is to define a curve through a relation between the seismic intensity level and the corresponding maximum response of the structural system. The intensity level and the structural response are described through an intensity measure (IM) and an engineering demand parameters (EDP) which refers also as damage index (DI). Incremental analysis are implemented through the following steps in this research: (i) Construct the local typical digital finite element model for performing nonlinear dynamic analyses; (ii) select a group of stochastic ground motion fitted with local response spectrum; (iii) select a proper intensity measure and an engineering demand parameter; (iv) employ an appropriate algorithm for selecting the record scaling factor in order to obtain the IM-EDP curve by performing the least required nonlinear dynamic analyses and (v) employ a summarization technique for exploiting the multiple waves results. In this work, the $S_a(T_1, 5\%)$ for damping equal to 5% is selected as IM indicator, since it is the most commonly used intensity measure in practice today for the analysis of buildings. At the same time, two kind of damage index: the maximum inter-storey drift $\theta_{\max}$ and maximum floor acceleration are chosen as EDPs, which are based on the maximum deformation of different damage state.

Actually scale factors is a key setting through IM in incremental analysis. The maximum inter-storey drift is recommended by FEMA-350 as the most suitable performance criterion for frame structures and is used in the research [6]. Depending on the problem and the performance that is needed to be calculated different intensity measures and performance factors can also be used. In this work two types of scaling be used: scaling all ground motion records in the same value of spectral acceleration or using a common scaling factor for all ground motion records. The $S_a(T_1, 5\%)$ is calculated from the hazard curve of the area of interest, such as Yinchuan of western China in this work shown in Eq. (3).

$$\overline{P}(DI > DI_i) = \frac{\gamma}{k^* \alpha_{\max}} + c \tag{3}$$

Where $\gamma = 1.3253$, $k = 2.9771 \times 10^{-2}$, $c = -0.005$in the function and the result was also shown in **Figure 9**.

$P_{50\%}$ is the exceedance probabilities in 50 years, and $\overline{P}_i$ is annual exceedance probabilities. IDA nonlinear procedure has been chosen for detect structural seismic vulnerability including structural damage and non-structural damage. So we set suggested 7 damage limit states (LS) in calculation on the base of post research. And emphasis of LS is been located in moderate damage and heavy damage corresponding to the damage ratio between 20–45% based structural damage condition. At the same time nonstructural damage also can be classify with 7 HL or LS using peak ground acceleration. Damage scale indicators in IDA have been shown in **Table 1**.

4.1 Damage analysis of multi-storey RC buildings

The IM scaling factor increase from 1 to 7.2 in IDA analysis. The whole damage LS of maximum inter-storey drift ratio (ISD%) and maximum floor acceleration (MFA) of every storey are shown in **Table 2**. That means all kind of seismic intensity waves have impacted on RC buildings in life-cycle period. So the

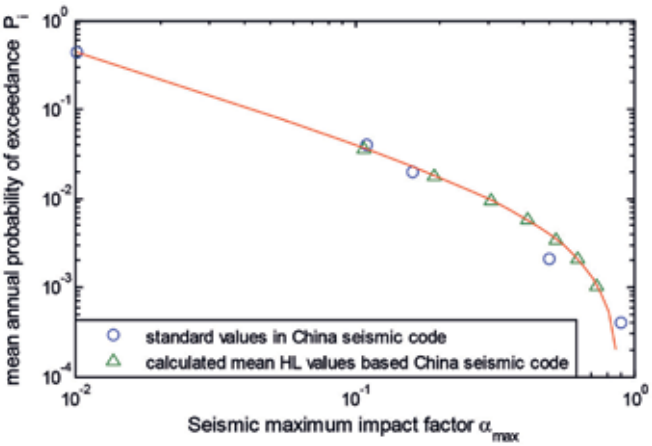

Figure 9.
The regression fitting curve for calculating the earthquake impact factor $\alpha_{\max}$ based China seismic code.

No.	Typical sample buildings in Research					
	Hazard level	Limit states	$\overline{P}_i$	α_{max}	P_i^{DI}%	Scaling factors
1	72/50	Slight damage	2.513	0.148	1.81	1.3
2	38/50	Light damage	0.951	0.307	0.379	2.1
3	25/50	Moderate damage I	0.574	0.415	0.227	3.7
4	16/50	Moderate damage II	0.348	0.525	0.139	4.7
5	10/50	Heavy damage I	0.21	0.627	0.107	6.2
6	5/50	Heavy damage II	0.103	0.739	0.063	7.2
7	2/50	Major damage	0.0404	0.824	0.040	9.0

Table 1.
Damage impact indicator in IDA.

Limit states	θ_{isd}(%)	$a_{floor}(g)$
(I)-None	$\theta \leq 0.1$	$a \leq 0.05$
(II)-Slight	$0.1 < \theta \leq 0.2$	$0.05 < a \leq 0.10$
(III)-Light	$0.2 < \theta \leq 0.28$	$0.10 < a \leq 0.16$
(IV)-Light II	$0.28 < \theta \leq 0.4$	$0.16 < a \leq 0.20$
(V)-Moderate I	$0.40 < \theta \leq 0.55$	$0.20 < a \leq 0.30$
(VI)-Moderate II	$0.55 < \theta \leq 0.90$	$0.30 < a \leq 0.50$
(VII)-Heavy	$0.90 < \theta \leq 1.70$	$0.50 < a \leq 0.75$
(VIII)-Major-Ma	$\theta > 1.70$	$a > 0.75$

Table 2.
Drift ratio and floor acceleration limits for RC buildings in Yinchuan.

structural and non-structural damage of every floor of RC buildings must be detected based the two EDPs parameters. The maximum ISD% locates in second floor and the MFA in the top floor at the same time. That means the most structural damage lie in second floor and the severe non-structural damage in top storey,

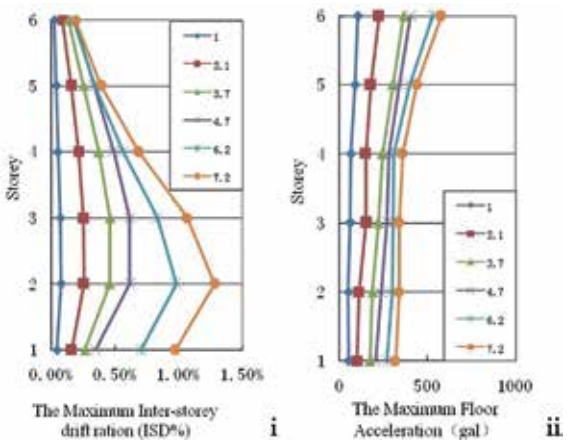

Figure 10.
The damage analysis based two EDPs parameters in IDA for Friuli Italy-02 (i: ISD%; ii: MFA).

which are shown in **Figure 10**. The tendency of the seismic vulnerability changed more obvious than ever.

The relation between the drift ratio limits with the limit state. Employed in this study is partly based on the work of Ghobarah [7] for ductile RC moment resisting frames, and at the same time vast stochastic sampling based Monte Carlo method based local construction code in Western China also impact the limit state setting in this research. The relation of the limit state with the values of the floor acceleration is partly based on the work of Elens and Meskouris [8].

The damage scatter distribution of multi-storey RC buildings is shown in **Figure 11**. The middle black curve means median values of whole damage data and blue curves means ±15% deviation limit.

4.2 Damage analysis of industrial buildings

Damage, in the context of life-cycle cost assessment, refers not only to structural damage but also to non-structural damage. The latter including the case of architectural damage, mechanical, electrical and plumbing damage and also the damage of furniture, equipment and other contents in factory buildings. The maximum inter-storey drift has been considered as the structural damage response parameter. On the other hand, the peak ground acceleration (PGA) is associated with the loss of contents, like furniture and equipment which located in ground.

Five thousand times stochastic calculation has been made using Monte Carlo sampling method consideration of random materials and structural variables and

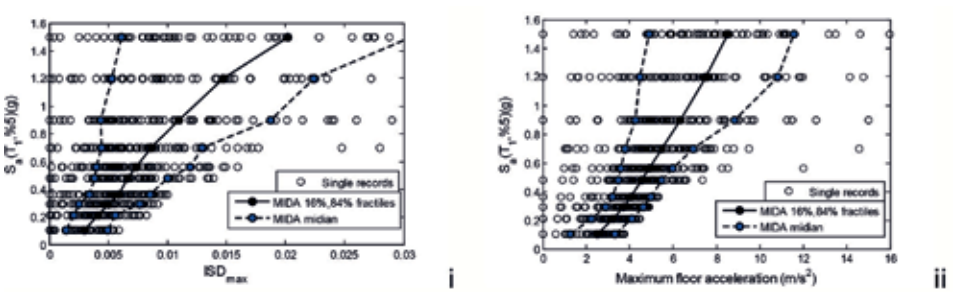

Figure 11.
The damage scatter distribution of RC buildings.

stochastic damage scattered points can be viewed in **Figure 12** with different color stripe, which represent limit state has shown in **Table 3**.

The damage zone of limit state can be represented from left to right respectively: none damage, slight damage, light damage, moderate damage, heavy damage and major damage or collapse. Statistics mean values and median values also be drawn

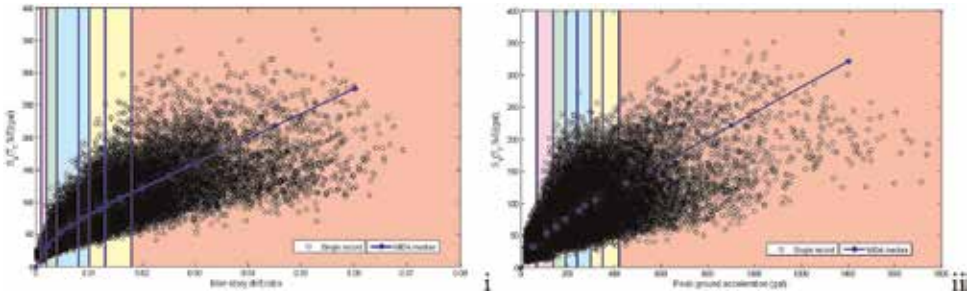

Figure 12.
Damage scattered distribution based limit states (i: ISD, ii: PGA).

No.	Single-storey industrial buildings		
	Limit state	**Inter-storey drift ratio%**	**PGA (g)**
1	(I) None	$\theta \leq 0.11$	$\alpha \leq 0.07$
2	(II) Slight	$0.11 < \theta \leq 0.21$	$0.07 < \alpha \leq 0.10$
3	(III) Light	$0.21 < \theta \leq 0.31$	$0.10 < \alpha \leq 0.14$
4	(IV) Moderate I	$0.31 < \theta \leq 0.45$	$0.14 < \alpha \leq 0.18$
5	(V) Moderate II	$0.45 < \theta \leq 0.66$	$0.18 < \alpha \leq 0.23$
6	(VI) Heavy I	$0.66 < \theta \leq 1.12$	$0.23 < \alpha \leq 0.30$
7	(VII) Heavy II	$1.12 < \theta \leq 2.55$	$0.30 < \alpha \leq 0.45$
8	(VIII) Major	$\theta > 2.55$	$\alpha > 0.45$

Table 3.
Limit state drift ratio, floor acceleration of factory buildings.

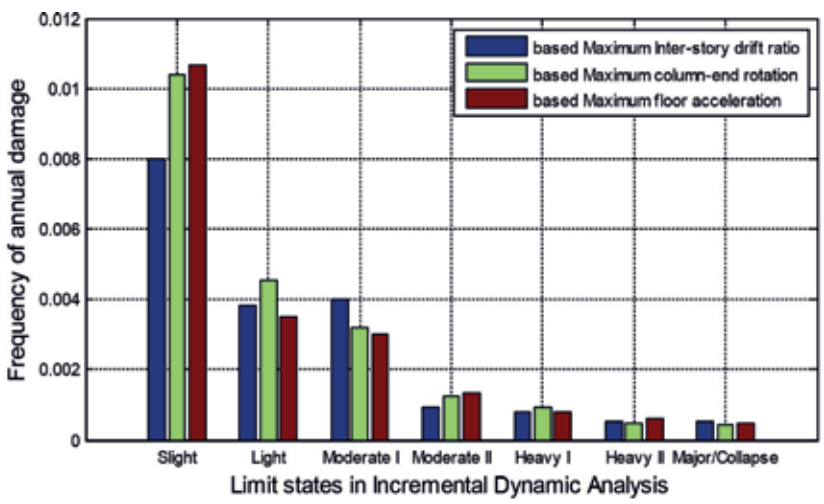

Figure 13.
The annual seismic column vulnerability in 50 years.

as blue line in scatter diagram. The trend of scatters has clearly radial and diverging pattern like a slant bell mouth and every circle point in figure means single time history wave.

The object of life-cycle seismic cost estimation is provide high reliable seismic insurance premium data for spread industrial buildings seismic catastrophe insurance of high seismic hazard region of China in consideration of multiple undetermined factors.

The basic calculation equations are based on the work of Lagaros and Mitropoulou [9] and background reference data come from our post research. So we can calculate statistical annual damage number according 7 limit states. Further the annual seismic column vulnerability according to 7 limit states after considering respective annual seismic exceedance probability at all Hazard levels shown in **Figure 13**.

5. Life-cycle seismic disaster insurance premium estimation

In the research the hazard levels are defined in accordance to the hazard curve transferred from China seismic code and of the city of Yinchuan, western of China (latitude(N)38.4°, longitude(W)106.2°). The life-cycle seismic cost (LCSC) was calculated finally through incremental dynamic analyses based on the post work of Jian Zhu [10, 11]. And then the seismic disaster insurance ratio is determined.

5.1 Seismic insurance ratio of RC buildings

The total cost C_{TOT} of a structure may refer either to the design life period of a new building or to the remaining life period of an existing or retrofitting one. The cost can be expressed as a function of time and the design vector s as follows Eqs. (4)–(11).

$$C_{TOT} = C_{IN}(s) + C_{LS}(t, s) \tag{4}$$

where C_{IN} is the initial cost of new or retrofitted buildings. C_{LS} is the present value of the limit state seismic damage cost, that means seismic loss of the RC buildings through different limit state to consider in the work.

$$C_{LS}^{i,\theta} = C_{dam}^{i} + C_{con}^{i,\theta} + C_{ren}^{i} + C_{inc}^{i} + C_{inj}^{i} + C_{fat}^{i} \tag{5}$$

$$C_{LS}^{i,a} = C_{con}^{i,a} \tag{6}$$

where C_{dam}^{i} is the damage repair cost, $C_{con}^{i,\theta}$ is the loss contents cost due to the structural damage C_{ren}^{i} is the loss of rental cost, C_{inc}^{i} is the income loss cost, C_{inj}^{i} is the cost of injuries and C_{fat}^{i} is the cost of human fatality. These cost components are related to the damage of the structural system. $C_{con}^{i,a}$ is the loss contents cost due to ground acceleration or floor acceleration.

Based on a Poisson process model of the earthquake occurrences and an assumption that damaged buildings are immediately retrofitted to their original intact conditions after every seismic damage due to seismic attack.

$$C_{LS} = C_{LS}^{\theta} + C_{LS}^{a} \tag{7}$$

$$C_{LS}^{\theta}(t, s) = \frac{\nu}{\lambda}\left(1 - e^{-\lambda t}\right) \sum_{i=1}^{N} C_{LS}^{i,\theta} \cdot P_{i}^{\theta} \tag{8}$$

$$C_{LS}^{a}(t,s) = \frac{\nu}{\lambda}\left(1 - e^{-\lambda t}\right)\sum_{i=1}^{N} C_{LS}^{i,a} \cdot P_i^a \tag{9}$$

where C_{LS}^{θ} and C_{LS}^{a} is respectively the seismic loss cost for the ith limit state violation calculated based $ISD_{\max}$ and PGA according to Eqs. (4) and (5). The annual monetary discount rate λ is taken constant and equal to 5%.

The probabilities P_i^{θ} and P_i^{a} of Eqs. (7) and (8) are calculated as follows:

$$P_i^{DI} = P(DI > DI_i) - P(DI > DI_{i+1}) \tag{10}$$

where DI_i, $DI_{i+1}$are the lower and upper bounds of the ith limit state for the two damage indices considered, while $P(DI > DI_i)$ is the exceedance probability given occurrence of the earthquake for every limit state given by the following expression:

$$P(DI > DI_i) = \frac{-1}{\nu t} \cdot \ln\left[1 - P_t(DI > DI_i)\right] \tag{11}$$

where $P_t(DI > DI_i)$ is the exceedance probability over a period [0,t]; and t is the service life, which is almost 50 years in China.

A more detailed description of the different damage rate and cost evaluation for each limit state cost can be found in **Tables 4** and **5**. The basic cost refers to the first component of the calculation formulas. While they are given in monetary units Yuan. The values of the mean damage index, loss of function, down time, expected minor injury rate, expected serious injury rate and expected death rate used in this study are based on [12]. Death rate denotes the number of persons that may die at a specific limit state and it is defined as the number of occupants × death rate. **Table 4** provides the revised limit state parameters of cost evaluation in this work on the base of FEMA-227 limit state dependent damage consequence severities.

After study local statistics data of construction engineering in Yinchuan, which located in high seismic hazardous region of western China. In this research $2500 Yuan/m^2$ is considered as C_{IN}, meantime ±10% variance is also included (**Figure 14**).

The statistics median covered area of typical RC building is 3600 m^2. The annual average LCC is 2.06 Yuan/m^2 after calculation using above procedure, and annual median LCC is 1.89 Yuan/m^2. There will add up 25% additional fee if insurance companies will establish catastrophe insurance at moment. The final insurance

Limit state	Calculate index based FEMA-227 [12]			
	Mean damage index %	Expected minor injury rate	Expected serious injury rate	Expected death rate
N	0	0	0	0
S	0.5	3.0×10^{-5}	4.0×10^{-6}	1.0×10^{-6}
LI	2	1.3×10^{-4}	1.8×10^{-5}	0.4×10^{-5}
LII	5	3.0×10^{-4}	4.0×10^{-5}	1.0×10^{-5}
MI	9	1.4×10^{-3}	1.6×10^{-4}	0.4×10^{-4}
MII	20	3.0×10^{-3}	4.0×10^{-4}	1.0×10^{-4}
H	45	3.0×10^{-2}	4.0×10^{-3}	1.0×10^{-3}
Ma	80	3.0×10^{-1}	4.0×10^{-2}	1.0×10^{-2}

Table 4.
Limit state parameters for cost estimation.

Cost category	Basic cost
Damage/repair (C_{dam})	1200 $Yuan/m^2$
Loss of contents (C_{con})	300 $Yuan/m^2$
rental (C_{ren})	20 $Yuan/month/m^2$
Income (C_{inc})	400 $Yuan/year/m^2$
Minor injury ($C_{inj,m}$)	2000 $Yuan/person$
Serious injury ($C_{inj,s}$)	2×10^4 $Yuan/person$
Human fatality (C_{fat})	8×10^5 $Yuan/person$

Table 5.
Limit state costs-calculation formula.

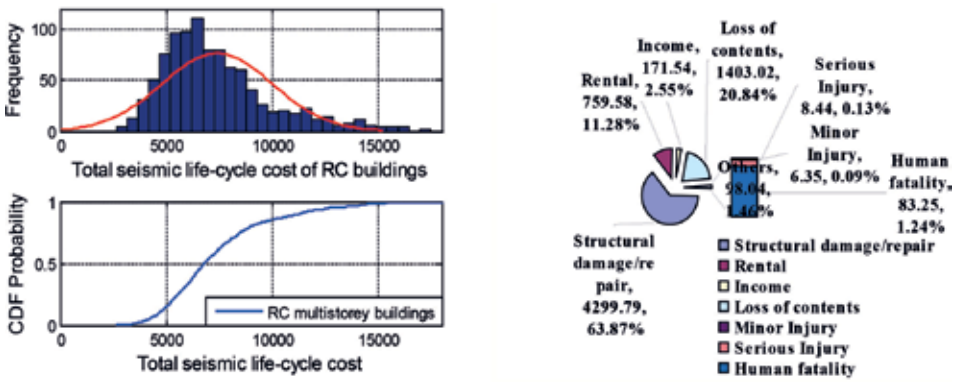

Figure 14.
The probability characteristics and constitution of RC buildings' LCC.

payment per people is about 70.9–77.2 Yuan annually in considering of local life endurance in this research on base of average living space per person equal 30 m^2. The result is complete acceptable level for local people in Yinchuan city of western China as research sample region finally and have applied into local insurance policy successfully.

5.2 Seismic insurance ratio of industrial buildings

Then we can use the Eqs. (4)–(11) based data of **Table 6** to calculate life-cycle seismic cost of factory buildings in selected region in consideration of random variables from ground vibration, material character and time cost.

The initial unit construction cost of the building is estimated ¥1200/m^2 and ±10% deviation is considered in calculation. The cost of machines and non-structural contents is supposed as ¥3000/m^2 and ¥300/m^2 respectively in research.

The annual median seismic cost of structural damage of industrial buildings is ¥3419 and corresponding annual median value of non-structural damage including machine and facilities in factory buildings is ¥8505 in **Figure 15**. The average and median values of every cost category are shown in **Table 7**.

Insurance is a highly legal business. Relevant insurance matters are regulated by the laws of various countries. Generally, the calculation formula of seismic catastrophe insurance premium rate is as follows.

Single-storey industrial buildings		
Cost category	**Calculation formula**	**Basic cost**
Damage/repair	Replacement cost × FA* × DI*	¥1200/m^2
Loss of machine & contents	Unit cost × FA* × DI*	¥3300/m^2
Rental	Rental rate × FA* × LF*	¥30/mo/m^2
Income	Rental rate × FA* × LF*	¥2000/ye/m^2
Minor injury	MI per cost × FA* × OR* × rate	¥2000/per
Serious injury	SI per cost × FA* × OR* × rate	¥2 × 10^5/per
Human fatality	HF per cost × FA* × OR* × rate	¥5 × 10^5/per

**FA = floor area, DI = damage index, LF = loss function, OR = occupancy rate.*

Table 6.
Limit state costs-calculation formula.

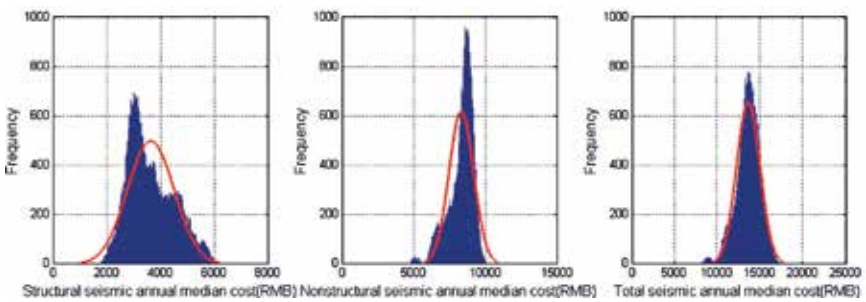

Figure 15.
The annual median SLCC probability distribution of factory buildings (from left to right: Structural damage, non-structural damage and total).

Cost category	Average value CNY	CoV (%)	Median value CNY	CoV (%)
Damage/repair	3603	5.67	3419	5.65
Rental	599	57.66	497	52.35
Income	742	63.35	603	57.12
Loss of contents	8286	1.24	8505	1.34
Minor & Serous Injury	39	186.2	27	156.7
Human fatality	221	189.8	155	157.7
Total seismic cost annually	13,491	1.11	13,577	1.12

Table 7.
LCC statistics results comparison.

$$p = \frac{\overline{L}}{1 - r - e}, e = e_1 + e_2 + e_3 + e_4 \tag{12}$$

Where p is insurance premium rate, $\overline{L}$ is expected loss rate, r is discount rate, e is additional charges rate including e_1 special reserve rate for claims, e_2 is commission rate, e_3 is development fund rate and e_4 is other fee rate. In research refer to Taiwan seismic insurance rate, $e_1 = 4\%$, $e_2 = 12.5\%$, $e_3 = 0.5\%$, $e_4 = 22\%$, $r = 5\%$.So the

insurance premium rate $p = 1.785$, and seismic catastrophe insurance of industrial buildings is ¥15.21–15.30 Yuan/year.m^2 in selected sampling region of China.

6. Conclusion

In this work a seismic risk & loss assessment procedure is proposed for a quantitative estimation of the seismic vulnerability and seismic catastrophe insurance premium of two types of typical buildings located in western China subjected to seismic actions. The numerical study was performed on 3D digital industrial modeling structures with two kind of roof structural system with different material. The life-cycle seismic cost estimation is examined on the basis of stochastic simulation with the big data buildings damage sampling. The most important findings of this study can be summarized as follows:

Double damage indicators including (ISD% & PGA) are imported into life-cycle seismic cost estimation firstly in inner research. The loss of non-structural cost is more than 60 percent in total LCC value and found more higher than the loss of structural damage.

The moderate damage I is most frequency through comparing stochastic incremental dynamic analysis results of every limit state damage. And light damage and major damage is followed.

The unit CIP statistical value of industrial buildings is ¥15.21-15.30/year.m2 in selected region. And in the future more precious results can be obtained through collecting buildings damage big data after large scale seismic investigation.

Acknowledgements

This research was financially supported by the National Science Foundation of China (51468050), Special Funding for Basic Scientific Research of China Central Universities (310828173402).

Author details

Jian Zhu[1,2*]

1 Department of Transportation and Civil Engineering, Foshan University, Foshan, Guangdong, China

2 Department of Civil Engineering, Chang An University, Xi An, Shanxi, China

*Address all correspondence to: zhuhoujian66@hotmail.com

References

[1] Porter KA, Kiremidjian AS, LeGrue JS. Assembly-based vulnerability of buildings and its use in performance evaluation. Earthquake Spectra. 2001; **18**:291-312. DOI: 10.1193/1.1586176

[2] Ministry of Construction P.R. China. Code for Seismic Design of Buildings (GB50011-2010). Beijing, China: China Construction Press; 2010. pp. 112-134

[3] Boore DM. Simulation of ground motion using the stochastic method. Pure and Applied Geophysics. 2001;**160**: 635-676. DOI: 10.1007/PL00012553

[4] Menegotto M, Pinto PE. Method of analysis for cyclically loaded R.C. plane frames including changes in geometry and non-elastic behavior of elements under combined normal force and bending. In: Symposium on the Resistance and Ultimate Deformability of Structures Acted on by Well Defined Repeated Loads, International Association for Bridge and Structural Engineering; Zurich, Switzerland. 1973. pp. 15-22. DOI: 10.12691/agcea-3-1-5.

[5] Mander JB, Priestley MJN, Park R. Theoretical stress-strain model for confined concrete. Journal of Structural Engineering. 1988;**114**(8):1804-1826. DOI: 10.1061/(ASCE)0733-9445(1988) 114:8(1804)

[6] Federal Emergency Management Agency. FEMA-350:Recommended Seismic Design Criteria for New Steel Moment-Frame Buildings. Washington, DC; 2000. DOI: 10.1193/1.1572495

[7] Ghobarah A. On drift limits associated with different damage levels. In: Proc. of the International Workshop on Performance-Based Seismic Design. Bled, CA: McMaster University; 2004. DOI: 10.1016/S0141-0296(01)00036-0

[8] Elenas A, Meskouris K. Correlation study between seismic acceleration parameters and damage indices of structures. Engineering Structures. 2001;**23**:698-704. DOI: 10.1016/ S0141-0296(0)00074-2

[9] Lagaros ND, Mitropoulou CC. The effect of uncertainties in seismic loss estimation of steel and reinforced concrete composite buildings. Structure and Infrastructure Engineering. 2013; **9**(21):546-556. DOI: 10.1080/ 15732479.2011. 593527

[10] Jian Z, Hai ZJ, Min JJ. Life-cycle seismic costs estimation and seismic insurance model for simple RC buildings in Western China. In: 2016 International Conference on Architectural Engineering and Civil Engineering (AECE-16); Shanghai, China. 2016. DOI: 10.2991/aece-16.2017.36

[11] Jian Z, Junhai Z, Pin T, Fulin Z. Seismic life-cycle loss estimation of single story factory buildings. Earthquake Engineering & Engineering Dynamics. 2018;**38**(1):51-64. DOI: 10.13197/j.eeev.2018.01.51.zhuj.007. (Paper write In Chinese)

[12] Federal Emergency Management Agency. FEMA 227: A Benefit-Cost Model for the Seismic Rehabilitation of Buildings. Washington, DC: Building Seismic Safety Council; 1992. pp. 102-135. DOI: 10.1193/1.2194529

Section 4

Finding Strength by Finding Weakness: Creating Resilience in Response to Vulnerabilities

Chapter 12

Multiset-Based Assessment of Resilience of Sociotechnological Systems to Natural Hazards

Igor Sheremet

Abstract

The chapter describes multiset-based approach to the assessment of resilience/vulnerability of the distributed sociotechnological systems (DSTS) to natural hazards (NH). DSTS contain highly interconnected and intersected consuming and producing segments, and also resource base (RB), providing their existence and operation. NH impacts may destroy some local elements of these segments, as well as some parts of RB, thus initiating multiple chain effects, leading to negative consequences far away from the NH local strikes. To assess DSTS resilience to such impacts, multigrammatical representation of DSTS is used. A criterion of DSTS sustainability to NH, being generalization of similar criterion, known for industrial (producing) systems, is proposed. Application of this criterion to critical infrastructures is considered, as well as solution of the reverse problem, concerning subsystems of DSTS, which may stay functional after NH impact.

Keywords: resilience and vulnerability, natural hazards, sociotechnological systems, critical infrastructures, multisets, multiset grammars, unitary multiset grammars

1. Introduction

Modern large-scale distributed sociotechnological systems (DSTS) include anthropogenic and technogenic components, i.e., humans and various technical devices, respectively, operating in common in order to provide sufficient quality of life to humans, and this sufficiency may be defined by some threshold amounts of resources, consumed by them during some fixed period of life. These resources, in turn, must be produced and relocated from places of their production to places of their consumption by application of the aforementioned devices and their aggregates. The last also uses specific resources, necessary for their operation.

By this, every DSTS may be represented as composition of two segments—consuming and producing (both containing humans and devices)—and resource base, which provides their existence and operation. These segments are highly interconnected and intersect, because a large number of humans and devices are consumers and creators of resources simultaneously.

Natural hazard impacts (NHI) may destroy some local elements of the aforementioned segments and resource base, and this destruction initiates multiple chain (or cascading) effects, caused by the absence or lack of resources,

necessary for normal operation of some devices and/or humans; such effects may lead to the destructive consequences far away from places (areas) where natural hazard (NH) occurred.

By growth of complexity of DSTS and degree of their internal interconnectivity, it becomes more and more difficult to assess such consequences and, as a whole, resilience (or, reversely, vulnerability) of DSTS to various NH. Here, we shall understand DSTS *resilience* to NH as its property not to reduce humans' quality of life lower than some predefined level (as was said higher, it may be determined by the amounts of resources, consumed by anthropogenic part of DSTS).

Well-known approaches to formal description and solution of DSTS resilience/vulnerability problems, integrally considered in [1], are not applicable to most practical cases by the reason of only partial adequacy of representation of the main structural and functional features of DSTS, as well as by the reason of sharply increasing computational complexity of detecting algorithms on real dimensions.

As it was shown in [1, 2], multiset-based approach to such assessment is one of the most suitable perspectives from both descriptional and computational points of view. The core of this approach is representation of technological base of the industrial systems (IS), producing necessary resources, by special multiset grammar (MG), and its resource base (RB)—by multiset (MS).

The simplest formal definition of resilience of IS, completing some order, is based on the presumption, that if RB, reduced by NHI, is, nevertheless, sufficient for this order completion by at least one possible way, then such IS is *resilient to this impact.*

However, this definition and all formalizing it relations concern only industrial systems (producing segments of DSTS) and single orders, so until now criterion of DSTS resilience in multiset-based form is unknown. The main reason for this is that there is no technique for the assessment of the whole set of orders, which may generate consuming segment of DSTS. So, this chapter is dedicated to consideration of such general case. The basic presumption for all lower discourse is that DSTS after NHI has no any opportunity to contact with external systems in order to compensate loss of resources, being the result of NHI, i.e., DSTS is a "closed system" in terms of [3, 4]. Also, NHI is considered as single instant strike, which touches some finite set of places (areas), destroying all material objects located there.

Section 2 contains brief consideration of the previous results on IS resilience. Section 3 is dedicated to generalization of the known criterion of IS resilience on the case, when resource base of IS contains not only primary (terminal) resources but also resources, produced by IS since the start of its operation upon the initial state of RB until the moment of NHI. Section 4 is dedicated to the multigrammatical representation of local sociotechnological systems (STS) and formulation of criterion of their resilience, while Section 5—to the general case of DSTS. The current global reality makes extremely important development of a toolkit for the assessment of resilience of multiple interconnected DSTS, producing and delivering to the consumers specific types of resources (electrical energy, fuel, water, etc.). Such DSTS are addressed usually as critical infrastructures (CI), following their critically important mission for whole countries and world regions [5–11]. The basic approach of the proposed criteria application to CI is considered in Section 6. After NHI, some subsystems of vulnerable DSTS may stay in the active state ready for operation. So, the reverse problem, concerning such subsystems detection, is studied in Section 7. Possible directions of development of the proposed approach is announced in the conclusion.

2. Assessment of resilience of industrial systems

Let us remind that *multiset* is a set of multiobjects (MO) that is written as

$$v = \{n_1 \cdot a_1, \ldots, n_m \cdot a_m\}, \tag{1}$$

where v is the name of multiset and $n_1 \cdot a_1, \ldots, n_m \cdot a_m$ are the multiobjects, entering this MS; the integer number n_i, $i = 1, \ldots, m$ is called multiplicity of object a_i, which means, that v contains n_1 identical objects $a_1, \ldots, n_m$ identical objects a_m, and for $i \neq j$ $a_i \neq a_j$. Set

$$\beta(v) = \{a_1, \ldots, a_m\} \tag{2}$$

is called *basis of multiset* v. Both object a and multiobject $n \cdot a$ are said to be entering v that is written without ambiguity as $a \in v$ and $n \cdot a \in v$. From the substantial point of view, object a and multiobject $1 \cdot a$ are equivalent. In general case, multiplicities may be not only positive integers but also positive rational numbers [12, 13]. Empty set and empty multiset are denoted $\{\varnothing\}$. Further in this chapter objects will be denoted also by symbol b with indices, as well as by strings of italic symbols.

The main multiset-based tool, which would be used below, is *unitary multiset grammars* (UMG) (we shall use also "multigrammar" as synonym of "multiset grammar") [12, 13].

UMG is a couple $S = < a_0, R >$, where a_0 is called *title object* and R is called *scheme*, being the set of *unitary rules* (UR), having the form

$$a \rightarrow n_1 \cdot a_1, \ldots, n_m \cdot a_m, \tag{3}$$

where object a is called *head* and list $n_1 \cdot a_1, \ldots, n_m \cdot a_m$—*body* of this UR. List is interpreted as multiset, i.e., $\{n_1 \cdot a_1, \ldots, n_m \cdot a_m\}$.

The so-called structural and technological interpretations of unitary rules are used in the IS resilience assessment [2].

According to *structural interpretation*, (3) means that some material (physical) object (unit of resource) a consists of n_1 objects $a_1, \ldots, n_m$ objects a_m (to distinguish mathematical notion "object" from the physical one, we shall use below notion "object/resource," abbreviated OR).

Technological interpretation is an extension of the structural one, so that the body of UR

$$a \rightarrow n_1 \cdot a_1, \ldots, n_m \cdot a_m, n'_1 \cdot a'_1, \ldots, n'_k \cdot a'_k \tag{4}$$

contains structural components (usually spare parts of the produced device), which are MO $n_1 \cdot a_1, \ldots, n_m \cdot a_m$, as well as resources, which are necessary for assembling (manufacturing) a from these components and are represented by MO $n'_1 \cdot a'_1, \ldots, n'_k \cdot a'_k$.

Example 1. Let $S = < aircraft, R >$, where R contains the following two unitary rules:

$$aircraft \rightarrow 1 \cdot fuselage, 2 \cdot wing,$$
$$wing \rightarrow 1 \cdot frame, 1 \cdot engine, 4 \cdot wheel.$$

According to structural interpretation, this means that aircraft consists of fuselage and two wings. Any of the wings consists, in turn, of frame and engine, as well as four wheels, all connected to the wing frame. Let now $S' = < aircraft, R' >$, where R' contains the following two URs:

$$aircraft \rightarrow 1 \cdot fuselage, 2 \cdot wing, 10 \cdot kW, 160 \cdot mbt\text{-}asm\text{-}aircraft, 150000 \cdot USD$$

$$wing \rightarrow 1 \cdot frame, 1 \cdot engine, 4 \cdot wheel, 12 \cdot kW, 240 \cdot mnt - asm - wing, 400000 \cdot usd.$$

According to the technological interpretation of UR, this means that assembling aircraft from a fuselage and two wings requires 160 min of operation of the aircraft's assembling line, 10 kW of electrical energy, as well as 150,000 dollars being the total cost of this work. Similarly, assembling one wing from the frame, engine, and four wheels requires 12 kW, 240 min of operation of the wing's assembling line, and 400,000 dollars. ∎

As seen, UMG provide easy and natural decomposition of complicated technological systems (devices) until elementary (non-decomposed) objects and resources, used in the manufacturing process.

A set of objects, having placed in the UMG S, is denoted A_S, while a set of so-called *terminal* objects, having placed only in bodies of UR, is denoted $\overline{A}_S$. Evidently, $\overline{A}_S \subset A_S$. Objects, entering set $A_S - \overline{A}_S$, are called *non-terminal*. Similarly, corresponding OR also may be terminal and non-terminal.

Mathematical semantics of unitary multiset grammars is defined in such a way that UMG $S = <a_0, R>$ is applied for generation of the set of multisets (SMS) V_S according to the following relations:

$$V_{(0)} = \{\{1 \cdot a_0\}\}, \tag{5}$$

$$V_{(i+1)} = V_{(i)} \cup \left(\bigcup_{v \in V_{(i)}} \bigcup_{r \in R} \{\pi(v, r)_0\} \right), \tag{6}$$

$$\pi(v, <a \rightarrow n_1 \cdot a_1, ..., n_m \cdot a_m>) = \begin{cases} v - \{n \cdot a\} + n * \{n_1 \cdot a_1, ..., n_m \cdot a_m\}, \\ \qquad\qquad\qquad\qquad if\ n \cdot a \in v \\ \{\varnothing\}\ otherwise \end{cases} \tag{7}$$

$$V_S = V_{(\infty)}, \tag{8}$$

where UR $a \rightarrow n_1 \cdot a_1, ..., n_m \cdot a_m$ for unambiguity is represented in the angle brackets, and $+, -, *$ are symbols of operations on multisets (addition, subtraction of multisets, and multiplication of constant on multiset, respectively) [1, 2, 12, 13].

As seen from (5) to (8), new multisets are generated by applying all unitary rules $r \in R$ to SMS $V_{(i)}$, created on previous i steps. Every such UR $a \rightarrow n_1 \cdot a_1, ..., n_m \cdot a_m$ is applied to MS $v \in V_{(i)}$ by a special function π. If v contains MO $n \cdot a$, it is replaced by MS $n * \{n_1 \cdot a_1, ..., n_m \cdot a_m\}$ and by semantics of MS addition, and after that multiplicities of the identical objects are summarized; otherwise, the result of π application is an empty set.

Described generation process is in general case infinite, and SMS V_S, defined by UMG S, is its fixed point $V_{(\infty)}$.

Terminal multiset (TMS) $v \in V_S$ contains only terminal objects, i.e.,

$$\beta(v) \subseteq \overline{A}_S, \tag{9}$$

and the set of terminal multisets (STMS) is denoted $\overline{V}_S$.

Further in this chapter if it will not be said the contrary, we shall consider only *finitary* UMG, which define finite STMS. UMG S is finitary, if these exists i such, that $V_{(i)} = V_{(i+1)}$, and if so, $V_{(i)} = V_S$. The problem of recognition of UMG finitarity is algorithmically decidable [12, 13].

Example 2. As may be seen, UMG S and S' from the previous example are finitary, and, according to (5)–(8),

$$\overline{V}_S = \{\{1 \cdot fuselage, 2 \cdot frame, 2 \cdot engine, 8 \cdot wheel\}\},$$
$$\overline{V}_{S'} = \{\{1 \cdot fuselage, 2 \cdot frame, 2 \cdot engine, 8 \cdot wheel, 34 \cdot KW, 160 \cdot mnt - asm - aircraft, 480 \cdot mnt - asm - wing, 950000 \cdot usd\}\}.\blacksquare$$

Returning to the considered application of UMG, i.e., description and assessment of industrial systems, we may represent *technological base* (TB) of IS (set of its producing devices) as scheme R of UMG:

$$S = <tb, R>, \tag{10}$$

where tb is the title object and R is the set of unitary rules in the technological interpretation.

Order, completed by IS with TB S, may be represented by MS

$$q = \{n_1 \cdot b_1, ..., n_l \cdot b_l\}, \tag{11}$$

which means goal of this order is to obtain n_1 OR b_1, ..., n_l OR b_l. The set of possible variants of resource amounts, necessary for order q completion, is nothing, but set of TMS, generated by UMG:

$$S_q = <tbq, R \cup \{<tbq \rightarrow n_1 \cdot b_1, ..., n_l \cdot b_l>\}>, \tag{12}$$

i.e., STMS $\overline{V}_{S_q}$ (for short we shall use $\overline{V}_q$ instead of it).

In general case $|\overline{V}_q| > 1$ because of the possibility of multiple ways of order completion, which usually is a consequence of some redundancy of TB (however, such redundancy is the background of IS resilience, as it will be shown below).

Resource base of IS may be represented by MS $v = \{n_1 \cdot a_1, ..., n_k \cdot a_k\}$ in such a way that n_1 OR a_1, ..., n_k OR a_k are available to technological base R while orders completion.

Described representation of TB and RB makes it quite simple to formulate *criterion of possibility of order completion*.

Statement 1. Order q to IS with technological base R and resource base v may be completed, if

$$(\exists \overline{v} \in \overline{V}_q)\overline{v} \subseteq v.\blacksquare \tag{13}$$

Such RB v is called *sufficient* for order q completion by IS.

For further consideration of resilience/vulnerability issues, it is useful to unify TB and RB by including to the bodies of UR_S in the technological interpretation of one additional multiobject $1 \cdot r$, where r is the name of the device, which provides manufacturing (assembling) OR, defined by the head of UR. By this, the presence of multiobject $n \cdot r$ in the resource base is equivalent to the possibility of n manufacturing cycles, executed by device r while current order completion.

Described techniques integrate TB and RB in the integral resource base, which does not contradict to the reality, because multiobjects like $n \cdot r$ represent, in fact, technological (active) resources of IS, along with passive resources, consumed by devices.

Note that there may be one and the same object r in different UR bodies that reflects the capability of device r to produce one and the same OR by various ways or even to produce various OR. Moreover, in general case, there may be not only multiobjects like $1 \cdot r$ in the UR bodies but also $l \cdot r$, where $l > 1$, that, in fact, allows to represent the duration of manufacturing cycle, providing

creation of one unit of OR a, represented by the head of the UR. This technique is simply implemented by the use of so-called composite objects, or *composites*, like t-r, where "-" is the divider, r is the unique identifier of manufacturing device, and t is the time unit (second, minute, etc.), so $l{\cdot}t$-r means that there are sufficient l time units of work of device r to produce one unit of OR a, represented by the head of the UR. Both r and t are strings in some basic alphabet, and t does not contain divider "-".

If resource base of IS contains multiobjects like $L{\cdot}t$-r, that means there are L units of time of work of device r available while current order completion.

Speaking about the use of time in UR, we must take into account that time is not fully an additive resource; it is additive regarding only separate device. If to consider the whole IS, then due to parallel operation of various devices, time, spent for order completion, may be less than in the case of their sequential application. Precise modeling of IS operation is possible on the basis of the so-called temporal multiset grammars, introduced in [2], which will be considered thoroughly in the separate publications.

Example 3. Let $S' = <aircraft, R>$ be as in Example 1, order $q = \{r \cdot aircraft\}$, and IS resource base is

$$v = \{6 \cdot fuselage, 10 \cdot frame, 12 \cdot engine, 40 \cdot wheel, 250 \cdot kW,$$
$$800 \cdot mnt - asm - aircraft, 2600 \cdot mnt - asm - wing,$$
$$1000000 \cdot usd\}\}.$$

As seen, order q may be completed with technological base R' and resource base v, which is sufficient for this order completion.

However, if

$$v = \{6 \cdot fuselage, 10 \cdot frame, 3 \cdot engine, 12 \cdot wheel, 250 \cdot kW,$$
$$800 \cdot mnt - asm - aircraft, 2600 \cdot mnt - asm - wing,$$
$$1000000 \cdot usd\}\},$$

then order q cannot be completed, and RB v is not sufficient, because there is lack of five engines for manufacturing four aircrafts. ∎

Let us consider now IS, affected by natural hazard *impact*, which may be represented by multiset Δv, defining amounts of resources, eliminated by NHI from IS resource base, so the last becomes $v - \Delta v$.

Concerning passive resources, such representation is quite evident: if NHI destroys n' OR a from n, which had placed in RB before the impact, then the remained amount of these OR will be $n - n'$ (if $n < n'$ or $n = n'$, all such OR will be eliminated from RB), so respective multiobject, entering $v - \Delta v$, will be $(n - n') \cdot a$. In the case of active resources, $n' \cdot t$-$r \in \Delta v$ means that n' time units of operation of ith devise r would be lost, so this device may not execute all work, which it would do while order completion, and this obstacle may be the reason for IS vulnerability. So, similar to passive resources, the result of NHI regarding active resource would be $(n - n') \cdot t$-r. If $n' = \infty$, the result of NHI would be elimination of MO $n \cdot t$-r from R; when implemented, ∞ may be replaced by some very large number $\boldsymbol{N}$, which is greater than any possible multiplicity, ever used in TB and RB representations.

Let IS has TB R and RB v, which is sufficient for order q completion.

Statement 2. IS, completing order q, is resilient to NHI Δv, if reduced RB $v - \Delta v$ is sufficient for this order completion. Otherwise, this IS is vulnerable to this NHI.∎

This criterion is basic for *distributed industrial systems* (DIS), in which facilities are located at different places (areas) and some of them may be affected by NHI. Every such impact may destroy some of the aforementioned facilities, eliminating some local parts of TB and RB, thus reducing its capabilities for order completion.

To represent DIS, OR, having placed in unitary rules and multisets, are extended by geospatial information in such a way that a/z, where "/" is the divider, means that OR a is located at place z. Both a and z are the strings in some basic alphabet, excepting "/", and z is the name of location.

We use names of locations instead of their usual coordinate representations (CR), supposing that there is a separate key-addressed database, containing couples $<z, X>$, where key z is the name of place and X is its CR in any possible form (points of perimeter, center of the circle along with its radius, etc.), most convenient for concrete location. This database provides the simplest implementation of intersection of two locations, which is the basic operation in the algorithmics of assessment of resilience of any distributed systems.

Since the described extension, all UR have the form

$$a/z \rightarrow n_1 \cdot a_1/z_1, \ldots, n_m \cdot a_m/z_m, \tag{14}$$

that means OR a may be produced at location z, if there are n_1 OR a_1 at location $z_1, \ldots, n_m$ OR a_m at location z_m. As seen, $a/z, a_1/z_1, \ \ldots, \ a_m/z_m$ are also composites.

Representation of time resource is just the same: if MO $n \cdot t\text{-}r/z$ enters UR body, that means follows: to produce OR a, located at place z, device r, located at place z, would operate for n time units.

Similarly, resource base would be

$$v = \{n_1 \cdot a_1/z_1, \ldots, n_k \cdot a_k/z_k\}, \tag{15}$$

as well as order

$$q = \{n_1 \cdot b_1/z_1, \ldots, n_l \cdot b_l/z_l\}. \tag{16}$$

The new moment is the representation of NHI by set z of affected by it locations (in general case, areas):

$$Z = \{z_1, \ldots, z_p\}. \tag{17}$$

For simplicity we shall limit a variety of locations having placed in (14)–(17) by points, while in (17) every z_i may be an area of any form. Also, we shall use denotation $\overline{Z}$ for the set of points entering Z (it is join of sets $z_1, \ldots, z_p$).

To formulate the criterion of resilience of DIS, we shall use relation $z \in \overline{Z}$ that means point z enters set $\overline{Z}$.

Let us define

$$\Delta v(Z) = \{n \cdot a/z \mid n \cdot a/z \in v \,\&\, z \in \overline{Z}\}, \tag{18}$$

i.e., multiset of OR, affected by NHI z, because they are located at the affected points. Thus, all these OR must be eliminated from the resource base, being destroyed by the impact.

Let DIS has TB R and RB v, which is sufficient for order q completion.

Statement 3. DIS, completing order q, is resilient to NHI z, if reduced by it RB, $v - \Delta v(Z)$ is sufficient for this order completion. Otherwise, this DIS is vulnerable to this NHI. ∎

Concerning affected active resources, it is reasonable to underline that NHI may destroy them up to unrecoverable state (this may be represented by inclusion to Δv MO $\boldsymbol{N} \cdot t\text{-}r/z$) or, in the better case, transfer them to the unoperational, but reparable, state, that may be represented by inclusion to Δv MO $n' \cdot t\text{-}r/z$, where n' is less than multiplicity n of OR $t\text{-}r/z \in v$.

By this we finish a short survey of known results on resilience of industrial systems. Before we move to sociotechnological systems, let us generalize the introduced criteria.

3. Generalized criterion of resilience of industrial systems

As seen, both introduced criteria of IS resilience operate only terminal resources, which are used by IS for production of amounts of OR, being the goal of order. By this, they trivially repeat criterion of order completeness (12) with the only replacement of the IS initial resource base by RB, reduced by NHI.

However, if to take into account that there may be some non-terminal OR, already manufactured by IS during time interval between the start of order completion and moment of NHI, it would be sensible to consider these OR during recognition of IS resilience, or, in the other words, to generalize notion of resource base, including to RB not only terminal, but also non-terminal OR.

But, evidently, this generalization makes the introduced criteria non-applicable. Let us propose correct criterion for the case of RB, containing not only terminal but also non-terminal OR.

For this purpose we propose here so-called unitary multiset grammars with reduced generation (UMG RG).

UMG RG is triple $S(v_0) = < a_0, R, v_0 >$, where a_0 and R are, as higher, the title object and scheme, respectively, and v_0 is the multiset, which may contain non-terminal multiobjects, used for elimination of the number of generation steps. So, this version of UMG has specific semantics, which fully corresponds to the sense of order completion by the use of aforementioned RB.

The main difference of UMG RG from UMG is that they generate not multisets, but pairs $< v, v' >$, where v is the MS, created while previous generations steps, and v' is the rest of RB, which may be used at the next such step.

If there is a non-terminal multiobject $n \cdot a$ in multiset v, and at the same times MS v' includes MO $n' \cdot a$, then following action depends on the relation between n and n'. If $n > n'$, then there are already n' OR a in the resource base, and there is no any need to manufacture them—it is sufficient to manufacture $n - n'$ OR a and eliminate n' OR a from v' to represent that they are already used while order completion. If $n' \leq n$, then all necessary OR a are already in the RB, and there is no need in generation here at all; it is sufficient to subtract $\{n \cdot a\}$, so there would be MO $(n - n') \cdot a$ in the RB after this action, because n OR a are spent (if $n' = n$, there would be no OR a in the RB).

Formal definition of semantics of UMG RG $S(v_0) = < a_0, R, v_0 >$, i.e., a set of relations, describing generation of a set $\overline{V}_{S(v_0)}$ of pairs $< v, v' >$, is as follows:

$$\overline{V}_{(0)} = \{ < \{1 \cdot a_0\}, v_0 > \}, \tag{19}$$

$$V_{(i+1)} = V_{(i)} \cup \left(\bigcup_{<v,\, v'> \,\in\, V_{(i)}} \; \bigcup_{r \,\in\, R} \{\varphi(v, v', r)\} \right), \tag{20}$$

$$\varphi(v, v', <a \to n_1 \cdot a_1, \ldots, n_m \cdot a_m>) = \\ = \begin{cases} <v - \{n \cdot a\}, v' - \{n \cdot a\}>, \textit{if } n \cdot a \in v \,\&\, n' \cdot a \in v' \,\&\, n' \geq n \\ <v - \{n \cdot a\} + (n - n') * \{n_1 \cdot a_1, \ldots, n_m \cdot a_m\}, v' - \{n' \cdot a\}>, \\ \qquad \textit{if } n \cdot a \in v \,\&\, n' \cdot a \in v' \,\&\, n' \neq 0 \,\&\, n' < n \vee \\ \qquad n \cdot a \in v \,\&\, n' = 0 \\ \{\varnothing\} \textit{ otherwise,} \end{cases} \tag{21}$$

$$\overline{V}_{S(v_0)} = V_{(\infty)}. \tag{22}$$

This definition fully corresponds to the previous verbal description and is similar to (5)–(8). The mission of function φ, defined by (21), is the same as the mission of function π, defined by (7). Some comments would be done to its second alternative, namely, the case where multiset v' does not contain OR a at all (or, just the same, multiplicity n' of multiobject $n' \cdot a$, entering v', is zero); this is equivalent to a more general case, when $n' \cdot a \in v'$ and non-zero multiplicity n' is less than n. As seen, the result of subtraction of the empty multiset $\{n' \cdot a\}$, where $n' = 0$, from multiset v', is unchanged v', and this branch of (21) is just the same, as the first alternative of (7).

The introduced UMG RG provide formulation of the generalized criterion of IS resilience.

Let $q = \{n_1 \cdot b_1, \ldots, n_l \cdot b_l\}$ be order, R—technological base of the industrial system, and v—its resource base, such that

$$\beta(v) \subseteq A_s. \tag{23}$$

(That is, it contains not only terminal but also non-terminal OR). Consider UMG RG $S_q(v) = <tbq, R_q, v>$, where

$$R_q = R \cup \{<tbq \to n_1 \cdot b_1, \ldots, n_l \cdot b_l>\}. \tag{24}$$

(Here, UR is written in the angle brackets for unambiguity.)

Statement 4. Order q to IS with technological base R and resource base v may be completed, if

$$\left(\exists <\overline{v}, \overline{v}'> \in \overline{V}_{S_q(v)} \right) \overline{v} \subseteq \overline{v}'. \blacksquare \tag{25}$$

As seen, if RB does not contain non-terminal OR, (25) and (13) are equivalent. As higher, RB, relevant to criterion 4, is called sufficient for order q completion by IS. Evidently, $\overline{v}' - \overline{v}$ is RB, remained after completion of order q.

Example 4. Let $S' = <aircraft, R'>$ be as in Example 1, order $q = \{4 \cdot aircraft\}$, and resource base of the industrial system is $v = \{6 \cdot fuselage, 12 \cdot wing, 300 \cdot kW, 800 \cdot mnt - asm - aircraft, 1100000 \cdot usd\}$.

As seen,

$$S_q(v) = <tbq, R_q, v>,$$

where

$$R_q = R' \cup \{<tbq \to 4 \cdot aircraft>\},$$

and resource base v contains non-terminal multiobject $12 \cdot wing$, which means 12 wings are already manufactured and ready to be mounted to fuselages in order to make aircrafts.

According to (19)–(21), $\overline{V}_{S_q}(v) = \{ <\overline{v}, \overline{v}'> \}$, where

$$\overline{v} = \{4 \cdot fuselage, 40 \cdot kW, 640 \cdot mnt - asm - aircraft, 600000 \cdot usd\},$$
$$\overline{v}' = \{6 \cdot fuselage, 4 \cdot wing, 300 \cdot kW, 800 \cdot mnt - asm - aircraft, 1100000 \cdot usd\}.$$

Because $\overline{v} \subset \overline{v}'$, order q may be completed by IS due to the number of already manufactured wings, which is greater than the required for manufacturing of four aircrafts. ∎

Let resource base v be sufficient for order q completion by IS with technological base R, and Δv is NHI on this system.

Statement 5. IS, completing order q, is resilient to NHI Δv, if

$$\left(\exists <\overline{v}, \overline{v}'> \in \overline{V}_{S_q(v-\Delta v)} \right) \overline{v} \subseteq \overline{v}'. \tag{26}$$

Otherwise, this IS is vulnerable to this NHI. ∎

This criterion may be generalized on distributed IS in the same manner, as it was done in [2] and described in the previous section.

Let RB v be sufficient for order q completion by DIS with TB R, and Z is NHI on this system.

Statement 6. DIS, completing order q, is resilient to NHI Z, if

$$\left(\exists <\overline{v}, \overline{v}'> \in \overline{V}_{S_q(v-\Delta v(Z))} \right) \overline{v} \subseteq \overline{v}'. \tag{27}$$

Otherwise, this DIS is vulnerable to this NHI. ∎

It is clear that DIS RB contains both terminal and non-terminal objects, located at various places.

Example 5. Let DIS be represented by UMG $S = <aircraft/z_1, R>$, where R contains the following unitary rules:

$$aircraft/z_1 \rightarrow 1 \cdot fuselage/z_1, 2 \cdot wing/z_1, 10 \cdot kW/z_1,$$

$$wing/z_2 \rightarrow 1 \cdot frame/z_2, 1 \cdot engine/z_2, 4 \cdot wheel/z_2, 12 \cdot kW/z_2,$$

$$wing/z_1 \rightarrow 1 \cdot wing/z_2, 1000 \cdot l - petrol/z_2, 1 \cdot vel/z_2,$$

$$l - petrol/z_2 \rightarrow 1 \cdot l - petrol/z_3, 1 \cdot link/z_3, 1 \cdot pump/z_3, 0.001 \cdot kW/z_3.$$

Here, the first two UR are slightly modified versions of technological base, described by UMG S; the only difference is that all OR are composites, including names of locations. As seen, aircrafts are assembled at place z_1, while wings—at place z_2. The third UR defines that to remove one wing to z_1 from z_2, some transportation vehicle *vel* must be used, and also 1000 liters of petrol for its refueling, necessary for wing removal to z_1 and return to z_2. At last, the fourth UR defines that to transport petrol from place z_3, where it is stored, there is used pipeline fragment, consisting of link and pump, the latter consuming 0.001 kW of electrical energy to remove 1 liter of petrol from z_3 to z_2. Assembling one aircraft and one wing is also an energy-consuming operation that is represented by multiobjects $10 \cdot kW/z_1$ and $12 \cdot kW/z_2$, having placed in the bodies of the first and the second UR, respectively.

Let order $q = \{2 \cdot aircraft/z_1\}$, and resource base of DIS is

$$v = \{3 \cdot fuselage/z_1, 2 \cdot wing/z_1, 4 \cdot frame/z_2, 5 \cdot engine/z_2, 8 \cdot wheel/z_2, \\ 500 \cdot l - petrol/z_2, 1 \cdot wing/z_2, 100 \cdot vel/z_2, 10000 \cdot l - petrol/z_3, \\ 100000 \cdot link/z_3, 100000 \cdot pump/z_3, 50 \cdot kW/z_1, 150 \cdot kW/z_2, 200 \cdot kW/z_3\}.$$

This means that at location z_1 there are three fuselages, ready to be mounted with wings, but there are only two wings at this location, so two more wings, necessary for the production of two aircrafts, must be removed to z_1 from z_2. However, there are two ready wings at z_2; there is only one such wing, as well as four frames, five engines, and eight wheels, which may be used for manufacturing of some additional number of wings. Moreover, there is transportation vehicle *vel* at z_2, which may remove ready wings from z_2 to z_1, and also 500 liters of petrol for refueling this vehicle. But, as seen, this amount of petrol is not sufficient for the relocation of two wings from z_2 to z_1. So, the required amount of petrol, i.e., 500 liters, must be removed by the pipeline to z_2 from z_3, where petrol storage is located, containing at the current moment 10,000 liters of this fuel. Multiobjects $100000 \cdot link/z_3$ and $100000 \cdot pump/z_3$ represent the technical state of petrol pipeline link and pump, which is sufficient for execution of 100,000 working cycles, each providing removal of 1 liter of petrol from z_3 to z_2. Similarly, MO $100 \cdot vel/z_2$ represents the technical state of the vehicle, which is able to make 100 transportation cycles from z_2 to z_1 and back without repair.

This verbal description makes it evident, how in fact order completion may be planned by UMG RG application. Let us consider how it is really done according to (19)–(21):

$$\begin{aligned}
\overline{V}_{S_q(v)} &= \{ < \{2 \cdot aircraft/z_1\}, v > \} \\
&= \{ < \{2 \cdot fuselage/z_1, 4 \cdot wing/z_1, 20 \cdot kW/z_1\}, v > \} \\
&= \{ < \{2 \cdot fuselage/z_1, 1 \cdot wing/z_1, 20 \cdot kW/z_1\}, v - \{3 \cdot wing/z_1\} > \} \\
&= \{ < \{2 \cdot fuselage/z_1, 1 \cdot wing/z_2, 1000 \cdot l - petrol/z_2, 1 \cdot vel/z_2\}, \\
&\quad v - \{3 \cdot wing/z_1\} > \} \\
&= \{ < \{2 \cdot fuselage/z_1, 20 \cdot kW/z_1, 1 \cdot frame/z_2, 1 \cdot engine/z_2, \\
&\quad 4 \cdot wheel/z_2, 12 \cdot kW/z_2, 1000 \cdot l - petrol/z_2, 1 \cdot vel/z_2\}, \\
&\quad v - \{3 \cdot wing/z_1\} > \} \\
&= \{ < \{2 \cdot fuselage/z_1, 20 \cdot kW/z_1, 1 \cdot frame/z_2, 1 \cdot engine/z_2, \\
&\quad 4 \cdot wheel/z_2, 12 \cdot kW/z_2, 500 \cdot l - petrol/z_3, 500 \cdot link/z_3, \\
&\quad 500 \cdot pump/z_3, 1 \cdot kW/z_3\}, v - \{3 \cdot wing/z_1, 500 \cdot l/petrol/z_2\} > \}.
\end{aligned}$$

Because

$$\{2 \cdot fuselage/z_1, 20 \cdot kW/z_1, 1 \cdot frame/z_2, 1 \cdot engine/z_2, 4 \cdot wheel/z_2, 12 \cdot kW/z_2, \\ 500 \cdot l - petrol/z_3, 500 \cdot link/z_3, 500 \cdot pump/z_3, 1 \cdot kW/z_3\} \\ \subset \{3 \cdot fuselage/z_1, 50 \cdot kW/z_1, 4 \cdot frame/z_2, 5 \cdot engine/z_2, 8 \cdot wheel/z_2, 150 \cdot kW/z_2, \\ 9500 \cdot l - petrol/z_3, 100000 \cdot link/z_3, 100000 \cdot pump/z_3, 200 \cdot kW/z_3\},$$

order q is completed by DIS with technological base R and resource base v; the latter is sufficient for this order completion.

If this DIS is affected by NHI $Z = \{z_3\}$, then

$$v - \Delta v(Z)$$
$$= \{3 \cdot fuselage/z_1, 50 \cdot kW/z_1, 4 \cdot frame/z_2, 5 \cdot engine/z_2, 8 \cdot wheel/z_2, 150 \cdot kW/z_2\},$$

and, as may be seen without generation, DIS is vulnerable to this NHI while order q completion. This means that destruction of petrol storage, necessary for refueling of transportation vehicle, which, in turn, is necessary for assembled wing removal to the place of the final assembling of aircraft, makes impossible completion of the order, i.e., manufacturing of two aircrafts. ∎

This example is a primary illustration of multigrammatical representation and modeling of chain effects, occurring in distributed industrial systems as a result of NHI.

Now, we have the widest criterion of resilience of distributed industrial system, completing single order, to natural hazard impact. The thing is that in general case there is a flow of such orders, generated by human segment of distributed sociotechnological system.

It is evident that DSTS would be considered resilient to NHI, if the aforementioned flow would be completed by the producing (industrial) segment of this system with resource base, reduced by this NHI.

Before we move to further discourse, let us clarify interconnections between basic notions, which will be used below.

As it was said in Section 1, any sociotechnological system includes anthropogenic and technogenic parts—humans and used by them technical devices (systems). We call them human and technological segments (STS HS and STS TS, respectively). From the order side, STS include producing (industrial) and consuming segments (STS IS and STS CS, respectively), both consisting of humans and devices. So, there are humans and devices that participate in the manufacturing process and produce resources, which, in turn, are necessary for their own existence and operation, as well as for all other humans and devices, not participating in the manufacturing process and thus entering only consuming segment.

The described decomposition of STS will be exclusively important while studying issues, concerning consequences of total robotization of the industry, logistics, and various services that lead to massive unemployment, and the main problem to solve this will be to assess, whether global technosphere and natural resource base would be able to provide sufficient quality of life of unemployed people, as well as other groups of population, being out of the producing segment.

However, here we shall use the described decomposition of STS for continuation of development of criterial base of their resilience. To consider distributed STS at all, we shall begin from the simplest case of local STS.

4. Multigrammatical representation of local sociotechnological systems and criterion of their resilience

Let us consider first the local case, where all humans live and work at a single place. If so, decomposition of the human socium, having placed at this location, may begin from the unitary rule

$$socium \rightarrow 1 \cdot structures, 1 \cdot persons, \tag{28}$$

where non-terminal object *structures* is a start point for all business and state structures, while non-terminal object *persons* is similarly a start point for individuals, not entering any of the aforementioned structures.

Object *structures* is the head of the single unitary rule

$$structures \rightarrow m_1 \cdot str_1, \ldots, m_k \cdot str_k, \tag{29}$$

that means there are m_1 structures (of type) $str_1, \ldots, m_k$ structures (of type) str_k; if any *str i* of $str_1, \ldots, str_k$ is unique, then $m_i = 1$.

Any structure may be decomposed to substructures, individual positions, and multiple access technological systems (MATS), used by personnel of this structure and its substructures. Relevant unitary rules would have the following form:

$$\begin{gathered} str \rightarrow n_1 \cdot pstn_1, n_p \cdot pstn_p, m_1 \cdot str_1, \ldots, m_s \cdot str_s, \\ l_1 \cdot tech_1, \ldots, l_t \cdot tech_t, \end{gathered} \tag{30}$$

which means there are $n_1, \ldots, n_p$ positions $pstn_1, \ldots, pstn_p$ and $m_1, \ldots, m_s$ substructures $str_1, \ldots, str_s$, as well as $l_1, \ldots, l_t$ MATS $tech_1, \ldots, tech_t$ (all, respectively). Every substructure is decomposed in the same way recursively until substructures, which multigrammatical representation is like

$$str \rightarrow n_1 \cdot pstn_1, \ldots, n_p \cdot pstn_p, l_1 \cdot tech_1, \ldots, l_t \cdot tech_t \tag{31}$$

or

$$str \rightarrow n_1 \cdot pstn_1, \ldots, n_p \cdot pstn_p, \tag{32}$$

i.e., they have no any substructures, but in general case may have MATS, providing their operation.

MATS, in turn, operate due to some attached (affiliated) personnel, which mission is to maintain technological system in the active state and apply it according to its destination. Also, MATS may consist of some subsystems, each with its own personnel, and its multigrammatical representation in general case may be as follows:

$$tech \rightarrow n_1 \cdot pstn_1, \ldots, n_p \cdot pstn_p, l_1 \cdot tech_1, \ldots, l_s \cdot tech_s, \tag{33}$$

$$tech \rightarrow l_1 \cdot tech_1, \ldots, l_s \cdot tech_s, \tag{34}$$

the latter case corresponding to the fully robotized (unmanned) system. Every $tech_i$, in turn, may be decomposed recursively until terminal objects, which names have been placed only in the bodies of unitary rules.

Concerning the second multiobject from the body of UR (28), it may be approved that all set of individuals of the considered STS may be divided to subsets (classes), each joining person with the similar sets of personal technical devices and consumed resources. This may be represented by unitary rule

$$person \rightarrow n_1 \cdot person_1, \ldots, n_l \cdot person_l, \tag{35}$$

and

$$person_i \rightarrow k_1^i \cdot res_1^i, \ldots, k_{r_i}^i \cdot res_{r_i}^i, m_1^i \cdot dev_1^i, \ldots, m_{l_i}^i \cdot dev_{l_i}^i, \tag{36}$$

that means each person, belonging to the ith class, during the predefined period of time consumes $k_1^i, \ldots, k_r^i$ units of resources $res_1^i, \ldots, res_{r_i}^i$ and is using $m_1^i, \ldots, m_{l_i}^i$ devices $dev_1^i, \ldots, dev_{l_i}^i$, respectively.

From here, it is evident that the same assignment of the consumed resources and used devices must be done regarding all positions, having placed in structures, described by UR (30)–(32). Relevant unitary rules are similar to (36):

$$pstn \rightarrow k_1 \cdot res_1, \ldots, k_r \cdot res_r, m_1 \cdot dev_1, \ldots, m_l \cdot dev_l, \tag{37}$$

or

$$pstn \rightarrow k_1 \cdot res_1, \ldots, k_r \cdot res_r \tag{38}$$

(the latter retains possibility of "deviceless" positions). All devices, represented by multiobjects, having placed in the body of UR (37), are in private use of a person; holding this position, for all time this person is assigned to this position (i.e., these devices are not of multiple access and are not the property of the person).

Let us take into account that every MATS, as well as every device, used by the person also consumes resources, necessary for its operation. To represent this obstacle, it is sufficient to use URs like

$$tech \rightarrow k_1 \cdot res_1, \ldots, k_t \cdot res_t, \tag{39}$$

regarding "terminal" MATS and subsystems of "non-terminal" MATS, which are not decomposed during STS description. Similar URs define resources, consumed by devices:

$$dev \rightarrow k_1 \cdot res_1, \ldots, k_d \cdot res_d. \tag{40}$$

Let us denote S_H unitary multiset grammar, which title object is *socium*, and scheme R_H contains all unitary rules, representing considered human segment of STS. By this it is evident that total amount of resources, consumed by this segment during predefined time interval, is $\overline{V}_{S_H}$ and, namely, this amount must be produced by the STS industrial segment for STS operation. Since then it is obvious that interconnection and intersection between human and technological segments are formed by URs, defining STS IS:

$$res \rightarrow k_1 \cdot res_1, \ldots, k_m \cdot res_m, \tag{41}$$

which means STS IS manufactures one unit of resource res_i, consuming during production cycle $k_1, \ldots, k_m$ units of resources $res_1, \ldots, res_m$, respectively.

As may be seen, industrial segments of considered STS do not produce nothing but OR, necessary for the existence of humans of this STS, and structures, having placed in (29)–(32), are also producing nothing. By this reason any such STS is closed not only in the sense it has no contact with external systems, which may supply it by resources, but also in the sense that it does not produce any OR for mentioned external systems, i.e., does not complete any orders of such systems.

However, it is not difficult to represent STS, which do complete orders of external systems: it is sufficient to join to the body of UR (28) multiobject $1 \cdot order$ and to include to the set R_H of unitary rules, representing human segment of STS, UR

$$order \rightarrow n_1' \cdot or_1, \ldots, n_m' \cdot or_m, \tag{42}$$

where MS $q = \{n'_1 \cdot or_1, ..., n'_m \cdot or_m\}$ is total external order (TEO), which would be completed by STS during the considered time period. Of course, set R would contain unitary rules, representing STS IS capabilities to complete TEO.

Before we shall formulate following statements, let us clarify one important issue, concerning representation of resources, consumed by producing MATS and devices, entering industrial segment of STS. Namely, if MATS/device enter STS IS, it seems that its resource consumption is accounted twice—in R_H as well as in R_I.

However, there is no any duplication.

R_H contains representation of resources, contained by producing MATS/device *during all considered time period independently of amounts of produced by OR*. Most often it may be electrical power, consumed for MATS/device maintenance in the state, ready for operation, which is represented by MO $n \cdot kW$ (number of consumed kW). In general case, this resource is "readiness" of MATS/device to work, represented by MO $1{\cdot}ready\text{-}tech$ or $1{\cdot}ready\text{-}dev$. Of course, the same MO must present in the resource base of STS. NHI may eliminate such OR from RB that reflects transfer of MATS/device out of operation, so RB becomes insufficient for STS.

At the same time, URs, representing MATS/device productive capabilities and having placed in the set R_I, describe resources, *consumed while STS produces OR and necessary, namely, for this operation cycle*. Obviously, amounts of resources, consumed while OR production, depend on amounts of produced OR.

As seen from the said, there is no any double count, and both parts of consumed collections of OR are summarized, when their total amounts are obtained.

To unify and to distinguish representation of producing MATS/devices, we shall include the body of any such unitary rule with head x multiobject $1{\cdot}ready\text{-}x$. Thus, all other MATS/devices, entering set R_H and represented by UR without such MO in their bodies, do not enter STS IS.

Now, we may formulate a primary criterion of sufficiency of the resource base of STS during the considered time period. Let TMS v be the resource base of STS at the beginning of this period, while unitary multigrammars $S_H = < socium, R_H >$ and $S_I = < tb, R_I >$ represent human and industrial segments of this STS.

Statement 7. Resource base v is sufficient to STS, if

$$\left(\exists\, \overline{v} \in \overline{V}_S\right) \overline{v} \subseteq v, \tag{43}$$

where $S = < socium, R_H \cup R_I >$.∎

If v contains not only terminal but also non-terminal (produced) OR, then sufficiency of this RB may be recognized according to (25), if to suppose $q = \{1 \cdot socium\}$. Not more difficult is generalized criterion of STS sustainability to NHI Δv.

Statement 8. STS, represented by UMG $S = < socium, R_H \cup R_I >$, with resource base v is resilient to NHI Δv, if

$$\left(\exists\, \langle \overline{v}, \overline{v}' \rangle \in \overline{V}_{S_q(v-\Delta v)}\right) \overline{v} \subseteq \overline{v}', \tag{44}$$

where $q = \{1\, socium\}$. Otherwise, this STS is vulnerable to this NHI. ∎

Example 6. Let sociotechnical system contain human segment, represented by the following set of unitary rules R_H:

$$socium \rightarrow 1 \cdot structures, 1 \cdot persons,$$

$$structures \rightarrow 1 \cdot office, 1 \cdot food\text{–}factory, 1 \cdot generation\text{–}facility,$$

$$office \rightarrow 1 \cdot top\text{–}manager, 1 \cdot department, 1 \cdot server - unit,$$

$$department \rightarrow 1 \cdot head\text{–}dpt, 3 \cdot manager,$$

$$persons \rightarrow 50 \cdot person,$$

$$top\text{–}manager \rightarrow 1 \cdot mob\text{–}phone, 1 \cdot desktop, 1 \cdot lunch,$$

$$head\text{–}dpt \rightarrow 1 \cdot mob\text{–}phone, 1 \cdot desktop, 1 \cdot lunch,$$

$$manager \rightarrow 1 \cdot mob\text{–}phone, 1 \cdot desktop, 1 \cdot lunch,$$

$$person \rightarrow 1 \cdot lunch,$$

$$server - unit \rightarrow 1 \cdot hardware, 1 \cdot engineer,$$

$$engineer \rightarrow 1 \cdot mob\text{–}phone, 1 \cdot desktop, 1 \cdot lunch,$$

$$food\text{–}factory \rightarrow 1 \cdot factory\text{–}director, 1 \cdot food\text{–}line,$$

$$food\text{–}line \rightarrow 1 \cdot food\text{–}complex, 3 \cdot food\text{–}maker,$$

$$factory\text{–}director \rightarrow 1 \cdot mob\text{–}phone, 1 \cdot desktop, 1 \cdot lunch,$$

$$food\text{–}ma\mathrm{ker} \rightarrow 1 \cdot mob\text{–}phone, 1 \cdot lunch,$$

$$generation\text{–}facility \rightarrow 1 \cdot generator, 1 \cdot engineer,$$

$$engineer \rightarrow 1 \cdot mob - phone, 1 \cdot desktop, 1 \cdot lunch,$$

$$generator \rightarrow 1 \cdot ready - generator,$$

$$mob - phone \rightarrow 0.001 \cdot kW,$$

$$desktop \rightarrow 0.1 \cdot kW,$$

$$hardware \rightarrow 1 \cdot kW,$$

$$food - complex \rightarrow 1 \cdot ready - food - complex, 5 \cdot kW.$$

As seen, STS HS contains three structures—office, power generation facility, and food factory—as well as 50 persons out of these structures. Office includes one top manager, three departments, and one MATS—server, providing office operation. Each department, in turn, consists of the head of the department and three managers. The server unit is composed of hardware and an engineer, providing its operation. Every listed position is provided with a mobile phone and desktop, and the person, holding this position, consumes lunch daily. Other structures, entering this socium, are MATS food factory, consisting of a factory director, and food line, producing food, necessary for all humans of the considered socium.

Food line, in turn, is broken down into food complex and three food makers. The factory director is provided with a mobile phone and desktop, while every food

maker—with a mobile phone. Every person from the food factory also consumes one lunch. All devices consume electrical energy, in which amounts are multiplicities of OR kW in the bodies of the last four URs. The amount of electrical power, consumed by food complex (5 kW), does not depend on the number of lunches it does produce and is constant for all considered time interval. The third structure is MATS power generation facility, containing a power generator and maintained by an engineer. Generator consumption is described by UR, entering set R and containing MO $1 \cdot ready\text{-}generator$, reflecting readiness of a generator to operation.

Let us consider industrial segment of STS, represented by the following set of unitary rules R_I:

$$tb \rightarrow 1 \cdot lunch,$$

$$tb \rightarrow 1 \cdot kW.$$

This means that technological base of STS IS produces two types of OR—lunches and electrical energy. The first contains "something to eat" and "something to drink". To produce 1 kW, it is necessary to deliver to the generator 0.01 cubic meter of gas:

$$lunch \rightarrow 1 \cdot lunch\text{–}eat, 1 \cdot lunch\text{–}drink,$$

$$kW \rightarrow 0.01 \cdot m3\text{–}gas,$$

$$lunch\text{–}eat \rightarrow 1 \cdot chease\text{–}cake,$$

$$lunch\text{–}eat \rightarrow 1 \cdot sandwich,$$

$$lunch\text{–}drink \rightarrow 1 \cdot coffee,$$

$$lunch\text{–}drink \rightarrow 1 \cdot tea,$$

$$lunch\text{–}drink \rightarrow 1 \cdot juice,$$

$$chease\text{–}cake \rightarrow 100 \cdot g\text{–}bread, 5 \cdot g\text{–}sugar, 10 \cdot g\text{–}chease,$$

$$sandwich \rightarrow 100 \cdot g\text{–}bread, 10 \cdot g\text{–}butter, 50 \cdot g\text{–}meat,$$

$$tea \rightarrow 200 \cdot g\text{–}water, 5 \cdot g\text{–}sugar, 1 \cdot tea\text{–}cube,$$

$$coffee \rightarrow 200 \cdot g\text{–}water, 5 \cdot g\text{–}sugar, 1 \cdot coffee\text{–}cube,$$

$$juice \rightarrow 200 \cdot g\text{–}fresh\text{–}juice.$$

As may be seen, the total order is

$$\overline{V}_{S_H} = \{\{1 \cdot ready - generator, 1 \cdot ready - food - complex,$$
$$0.07619 \cdot m3\text{–}gas, 69 \cdot lunch\}\},$$

while

$$\begin{aligned}\overline{V}_S = \{&\{1 \cdot ready - generator, 1 \cdot ready - food - complex, 0.07619 \cdot m3\text{–}gas,\\ &6900 \cdot g\text{–}bread, 690 \cdot g\text{–}sugar, 690 \cdot g\text{–}chease,\\ &13800 \cdot g\text{–}water, 69 \cdot tea\text{–}cube\},\\ &\{1 \cdot ready - generator, 1 \cdot ready - food - complex,\\ &0.07619 \cdot m3\text{–}gas, 6900 \cdot g\text{–}bread, 345 \cdot g\text{–}sugar, 690 \cdot g\text{–}chease,\\ &13800 \cdot g\text{–}fresh\text{–}juice\},\\ &\{1 \cdot ready - generator, 1 \cdot ready - food - complex,\\ &0.07619 \cdot m3\text{–}gas, 6900 \cdot g\text{–}bread, 690 \cdot g\text{–}sugar, 13800 \cdot g\text{–}chease,\\ &13800 \cdot g\text{–}water, 69 \cdot coffee\text{–}cube\},\\ &\{1 \cdot ready - generator, 1 \cdot ready - food - complex,\\ &0.07619 \cdot m3\text{–}gas, 6900 \cdot g\text{–}bread, 690 \cdot g\text{–}butter, 3450 \cdot g\text{–}meat,\\ &13800 \cdot g\text{–}water, 345 \cdot g\text{–}sugar, 69 \cdot tea\text{–}cube\},\\ &\{1 \cdot ready - generator, 1 \cdot ready - food - complex,\\ &0.07619 \cdot m3\text{–}gas, 6900 \cdot g\text{–}bread, 690 \cdot g\text{–}butter, 3450 \cdot g\text{–}meat,\\ &13800 \cdot g\text{–}fresh\text{–}juice\},\\ &\{1 \cdot ready - generator, 1 \cdot ready - food - complex,\\ &0.07619 \cdot m3\text{–}gas, 6900 \cdot g\text{–}bread, 690 \cdot g\text{–}butter, 3450 \cdot g\text{–}meat,\\ &13800 \cdot g\text{–}water, 345 \cdot g\text{–}sugar, 69 \cdot coffee\text{–}cube\}\}.\end{aligned}$$

So if $v = \{1 \cdot ready - generator, 1 \cdot ready - food - complex,$
$1 \cdot m3\text{–}gas, 10000 \cdot g\text{–}bread, 1000 \cdot g\text{–}sugar, 1000 \cdot g\text{–}chease,$
$20000 \cdot g\text{–}water, 100 \cdot tea\text{–}cube, 15000 \cdot g\text{–}fresh\text{–}juice,$
$100 \cdot coffee\text{–}cube, 100 \cdot tea\text{–}cube, 5000 \cdot g\text{–}meat, 1000 \cdot g\text{–}butter\},$

this resource base is sufficient for this STS.

If $\Delta v = \{0.91 \cdot m3\text{–}gas\}$, then the considered STS is resilient to this impact, while in the case $\Delta v = \{0.91 \cdot m3\text{–}gas, 15000 \cdot g\text{–}water\}$, this STS is vulnerable to the impact. The same result would be, if $\Delta v = \{1 \cdot ready - food - complex\}$, that means food complex is destructed by the impact.∎

Let us consider now a general case of distributed sociotechnological systems.

5. Resilience of distributed sociotechnological systems

We shall describe distributed STS by application of techniques, considered in Section 2 regarding distributed IS, to local STS, considered in the previous Section 4.

However, we shall minimize the number of multiobjects, extended by geospatial information, by doing this only to those MO, which represent resources. This techniques not only essentially reduces the amount of work, necessary for knowledge base creation, but also excludes the necessity of consideration of rather

complicated issues, concerning MATS/device division to producing and nonproducing, as well as implanting associated information to unitary rules, entering set R_I and representing producing capabilities of the industrial segment of STS.

If so, all multiobjects like $n \cdot res$ in URs, entering both $R_H$and R_I, would be replaced by $n \cdot res/z$, where z, as higher, is the name of place (area) where n units of resource *res* are (would be) located.

Let us now define the so-called total order (TO), being multiset representation of the aforementioned flow of orders, generated by human segment of DSTS. This total order must be completed by STS IS to provide STS HS after NHI by necessary resources. After that we may apply Statement 8 to TO and UMG RG, which scheme represents technological base of STS IS, reduced by elimination of unitary rules, representing elements of STS IS, which are destroyed by NHI, and to resource base, which, similarly, is reduced by elimination of MO, representing OR, located at places, destroyed by NHI.

We shall introduce the following definition of the aforementioned total order $Q(Z)$:

$$Q(Z) = \left\{n \cdot a/z \mid n \cdot a/z \in \overline{v} \;\&\; \overline{v} \in \overline{V}_H \;\&\; \neg\left(z \in \overline{Z}\right)\right\}, \tag{45}$$

because it is necessary to produce only those resources, which are consumed at locations, not destroyed by NHI. Here, $\overline{V}_H = \{\overline{v}\}$ is one-element set of TMS, generated by UMG $S_H = <socium, R_H>$ (let us remember that all locations of OR are points).

On the other hand, TO would be completed by technological base, also affected (partly destroyed) by the same NHI. The result of this impact may be adequately represented by elimination from the set R_I those unitary rules, in which heads contain affected locations: it is clear that if point of origination of OR is destroyed, no OR is created.

So, TB of STS IS after NHI may be defined as follows:

$$\begin{aligned} R(Z) = \{&\langle a/z \to n_1 \cdot a_1/z_1, \ldots, n_m \cdot a_m/z_m\rangle \mid \\ &\langle a/z \to n_1 \cdot a_1/z_1, \ldots, n_m \cdot a_m/z_m\rangle \in R \& \neg\left(z \in \overline{Z}\right)\}. \end{aligned} \tag{46}$$

Similarly, STS IS resource base after NHI is

$$v(Z) = \left\{n \cdot a/z \mid n \cdot a/z \in v \& \neg\left(z \in \overline{Z}\right)\right\}. \tag{47}$$

By this it is easy to formulate criterion of sustainability of distributed sociotechnological system; generalization of (43) is evident.

Statement 9. DSTS, represented by UMG $S = <socium, R_H \cup R_I>$, with resource base v is resilient to NHI Z, if

$$\left(\exists <\overline{v}, \overline{v}'> \in \overline{V}_{S'_{Q(Z)}(v(Z))}\right) \overline{v} \subseteq \overline{v}', \tag{48}$$

where

$$Q(Z) = <n_1 \cdot a_1/z_1, \ldots, n_m \cdot a_m/z_m>, \tag{49}$$

$$S'_{Q(Z)} = <q, R(Z) \cup \{<q \to n_1 \cdot a_1/z_1, \ldots, n_m \cdot a_m/z_m>\}>. \tag{50}$$

Otherwise, this DSTS is vulnerable to this NHI. ∎

As seen, (45)–(50) fully correspond to verbal description of this criterion.

Now, it would be reasonable to consider in more details multigrammatical representation of the most significant elements of DSTS IS, usually named critical infrastructures.

6. Multigrammatical representation of critical infrastructures and their interconnections

We shall consider the most important critical infrastructures, which operation is absolutely necessary to provide human segment of DSTS by all required resources and services. Until it is said otherwise, we assume that all elements of these CI are stationary.

Let us begin with *electricity infrastructure* (EI), containing generation facilities (power plants), transforming/distributing substations (TDS), and terminal units (TU), providing delivery of electrical energy to the consumers. All listed elements are connected by links and joined by transmission networks together into electrical grids, which all together form EI [14–16].

We shall analyze EI, beginning from terminal units. Any TU in order to deliver one unit of power to the consumer, switched to this TU, must get it from the closest TDS, connected with it by link. So, unitary rule, representing this fragment of EI, would be as follows:

$$kW/z \to n \cdot kW/z', 1 \cdot link/z'', \tag{51}$$

where z, z', and z'' are, respectively, locations of TU, supplying it TDS, and connecting them link. Here, z and z' may be, as usual, the points, while z'' is the line, represented by coordinates of its basic points (if it is straight, two such points—start and final—are sufficient, and they are, evidently, z' and z). Value $n > 1$ depends, finally, on losses of power while its transfer by the link; n is a rational number (as higher in Section 4, we use multiobjects with rational multiplicities, which do not change any of definitions, introduced higher for integer case [12, 13]).

If TDS, located at point z', is connected to terminal units, located at points $z_1, \ldots, z_m$, this fragment of EI is represented by m unitary rules:

$$\begin{gathered} kW/z_1 \to n_1 \cdot kW/z', 1 \cdot link/z''_1, \\ \ldots. \\ kW/z_m \to n_m \cdot kW/z', 1 \cdot link/z''_m. \end{gathered} \tag{52}$$

where $z''_1, \ldots, z''_m$ are the lines, beginning at z' and ending at $z_1, \ldots, z_m$, respectively.

Similarly, fragments of EI, consisting of connected TDS, may be described. In this case z' would be the location of delivering substation, while $z_1, \ldots, z_m$—the locations of substations, consuming power from it.

Thus, treelike fragment of EI is described, until z' is the location of power plant, generating electrical energy.

Power plant, in turn, may be represented by UR:

$$kW/z \to n_1 \cdot res_1/z_1, \ldots, n_k \cdot res_k/z_k, \tag{53}$$

where $n_1, \ldots, n_k$ are the amounts of resources $res_1, \ldots, res_k$, which must be delivered to locations $z_1, \ldots, z_k$, respectively, in order to generate 1 kW of electrical energy at location z, from which it may be delivered by links to the closest TDS. By this, evidently, $z_1, \ldots, z_k$ are locations of terminal units of other CI, which, in turn,

deliver aforementioned resources (energy carriers, EC)—most frequently, natural gas and oil products—transferred to power plants by pipelines, forming *fuel infrastructure* [6–9, 17].

Terminal units of the pipeline, which deliver resources to consumers, are represented as heads of unitary rules of the form

$$res/z \to n \cdot kW/z', 1 \cdot link/z', 1 \cdot res/z', \tag{54}$$

where multiobject $n \cdot kW/z'$ represents the TU of electricity infrastructure, providing delivery of one unit of resource *res* from location z' to location z. This amount of energy is consumed by pump, executing resource transfer. If there are some losses during such transfer, then MO $n' \cdot res/z'$, where $n' > 1$, would be used in (54) instead of $1 \cdot res/z'$.

Distributing facilities of pipelines may be represented similarly to (52):

$$\begin{gathered} res/z_1 \to n_1 \cdot kW/z', 1 \cdot link/z'_1, n_1 \cdot res/z'_1, \\ \dots \\ res/z_m \to n_m \cdot kW/z', 1 \cdot link/z'_m, n_k \cdot res/z'_m, \end{gathered} \tag{55}$$

which means delivered energy carrier, entering this facility, is distributed to m pipes by application of the corresponding amounts of electrical power. As higher, $z'_1, \dots, z'_m$ are the lines, beginning at z' and ending at $z_1, \dots, z_m$, respectively.

As it is clear, described techniques may be applied in the case of place of origination of EC, i.e., facility, producing various oil derivatives and pipeline gas, used as fuel by power plants. This facility is described as follows:

$$res/z \to n_1 \cdot res_1/z_1, \dots, n_k \cdot res_k/z_k, \tag{56}$$

where all multiobjects are interpreted as higher.

The same techniques may be easily applied to *water supply* [18–20], *heating networks* [21–23], as well as *sewage networks* [24]. The latter differ from all previous by direction—"generation" of sewage waters is performed by terminal points, and "delivery" is performed to the root of the network, being the outflow point.

As may be seen from this short description, different critical infrastructures contain stationary facilities, producing various resources, as well as intermediate nodes and links, delivering necessary amounts of these resources to terminal units, contacting with objects of another CI, which operation depends on the mentioned amounts.

Let us note that operation of any DSTS is based not only on stationary objects of CI but also on its logistical capabilities—first of all, on mobile component of DSTS, providing relocation of material objects. Thus, sustainability of DSTS in a great degree depends on capabilities of transportation vehicles, which remained in the active state after NHI, as well as of stationary objects of *transportation infrastructure*, providing motion of these vehicles, as well as of the required resources (first of all, fuels and electrical energy). Such capabilities are necessary for relocation of mentioned objects from places of their creation or storage to places of their consumption.

To represent transportation capabilities of DSTS, we shall use the following techniques. Unitary rule

$$res/z \to m \cdot way - z' - z, 1 \cdot res/z' \tag{57}$$

means that one unit of resource *res* may be removed from the place of its storage z' to the place of its consumption z by any of ways, which are available by mobile component of technological segment of DSTS. It is important that multiplicity m is the mass of one unit of resource *res*, measured in some fixed for DSTS units (e.g., kg). According to the techniques of multigrammatical representation of similar problems, proposed in [12, 13], OR $way - z' - z$ is detailed by unitary rules like

$$way - z' - z \rightarrow 1 \cdot z_1, l_1 \cdot e/z', \tag{58}$$

$$z_1 \rightarrow 1 \cdot z_2, l_2 \cdot e/z', \tag{59}$$

$$\ldots$$

$$z_{k-1} \rightarrow 1 \cdot z_k, l_k \cdot e/z', \tag{60}$$

$$z_k \rightarrow 1 \cdot z', l_{k+1} \cdot e/z', \tag{61}$$

which describe path from z' to z, passing through points $z_1, \ldots, z_k$, such that distance from z' to z_k is l_{k+1} km; from z_k to z_{k-1} — l_k km, ...; from z_2 to z_1 — l_2 km; and from z_1 to z — l_1 km. As becomes evident, application of unitary rules (57)–(61) provides generation of multiset:

$$\{1 \cdot res/z', m \cdot z', K \cdot e/z'\}, \tag{62}$$

where

$$K = m \cdot \sum_{i=1}^{k+1} l_k \tag{63}$$

is the number of kg-km, which must be removed from point z' to point z by the aforementioned mobile segment of DSTS in order to relocate one unit of resource *res* from z' to z. If the total order contains multiobject $M \cdot res/z$, then it is necessary to remove from z' to z $M \cdot K$ kg km. So if the resource base of DSTS, no matter, before NHI or after it, contains such or more amount of kg-km, this operation is possible; otherwise, it is not.

As seen, the presence of multiobjects like $K \cdot e/z'$ in the RB describes the capability of mobile segment of DSTS to relocate resources between its points, no matter what kind of transport is used (trains, trucks, aircrafts, helicopters, ships, etc.). NHI may eliminate some part of such resource, thus reducing transportation capabilities of DSTS. Also, if NHI strikes some points, entering path from z' to z, corresponding URs will be extracted from scheme R. So, NHI may destroy transportation segment of DSTS both in topological and resource dimensions.

Of course, there may be different ways of one and the same resource relocation. Representation of any of them begins from UR like (58), which the head is $way - z' - z$.

One more issue to be considered here is interconnection of the transportation infrastructure with other CI (first of all, electricity and fuel). This one may be done by including to scheme R unitary rules like

$$e/z' \rightarrow 1 \cdot vel/z', k \cdot res - mov - vel/z', \tag{64}$$

which means relocation of one kg km from place z' may be done by vehicle *vel* and this operation requires k units of resource, used by this vehicle for motion. If electricity-moved ground transport is used, then (64) becomes

$$e/z' \rightarrow 1 \cdot vel/z', k \cdot kW/z', \tag{65}$$

and electricity infrastructure is connected by terminal unit, having placed at z'. If petrol-moved ground transport is used, then (65) becomes

$$e/z' \rightarrow 1 \cdot vel/z', k \cdot l - petrol/z', \tag{66}$$

where multiobject $k \cdot l - petrol/z'$ represents the amount of liters of petrol, required for relocation of one kg-km by vehicle vel. Thus, connection of fuel infrastructure to transportation infrastructure is represented.

The same description may be used for aircrafts, helicopters, ships, etc., and such detailing may be done for every concrete vehicle, not only a class of vehicles.

Possibility of non-terminal multiobjects in the resource base of DSTS provides opportunity of representation of such ways of resource relocation, which use different vehicles, moving over one and the same path, and even different vehicles, moving over sequential fragments of the path. Such techniques will be considered in the separate publication, as well as issues, concerning recovery of the vulnerable DSTS.

Some primary results on the assessment of capabilities of vulnerable DSTS are presented in the next section; these results are based on the approach, applied to industrial systems in [2].

7. Assessment of maximal acting subsystem of vulnerable DSTS

Problem, which is considered in this section, is reverse to the previous one and may be formulated as follows.

Let DSTS be vulnerable in the sense of criterion, formulated by Statement 9, i.e., its producing segment and resource base, affected by NHI, are not sufficient for completion of total order, generated by human segment of DSTS.

Question is that what maximal part (subsystem) of DSTS may stay active, being supplied by sufficient amounts of resources, produced by the remained manufacturing facilities and resources. Similar question was for the first time posed in [2], where its objective was to get part of the order, which may be completed by the affected industrial system and its resource base.

Solution of this problem, proposed in [2], is based on application of the so-called dual multiset grammars for generation of orders, which may be completed given the remained resource base.

Let us consider at first local case, which in the simplest form may be described by UMG $S = <socium, R_H \cup R_I>$, resource base v, and NHI Δv, which in aggregate do not satisfy generalized criterion, represented by Statement 8.

We shall use MG $S^{-1} = <v - \Delta v, R^{-1}>$, where $R = R_H \cup R_I$, which is called *dual to UMG S*.

As may be seen, every terminal multiset $v \in \overline{V}_{S^{-1}}$ in general case may be a join of the following multisets:

1. $\{n_1 \cdot str_1, \ldots, n_l \cdot str_l\}$, representing integral structures, which may be active after NHI, because they have sufficient amounts of resources for operation

2. $\{n_1 \cdot pstn_1, \ldots, n_k \cdot pstn_k\}$, representing separate positions, entering some structures, which as a whole do not enter the previous set by the reason some of their positions cannot be supplied by all necessary resources

3. $\left\{n_1 \cdot person_1, \ldots, n_p \cdot person_p\right\}$, representing amounts of different types of persons, which may stay alive after NHI, because they would be supplied by necessary resources

4. $\{n_1 \cdot tech_1, \ldots, n_s \cdot tech_s\}$, representing amounts of the types of technical systems, which may operate after NHI, because resource base of STS contains all necessary resources for their operation

5. $\{n_1 \cdot dev_1, \ldots, n_q \cdot dev_q\}$, representing amounts of the types of separate devices, which do not enter any technical system from the previous set, but may operate separately because they may be supplied by necessary resources

6. $\{n_1 \cdot res_1, \ldots, n_t \cdot res_t\}$, representing amounts of resources, which would remain in the resource base of STS after all the rest RB would be attached to all previous elements of STS

In general case

$$\left|\overline{V}_{S^{-1}}\right| \geq 1, \tag{67}$$

so the only TMS, representing the final variant of distribution of the resources, remained in the RB after NHI, would be selected by application of some additional conditions. This task may be easily done by the use of filtering multigrammars (FMG); each FMG $S = < v_0, R, F >$ along with kernel v_0 and scheme R contains filter F, joining conditions, which provide selection of terminal multisets, generated by application of rules from scheme R [12, 13].

General case of the distributed STS is not more complicated and may be easily solved by application of the introduced techniques.

8. Conclusion

Proposed multiset-based framework for the assessment of resilience of distributed sociotechnical systems to natural hazards provides flexible and sufficiently easy representation of knowledge about DSTS operation, understood as resource production, relocation, and consumption. Criterial base, introduced in this paper, may be effectively applicable in a posteriori as well as in a priori mode, i.e., for detection of "weak places" in DSTS and their strengthening, not waiting, when NH will occur.

As it was said higher, analytical capabilities of the described framework may be extended by implanting universal time scale into the basic knowledge representation, i.e., into multiset grammars and their various modifications. Such extension would provide full description of dynamics of manufacturing processes, implemented by DSTS in normal state as well as by DSTS, partly destroyed by NHI, and estimation of time periods, necessary for production of various amounts of resources in both cases. This approach makes possible also precise solution of different problems, concerning DSTS recovery [25, 26], on the unified background of resource-based techniques. The main tool for such work is the aforementioned temporal multiset grammars, which will be described in the following publications.

Acknowledgements

The author is grateful to Prof. Fred Roberts and Prof. Don Saari for their useful discussions and to Prof. Alexey Gvishiani for his permanent support.

Author details

Igor Sheremet
Financial University under the Government of Russian Federation, Moscow, Russia

*Address all correspondence to: sheremet@rfbr.ru

References

[1] Gvishiani AD, Roberts FS, Sheremet IA. On the assessment of sustainability of distributed sociotechnical systems to natural disasters. Russian Journal of Earth Sciences. 2018;**18**:ES4004. DOI: 10.2205/2018ES000627

[2] Sheremet IA. Multiset analysis of consequences of natural disasters impacts on large-scale industrial systems. Data Science Journal;**17, 4**:1-17. DOI: 10.5334/dsj-2018-004

[3] Bertalanffy L. General System Theory: Foundations, Development, Application. New York: George Braziller; 1988. p. 289

[4] Vernadsky V. The Biosphere: Complete Annotated Edition. New York: Copernicus; 1998. p. 196

[5] National Infrastructure Protection Plan. Energy Sector. https://www.dhs.gov/nipp

[6] Macaulau T. U.S. Critical Infrastructure Interdependency Wheel (CIIW). http:/www.tysonmacaulay.com/CIIWwhitepaperUS-july142008.pdf

[7] Alcaraz C, Zeadally S. Critical infrastructure protection: Requirements and challenges for the 21st century. International Journal of Critical Infrastructure Protection. 2015;**8**:53-66. DOI: 10.1016/j.ijcip.2014.12.002

[8] Rinaldi S, Peerenboom JP, Kelly TK. Identifying, understanding, and analyzing critical infrastructure interdependencies. IEEE Control Systems Magazine. 2001;**21**:11-25. DOI: 10.1109/37.960131

[9] Vespignani A. Complex networks: The fragility of interdependency. Nature. 2010;**464**:984-985. DOI: 10.1038/464984a

[10] Rehak D, Senovsky P, Hromada M, Lovecek T, Novotny P. Cascading impact assessment in a critical infrastructure system. International Journal of Critical Infrastructure Protection. 2018;**22**:125-138. DOI: 10.1016/j.ijcip.2018.06.004

[11] Haimes YY, Jiang P. Leontief-based model of risk in complex interconnected infrastructures. Journal of Infrastructure Systems. 2001;**7**:1-12. DOI: 10.1061/(ASCE)1076-0342(2001)7:1(1)

[12] Sheremet IA. Recursive Multisets and their Applications. Moscow: Nauka; 2010. p. 292 (in Russian)

[13] Sheremet IA. Recursive Multisets and their Applications. Berlin: NG Verlag; 2011. p. 249

[14] Li H, Rosenwald GW, Jung J, Liu C-C. Strategic power infrastructure defense. Proceedings of the IEEE. 2005;**93**(5): 918-933. DOI: 10/1109/JPROC.2005.847260

[15] Amin M. Security challenges for the electricity infrastructure (supplement to computer magazine). Computer. 2002; **35**(4):8-10 http://doi.ieeecomputersociety.org/10.1109/MC.2002.10042

[16] Katay ME. Electric power industry as critical infrastructure. Network World. 2010. https://www.networkworld.com/article/2217677/data-center/electric-power-industry-as-critical-infrastructure.html

[17] Liu K, Wang M, Zhu W, Wu J, Yan X. Vulnerability analysis of an urban gas pipeline network considering pipeline-road dependency. International Journal of Critical Infrastructure Protection. 2018;**22**:125-138. DOI: 10.1016/j.ijcip.2018.08.008

[18] Peri-urban Water and Sanitation Services. Kurian M, McCarney P, editors. Policy, Planning and Method. New York: Springer; 2010. p. 300. DOI: 10.1107/978-90-481-9425-4_11.

[19] Water supply. www.who.int.read/em2002chap7. 2018. pp. 92-126

[20] Water supply system. Encyclopedia Britannica. https://www.britannica.com/technology/water-supply-system

[21] Mazher AR, Liu S, Shukla A. A state of art review on the district heating systems. Renewable and Sustainable Energy Reviews. 2018;**96**:420-439. DOI: 10.1016/j.rser.2018.08.005

[22] Lund H, Werner S, Wiltshire R, Svendsen S, Thorsen J-E, Hvelplund F, et al. 4th Generation District Heating (4GDH): Integrating smart thermal grids into future sustainable energy systems. Energy. 2014;**68**:1-11. https://doi:10.1016/j.energy.2014.02.019

[23] Werner S. International review of district heating and cooling. Energy. 2017;**137**:617-631. DOI: 10.1016/j.energy.2017.04.045

[24] Makropoulos C, Rozos E, Tsoukalas I, Plevri A, Karakatsanis L, Karagiannidis L, et al. Sewer-mining: A water reuse option supporting circular economy, public service provision and entrepreneurship. Journal of Environmental Management. 2018;**216**: 285-298. DOI: 10.1016/j.jenvman.2017.07.026

[25] Stergiopoulos G, Kotzanikolaou P, Theocharidou M, Lykou G, Gritzalis D. Time-based critical infrastructure dependency analysis for large-scale and cross-sectoral failures. International Journal of Critical Infrastructure Protection. 2016;**12**:46-60. DOI: 10.1016/j.ijcip.2015.12.002

[26] Cavdaregla B, Hammel E, Mitchell JE, Sharkey TC, Wallace WA. Integrating restoration and scheduling decisions for disrupted interdependent infrastructure systems. Annals of Operations Research. 2013;**203**:279-294. DOI: 10.1007/S10479-011-0959-3

Edited by John P. Tiefenbacher

Natural Hazards — Risk, Exposure, Response, and Resilience demonstrates advanced techniques to measure risks, exposures, responses, and solutions to hazards in an array of communities. Eleven original research reports by international scholars on hazard assessment and management are organized into four sections: studies assessing risk using in-depth modeling and technological detection to provide insight into problems associated with earthquakes, torrential rains, and nuclear power plant safety; studies revealing the spatial distributions of exposure and impacts from an assortment of hazards; studies examining human response to increased awareness of the patterns of hazard; and a study demonstrating assessment of resilience of sociotechnological systems to natural hazards. This volume contributes new conceptual and practical commentaries to assess, mitigate, and plan for disasters.

Published in London, UK

IntechOpen

ISBN 978-1-78985-441-1
9 781789 854411